UNIVERSITY OF OKLAHOMA

GRADUATE COLLEGE

EXPERIMENTAL AND NUMERICAL STUDIES ON THE STRUCTURAL DYNAMICS OF FLAPPING BEAMS

A DISSERTATION

SUBMITTED TO THE GRADUATE FACULTY

in partial fullfillment of the requirements for the

Degree of

DOCTOR OF PHILOSOPHY

By

ORHAN OZCELIK
Norman, Oklahoma
2015

EXPERIMENTAL AND NUMERICAL STUDIES ON THE STRUCTURAL DYNAMICS OF FLAPPING BEAMS

A DISSERTATION APPROVED FOR THE
SCHOOL OF AEROSPACE AND MECHANICAL ENGINEERING

BY

Dr. Peter J. Attar, Chair

Dr. M. Cengiz Altan, Co-Chair

Dr. J. David Baldwin

Dr. Robert L. Shambaugh

Dr. Prakash Vedula

Acknowledgements

I would like to express my sincere gratitude and thanks to my advisor, Dr. Peter J. Attar, for his invaluable guidance and support throughout this study. This work would not have been possible without his supervision and continuous help. I would also like to thank Dr. M. Cengiz Altan for his encouragement and mentorship throughout my graduate studies.

I would like to thank the members of my dissertation committee, Dr. J. David Baldwin, Dr. Robert L. Shambaugh, and Dr. Prakash Vedula, for their valuable comments and suggestions.

During my doctoral study at the University of Oklahoma, numerous individuals contributed to this research in various ways. All of them will long be remembered with appreciation for their friendship and assistance.

Finally, my special thanks and gratitude go to my parents, Ayse and Ibrahim, and my sister Mine for their unconditional support and encouragement.

Table of Contents

List of Tables

List of Figures

Abstract

The nonlinear structural dynamics of slender cantilever beams in flapping motion is studied through experiments, numerical simulations, and perturbation analyses.

A flapping mechanism which imparts a periodic flapping motion of certain amplitude and frequency on the clamped boundary of the appended cantilever beam is constructed. Centimeter-size thin aluminum beams are tested at two amplitudes and frequencies up to, and slightly above, the first bending mode to collect beam tip displacement and surface bending strain data. Experimental data analyzed in time and frequency domains reveal a planar, single stable (for a given flapping amplitude-frequency combination) periodic beam response with superharmonic resonance peaks. Numerical simulations performed with a nonlinear beam finite element corroborate the experiments in general with the exception of the resonance regions where they overpredict the experiments. The discrepancy is mainly attributed to the use of a linear viscous damping model in the simulations. Nonlinear response dynamics predicted by the simulations include symmetric periodic, asymmetric periodic, quasi-periodic, and aperiodic motions.

To investigate the above-mentioned discrepancy between experiment and simulation, linear and nonlinear damping force models of different functional forms are incorporated into a nonlinear inextensible beam theory. The mathematical model is solved for periodic response by using a combination of Galerkin and a time-spectral numerical scheme; two reduced order methods

which, along with the choice of the inextensible beam model, facilitate parametric study and analytical analysis. Additional experiments are conducted in reduced air pressure to isolate the air damping from the material damping. The frequency response curves obtained with different damping models reveal that, when compared to the linear viscous damping, the nonlinear external damping models better represent the experimental damping forces in the regions of superharmonic and primary resonances. The effect of different damping models on the stability of the periodic solutions are investigated using the Floquet theory. The mathematical models with nonlinear damping yield stable periodic solutions which is in accord with the experimental observation.

The effect of excitation and damping parameters on the steady-state superharmonic and primary resonance responses of the flapping beam is further investigated through perturbation analyses. The resonance solutions of the spatially-discretized equation of motion (via 1-mode Galerkin approximation of the inextensible beam model), which involves both quadratic and cubic nonlinear terms, are constructed as first-order uniform asymptotic expansions via the method of multiple time scales. The critical excitation amplitudes leading to bistable solutions are identified and are found to be consistent with the experimental and numerical results. The approximate analytical results indicate that a second harmonic is required in the boundary actuation spectra in order for a second order superharmonic response to exist. The perturbation solutions are compared with numerical time-spectral solutions for different flapping amplitudes. The first-order perturbation solution is determined to be in very good agreement with the numerical solution up to 5° while above this angle differences in the two solutions develop, which are attributed to phase estimation accuracy.

CHAPTER 1

Introduction

1.1 Motivation and Literature Review

The characterization of the structural dynamics of rapidly actuated slender beams has been of interest in a number of traditional engineering disciplines such as the rotorcraft dynamics [1–5], robotic manipulators [6] and wind-turbine blades [7]. Recently, there has been considerable research interest in the nonlinear structural dynamics of slender (i.e., flexible) cantilever beams which are put into "flapping motion." The interest stems primarily from the fact that "flapping beams" have now found novel applications in emerging technologies which are motivated by biomimetics and energy harvesting. These application areas include flapping-wing micro aerial vehicles (MAVs) [8–12], fish-like underwater propulsion [13–16], and power extraction via flapping harvesters [17–21].

In many of these applications the amplitude of vibration is large thus rendering various types of nonlinearities important [22] and placing the problem in the realm of nonlinear structural dynamics. Therefore, it can be expected that the structural dynamics of flapping beams would possess many of the complex phenomena (bifurcation, quasi-periodicity, chaos, etc.) noted in nonlinear dynamics [22–24], and in particular nonlinear beam dynamics [25–31].

In the last couple of decades there have been many research efforts which aimed to characterize, through numerical simulation and experiment, the non-

linear structural dynamics of beams. Mathematical and numerical models used in the simulation of nonlinear beam dynamics have contained various degrees of complexity ranging from finite element solutions for geometrically exact formulations of curved composite beams [32] to single-mode solutions for the chaotic vibrations of beams with nonlinear boundary conditions [28]. The literature on nonlinear dynamics and, more specifically, beam dynamics is vast and the review of the literature to be given here will include only references deemed most relevant for the current study. For a more extensive review of the literature the reader is referred to references [24,33] (nonlinear dynamics), [22] (nonlinear vibrations) and [34] (nonlinear vibration of beams).

There have been a number of studies in which beams were excited through base motion [35–40]. Pai and Nayfeh [35] studied the non-planar oscillations of cantilever beams subjected to base excitation. Through a combination of Galerkin projection and the method of multiple scales, they found that the consideration of geometric nonlinearity was necessary to properly characterize the response of low-frequency modes while inertial nonlinearity dominated the response of high-frequency modes. Pai and Nayfeh [35] also characterized the dynamic behavior of non-planar motions and found that, for different parameters, the motion ranged from steady whirling to chaotic. In the work of Zaretzky and Crespo da Silva [39] the dynamic response of a beam forced with periodic transverse base excitation was studied. They investigated the effects of base stiffness, small imperfections along the beam span, and linear and nonlinear damping. Of particular relevance to the current study, they found that in order to correctly predict the experimentally-measured peak response (on a frequency response curve) of the beam's third mode, which had planar motion, it was necessary to use a nonlinear viscous damping model.

Not doing so resulted in a predicted response magnitude which was almost twice the experimentally measured value.

The flapping motion of the beam can be realized in the mathematical or computational model through imposition of time-dependent boundary conditions on the governing equation of motion. It appears that the earliest work in the area of analytical solutions for beams with time-dependent boundary conditions is due to Mindlin and Goodman [41]. Other early works include those of Herrmann [42] and Berry and Naghdi [43]. Aravamudan and Murthy [44], using the Galerkin method and the transformation introduced by Mindlin and Goodman [41], derived equations of motion which govern nonlinear, planar transverse vibrations of slender uniform beams with mid-line extensibility and time-dependent boundary conditions. Vibration response of beams with various time-dependent boundary conditions was studied for different slenderness ratios and the stability of periodic solutions was investigated. Frequency response curves obtained for the first and second mode revealed a spring-hardening type behavior for all boundary conditions considered. For the clamped-free (cantilever) beam, stability analysis revealed a branch of unstable periodic solutions which was a function of the forcing magnitude. More recent work which has studied elastodynamics with time-dependent boundary conditions includes the analytical work of Lin and Lee [45] involving forced vibration and boundary control of pre-twisted beams and the investigation, by Paraskevopoulos *et al.* [46], of penalty-type formulations for implementing time-dependent boundary conditions in finite element solutions.

Stanford *et al.* [47] investigated strategies for model order reduction for flapping beams with periodic base actuation. Through comparison with a finite element model, which included a co-rotational formulation for the elas-

tic terms and a multi-body dynamics formulation for the inertial terms, the efficiency and accuracy of computational models based upon proper orthogonal decomposition and a spectral (in time) element method were studied. Of particular interest to the current study, it appears that undamped, full order (finite element) simulations predicted aperiodic response for flapping at 45° amplitude and at a frequency much below the beam's first natural frequency. As the main purpose of the paper was not to explore the physics of nonlinear flapping beams, Stanford *et al.* [47] did not discuss this response in detail.

While the simple geometry of beams would appear to make their response characterization somewhat simple, when the amplitude of vibration becomes comparable to their length, various effects including geometric, inertial, and damping nonlinearities complicate the analysis. In view of the fact that the characterization of the large amplitude vibration of actuated, slender beam structures is important for many engineering applications including developing technologies such as flapping-wing micro aerial vehicles (MAVs) [11, 12], biomimetic robotic propulsion [13, 14], electronic cooling devices [48, 49], and energy harvesting mechanisms [17, 18], gaining a better understanding of the effect of *nonlinear damping* on the large amplitude flapping motion of slender beams is important.

Dissipation of mechanical energy in vibrating structures is most often referred to as damping and is related to a number of different mechanisms which operate inside (internal) or outside (external) of the structure. Internal damping (or material damping) can be associated with several mechanisms which include, to name only a few particular to metals, grain boundary viscosity, point defect relaxations, intercrystalline thermal currents, dislocation mechanisms, and localized plastic deformation [50, 51]. In general, damping forces

which arise from external mechanisms are larger than those which are due to internal mechanisms. These external damping mechanisms may include dry friction at the structure's contact joint and various forms of fluid-structure interactions governed by the viscous, inertial, and convective forms of momentum transport which take place between the structure and the surrounding fluid medium [52].

The fluid forces acting on a bluff body, a cylinder for instance, which undergoes oscillatory motion in an incompressible viscous fluid have been approximated for decades based upon a semiempirical approach proposed by Morison *et al.* [53]. According to the Morison model, the oscillatory fluid force exerted on the body is regarded as being contributed by two components termed "added mass" and "fluid damping" which are in-phase and out-of-phase with the acceleration of the body, respectively [53–55]. These force components are expressed as velocity-squared-dependent drag force and acceleration-dependent inertial force with the coefficients determined experimentally [56]. The added mass component is known to be responsible for lowering the *in vacuo* resonance frequencies of the structure while the fluid damping component is the primary cause of the dissipation of the structure's mechanical energy. The added mass (or virtual mass) force is due to the acceleration imparted on the mass of the fluid displaced by the body. On the other hand flow separation in viscous fluids produces vortices with out-of-phase transport velocities which in turn give rise to vortex-shedding-induced fluid damping forces on the body [55, 57].

When a body with salient edges is moved through a placid fluid, the flow separation occurs almost immediately after the motion begins [58]. In order to model the separated flow around a *rigid* flat plate with sharp edges,

and to determine the fluid forces acting on the plate, Jones [59] derived ordinary differential equations governing the evolution of the velocity field using a boundary integral formulation and an inviscid flow assumption. The motion of the plate, which is assumed to be normal to the quiescent inviscid fluid, gives rise to a two dimensional flow field comprised of a bound vortex sheet on the plate surface and free vortex sheets emanating from both edges. Inspired by the movements of flapping insect wings, Jones [59] numerically investigated the fluid vortex patterns and pressure forces induced by the unsteady motion of the flat plate during its deceleration, stopping, and re-acceleration in the reverse direction. It was determined that, during motion reversal of the plate, new starting vortices form and merge into the stopping vortices, resulting in a highly nonlinear fluid forcing regime.

In the case of a slender flexible beam executing large amplitude oscillations, the mathematical modeling of damping forces exerted on the beam structure by the surrounding quiescent fluid is a much more difficult task. The damping forces acting on the structure are strongly coupled with the structural motion and have nonlinear dependence on both the amplitude and frequency of the structural oscillations [57, 60]. Recently, Bidkar *et al.* [57] combined an inviscid vortex-shedding fluid model of Jones [59] and a linear Euler-Bernoulli beam model to develop a fluid-structure interaction model for predicting the nonlinear aerodynamic damping force acting on piezoelectrically excited cantilever beams oscillating with large amplitudes compared to their widths. The model is based upon a small deflection, single harmonic response assumption and requires experimentally-measured *in vacuo* mode shape, frequency, and amplitude in order capture large deflection effects. Despite the slight overestimation of the aerodynamic damping force, the semi-empirical model utilized

in this work gives better predictions when compared to previous studies which were based on purely inviscid or purely viscous diffusion theories [61].

In recent studies, Aureli *et al.* [52, 62] improved the complex hydrodynamic function approach of Sader [61] to take into account the effect of vortex shedding and added mass on the nonlinear fluid damping loads experienced by the cantilever beams undergoing large amplitude oscillations. They concluded that the proposed theoretical and numerical framework is generally able to accurately predict the resonance frequencies and damping factors. Kopman and Porfiri [15] combined the Morison's fluid force model with the Euler-Bernoulli beam model in an effort to predict the thrust force produced by the flexible caudal fin of a robotic fish. The Morison model coefficients were determined empirically for three different fin geometries and a range of tail-beating frequencies (1-2 Hz) and amplitudes (10°-20°). The model prediction agreed well with the experimental thrust data in the studied range of input parameters. In their piezohydroelastic model, Cha *et al.* [19] utilized the Morison formula to simulate the damping effect of the encompassing water medium on the piezoelectric energy harvesting efficiency of slender, base-excited cantilever beams. Model results were found to corroborate the experimental results for a number of submersion lengths.

Justifying the implementation of flapping beams in place of their traditional competitors, e.g., fixed-wing aerial vehicles, screw propellers, etc., is challenging due, in part, to the trade-off between demanding power requirements and output of flapping actuation [63–66]. One way to maximize energy efficiency appears to be exploiting the *resonance response* of the flapping beams. From this perspective, gaining a thorough understanding of the response of flapping beams to various resonant excitations appears to be of paramount importance.

It is well-known that the response of a single degree of freedom forced spring-mass-damper system is mathematically expressed as a superposition of homogeneous and particular solutions which are termed (damped) "free oscillations" and "forced oscillations," respectively [67]. The free oscillation term which has the same frequency as the (damped) natural frequency of the system decays with time; whereas, the latter (forced oscillation term) having the same frequency as the forcing persists and leads to the steady-state response of the system. Without damping, when the forcing frequency is equal to the natural frequency, the amplitude of the response grows without bound, which is termed *resonance*. With light damping, the response amplitude gets very close to a maximum value at the resonance. In addition to the aforementioned resonance, i.e., *primary resonance*, when the system is *nonlinear*, there can be *secondary resonances* (e.g., superharmonic and subharmonic resonances) which occur at fraction or integer multiples of the natural frequency [68, 69].

In the steady-state response of a nonlinear system, free oscillations can persist with time and coexist with the forced oscillations despite the presence of damping. For example, depending on the initial conditions, a cubic nonlinearity would sustain free oscillations in the steady-state and adjust their frequency to three times the frequency of accompanying forced oscillations. The large-amplitude steady-state motion of this kind, namely, third-order superharmonic response, is activated by the resonance condition which occurs when the forcing frequency nears one-third of the system's natural frequency. Depending on the degree of nonlinearity, number of degrees of freedom, and nature of forcing, many different resonance conditions may be identified in nonlinear systems [69].

Superharmonic and primary resonance responses of generic nonlinear mod-

els, such as the Duffing oscillator, have been investigated in detail with varying emphasis placed on the stability and effect of system parameters [70–72]. Using multiple scales perturbation (up to second order) and numerical time integration methods in a comparative manner, Rahman and Burton [70] studied the steady-state response amplitude and stability of a Duffing oscillator in the vicinity of third-order superharmonic resonance. Regarding the response amplitude, the second-order perturbation solution did not differ from the first-order solution and yielded a mediocre agreement with the numerical solution. In a recent work, Dai *et al.* [72] applied a time-spectral method to gain insight into the multi-valued response and jump phenomenon associated with the third-order superharmonic response curves of the Duffing equation. Variation of amplitude of each harmonic component with frequency for multi-valued and single-valued solutions were analyzed, effects of damping coefficient and excitation amplitude on the response curves were explored.

In addition to these mainly theoretical investigations, there have been some recent papers which explore resonant oscillations in a more applied setting. For example, it has been known that the induced power requirement for flapping flight decreases with increasing flapping amplitude and decreasing flapping frequency [63]. Accordingly, maximizing the passive bending of a flexible wing via flapping nearby its natural frequency has been thought of as a means of reducing the input power required for flapping. Thus, a number of flapping-wing MAVs has been designed to operate in the vicinity of the primary resonance yielding promising results [73, 74]. Computational efforts of Masoud and Alexeev [75] revealed that the large-amplitude resonance oscillations of elastic flapping wings drastically enhance aerodynamic efficiency. Later studies [76, 77] which utilized nonlinear models suggested that flapping in a fre-

quency range close to the third-order superharmonic resonance, as opposed to primary resonance, would maximize the aerodynamic performance of flapping wings. Similarly, in a recent numerical study, Zhu and Zhou [78] reported that flexibility increases the energy efficiency of a flapping wing when the flapping frequency is less than the natural frequency.

Piezoelectric patch actuators have been used to drive flapping wings [79,80] and, recently, Lindholm and Cobb [80] demonstrated experimentally that a piezoelectrically-actuated flapping wing is most power efficient when flapping at the system's resonant frequency. They pointed out that future research with piezoelectrically-driven flapping-wing MAVs should focus primarily on the resonant flapping.

Additionally, over the past decade or so, base-excited flexible cantilever beams with piezoelectric patches attached near its clamped-end (where the strains are large) have received tremendous research interest for harvesting of vibratory mechanical energy (i.e., base excitation) drawn from the environment in the form of electrical energy [81, 82]. Advancements in the realm of vibratory energy harvesting research have shown that piezoelectric patches are efficient only if a steady-state peak amplitude (i.e., resonance response) *with large frequency bandwidth* is furnished by the "carrier" oscillator [82]. In this regard, features such as the existence of secondary resonances, broadening and bending of primary/secondary resonance peaks, and jump phenomena, which are peculiar to nonlinear oscillators, have been deemed favorable as they could be exploited to solve small bandwidth and low-frequency excitation problems and, thus, to improve the effectiveness of the vibratory energy harvesting. For instance, Barton *et al.* [83] demonstrated that the superharmonic resonances of a Duffing oscillator can be used to harvest energy from low-frequency exci-

tations.

1.2 Objectives and Scope of the Dissertation

The primary goal of the present dissertation is to improve the state of knowledge regarding the structural dynamic response of base-actuated (flapping) beams. In order to achieve this goal experimental, numerical, and analytical methods are used to characterize the time-dependent strain and displacement fields of flapping aluminum beams operating at both standard and reduced air pressures.

The remainder of the dissertation is organized in the following manner. First, in Chapter 2 a comprehensive description of the experimental setup is provided. The details of the experimental procedure are given and the associated difficulties are addressed thoroughly. In Chapter 3, the nonlinear structural dynamics of the flapping beam is explored through experiment and numerical simulation. A brief outline of the experiments and a detailed description of the computational model are provided. The experimental beam tip displacement and surface bending strain data are compared with those gathered from the numerical simulations in both time and frequency domains. These comparisons not only provide valuable insight towards the overall goal of the dissertation but also allow for various modeling assumptions to be tested. Additional numerical simulations are performed to analyze the beam response characteristics in terms of the bifurcations possible for the present problem.

One of the modeling assumptions which is made in Chapter 3 is that of a linear viscous damping model. In Chapter 4 this restriction is removed and the effects of nonlinear damping on the structural dynamics of flapping beams

are studied via experiment and numerical simulation. Experimental apparatus consisting of the flapping mechanism and the vacuum chamber is briefly summarized. A nonlinear inextensible beam model and the time-dependent boundary conditions used to approximate the experimental mechanism actuation are given. Then, the approximate solution of the problem in the spatial and time domains are presented along with the linear and nonlinear damping models. The utilized nonlinear damping models are of various simple functional forms which contain empirically determined constants. Such simple analytical models for damping are used to compensate for the inability, or unwillingness, to solve the true (complex) fluid-structure interaction problem [60]. Such an approach is widely used in the literature [39, 84–87], and if the parameters are chosen correctly it yields an analysis framework which can accurately and efficiently predict large amplitude beam vibration response. The numerical solution consists of a 1-mode Galerkin method for spatial discretization and a high-order time-spectral method for temporal discretization. In addition, to explore the effect of damping on the stability of periodic solutions, Floquet theory is used in conjunction with the numerical solutions. The experimental setup consists of the flapping mechanism and a vacuum chamber as well.

While numerical simulation can provide detail and fidelity, oftentimes analytical solutions can provide insight into parameter dependence which is unattainable through simulation. In addition, approximate analytical solutions can be used to improve simulation efforts by uncovering possible scaling laws, thereby providing information to reduce the number of simulations needed. Furthermore, analytical solutions can provide guidance in how to improve numerical methods for solving the problem in question. As such, in Chapter 5, the nonlinear response of flapping beams to resonant excitations

under nonlinear damping is studied analytically. Using the method of multiple time scales, modulation equations governing the steady-state amplitude phase evolution of the superharmonic and harmonic oscillations are obtained for the nonlinear ordinary differential equation which results from a 1-mode Galerkin spatial discretization of the inextensible beam theory. Frequency-response relationships and first-order approximate steady-state solutions at the superharmonic and primary resonances are determined. Approximate expressions for the critical excitation amplitudes which lead to bistable solutions are calculated. The approximate results are determined to corroborate the experimental and numerical observations of the single-valued stable response amplitudes. The analytical results are compared with those obtained with numerical solutions based upon a time-spectral method in order to ascertain the validity of the approximate solutions.

Finally, summary of conclusions and suggestions for the future works are given in Chapter 6. In particular, a future work is given, and expanded upon in Appendix K, regarding the improved modeling of fluid damping.

CHAPTER 2

Experimentation

2.1 Scope of the Chapter

In this chapter, the details of the experimental setup constructed to simulate the flapping beam problem are presented. The highly dynamic and nonlinear nature of the problem requires a robust, reliable flapping mechanism and appropriate measurement procedures. As such, the flapping mechanism should be able to produce the commanded output (i.e., flapping frequency and flapping amplitude) as accurately as possible while operating under large dynamic forces. On the other hand the measurement hardware and installation methods should be selected carefully for demanding cyclic response measurements. All these challenges and remedies are discussed in the present chapter.

The experimental setup consists of a *flapping mechanism*, a *beam specimen*, *response measurement equipment*, and a *vacuum chamber*. The response measurement equipment include data acquisition peripherals for strain measurement, a high-speed camera, tungsten halogen lamps, and a speed controller for the electric motor which actuates the mechanism. A picture showing all major components of the experimental setup is given in Figure 2.1.

2.2 Flapping Mechanism

In the course of this study, two flapping mechanisms (flapping test bed) were designed and constructed progressively to put an appended cantilever beam

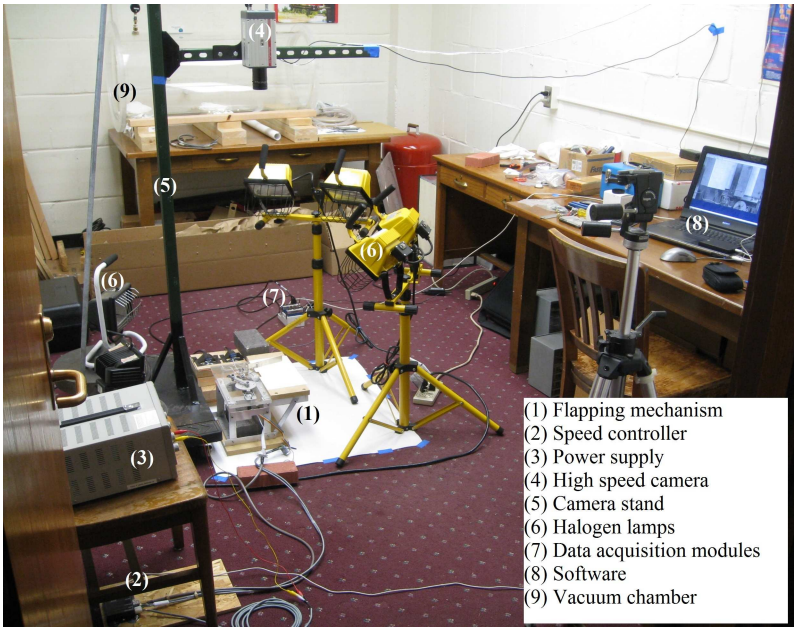

Figure 2.1: General view of the experimental setup.

structure into flapping motion. The initial design aimed at obtaining a three degrees of freedom (d.o.f) motion which consists of a flapping motion (in xy-plane), sweeping motion (in xz-plane), and rotation (about x-axis). This design, which will be referred to as the *initial design*, was determined to be unreliable and incapable of meeting the objectives of the present research. As such, realizing and controlling the second and third degrees of freedom (i.e., sweeping and rotation) were found to be very difficult and hampering the robustness of the principal degree of freedom (flapping motion). Therefore, the initial design was abandoned and modified to obtain a robust one d.o.f. flapping motion. The *final design* is based upon the same 4-bar crank-and-rocker mechanism as the initial design but differs in the manner by which the rocking motion of the 4-bar mechanism is transformed into flapping motion. In the remainder of this section, details of the *final* flapping mechanism will be presented. The initial flapping mechanism design is described in Appendix A.

2.2.1 Flapping Mechanism: Final Design

A robust flapping test bed which is capable of producing a reliable one d.o.f. flapping motion is constructed based on the 4-bar crank-and-rocker mechanism used in the *initial* design (see Appendix A). Front and rear views of the final design are shown in Figure 2.2. In order to reduce the effect of gravity, the appended beam is set into flapping motion in the horizontal plane.

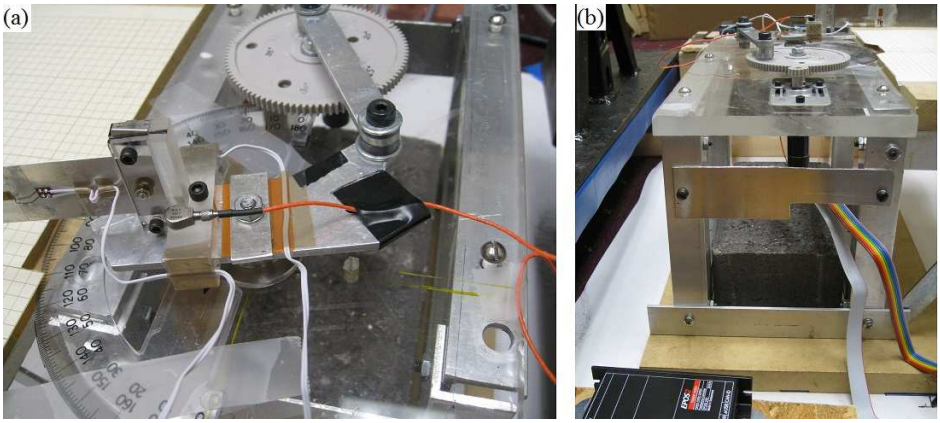

Figure 2.2: (a) Front view of the flapping mechanism, (b) rear view of the flapping mechanism.

Figure 2.3 depicts the top view of the test bed and underlying crank-and-rocker mechanism. A 96-tooth acetal spur gear (pitch diameter: 76.2 mm) functions as the crank link for the mechanism (Figure 2.3a). The flapping amplitude is adjusted by connecting the coupler link to a particular hole (joint C, Figure 2.3b) drilled on the gear. These radial holes on the gear provide different crank lengths and, thus, different flapping amplitudes varying between 15° and 35°. Kinematic analysis is performed to determine the mechanism dimensions needed to obtain a flapping motion which is approximately sinusoidal. Based on the kinematic analysis, the lengths of the *frame*, *coupler*, and *rocker* links are determined to be 95.3 mm, 82.6 mm, and 50.8 mm, respectively. As

depicted in Figure 2.2a, a beam to be tested is attached to the offset of the rocker link using an acrylic clamping fixture. The fixture provided an appropriate fixed (clamped) boundary condition. The offset distance, δ, between the beam's clamped base (point E) and joint A is set to 33.3 mm. Also, it is found that the obtuse angle between the segments AD and AE of the rocker link needs to be 150° in order to obtain a flapping motion which is symmetric about the reference axis (see Figure 2.3b). When the beam's clamped base, point E, is in line with the reference axis, the flapping angle, θ_f, is said to be zero (neutral position).

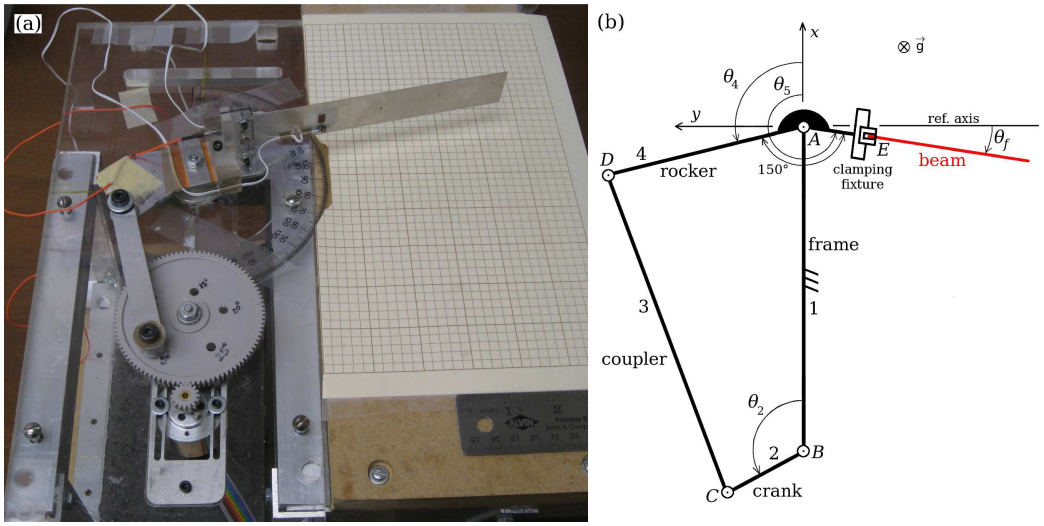

Figure 2.3: (a) Top view of the flapping mechanism, (b) 4-bar crank-and-rocker mechanism.

The analysis of the flapping mechanism kinematics (position, velocity, and acceleration) is straightforward and details can be found in many textbooks, such as Reference [88]. See Appendix B (and Appendix A) for the results of such an analysis. In Figure 2.4, the expected motion of the base point obtained from the kinematic analysis is compared with idealized (sinusoidal) flapping

motion at 1 Hz. The comparison is given for two flapping amplitudes 15° and 30°. It is noted that the flapping motion (angle) produced (theoretically) by the mechanism is close to the sinusoidal motion for the smaller flapping amplitude and deviates slightly for the larger amplitude. On the other hand the instantaneous velocity and acceleration of the base point deviate more significantly from a simple harmonic motion, a result which cannot be prevented due to crank-and-rocker nature of the mechanism.

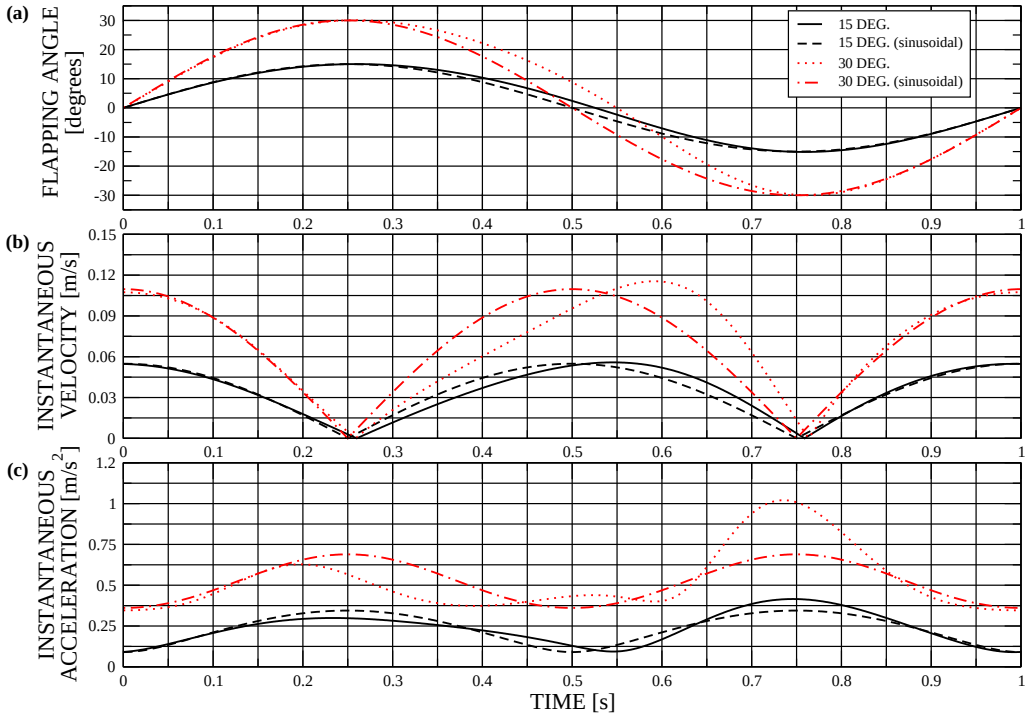

Figure 2.4: Comparison of idealized (sinusoidal) and designed kinematics of the beam's base point over one-cycle of flapping at two different flapping amplitudes (15° and 30°) at 1 Hz: (a) flapping angle θ_f, (b) magnitude of instantaneous velocity, (c) magnitude of instantaneous acceleration.

The flapping mechanism is actuated using a 40-Watt brushless DC electric motor Maxon® EC16 (Maxon Precision Motors, Inc.) which can be seen in Figure 2.2b. The motor is attached to an aluminum sleeve that can be mounted

at a desired distance from the main gear (see Figure 2.3a). A 16-tooth pinion is used to obtain 6:1 speed reduction ratio and the motor speed is controlled in a closed-loop feedback fashion with a Maxon® EPOS2 24/5 speed and position controller operating with a sampling rate of 100 kHz. Control signals are provided by a 3-channel, 512 counts-per-turn magneto-resistant encoder and Hall-effect encoder which are enclosed in the motor casing. This motor-controller drive system maintains precise control of the flapping frequency which would otherwise be compromised due to high inertial loads induced by the beam.

2.3 Beam Specimens

In the present study, the beam specimens are prepared from a flat sheet of aluminum alloy 6061-T6 (McMaster-Carr Supply Co., Atlanta, GA). Each beam specimen is cut from the flat sheet with nominal dimensions of 160 mm $\times$ 25 mm $\times$ 0.4 mm (Figure 2.5). The nominal length of the specimens used in the experiments (i.e., cantilever length) measure 150 mm and the remaining 10 mm is considered for the purpose of clamping. The physical and mechanical properties of the beams are listed in Table 2.1. The linear first bending mode frequency of the beam (with clamped-free boundary conditions) is calculated (and verified experimentally) as 14.5 Hz based on the selected dimensions. At high flapping frequencies it is likely that fatigue will occur in the strain gage and beam. To prevent prolonged use of a beam specimen several identical specimens are prepared.

The beam is mounted on the flapping test-bed with the aid of a clamping fixture. In order to reduce weight and inertial forces, the fixture is machined

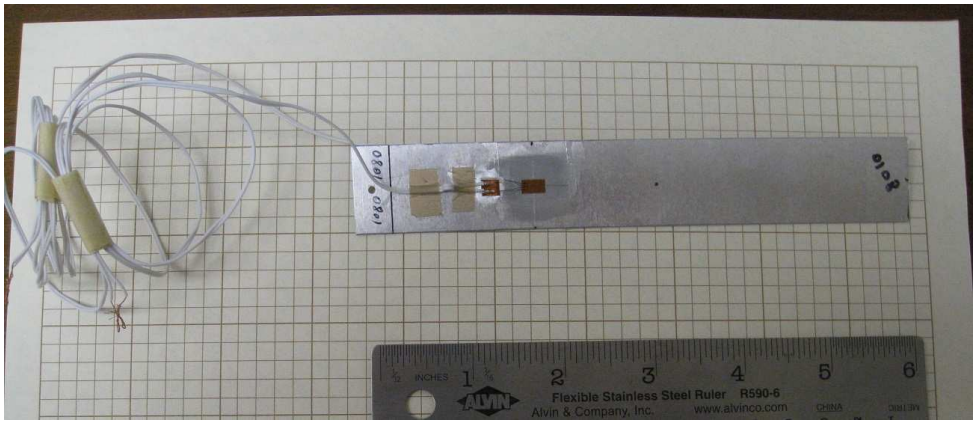

Figure 2.5: Aluminum 6061-T6 beam specimen.

from an acrylic plastic. The acrylic clamping fixture and an attached beam specimen are shown in Figure 2.6. The fixture is firmly bolted to the rocker link of the mechanism. The slotted bottom surface of the fixture where it is mounted on the rocker link ensures that the fixture does not swivel around the mounting bolt during flapping. The beam is clamped between the flat surfaces of a machined lug and a separate rectangular piece. The rectangular acrylic piece is attached to the lug using a pair of clamping bolts (socket-head cap screws). The beam to be clamped is placed in the space between these clamping bolts. A third bolt, whose sole purpose is preventing the beam from flying off if the clamp fails during operation, is located between the clamping bolts (see Figure 2.6). The rectangular acrylic piece may bulge out upon tightening and compromise uniform clamping. Therefore, two little aluminum shims of the same thickness as the beam are placed in the unsupported sides of the clamping bolts.

Table 2.1: Physical and mechanical properties of the beam specimens.

Measured overall length [mm]	160.0
Measured cantilever length, L [mm]	150.0
Measured width [mm]	25.37 ± 0.05
Measured thickness [μm]	398.1 ± 07
Measured bare (without strain gage installation) mass [g]	4.308 ± 0.001
Measured installation (2 strain gages and pressure pads) mass [g]	0.058 ± 0.003
Young's modulus [GPa][a]	68.3
Poisson's ratio[a]	0.33
Mass density [kg/m^3][a]	2713
Tensile yield stress [MPa][a]	248
Fatigue life equation based upon maximum normal stress σ_{max} [ksi] under fully-reversed loading conditions [cycles][a]	$10^{20.68-9.84\ \log_{10}(1.55\,\sigma_{max})}$

[a]Data obtained from Table 3.6.2.0 and Figure 3.6.2.2.8 of Reference [89].

2.4 Dynamic Response Measurements

The structural dynamic response of the flapping beam is characterized based on surface strain and tip displacement. Surface strain data is taken using a strain gage located 40 mm from the clamp. A high-speed camera is used to collect image data of the entire beam during flapping at very small time intervals. Collected image data is then processed to calculate the tip displacement.

2.4.1 Surface Strain

Electrical-resistance strain gage. The electrical-resistance foil strain gage is the most widely used versatile tool for strain measurement. A typical gage

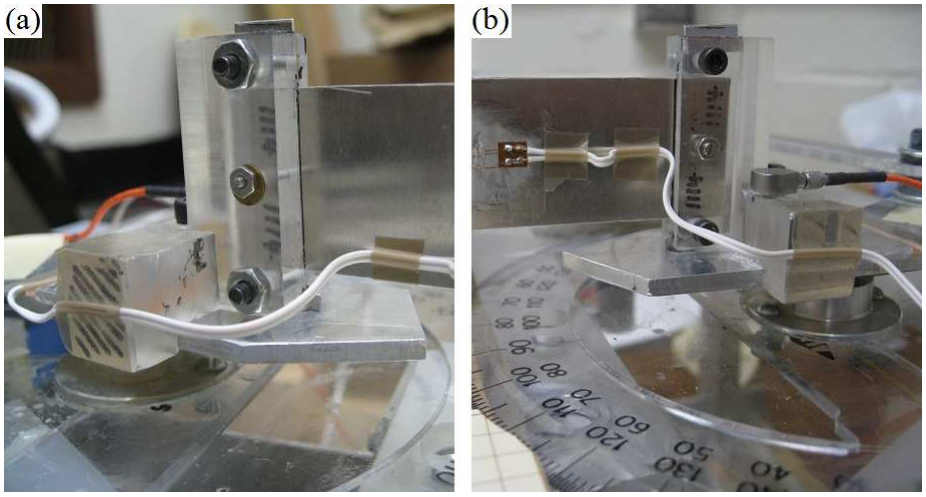

Figure 2.6: Close-up view of clamping fixture from (a) nut side, (b) bolt side. Note little shims placed top and bottom sides to prevent bowing of the clamp upon tightening.

consists of a strain-sensitive metal foil and plastic backing material (carrier) on which the foil is mounted. The metal foil is formed into a grid pattern to keep the gage length at a minimum while its sensitivity is retained. Its operation is based upon the principle that the electrical resistance of the strain-sensing metal foil changes in proportion to the strain to which it is subjected. This proportion is defined in terms of the *gage factor* which is the ratio of the unit change in resistance to the strain [90, 91].

Strain gage selection. Strain gage selection is of prime importance as there are number of parameters that contribute to obtaining reliable, accurate measurements and ease of installation. These parameters include type of strain measurement (static or dynamic), foil/carrier combination, gage length, gage resistance, leadwire attachment, environmental conditions (temperature, humidity, etc.), and stock availability. When strain gages are used to measure cyclic strains, which is the case in the present study, the fatigue life of

the gage installation, which depends on the amplitude levels sought in the application [92, 93], becomes very important.

Most commercial gages employ variants of Constantan (Cu-Ni), Karma (Ni-Cr-Al-Fe), or Isoelastic (Ni-Cr-Fe-Mo) alloy for the strain-sensing foil grid and polyimide or glass-fiber-reinforced phenolic (commonly called Bakelite) for the grid-backing (carrier) material [91]. Karma grid is known to exhibit better fatigue life, stability, and temperature compensation compared to the more widely-used Constantan grid. Isoelastic grid is specifically recommended for purely dynamic strain measurements and has a high gage factor which improves signal-to-noise ratio. Unfortunately Isoelastic grid construction exhibits nonlinearity above certain strain levels, poor temperature compensation, and susceptibility to magnetic fields (due to the constituent Fe). Owing to its limited range of applications and market size, manufacturers consider the Isoelastic grid gages as specialty products and mostly keep them as understocked items with narrow range of options (size, wiring, etc.) [93].

Gages are available with gage lengths ranging from 0.2 mm to 100 mm. The gage length is the active or strain-sensing length of the grid and is distinguished from the carrier (matrix) length which is the total length of the sensor. As the resulting strain measurement is an average of the strain over the gage length, shorter gage lengths are preferred if large strain gradients need to be captured. If the installation area is a hole or fillet or the test specimen experiences large bending curvatures, which is the case in the present study, shorter gage lengths (no greater than 10% of the radius) should be chosen. On the other hand, larger gages are easier to handle, have greater capacity for dissipating the heat produced by the gage current (i.e., lower power per unit grid area for the same gage resistance), and exhibit slightly better fatigue

endurance.

Typical values for the gage resistance are 120 Ω and 350 Ω while other resistance values are also available. Configuration of most strain acquisition systems requires the use of 120 Ω and 350 Ω gages. The high-resistance gages are mainly intended for use in circuits having sources of random resistance changes as the higher gage resistance increases the electrical output per unit of strain and maximizes signal-to-noise ratio for a constant power level. Moreover, for the same applied voltage, the high-resistance gage reduces the heat generation rate by a factor proportional to the resistance ratio. A high-resistance gage is also preferable as it suppresses unwanted signal fluctuations due to leadwire resistance effects [93].

One of the more formidable tasks in strain gage installation is the attachment of leadwires. When a gage with miniature dimensions and Karma alloy grid is selected, preattached leadwires definitely save significant time and effort. Soldering to Karma alloy is very difficult and requires special treatments and accessories (soldering station, pencil, flux, etc.). Although larger solder tabs are offered as an option, they take up extra space and result in extended total length. Therefore, the gages with preattached leadwires should be selected to facilitate installation and maintain consistency in measurements. Further details of the strain gage selection procedure can be found in References [91, 93, 94].

Based on the highlighted points given above, the strain gage with manufacturer's designation WK-13-062AP-350 (Micro-Measurements, Inc.) was selected and employed in the present study. The gage is designed for measuring strain in a single direction and consists of a modified Karma alloy grid and fiber-reinforced phenolic carrier. Each terminal is furnished with a pair of

high-endurance beryllium-copper leadwires. Nominal grid and carrier dimensions (length×width) measure 1.57 mm × 1.57 mm and 6.6 mm × 4.1 mm, respectively. Overall gage thickness is approximately 0.071 mm. Nominal grid resistance is 350 Ω. It is rated for the strain levels ±15000 μ-strain and the temperature interval from −269℃ to +290℃.

A pair of strain gages was installed along the midline, 40 mm away from the clamp, of each beam. One of the gages was installed along the axial (longitudinal) direction, while the other strain gage was installed on the other surface in the lateral direction. Data obtained from the gage in lateral direction was not used in the present study. In the following section, gage installation is discussed with particular attention given to the fatigue endurance.

Strain gage installation. The strain gage installation is composed of four phases: beam surface preparation, gage bonding, pressure pad (also called terminal strips) bonding, and wire soldering.

Surface preparation practices for the strain gage bonding are discussed in detail in Reference [95]. After the beam is laid on a flat surface and secured with the Scotch® tape as needed, the following steps are followed using the products of Micro-Measurements, Inc. (Raleigh, NC):

i. *Chemically cleaning the surface (removing grease, organic contaminants, etc.).* The CSM-2 degreasing solvent is sprayed on an area larger than the installation site. The area is cleaned with gauze pads by wiping in one direction. Each piece of gauze pad is used once to prevent contamination.

ii. *Roughening the surface with silicon-carbide paper.* To remove protrusions and develop a surface texture suitable for gage bonding, the gage area

is abraded. The gage site is dry-abraded with coarse-grit (320 grit) silicon-carbide paper. Next, it is wet-abraded using water-based acidic cleaner Conditioner A with coarse-grit silicon-carbide paper. Then, wet-abrading operation is continued with fine-grit (400 grit) silicon-carbide paper. Finally, the surface is wetted using Conditioner A and cleaned with gauze pads.

iii. *Drawing layout lines.* As there are 2 orthogonal layout lines needed for proper alignment of the strain gage, two pairs of tick marks which help burnishing the longitudinal and lateral layout lines are made beforehand. Taking the tick marks as reference, a metallic ruler and 4H grade pencil are used to burnish two orthogonal layout lines (in longitudinal and lateral directions). The residue of the pencil is then removed by using Conditioner A and cotton swabs.

iv. *Conditioning the surface.* After the layout lines are burnished, the installation site is wiped repeatedly with cotton swabs using Conditioner A.

v. *Neutralizing the surface.* Since the Conditioner A is a mildly acidic solution, the surface pH needs to be brought back to optimum alkalinity of 7.0 to 7.5, which is required by the gage bonding systems for good adhesion. This is achieved by applying Neutralizer 5A with cotton swabs.

In order to prevent contamination, the strain gage should be bonded shortly after the surface preparation. As the present study is concerned with the fully-reversed cyclic strain measurements, special care is given during gage bonding. The gage bonding is performed according to the steps listed in Reference [96] and installation recommendations for maximum fatigue endurance given in

Reference [97]. In the following, we summarize how the strain gage is bonded by using the products of Micro-Measurements, Inc. (Raleigh, NC):

i. In order to not leave any adhesive residue on the beam surface, masking tape (Scotch® tape can be used) is applied to the proximity of installation area. This is to restrict the spread of bonding adhesive.

ii. A piece of ($\sim$10 cm $\times$ 10 cm) clean float glass is secured nearby the beam whose surface had been prepared. The glass surface is conditioned using Neutralizer 5A with gauze pad. The strain gage is removed from its protective envelope by holding it from the leadwires with a pair of clean tweezers. It is then placed on the glass surface (bonding side facing down).

iii. A piece of ($\sim$10 cm) PCT-2M gage installation tape is laid onto the gage by centering it on the tape. Adhesive tapes similar to Scotch® tape should not be used for this purpose. The tape should be laid perpendicular to the grid axis (as opposed to the procedure recommended in Reference [96]). If the tape is laid along the grid axis (as the reference suggests), the gage is likely to get damaged while being lifted because of the additional resistance of the preattached leadwires. Next, the tape is lifted gently at a shallow angle (to prevent bending of the grid) together with the gage.

iv. The gage-tape assembly is positioned over the installation point such that the alignment marks etched on the gage are lined up with the burnished layout lines. One end of the tape is firmly anchored to the surface to form a hinge-like fixture which helped maintaining the gage alignment

during adhesive application.

v. The other end of the tape is peeled off gently at a shallow angle until the gage is freed from the beam surface by approximately 3 mm. A piece of (∼5 cm) Teflon® film TFE-1 is prepared for being utilized during bonding. A small amount of M-Bond 200 Catalyst-C is applied to the gage's bonding surface as a thin, uniform coat. As soon as the catalyst dries (within seconds), one or two drops of M-Bond 200 adhesive is applied to the hinge (not to the gage surface) formed by the tape and beam surface. The tape is rotated immediately and the gage is bridged over the installation point at a shallow angle while holding the tape taut. Finally, the gage-tape assembly is lightly pressed onto the specimen with the aid of Teflon® film. Application of thumb pressure and heat for ∼3 minutes is sufficient for curing of the adhesive.

vi. Experience showed that waiting for a period of 24 hours (unlike 2 minutes as suggested in Reference [96]) before removing the tape proves beneficial for ease of removal and reducing the risk of peeling off the gage.

The third phase of the gage installation is pressure pad bonding. The pressure pads (also called intermediate terminal strips) are used to increase fatigue life of the gage installation (see Figure 2.7). They function as an intermediate junction between the gage and relatively heavy instrument leadwires. This prevents direct connection of the instrument leadwires to the gage and significantly reduces the loading on the gage. The pressure pads are located close to the gage carrier and bonded by using the same adhesive (M-Bond 200) used for the gage.

The second strain gage which is to be installed on the other surface needs to be bonded before soldering the wires of the previously bonded first gage. The beam surface which already has a strain gage is entirely masked with multiple layers of paper to obtain a uniform, level surface. The beam is then turned over and the surface preparation, strain gage and pressure pad bonding procedures are repeated sequentially on the area where the second gage is installed.

In the final phase, the beryllium-copper leadwires and instrument leadwires are soldered to the pressure pads. The gage area and the beam surface are properly masked and stress relief loops are formed in the leadwires prior to soldering (see Figure 2.7). The wires are soldered using rosin-core 361A-20R (Micro-Measurements, Inc.) solder (63% Sn, 36.65% Pb, 0.35% Sb) with the aid of a 15-W soldering iron. Solder gives rise to stress concentration regions in the connection and is known to exhibit poor fatigue endurance. Therefore, extra caution should be taken during soldering. Tip temperature of the soldering iron should not be higher than the temperature required to melt the solder. A high tip temperature makes solder flow control difficult and may damage the strain gage. A minimum amount of solder should be applied by simultaneously lifting the iron tip and solder wire from the junction. Lifting the tip prior to the solder wire will produce a solder spike on the junction. A proper soldering practice should produce a small mass of smoothly-tinned hemispherical solder joint.

In order to solder the wires of the gage on the other surface, a flat surface with a slot which is slightly wider than the gage width to accommodate the soldered installation is needed. Two half-inch thick flat rectangular acrylic plates are brought closer and firmly taped on a table while leaving a small space in between. The beam is then placed on the plates as the gage with

soldered wires are coincided with the slot (space) between the plates. Once the beam is taped onto the plates, the leadwire soldering is performed on the second gage. The foregoing procedure protects the initially installed gage, its soldered wires and relief loops, etc.

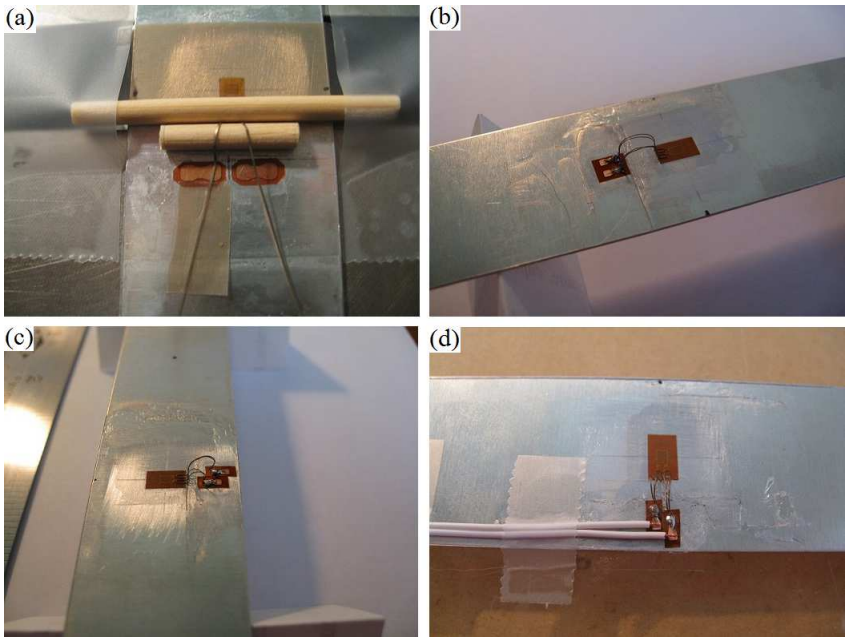

Figure 2.7: Installation steps following the strain gage and pressure pad bonding: a) forming flexible loops in beryllium-copper leadwires, b) & c) strain gages (in longitudinal and lateral directions) connected to the pressure pads, d) routing the instrument leadwires.

Strain data acquisition & measurement verification. Prior to connecting the strain gage to the measurement circuitry, the gage resistance (350 Ω) and gage-to-specimen resistance (should be greater than 10000 MΩ, Reference [91]) are measured to ensure that the gage has been installed properly. Once the installation is verified the strain gage is connected to data acquisition system (National Instruments Corp., Austin, TX) consisting of a 4-slot chassis NI cDAQ-9174, a 4-channel bridge module NI 9237, and a bridge completion

accessory NI 9945. The measurement circuitry (Wheatstone bridge) is based upon a quarter-bridge configuration in which the strain gage replaces one of the four resistances. The remaining three resistances are provided by the bridge completion accessory NI 9945. A virtual instrument (VI) program is created in the NI LabVIEW™ environment to collect, process, and record the strain data in an efficient manner. The program runs for a predetermined time period and displays time history plot, frequency spectra plot, and relevant statistical analysis results (maximum, minimum, arithmetic mean, standard deviation, and root-mean-square values of the strain data) on the user interface (front panel) shown in Figure 2.8. The program also creates two output files which contain the raw data (i.e., strain versus time) and analysis results after each run.

To ensure that the strain gage readings agree with the elementary beam theory, all beams equipped with strain gages are tested under static point loads before they are approved for use in the flapping experiments. The static tests are conducted by using a simple setup which furnishes the beam with appropriate clamped-free boundary conditions. The setup is arranged by securing a clamping fixture, which is identical to the one mounted on the test bed, to the edge of a table using a miniature C-clamp. Each beam is subjected to a point load acting at the mid-span (7.5 cm) and, subsequently, at nearby the tip (14.5 cm). Figure 2.9 depicts a static bending test performed by loading the beam with a calibration mass at the mid-span. Point loads are applied with the aid of calibration masses weighing 2, 5, 10, and 20 g. In order to verify the reading of a strain gage in both tension and compression, a series of loading tests (i.e., loadings at the mid-span and the tip with different masses) are performed on both surfaces of each beam. In Figure 2.10, longitudinal strain gage readings

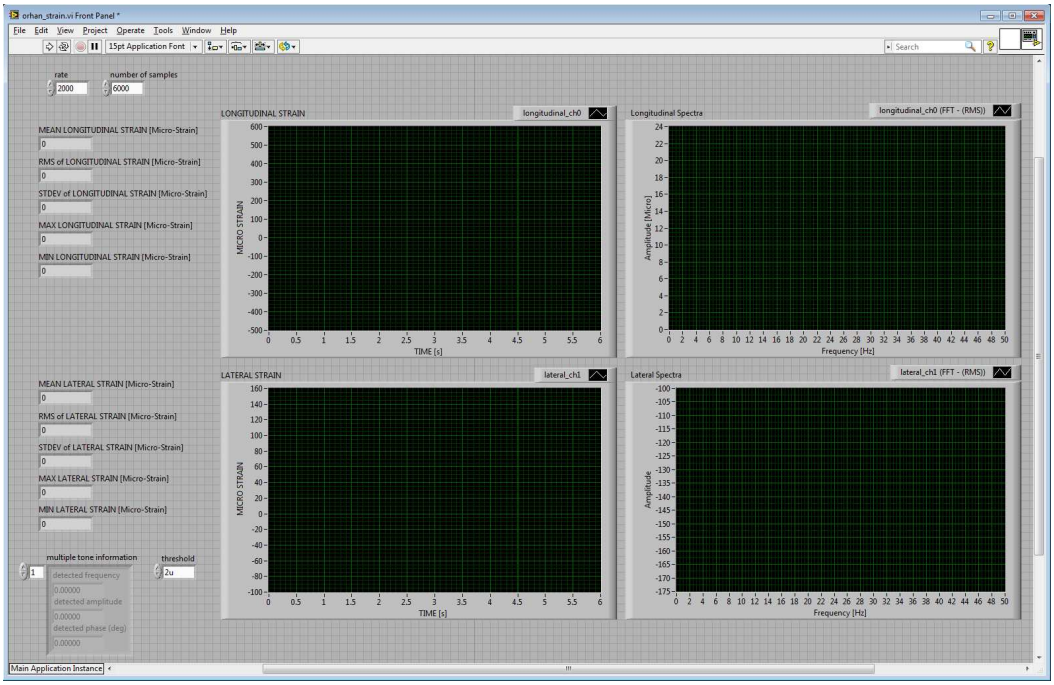

Figure 2.8: User interface (front panel) of NI LabVIEW™ strain measurement program. Four graphical indicators display time history and frequency spectra of longitudinal and lateral strains. Digital indicators located on the left display statistical analysis results and frequency content of the sampled data.

of a representative beam tested under twelve different loading configurations are compared with the values obtained from the elementary beam theory. All beams used in the present study reveal similar test results. The gage readings agree well with the theory and show negligible difference with respect to the loading direction. As the applied bending moment increases, deviation from the theory and difference with respect to the loading direction reveal a negligible increase. To make sure that the strain data acquisition system functions properly, the strain gage readings are also compared with those obtained from a portable strain indicator P3 (Micro-Measurements, Inc.).

Before proceeding, it would be appropriate to briefly mention how fatigue failure in the gage manifests itself in the experimental data. Under cyclic

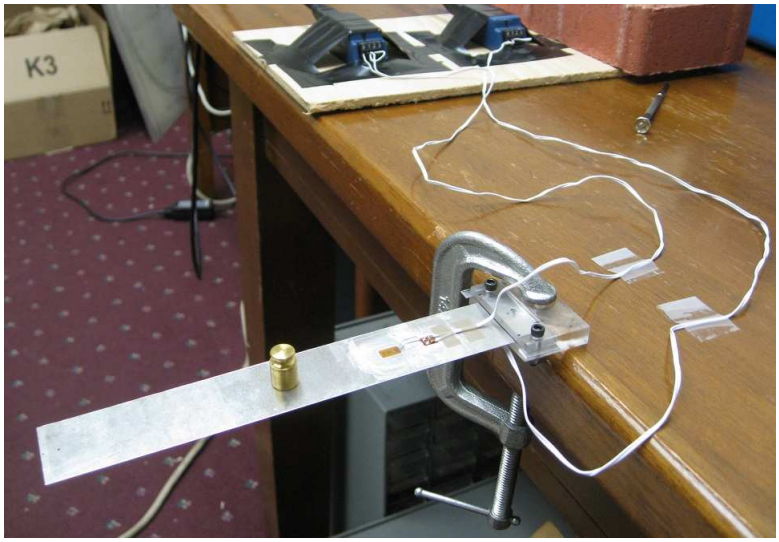

Figure 2.9: Static bending test for verification of the strain gage readings. Beam loaded with a calibration mass at the mid-span, clamping fixture, and bridge completion accessories (NI 9945) of the strain gage circuitry are seen in the picture.

stress conditions the gage grid hardens gradually and its specific resistance changes. The resulting permanent change in the unstrained resistance of gage is evidenced as non-zero strain under no loading which is termed *zero-shift*. Strain gage fatigue lives are commonly reported based on number of cycles at which a 100 μ-strain zero-shift would be observed. Although this value can be considered as a criterion to call a gage "failed" in static strain measurements, the gage can still be considered functional beyond the 100 μ-strain zero-shift level in purely dynamic strain measurements. For the series of the gage used in the present study (WK-series), number of cycles at which a 100 μ-strain zero-shift can be expected are reported for 10^6, 10^5, 10^4, 10^3, and 10^2 for cyclic strain levels of $\pm$2500, $\pm$3000, $\pm$3750, $\pm$4500, and $\pm$5200 μ-strain, respectively [97]. Cracks start developing beyond the zero-shift level and open up only in tension part of the cycle at earlier stages. The failure at this level is referred to as *super sensitivity* and reveals itself as significant distortions in upper half (tension

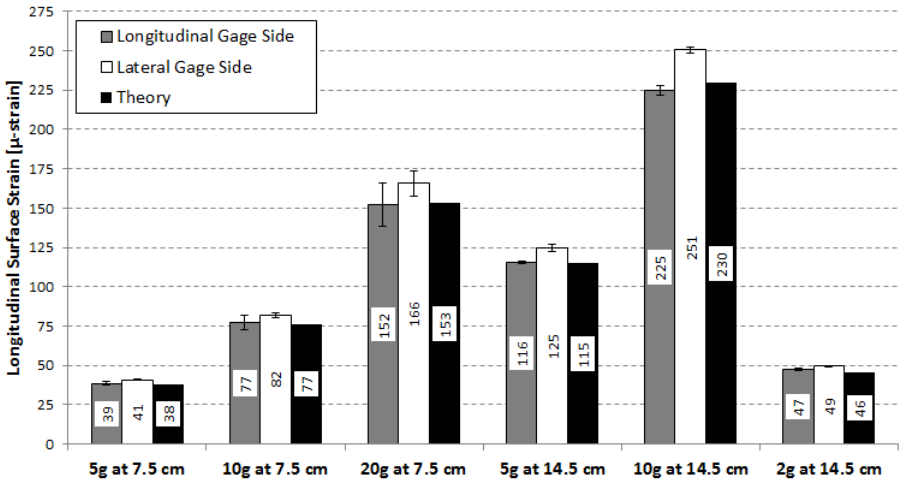

Figure 2.10: Longitudinal strain gage readings corresponding to different loading cases [i.e., magnitude and location (mid-span: 7.5 cm, tip: 14.5 cm) of the calibration mass] obtained in static bending tests of a beam (labeled ALM0803). The beam surface upon which the loading is acted can be deduced from the figure legend. Error bars represent 95% confidence interval based on three measurements.

side) of the waveform. A gage subjected to fatigue damage at the level of super sensitivity is regarded as failed. Further information and recommendations regarding dynamic strain measurements with strain gages can be found in References [91, 97].

2.4.2 Tip Displacement

High-speed camera imaging. In-plane deformation of the entire beam in flapping motion is recorded with a high-speed camera MotionPro X3™ (IDT, Inc.). Beam transverse tip displacement is calculated based on the image data. The camera uses a CMOS (complementary metal-oxide semiconductor) image sensor which provides a maximum image resolution of 1280 pixels × 1024 pixels. The maximum frame rate that can be achieved at full resolution is 1000 fps (frames per second).

There are number of coupled parameters which bring limitations to the camera configuration. These are field dimensions, image resolution, number of frames per flapping cycle, camera frame rate, lens type (focal length), and object distance. The number of image frames captured over a cycle of flapping should be the same at all tested flapping frequencies if a comparison is to made between different frequencies. Accordingly, the camera frame rate needs to be reset at different flapping frequencies. The image resolution should be the same in all test cases for consistency. As image resolution decreases with increasing frame rate the aforementioned parameters need to be selected judiciously. Camera software VidiMotion™ (IDT, Inc.) helps determining the object distance when other parameters are provided as inputs.

The experimental area to be filmed measures (i.e., field dimensions) 38 cm $\times$ 20 cm. The image resolution is set to 760 pixels $\times$ 400 pixels such that the width of each pixel measures 0.50 mm. Based upon the selected image resolution, the maximum frame rate is limited by 2451 fps at the highest flapping frequency (19 Hz) sought in the experiments. In other words, a total of 129 frames can be recorded over one cycle at 19 Hz. The camera frame rate is reset at lower flapping frequencies so as to obtain the same number of frames per cycle regardless of the flapping frequency. For instance, the frame rate is set to 387, 1161, and 1806 fps at flapping frequencies 3, 9, and 14 Hz, respectively.

The camera needs to be positioned directly above the flapping test bed; hence, keeping the object distance (i.e., distance between the object and the camera lens) shorter is of considerable importance for experimental convenience. Shorter object distance and larger depth of field (i.e., distance through which the object can be kept in focus) can be achieved by utilizing a lens with

a shorter focal length. A camera lens Fujinon™ CF25HA-1 (Fujifilm Corp.) with a 25-mm fixed focal length is used in the present study. Given focal length and field dimensions, the object distance is calculated to be 104 cm using the camera software VidiMotion™.

The fact that a 3.4-kg camera has to be placed above a highly dynamic test subject whose vicinity is expected to be spacious (to accommodate a vacuum chamber) and free of any physical interference requires a stringent sighting condition which cannot be achieved with a tripod. Therefore, a platform is built to allow the camera to be positioned in three directions without intruding into experiment site (see Figure 2.1). The camera is attached to the platform such that the distance between the lens face and the beam edge measures 104 cm. A "bull's eye" spirit level is used to level the camera (lens face) with respect to the leveled test setup. Also, the camera (optical axis) is lined up with a point taken along the beam edge with the aid of a simple plumb-bob. This helps to ensure that the beam is located beneath the lens and reduces image bias toward one side of the reference axis depicted in Figure 2.3b.

The camera is operated using an application software MotionStudio™ installed on a dedicated computer. It allows the user to display live-action images for immediate observation, configure various parameters (frame rate, exposure time, region of interest, filming duration, gamma correction, etc.), acquire images, and save them to a storage device. The imaging system permits live play of images (without recording); hence, one can experiment with various settings to find optimal parameters to reduce out-of-focus aberration and get a sharp image of the beam. However, at high flapping frequencies (e.g., 19 Hz) *motion blur* could not be prevented in some frames (where the beam reaches maximum speed) due to exposure time limitations. All images

are taken as greyscale with the following parameter settings: exposure time (shutter speed) 150 μs (or 120 μs), lens aperture size $f/1.4$ (f-number 1.4), gamma correction 1.8. The experiment site is illuminated with a total of six tungsten halogen work-lights (500-Watt each). The work-lights are arranged around the flapping test-bed (side lighting, see Figure 2.1) in a manner to eliminate shadows.

To be able to distinguish featured points (tip, mid-span, root, gage location) along the edge of the beam, they are made visible with a black-ink marker. The camera is focused on the beam upper edge (i.e., the edge closer to the camera, see Figure 2.11b) in all experiments. A grid paper and a protractor (see Figures 2.3a and 2.6b) are placed on the background to serve as reference aids for image calibration and data reduction. Because the depth of field falls short of the beam width, it becomes quite difficult to discern where the limits of flapping angle coincide in the image when the focus is kept at the upper edge. Therefore, a simple indicator needle is made solely for angle calibration (i.e., it is removed during the experiments) and gently taped to the beam as shown Figure 2.11. Prior to experiments, the camera is focused on the needle indicator-protractor and a calibration footage is taken at each flapping amplitude.

Image analysis. Image analysis is concerned with determining the transverse tip displacement of the beam based on pixel coordinates of the point of interest (beam tip) in a sequence of images. A Matlab® code is written to perform the image analysis conveniently. The code acquires sequence of images (image stack) and allows the user to play them continuously at a certain frame rate or jump to a particular frame in the sequence. Figure 2.12 shows movie

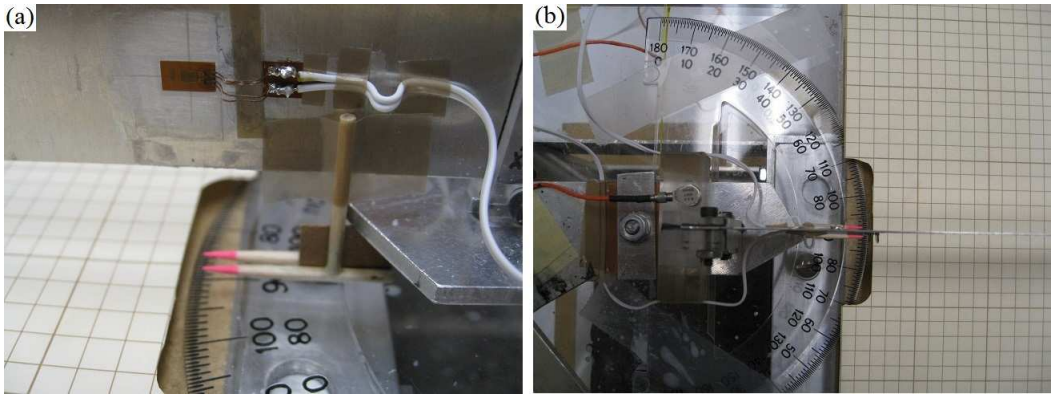

Figure 2.11: Flapping angle calibration: a) simple indicator needle taped on the beam, b) indicator needles and beam upper edge at 0° viewed from top.

player and pixel region tool launched by the code. The movie player displays entire image along with its frame number and provides the user with pixel region tool to retrieve information about a group of pixels. Pixel region tool (Figure 2.12b) gives coordinates (indices) of a single pixel under the pointer.

Tip displacement is calculated based on a sequence of frames corresponding to one cycle of flapping. A total of 33 frames which coincide with 2 extrema, 3 neutral (0° flap angle), and 28 intermediate points over a period T of cycle is considered. One of the initially captured frames in which the beam root is observed to be aligned with the reference axis (i.e., 0° flap angle, see Figure 2.3b) is designated as the reference (initial) frame. Since duration between consecutive frames is known based on the camera frame rate, the frames corresponding to other 32 points in a cycle [i.e., frames at extrema ($t/T = 0.25$ and 0.75), neutral ($t/T = 0.5$ and 1.0), and intermediate points] could easily be identified. Coordinates of a pixel which corresponds to tip of the *undeformed beam* are identified with the aid of pivot axis location and beam length. Then, pixel coordinates of the beam tip in all selected frames are resolved. Transverse tip displacement is evaluated by subtracting the transverse pixel coordinate

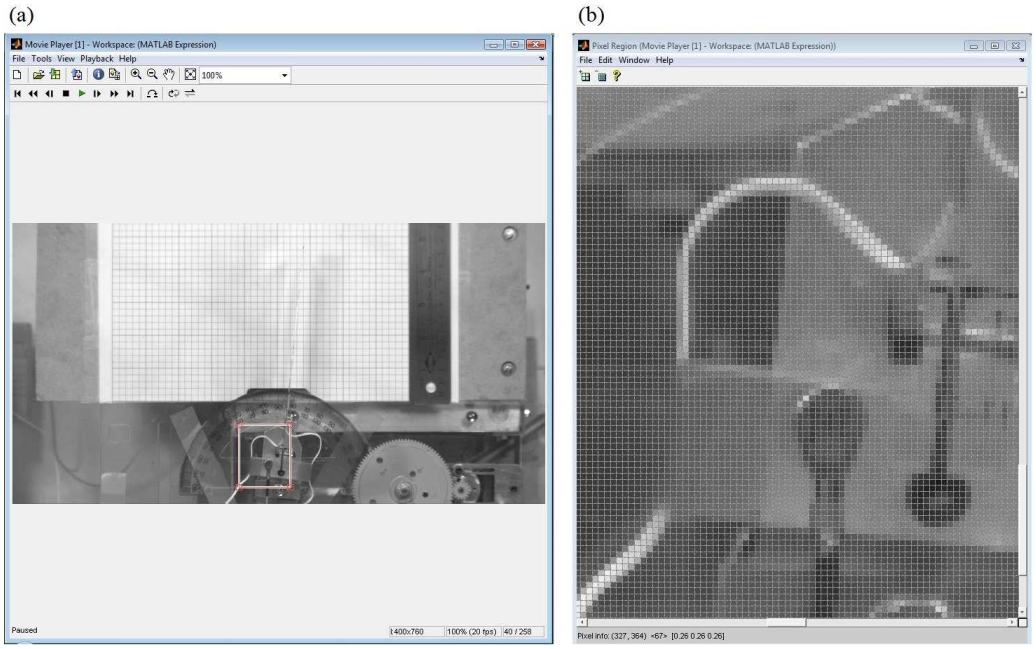

Figure 2.12: Image processing with Matlab®; a) movie player, b) pixel region tool.

of the beam tip (in a certain frame) from that of the undeformed beam tip. Values obtained in pixels are converted to metric units via calibration based on a known length. Through calibration with a reference scale, it is determined that 1 pixel measures 0.53 mm. In order to determine the flapping angle, two pixels corresponding to the straight edge of the rocker link are considered in each frame. These points are then used to form a line (vector) whose angle with respect to the line in the reference frame gives the flapping angle.

2.5 Vacuum Chamber

In order to study the effects of air damping on the structural dynamics of flapping beams a vacuum chamber is constructed as shown in Figure 2.13. The chamber is constructed from a 112-cm long, 9.5-mm thick clear acrylic cylinder with internal diameter 46 cm. The ends of the acrylic cylinder are

closed with square aluminum plates (12.7-mm × 61 cm × 61 cm). One of the ends of the chamber is intended to be kept closed at all times while the other end is used for access to the chamber. A pair of O-rings (4.76-mm thick, 48.3 and 50.8-cm internal diameter) are installed to the grooves machined on the end plates. High vacuum grease (Dow Corning Corp., Midland, MI) is applied to the O-ring areas for better sealing.

Motor controller cables and strain gage instrument leadwires are passed through 7-cm long threaded pipes. Epoxy resin is filled in the through hole to seal the gap between the pipe inner wall and cables. The stationary end plate of the chamber is outfitted with the electrical feedthrough (see Figure 2.13a). Electrical connectors are then attached to the feedthrough cables to complete circuitry. A fitting located on the cylindrical section of the chamber is configured for vacuum pump outlet, vacuum gauge, and release valve. The chamber is connected to a diaphragm vacuum pump DAA-V715A-EB (Gast Manufacturing, Inc., Benton Harbor, MI) with reported dry-air capacity of 32.5 L/min. With this configuration, the maximum vacuum pressure that can be achieved in a reasonable time period is determined to be 21 inHg vacuum; i.e., 70% vacuum.

2.6 Experimental Procedure

In this section, a general procedure for conducting experiments (at ambient and reduced pressures) with the flapping test-bed will be summarized:

i. All joints of the flapping test-bed are lubricated with white lithium grease to maintain a frictionless motion. The mechanism is brought to the neutral position (i.e., set to 0° flapping angle, see Figure 2.3b) and mov-

Figure 2.13: Vacuum chamber: (a) stationary cover end with electrical feedthrough for strain gage and motor cables, (b) flapping mechanism placed in the chamber, (c) access cover end, (d) aluminum cover with double O-rings.

ing parts (main gear and rocker link) are immobilized with the aid of Scotch® tape.

ii. The test-bed frame is supported with a dead weight and leveled with a "bull's eye" spirit level. The beam to be tested is attached to the clamping fixture and leveled. Strain gage instrument leadwires are connected to the bridge completion accessories.

iii. The strain measurement program is turned on and null correction (offset calibration) is performed to remove any offset value from the unstrained gage readings. First bending mode natural frequency of the beam is measured by slightly deflecting the beam and setting it into free vibration. The tapes preventing the mechanism from motion are removed after the

free vibration test is performed.

iv. Strain data acquisition period ($3 \sim 6$ s), sampling frequency (2000 Hz), and folders in which the raw data and analysis results to be saved are set on the strain measurement program.

v. The high-speed camera is focused on the beam edge and the filming parameters (e.g., frame rate, number of frames, etc.) are adjusted for the initial test. A low-speed camera (Canon, Inc.) is mounted on a tripod, focused on the experiment site and brought to stand-by.

vi. The motor controller is powered up and the settings related to desired velocity profile are configured. The motor speed data recorder is brought to motion-trigger mode. The trapezoidal velocity profiles consist of acceleration, constant speed (target speed), and deceleration regions. In all experiments the same duration (or velocity rate) is used for both acceleration and deceleration with values varying between 2 s and 5 s depending on the target speed (slower rates were used for higher target speeds).

vii. All lights are connected to the same switch to turn them on/off at the same time.

viii. With the experimental setup ready, the low-speed Canon camera is started first, lights are turned on and the motor is activated; strain data acquisition and high-speed camera are triggered once target speed is reached and stabilized.

ix. Immediately after the strain and image data acquisitions are stopped,

the motor is set to decelerate and halt. The lights are turned off and low-speed camera is stopped.

Testing at other flapping frequencies, at the same flapping amplitude, are carried out starting from the third item in the above list. For the tests conducted in the vacuum chamber; the test-bed is placed in the chamber and items listed above are followed by excluding the recording with the high-speed camera and illumination with the halogen work-lights. As an exception, the chamber "door" is sealed following the third item and the vacuum pump is run until the desired level of reduced pressure is reached at which point the pump is stopped and remaining steps of the above-mentioned list are performed. Other flapping frequencies, at the same amplitude, are tested after pulling vacuum, if needed, to compensate for the loss. The vacuum pump is not run during the flapping experiments.

CHAPTER 3

Experimental & Numerical Characterization of the Structural Dynamics of Flapping Beams

3.1 Scope of the Chapter

In this chapter,* the nonlinear structural dynamics of aluminum slender beams is examined both experimentally and computationally. In the experiments the periodic flapping motion is imposed on the clamped edge of the cantilever beam using the 4-bar crank-and-rocker mechanism. Aluminum beams with nominal dimensions of 150 mm $\times$ 25 mm $\times$ 0.4 mm are tested in air over a range of flapping frequencies up to 1.3 times the linear first modal frequency at two different flapping amplitudes, 15° and 30°. The response of the beam is characterized experimentally through bending strain and tip displacement data obtained from a foil strain gage and high-speed camera, respectively. It was determined that for the particular combination of beam specimen (dimensions, material properties) and forcing parameters investigated, all experimental responses were periodic. The frequency response curves based upon the experimental bending strain data reveal a secondary superharmonic peak in addition to the primary resonance peak. As the flapping frequency is increased, the response of the beam is observed to change from symmetric (with respect to equilibrium position) periodic vibrations with a period equal to the flapping period to asymmetric vibrations with higher harmonic content fea-

*The material presented in this chapter was published in *Journal of Sound and Vibration*, 332 (21): 5393-5416, 2013.

turing local oscillations in the time histories. Experimental tip displacement results show that the beam spends more time during stroke reversals when the flapping frequency is near the primary and secondary resonance regions. In addition to experiment, numerical simulations are performed using two-node, isoparametric degenerate-continuum based geometrically nonlinear beam elements. The HHT-α version of the Newmark finite difference scheme is used to discretize the problem in time and a linear viscous damping model is assumed. Overall the numerical simulations agree well with the experiments and capture most of the nonlinear dynamical features of the beam response. It is, however, found that in resonance regions the simulations overpredict response magnitudes, possibly due to the use of the linear damping model and linear elastic constitutive model. Additional numerical simulations of the beam tip response reveal dynamics which include periodic, asymmetric periodic, quasi-periodic, and aperiodic motions.

In Section 3.2, the computational model which is comprised of a beam finite element and finite difference time integration scheme is presented in detail. In Section 3.3, the experimental setup is briefly explained since more detailed presentation is given previously in Chapter 2. In Section 3.4, the results gathered from the experiments will be analyzed and compared with those obtained from the finite element simulations. In Section 3.5, additional numerical simulations will be performed to explore the beam response characteristics with varying flapping frequency and flapping amplitude. Finally, conclusions are given in Section 3.6.

3.2 Computational Model

3.2.1 Overview

The computational model used in the present chapter is based upon a continuum-based (CB) beam formulation which imposes the beam kinematic assumptions on the semi-discretized (in spatial domain) equations of continuum [98]. This differs from the development path of most typical structural elements which use the kinetic (stress) and kinematic assumptions to derive the strong form through the principle of virtual work. To develop the necessary weak form for the finite element discretization, it then requires going back to the principle of virtual work. Hence the CB methodology is a more straightforward approach to the development of structural (beams, plates, shells, etc.) elements.

The semi-discretized equations are derived using two-dimensional, four-node, isoparametric elements in a total Lagrangian framework with Green strains, second Piola-Kirchhoff (PK2) stresses and a linear elastic constitutive model. As illustrated in Figure 3.1, after the kinematic assumptions are applied each of 2 nodes in the finite element beam model has 3 degrees of freedom which include displacements u and v in two coordinate directions (x and y) and rotation θ about the third coordinate z. To discretize the problem in the time domain, we use the Hilber-Hughes-Taylor-α (HHT-α) implicit time-marching method [99]. The value of the algorithmic damping parameter in the HHT-α scheme is $\alpha_{HHT} = -0.05$. Preliminary studies of the beam response (tip displacement and axial strain) determined that a finite element mesh with 50 elements and a time step of 1.0×10^{-4} s is sufficient for convergence of the response measures of interest and all simulation results to be presented in this chapter are generated using this level of resolution (see Ap-

pendix C). A small amount of linear viscous damping is applied through the use of Rayleigh proportional damping (see Reference [100]) with values for the mass and stiffness matrix multipliers of $\alpha_d = 1$ and $\beta_d = 0$, respectively. This choice of damping which, unless otherwise mentioned, is used throughout the present computational study gives a first modal damping ratio of 0.006. Based on the cyclic decay of free (small) vibrations, the first mode damping ratio in the experiment is determined to be 0.013 from the logarithmic decrement. The choice of neglecting the stiffness proportional damping is made based upon the idea that the beam model is geometrically nonlinear and, thus, the numerical solution of this model produces a stiffness matrix, and hence damping force ($\beta_d \neq 0$), which is a function of displacement. While in Chapter 4 we will explore nonlinear damping, it is unlikely that this damping force would change in a manner similar to the force due to internal stresses.

The flapping motion of the beam is modeled by imposing, on the fully discretized model, time-dependent boundary conditions on all 3 degrees of freedom at the clamped boundary of the beam [101]. The motion is imposed by considering the theoretical position of the boundary (point E shown in Figure 2.3b) based upon the 4-bar mechanism kinematics (see Eq. (B.5) in Appendix B). The rigid link (33.3 mm portion shown in Figure 2.3) is not modeled in the simulation. The choice to not model the rigid link is made primarily for numerical reasons as including this in the model would introduce high frequency components into the simulation which would likely necessitate the use of timesteps smaller than those which are required to accurately capture the timescales of the flexible beam model. As will be shown in Section 3.4, outside of the regions of resonance, the experiment and simulation show good agreement which provides some justification for this modeling assumption.

The details of CB beam element formulation is given in Sections 3.2.2 and 3.2.3. The formulation was implemented into an in-house nonlinear finite element analysis program ATFEM which has been developed and maintained over the past decade or so [102]. ATFEM has been written in Fortran 90 [103] language and consists of numerous subroutines and modules. Validation and convergence studies associated with the CB beam element are given in Appendix C.

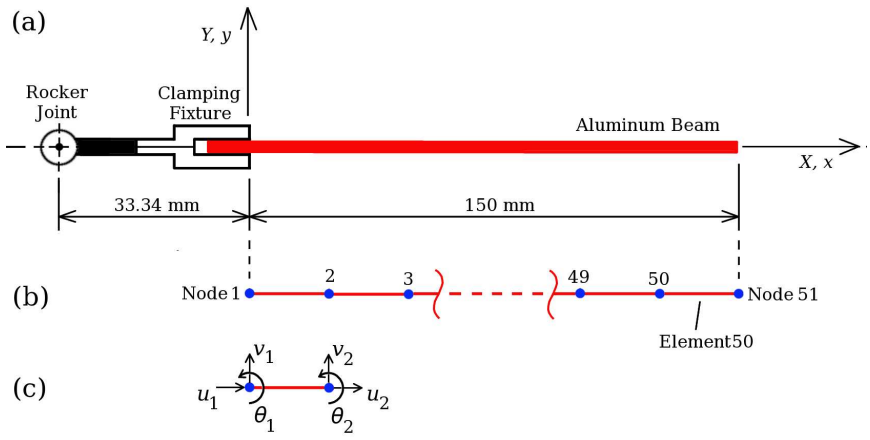

Figure 3.1: (a) Schematic of the flapping beam problem, (b) corresponding finite element mesh, and (c) 2-node beam element with nodal degrees of freedom.

3.2.2 Total Lagrangian Continuum Formulation

In this section, we will describe the finite element procedure undertaken in the present study and highlight the important aspects of the beam element used in the computational model. The following presentation closely follows the works of Belytschko *et al.* [104] and Crisfield [98].

The partial differential equations governing the motion of the beam and the boundary conditions are collectively referred to as the *strong form* of the

problem. Finite element discretization of the strong form is not possible and therefore the *weak form*, which is an integral expression of the governing equation and the boundary conditions, is needed. The weak form is equivalent to the strong form and requires "less smooth" (C^0 *vs.* C^2 continuous) solution functions. In solid mechanics, it is also called *principle of virtual work*. In order to obtain the weak form, the governing differential equation is multiplied by an arbitrary function called "test (weight) function" and integrated over the domain. The test function is required to vanish on the prescribed displacement boundary (essential boundary condition). For the solution of weak form, a set of smooth functions called "trial functions" are considered. The trial function satisfying the essential boundary condition is the solution of the weak form [105].

The continuum-based (CB) beam element is formulated in a total Lagrangian framework. Accordingly, Green strain $\mathbf{E}$ and second Piola-Kirchhoff (PK2) stress $\mathbf{S}$ are used as strain and stress measures, and the motion of the element is described with respect to initial (undeformed) configuration. We now summarize important concepts pertaining to a continuum finite element which will be subsequently used in the formulation of CB beam element. The equation of motion (i.e., conservation of linear momentum) of a body (continuum) in the undeformed configuration can be expressed as (p.550 [106], p.194 [104]):

$$\nabla_0 \cdot (\mathbf{S} \cdot \mathbf{F}^T) + \rho \mathbf{b} = \rho \frac{\mathrm{D}^2 \mathbf{u}}{\mathrm{D}t^2}, \tag{3.2.1}$$

where ∇_0 is the gradient operator with respect to initial (material) coordinates $\mathbf{X}$, $\mathbf{S}$ is the second Piola-Kirchhoff stress tensor, $\mathbf{F}$ is the deformation gradient tensor, ρ is the density, $\mathbf{b}$ is the vector of body forces per unit mass, $\mathbf{u}$ is

the vector of displacements ($\mathbf{x} = \mathbf{X} + \mathbf{u}$), and $\frac{\mathrm{D}()}{\mathrm{D}t}$ denotes the material time derivative. The deformation gradient is defined as $\mathbf{F} = \frac{\partial \mathbf{x}}{\partial \mathbf{X}}$ and it relates current configuration $\mathbf{x}$ to initial configuration $\mathbf{X}$. $\mathbf{F}$ is related to the Green strain according to $\mathbf{E} = \frac{1}{2}(\mathbf{F}^T \cdot \mathbf{F} - \mathbf{I})$, where $\mathbf{I}$ is the identity matrix. Note that while the numerical simulations include linear viscous damping, and the numerical implementation of this will be discussed later in this section, Eq. (3.2.1) does not include a viscous damping term.

In order to obtain the weak form, we multiply Eq. (3.2.1) by test function (i.e., virtual displacement) $\delta\mathbf{u}$ and integrate over the initial domain Ω_0 of the body, to obtain:

$$\delta W^{int} - \delta W^{ext} + \delta W^{kin} = 0, \tag{3.2.2}$$

where δW^{int}, δW^{ext}, δW^{kin} are the virtual works associated with internal, external, and inertial forces, respectively, and are defined as (p.197 [104], p.108 [107]):

$$\delta W^{int} = \int_{\Omega_0} \mathbf{S} : \delta\mathbf{E} \, \mathrm{d}\Omega_0, \tag{3.2.3a}$$

$$\delta W^{ext} = \int_{\Omega_0} \rho\delta\mathbf{u} \cdot \mathbf{b} \, \mathrm{d}\Omega_0 + \sum_{i=1}^{n_{SD}} \int_{\Gamma^0_{t_i}} (\delta\mathbf{u} \cdot \mathbf{e}_i)(\mathbf{e}_i \cdot \bar{\mathbf{t}}^0_i) \, \mathrm{d}\Gamma_0, \tag{3.2.3b}$$

$$\delta W^{kin} = \int_{\Omega_0} \delta\mathbf{u} \cdot \rho\ddot{\mathbf{u}} \, \mathrm{d}\Omega_0. \tag{3.2.3c}$$

In Eqs. (3.2.3)a and b, the symbol ":" denotes double contraction,[†] n_{SD} stands for number of space dimensions, $\Gamma^0_{t_i}$ denotes initial boundary over which tractions are prescribed, $\bar{\mathbf{t}}^0_i$ represents prescribed tractions, $\mathbf{e}_i$ denotes the unit normal of the boundary over which the traction is prescribed, and Γ_0 is the initial boundary. Equation (3.2.2) constitutes the weak form equivalent of the

[†]If $\mathbf{A}$ and $\mathbf{B}$ are second-order symmetric tensors, $\mathbf{A} : \mathbf{B} = \mathrm{tr}(\mathbf{A}^T\mathbf{B}) = \sum_{i,j=1}^{3} a_{ij}b_{ij}$, where a_{ij} and b_{ij} are the elements of the tensors.

momentum equation in a total Lagrangian frame.

We can now perform finite element discretization which amounts to discretizing the domain Ω_0 into a set of subregions (elements) connected appropriately at their nodes and then approximating the unknown displacement field $\mathbf{u}$ of the element domain in terms of the unknown nodal displacements $\mathbf{u}_I$ at these nodes by using interpolation functions N_I (called *shape functions* in the finite element literature). For the 4-node quadrilateral continuum element shown in Figure 3.2, nodes n_I are denoted by 1^-, 2^-, 2^+, 1^+; thus, $I = 1^-$, 2^-, 2^+, 1^+. The finite element approximation of the trial and test functions are given as:

$$\mathbf{u} = \mathbf{u}_I(t)\mathrm{N}_I, \tag{3.2.4a}$$

$$\delta\mathbf{u} = \delta\mathbf{u}_I\mathrm{N}_I, \tag{3.2.4b}$$

where summation over the range of repeated index is implied. For the purpose of describing local approximation over each element, the elements can be considered disjoint (see pp. 73-77, [108]) and hence we can focus our development to a typical element with domain Ω_0^e. In what follows we will drop the superscript e but it should be understood that all integrals are over an element domain.

At this point we define element nodal forces. Accordingly, the virtual works done by the element nodal forces in moving through virtual nodal displacements $\delta\mathbf{u}_I$ are expressed as:

$$\delta W^{int} = \delta\mathbf{u}_I^T\mathbf{f}_I^{int}, \tag{3.2.5a}$$

$$\delta W^{ext} = \delta\mathbf{u}_I^T\mathbf{f}_I^{ext}, \tag{3.2.5b}$$

$$\delta W^{kin} = \delta \mathbf{u}_I^T \mathbf{f}_I^{kin}, \tag{3.2.5c}$$

where $\mathbf{f}_I^{int}$, $\mathbf{f}_I^{ext}$, and $\mathbf{f}_I^{kin}$ are internal, external, and inertial nodal forces, respectively.

Substituting Eqs. (3.2.5) into Eq. (3.2.2) and enforcing the arbitrariness of the test functions $\delta \mathbf{u}_I$ yields the *semi-discretized* (in space) equations of motion at the element level:

$$\mathbf{M}_{IJ} \ddot{\mathbf{u}}_J + \mathbf{f}_I^{int} = \mathbf{f}_I^{ext}. \tag{3.2.6}$$

The expressions for the quadrilateral element nodal forces can be obtained by equating the virtual works, Eqs. (3.2.3), to the virtual works of the nodal forces, Eqs. (3.2.5), and utilizing the finite element approximations Eqs. (3.2.4). Combining Eqs. (3.2.3b) and (3.2.5b) and using Eq. (3.2.4b) yields:

$$\begin{aligned} \delta W^{ext} = \delta \mathbf{u}_I^T \mathbf{f}_I^{ext} &= \int_{\Omega_0} \rho \delta \mathbf{u} \cdot \mathbf{b} \, \mathrm{d}\Omega_0 + \int_{\Gamma_{t_i}^0} (\delta \mathbf{u} \cdot \mathbf{e}_i)(\mathbf{e}_i \cdot \bar{\mathbf{t}}_i^0) \, \mathrm{d}\Gamma_0 \\ &= \delta \mathbf{u}_I^T \left\{ \int_{\Omega_0} \rho \mathrm{N}_I^T \mathbf{b} \, \mathrm{d}\Omega_0 + \int_{\Gamma_{t_i}^0} \mathrm{N}_I^T \bar{\mathbf{t}}_i^0 \, \mathrm{d}\Gamma_0 \right\}, \end{aligned} \tag{3.2.7}$$

and arbitrariness of the test function $\delta \mathbf{u}_I$ gives the external nodal forces acting on the quadrilateral element:

$$\mathbf{f}_I^{ext} = \int_{\Omega_0} \rho \mathrm{N}_I^T \mathbf{b} \, \mathrm{d}\Omega_0 + \int_{\Gamma_{t_i}^0} \mathrm{N}_I^T \bar{\mathbf{t}}_i^0 \, \mathrm{d}\Gamma_0, \tag{3.2.8}$$

where the first and second terms represent the body forces and prescribed tractions (e.g., applied surface pressure), respectively.

In the present study, external forces due to surrounding air pressure are not

considered. Also, the effect of gravitational force, which acts in the vertical (z) direction, on the motion of the beam is minimized by setting the flapping motion in the horizontal plane (xy-plane in Figures 3.1a and 3.2). Therefore, further details on the derivation of the external nodal forces $\mathbf{f}_I^{ext}$ will not be given as they are not included in the computational model.

To determine the inertial nodal forces, we combine Eqs. (3.2.3c) and (3.2.5c) and use Eqs. (3.2.4a) and (3.2.4b):

$$\begin{aligned}\delta W^{kin} = \delta \mathbf{u}_I^T \mathbf{f}_I^{kin} &= \int_{\Omega_0} \delta \mathbf{u} \cdot \rho \ddot{\mathbf{u}} \, \mathrm{d}\Omega_0 \\ &= \delta \mathbf{u}_I^T \left\{ \int_{\Omega_0} \rho \mathrm{N}_I \mathrm{N}_J \, \mathrm{d}\Omega_0 \ddot{\mathbf{u}}_J \right\}, \end{aligned} \tag{3.2.9}$$

and consider the arbitrariness of the test function $\delta \mathbf{u}_I$ to obtain:

$$\mathbf{f}_I^{kin} = \int_{\Omega_0} \rho \mathrm{N}_I \mathrm{N}_J \, \mathrm{d}\Omega_0 \ddot{\mathbf{u}}_J = \mathbf{M}_{IJ} \ddot{\mathbf{u}}_J. \tag{3.2.10}$$

The mass matrix given in Eq. (3.2.10) is referred to as a "consistent" mass matrix as it results from a consistent derivation from the weak form [104]. The fact that the consistent mass matrix is not a diagonal matrix makes its use computationally prohibitive in certain circumstances. Therefore, diagonal mass matrices called "lumped" mass matrices have been developed based upon various procedures such as row-sum technique, physical lumping, HRZ lumping, and optimal lumping [100]. The mass matrix of the beam element is obtained from the consistent or lumped form of the mass matrix (given in Eq. (3.2.10)) of the continuum element via master-slave transformation [104]. However, the transformation does not yield a diagonal mass matrix even if the lumped form of the quadrilateral element mass matrix is used. Therefore, the

following diagonal mass matrix given for the CB beam element is used in the computational model [104]:

$$\mathbf{M}_{IJ} = \frac{\rho_0 t_0 l_0 w_0}{420} \begin{bmatrix} 210 & 0 & 0 & 0 & 0 & 0 \\ 0 & 210 & 0 & 0 & 0 & 0 \\ 0 & 0 & \frac{1}{24} t_0^2 & 0 & 0 & 0 \\ 0 & 0 & 0 & 210 & 0 & 0 \\ 0 & 0 & 0 & 0 & 210 & 0 \\ 0 & 0 & 0 & 0 & 0 & \frac{1}{24} t_0^2 \end{bmatrix}, \tag{3.2.11}$$

where ρ_0, t_0, l_0, and w_0 are the density, thickness, length, and width of the beam element in the initial configuration, respectively.

3.2.3 Continuum-Based Beam Element

In Figure 3.2, both the 2-node CB beam element and the underlying 4-node quadrilateral continuum element are shown. The nodes labeled 1^-, 1^+, 2^-, and 2^+ belong to the quadrilateral element and are termed "slave nodes." On the other hand, the nodes labeled 1 and 2 belong to the beam element and are called "master nodes." Each master node is located on a line connecting a pair of slave nodes. These lines are referred to as "fibers." The unit vectors $\mathbf{d}_1$ and $\mathbf{d}_2$ along the fibers are called "directors." Master nodes are located on the beam reference line (centerline). Note that each (slave) node of the quadrilateral element has 2 degrees of freedom: displacements u and v along x and y axes, respectively. Whereas, each (master) node of the CB beam element has 3 degrees of freedom: displacements u and v along x and y axes, respectively, and rotation θ about z axis.

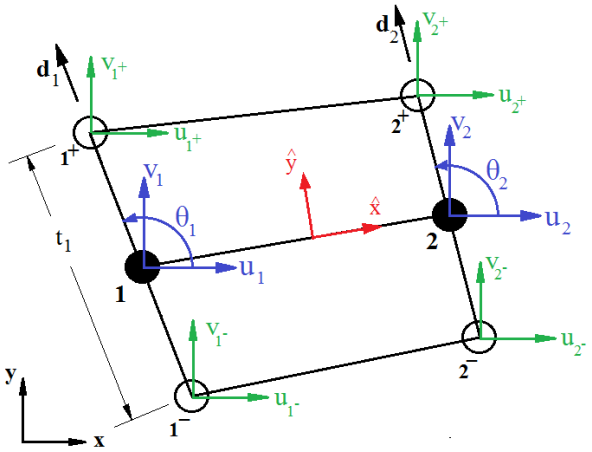

Figure 3.2: 2-node continuum-based beam element and underlying 4-node quadrilateral continuum element.

Now let us state the assumptions made on the motion and stress state of the continuum. These assumptions, which under certain conditions (satisfied here) result in a displacement field which corresponds exactly to that given by the classical Timoshenko beam theory [104], will convert the continuum into a beam structure. The assumptions are given as follows. (1) Fibers remain straight; i.e., plane cross-sections before bending remain plane after bending. Moreover, the fibers need not be normal to the reference line before bending or after bending. (2) Fibers are inextensional; i.e., thickness of the beam does not change. (3) The normal stress perpendicular to the reference line must vanish; i.e., plane stress assumption.

The motion of the CB beam is described and approximated as:

$$\mathbf{x} = \left(\mathbf{x}_I + \frac{1}{2}\eta t_I^0 \mathbf{d}_I\right) N_I(\xi) = \sum_{I=1}^{2} \mathbf{x}_I N_I(\xi) + \sum_{I=1}^{2} \frac{1}{2}\eta t_I^0 N_I(\xi)\mathbf{d}_I, \qquad (3.2.12)$$

with the unit director vector defined as:

$$\mathbf{d}_I = \frac{\mathbf{x}_{I^+} - \mathbf{x}_{I^-}}{\|\mathbf{X}_{I^+} - \mathbf{X}_{I^-}\|} = \frac{\mathbf{x}_{I^+} - \mathbf{x}_{I^-}}{t_I^0} = \mathbf{i}\cos\theta_I + \mathbf{j}\sin\theta_I, \qquad I = 1, 2. \quad (3.2.13)$$

The one-dimensional standard shape functions $N_I(\xi)$ in terms of parent coordinates are defined as:

$$N_1(\xi) = \tfrac{1}{2}(1-\xi), \quad N_2(\xi) = \tfrac{1}{2}(1+\xi), \quad \xi \in [-1, +1]. \quad (3.2.14)$$

Note that Eq. (3.2.12) reflects the kinematic assumptions (1) and (2) given above. Accordingly, in order for the plane sections remain plane, the motion must be linear in η, i.e., along the thickness direction. Also, it can be shown that fibers are inextensible. To this end we note that top and bottom surfaces of the beam correspond to $\eta = +1$ and $\eta = -1$, respectively. Hence, the length of a fiber t_I in the deformed configuration is:

$$t_I = \left\| (\mathbf{x}_I + \frac{1}{2}(+1)t_I^0\mathbf{d}_I) - (\mathbf{x}_I + \frac{1}{2}(-1)t_I^0\mathbf{d}_I) \right\| = \|t_I^0\mathbf{d}_I\| = t_I^0, \quad (3.2.15)$$

which confirms the fiber inextensibility condition.

In line with the isoparametric formulation, displacements are interpolated by the same shape functions as used in the interpolation of geometry, Eq. (3.2.12).

That is:

$$\begin{aligned}\mathbf{u} &= \left(\tilde{\mathbf{u}}_I + \frac{1}{2}\eta t_I^0(\mathbf{d}_I - \mathbf{d}_I^0)\right) N_I(\xi) \\ &= \left(\tilde{\mathbf{u}}_I + \frac{1}{2}\eta t_I^0\left[\mathbf{i}(\cos\theta_I - \cos\theta_I^0) + \mathbf{j}(\sin\theta_I - \sin\theta_I^0)\right]\right) N_I(\xi) \\ &= \sum_{I=1}^{2} \tilde{\mathbf{u}}_I N_I(\xi) + \frac{1}{2}\eta \sum_{I=1}^{2} t_I^0 N_I(\xi)\left[\mathbf{i}(\cos\theta_I - \cos\theta_I^0) + \mathbf{j}(\sin\theta_I - \sin\theta_I^0)\right],\end{aligned} \tag{3.2.16}$$

where $\tilde{\mathbf{u}}_I$ is the vector of master node displacements u_I and v_I. As an illustration of the component form of Eq. (3.2.16), the finite element approximation of the displacement u, for example, can be expressed as:

$$\begin{aligned}u =& N_1(\xi)u_1 + N_2(\xi)u_2 + \\ & \tfrac{1}{2}\eta\left[N_1(\xi)t_1^0(\cos\theta_1 - \cos\theta_1^0) + N_2(\xi)t_2^0(\cos\theta_2 - \cos\theta_2^0)\right].\end{aligned} \tag{3.2.17}$$

For two-dimensional continuum, the Green strain can be expressed as:

$$\begin{aligned}\mathbf{E} &= \begin{bmatrix} 1 & 0 & 0 & 0 \\ 0 & 0 & 0 & 1 \\ 0 & 1 & 1 & 0 \end{bmatrix} \begin{Bmatrix} \frac{\partial u}{\partial X} \\ \frac{\partial u}{\partial Y} \\ \frac{\partial v}{\partial X} \\ \frac{\partial v}{\partial Y} \end{Bmatrix} + \frac{1}{2} \begin{bmatrix} \frac{\partial u}{\partial X} & 0 & \frac{\partial v}{\partial X} & 0 \\ 0 & \frac{\partial u}{\partial Y} & 0 & \frac{\partial v}{\partial Y} \\ \frac{\partial u}{\partial Y} & \frac{\partial u}{\partial X} & \frac{\partial v}{\partial Y} & \frac{\partial v}{\partial X} \end{bmatrix} \begin{Bmatrix} \frac{\partial u}{\partial X} \\ \frac{\partial u}{\partial Y} \\ \frac{\partial v}{\partial X} \\ \frac{\partial v}{\partial Y} \end{Bmatrix} \\ &= \left[\mathbf{H} + \tfrac{1}{2}\mathbf{A}(\mathbf{\Phi})\right]\mathbf{\Phi}.\end{aligned} \tag{3.2.18}$$

The Jacobian of the map between the element parent domain Ω_ξ and initial (reference) domain Ω_0 is given by:

$$\mathbf{J} = \begin{bmatrix} \frac{\partial X}{\partial \xi} & \frac{\partial Y}{\partial \xi} \\ \frac{\partial X}{\partial \eta} & \frac{\partial Y}{\partial \eta} \end{bmatrix}. \tag{3.2.19}$$

Having expressed the Jacobian $\mathbf{J}$, one can evaluate the elements of the displacement derivative vector $\mathbf{\Phi}$ in Eq. (3.2.18) as:

$$\left\{ \begin{array}{c} \frac{\partial u}{\partial X} \\ \frac{\partial u}{\partial Y} \end{array} \right\} = \mathbf{J}^{-1} \left\{ \begin{array}{c} \frac{\partial u}{\partial \xi} \\ \frac{\partial u}{\partial \eta} \end{array} \right\}, \qquad \left\{ \begin{array}{c} \frac{\partial v}{\partial X} \\ \frac{\partial v}{\partial Y} \end{array} \right\} = \mathbf{J}^{-1} \left\{ \begin{array}{c} \frac{\partial v}{\partial \xi} \\ \frac{\partial v}{\partial \eta} \end{array} \right\}. \tag{3.2.20}$$

where $\frac{\partial u}{\partial \xi}$, $\frac{\partial u}{\partial \eta}$, *etc.*, are determined from Eq. (3.2.16) as, for example:

$$\begin{aligned} \frac{\partial u}{\partial \xi} =& \tfrac{\mathrm{d}N_1}{\mathrm{d}\xi} u_1 + \tfrac{\mathrm{d}N_2}{\mathrm{d}\xi} u_2 + \\ & \tfrac{1}{2}\eta \left[\tfrac{\mathrm{d}N_1}{\mathrm{d}\xi} t_1^0 (\cos\theta_1 - \cos\theta_1^0) + \tfrac{\mathrm{d}N_2}{\mathrm{d}\xi} t_2^0 (\cos\theta_2 - \cos\theta_2^0) \right]. \end{aligned} \tag{3.2.21}$$

In order to determine the internal nodal forces, we combine Eqs. (3.2.3a) and (3.2.5a) to get:

$$\delta W^{int} = \delta \mathbf{u}_I^T \mathbf{f}_I^{int} = \int_{\Omega_0} \mathbf{S} : \delta \mathbf{E} \, \mathrm{d}\Omega_0, \tag{3.2.22}$$

where variation of the Green strain can be expressed, through the use of Eq. (3.2.18), as:

$$\begin{aligned} \delta \mathbf{E} &= \mathbf{H} \delta \mathbf{\Phi} + \tfrac{1}{2} \mathbf{A}(\mathbf{\Phi}) \delta \mathbf{\Phi} + \tfrac{1}{2} \delta \mathbf{A}(\mathbf{\Phi}) \mathbf{\Phi} = \mathbf{H} \delta \mathbf{\Phi} + \mathbf{A}(\mathbf{\Phi}) \delta \mathbf{\Phi} \\ &= \left[\mathbf{H} + \mathbf{A}(\mathbf{\Phi}) \right] \delta \mathbf{\Phi}, \end{aligned} \tag{3.2.23}$$

where we used $\frac{1}{2}\delta \mathbf{A}(\mathbf{\Phi})\mathbf{\Phi} = \frac{1}{2}\mathbf{A}(\delta\mathbf{\Phi})\mathbf{\Phi} = \frac{1}{2}\mathbf{A}(\mathbf{\Phi})\delta\mathbf{\Phi}$.

Now, we will relate $\delta\mathbf{\Phi}$ (and thus $\delta\mathbf{E}$ via Eq. (3.2.23)) to the variation of nodal variables (u_I, v_I, and θ_I), $\delta\mathbf{u}_I$, in Eq. (3.2.22). Using Eq. (3.2.20), $\delta\mathbf{\Phi}$

can be expressed as:

$$\delta\mathbf{\Phi} = \begin{Bmatrix} \frac{\partial \delta u}{\partial X} \\ \frac{\partial \delta u}{\partial Y} \\ \frac{\partial \delta v}{\partial X} \\ \frac{\partial \delta v}{\partial Y} \end{Bmatrix} = \begin{bmatrix} J^{-1}(1,1) & J^{-1}(1,2) & 0 & 0 \\ J^{-1}(2,1) & J^{-1}(2,2) & 0 & 0 \\ 0 & 0 & J^{-1}(1,1) & J^{-1}(1,2) \\ 0 & 0 & J^{-1}(2,1) & J^{-1}(2,2) \end{bmatrix} \begin{Bmatrix} \frac{\partial \delta u}{\partial \xi} \\ \frac{\partial \delta u}{\partial \eta} \\ \frac{\partial \delta v}{\partial \xi} \\ \frac{\partial \delta v}{\partial \eta} \end{Bmatrix}, \tag{3.2.24}$$

where in Eq. (3.2.24) $J^{-1}(i,j)$ refers to the i,j element of the inverse of Jacobian matrix. Note that variation of displacements, Eq. (3.2.16), can be expressed as:

$$\begin{aligned} \delta u &= \sum_I N_I(\xi)\delta u_I - \tfrac{1}{2}\eta \sum_I \left[N_I(\xi) t_I^0 \sin\theta_I \delta\theta_I\right], \\ \delta v &= \sum_I N_I(\xi)\delta v_I + \tfrac{1}{2}\eta \sum_I \left[N_I(\xi) t_I^0 \cos\theta_I \delta\theta_I\right]. \end{aligned} \tag{3.2.25}$$

Taking derivatives of Eqs. (3.2.25) with respect to ξ and η leads to the rightmost vector in Eq. (3.2.24):

$$\begin{Bmatrix} \frac{\partial \delta u}{\partial \xi} \\ \frac{\partial \delta u}{\partial \eta} \\ \frac{\partial \delta v}{\partial \xi} \\ \frac{\partial \delta v}{\partial \eta} \end{Bmatrix} = \begin{Bmatrix} \sum_I \frac{\mathrm{d}N_I}{\mathrm{d}\xi}\delta u_I - \frac{1}{2}\eta \sum_I \left[\frac{\mathrm{d}N_I}{\mathrm{d}\xi} t_I^0 \sin\theta_I \delta\theta_I\right] \\ -\frac{1}{2}\sum_I \left[N_I(\xi) t_I^0 \sin\theta_I \delta\theta_I\right] \\ \sum_I \frac{\mathrm{d}N_I}{\mathrm{d}\xi}\delta v_I + \frac{1}{2}\eta \sum_I \left[\frac{\mathrm{d}N_I}{\mathrm{d}\xi} t_I^0 \cos\theta_I \delta\theta_I\right] \\ \frac{1}{2}\sum_I \left[N_I(\xi) t_I^0 \cos\theta_I \delta\theta_I\right] \end{Bmatrix} \tag{3.2.26}$$

Hence, inserting Eq. (3.2.26) into Eq. (3.2.24) we express $\delta\mathbf{\Phi}$ as:

$$\delta\mathbf{\Phi} = \frac{1}{2}\begin{bmatrix} 2J^{-1}(1,1)\sum_I \frac{\mathrm{d}N_I}{\mathrm{d}\xi} & \mathbf{0}^T & \mathring{\mathrm{b}}_1 \\ 2J^{-1}(2,1)\sum_I \frac{\mathrm{d}N_I}{\mathrm{d}\xi} & \mathbf{0}^T & \mathring{\mathrm{b}}_2 \\ \mathbf{0}^T & 2J^{-1}(1,1)\sum_I \frac{\mathrm{d}N_I}{\mathrm{d}\xi} & \mathring{\mathrm{b}}_3 \\ \mathbf{0}^T & 2J^{-1}(2,1)\sum_I \frac{\mathrm{d}N_I}{\mathrm{d}\xi} & \mathring{\mathrm{b}}_4 \end{bmatrix} \begin{Bmatrix} \delta u_I \\ \delta v_I \\ \delta\theta_I \end{Bmatrix}$$
$$= \mathbf{G}\begin{Bmatrix} \delta u_I \\ \delta v_I \\ \delta\theta_I \end{Bmatrix} = \mathbf{G}\delta\mathbf{u}_I, \tag{3.2.27}$$

with,

$$\begin{aligned}
\mathring{\mathrm{b}}_1 &= -\eta J^{-1}(1,1)\sum_I \left[\tfrac{\mathrm{d}N_I}{\mathrm{d}\xi} t_I^0 \sin\theta_I\right] - J^{-1}(1,2)\sum_I \left[N_I(\xi) t_I^0 \sin\theta_I\right], \\
\mathring{\mathrm{b}}_2 &= -\eta J^{-1}(2,1)\sum_I \left[\tfrac{\mathrm{d}N_I}{\mathrm{d}\xi} t_I^0 \sin\theta_I\right] - J^{-1}(2,2)\sum_I \left[N_I(\xi) t_I^0 \sin\theta_I\right], \\
\mathring{\mathrm{b}}_3 &= \eta J^{-1}(1,1)\sum_I \left[\tfrac{\mathrm{d}N_I}{\mathrm{d}\xi} t_I^0 \cos\theta_I\right] + J^{-1}(1,2)\sum_I \left[N_I(\xi) t_I^0 \cos\theta_I\right], \\
\mathring{\mathrm{b}}_4 &= \eta J^{-1}(2,1)\sum_I \left[\tfrac{\mathrm{d}N_I}{\mathrm{d}\xi} t_I^0 \cos\theta_I\right] + J^{-1}(2,2)\sum_I \left[N_I(\xi) t_I^0 \cos\theta_I\right].
\end{aligned} \tag{3.2.28}$$

Substituting Eq. (3.2.27) for $\delta\mathbf{\Phi}$ in Eq. (3.2.23) gives:

$$\delta\mathbf{E} = \left[\mathbf{H} + \mathbf{A}(\mathbf{\Phi})\right]\mathbf{G}\delta\mathbf{u}_I = \mathbf{B}_{nl}\delta\mathbf{u}_I. \tag{3.2.29}$$

Finally, using Eq. (3.2.29) in Eq. (3.2.22) and considering the arbitrariness of $\delta\mathbf{u}_I$ yields the internal nodal forces:

$$\mathbf{f}_I^{int} = \int_{\Omega_0} \mathbf{B}_{nl}^T \mathbf{S}\,\mathrm{d}\Omega_0. \tag{3.2.30}$$

In Eq. (3.2.30), PK2 stress $\mathbf{S}$ is related to Green strain $\mathbf{E}$ via a constitutive model. In the present study, the beam material is assumed to behave in a linear elastic manner. Prior to relating $\mathbf{S}$ to $\mathbf{E}$, the aforementioned kinetic assumption, i.e., plane stress assumption, must be enforced such that the normal stress $S_{\hat{y}}$ perpendicular to the beam reference line vanishes. Notice that the plane stress assumption must be imposed in the local material coordinates $\hat{x}$ and $\hat{y}$ (shown in Figure 3.2) which are attached to the beam [98, 104]. Accordingly, the linear elastic constitutive matrix $\mathbf{C}_l$ which is given as [100]:

$$\hat{\mathbf{S}} = \mathbf{C}_l \hat{\mathbf{E}}, \qquad \begin{Bmatrix} S_{\hat{x}} \\ S_{\hat{y}} \\ S_{\hat{x}\hat{y}} \end{Bmatrix} = \frac{E}{1-\nu^2} \begin{bmatrix} 1 & \nu & 0 \\ \nu & 1 & 0 \\ 0 & 0 & \frac{1-\nu}{2} \end{bmatrix} \begin{Bmatrix} \epsilon_{\hat{x}} \\ \epsilon_{\hat{y}} \\ \epsilon_{\hat{x}\hat{y}} \end{Bmatrix}, \tag{3.2.31}$$

is modified to account for the zero normal stress assumption, $S_{\hat{y}} = 0$, as:

$$\mathbf{C}_{l,\diamond} = \frac{E}{1-\nu^2} \begin{bmatrix} 1 & 0 & 0 \\ 0 & 0 & 0 \\ 0 & 0 & \frac{1-\nu}{2} \end{bmatrix}, \tag{3.2.32}$$

where E and ν are modulus of elasticity and Poisson's ratio of the beam material. Finally, the modified constitutive matrix $\mathbf{C}_{l,\diamond}$ is rotated from the local material coordinates to global coordinates via:

$$\mathbf{C}_t = \mathbf{R}\mathbf{C}_{l,\diamond}\mathbf{R}^T, \tag{3.2.33}$$

where $\mathbf{R}$ is the matrix for rotation from local material system to global system [98, 104].

Having obtained the constitutive matrix $\mathbf{C}_t$, PK2 stress can be related to

Green strain according to:

$$\mathbf{S} = \mathbf{C}_t \mathbf{E}, \tag{3.2.34}$$

and the internal nodal forces, Eq. (3.2.30), can now be expressed as:

$$\mathbf{f}_I^{int} = \int_{\Omega_0} \mathbf{B}_{nl}^T \mathbf{C}_t \mathbf{E} \, \mathrm{d}\Omega_0. \tag{3.2.35}$$

A linear viscous dissipation mechanism is included in the computational model by adding Rayleigh proportional damping force (see Reference [100]) $\mathbf{f}_I^{damp}$ to the discretized equations of motion, Eq. (3.2.6). The damping force is given by:

$$\begin{aligned} \mathbf{f}_I^{damp} &= \mathbf{C}_{IJ} \dot{\mathbf{u}}_J = \left(\alpha_d \mathbf{M}_{IJ} + \beta_d \mathbf{K}_{IJ} \right) \dot{\mathbf{u}}_J \\ &= \alpha_d \mathbf{M}_{IJ} \dot{\mathbf{u}}_J. \end{aligned} \tag{3.2.36}$$

As can be noted in Eq. (3.2.36), the damping force is considered to be "mass proportional" by setting the stiffness matrix multiplier, β_d, to zero. With the inclusion of the damping force, Eq. (3.2.36), the discretized equation of motion can be expressed as:

$$\mathbf{M}_{IJ} \ddot{\mathbf{u}}_J + \mathbf{f}_I^{damp} + \mathbf{f}_I^{int} = \mathbf{f}_I^{ext}. \tag{3.2.37}$$

As will be seen in the next section, the implicit discretization of the assembled form of Eq. (3.2.37) in the time domain will require the use of the Jacobian of the internal nodal forces which is termed the *tangent stiffness matrix*. The tangent stiffness matrix $\mathbf{K}_t$ is used to relate the change (or variation, differential) of internal nodal forces to the change of nodal degrees of freedom.

In order to derive $\mathbf{K}_t$, variation of Eq. (3.2.30) is taken to yield:

$$\begin{aligned}\delta \mathbf{f}_I^{int} &= \int_{\Omega_0} \left(\mathbf{B}_{nl}^T \delta \mathbf{S} + \delta \mathbf{B}_{nl}^T \mathbf{S} \right) \, \mathrm{d}\Omega_0 = \mathbf{K}_t \delta \mathbf{u}_I \\ &= [\mathbf{K}_{t,mat} + \mathbf{K}_{t,\sigma}] \delta \mathbf{u}_I \\ &= [\mathbf{K}_{t,mat} + \mathbf{K}_{t,\sigma 1} + \mathbf{K}_{t,\sigma 2}] \delta \mathbf{u}_I, \end{aligned} \tag{3.2.38}$$

where $\mathbf{K}_{t,mat}$ and $\mathbf{K}_{t,\sigma}$ are called material and geometric tangent stiffness matrices, respectively. The material tangent stiffness matrix is given by:

$$\mathbf{K}_{t,mat} = \int_{\Omega_0} \mathbf{B}_{nl}^T \mathbf{C}_t \mathbf{B}_{nl} \, \mathrm{d}\Omega_0, \tag{3.2.39}$$

where $\mathbf{B}_{nl}$ and $\mathbf{C}_t$ are given by Eqs. (3.2.29) and (3.2.33), respectively. The first part of the geometric stiffness matrix is expressed as:

$$\mathbf{K}_{t,\sigma 1} = \int_{\Omega_0} \mathbf{G}^T \tilde{\mathbf{S}} \mathbf{G} \, \mathrm{d}\Omega_0, \tag{3.2.40}$$

where $\mathbf{G}$ is given by Eq. (3.2.27) and $\tilde{\mathbf{S}}$ is defined as:

$$\tilde{\mathbf{S}} = \begin{bmatrix} \mathbf{S} & \mathbf{0} \\ \mathbf{0} & \mathbf{S} \end{bmatrix}. \tag{3.2.41}$$

The second part of the geometric stiffness matrix is obtained from Eq. (3.2.38) as:

$$\mathbf{K}_{t,\sigma 2} \delta \mathbf{u}_I = \int_{\Omega_0} \left(\mathring{S}_1 \delta \mathbf{G}_1 + \mathring{S}_2 \delta \mathbf{G}_2 + \mathring{S}_3 \delta \mathbf{G}_3 + \mathring{S}_4 \delta \mathbf{G}_4 \right) \, \mathrm{d}\Omega_0, \tag{3.2.42}$$

with,

$$\begin{aligned}
\mathring{S}_1 &= S_x(1+\tfrac{\partial u}{\partial X}) + S_{xy}\tfrac{\partial u}{\partial Y} \\
\mathring{S}_2 &= S_{xy}(1+\tfrac{\partial u}{\partial X}) + S_y\tfrac{\partial u}{\partial Y} \\
\mathring{S}_3 &= S_{xy}(1+\tfrac{\partial v}{\partial Y}) + S_x\tfrac{\partial v}{\partial X} \\
\mathring{S}_4 &= S_y(1+\tfrac{\partial v}{\partial Y}) + S_{xy}\tfrac{\partial v}{\partial X},
\end{aligned} \tag{3.2.43}$$

where, PK2 stress components (S_x, S_y, and S_{xy}) are given in Eq. (3.2.34), and $\frac{\partial u}{\partial X}$, $\frac{\partial v}{\partial X}$, *etc.*, are given by Eqs. (3.2.20). In Eq. (3.2.42), the $\delta\mathbf{G}_k$ ($k = 1, \ldots, 4$) are obtained by taking variation of k^{th} column of matrix $\mathbf{G}$ in Eq. (3.2.27). Accordingly, we can write:

$$\delta\mathbf{G}_k = \mathring{\mathbf{G}}_k \delta\mathbf{u}_I = \begin{bmatrix} 0 & 0 & 0 & 0 & 0 & 0 \\ 0 & 0 & 0 & 0 & 0 & 0 \\ 0 & 0 & D_k(1,1) & 0 & 0 & 0 \\ 0 & 0 & 0 & 0 & 0 & 0 \\ 0 & 0 & 0 & 0 & 0 & 0 \\ 0 & 0 & 0 & 0 & 0 & D_k(2,2) \end{bmatrix} \delta\mathbf{u}_I, \tag{3.2.44}$$

where nonzero components of matrix $\mathring{\mathbf{G}}_k$ are given by:

$$\begin{aligned}
D_1(I,I) &= \tfrac{-1}{2}\left(\eta J^{-1}(1,1)\tfrac{\mathrm{d}N_I}{\mathrm{d}\xi} + J^{-1}(1,2)N_I(\xi)\right) t_I^0 \cos\theta_I \\
D_2(I,I) &= \tfrac{-1}{2}\left(\eta J^{-1}(2,1)\tfrac{\mathrm{d}N_I}{\mathrm{d}\xi} + J^{-1}(2,2)N_I(\xi)\right) t_I^0 \cos\theta_I \\
D_3(I,I) &= \tfrac{-1}{2}\left(\eta J^{-1}(1,1)\tfrac{\mathrm{d}N_I}{\mathrm{d}\xi} + J^{-1}(1,2)N_I(\xi)\right) t_I^0 \sin\theta_I \\
D_4(I,I) &= \tfrac{-1}{2}\left(\eta J^{-1}(2,1)\tfrac{\mathrm{d}N_I}{\mathrm{d}\xi} + J^{-1}(2,2)N_I(\xi)\right) t_I^0 \sin\theta_I\,, \quad I = 1,2.
\end{aligned} \tag{3.2.45}$$

Hence, the second part of the geometric stiffness matrix can be expressed as:

$$\mathbf{K}_{t,\sigma 2} = \int_{\Omega_0} \left(\mathring{S}_1 \mathring{\mathbf{G}}_1 + \mathring{S}_2 \mathring{\mathbf{G}}_2 + \mathring{S}_3 \mathring{\mathbf{G}}_3 + \mathring{S}_4 \mathring{\mathbf{G}}_4 \right) \mathrm{d}\Omega_0. \tag{3.2.46}$$

Finally, the complete tangent stiffness matrix is given as:

$$\mathbf{K}_t = \mathbf{K}_{t,mat} + \mathbf{K}_{t,\sigma 1} + \mathbf{K}_{t,\sigma 2}, \tag{3.2.47}$$

where $\mathbf{K}_{t,mat}$, $\mathbf{K}_{t,\sigma 1}$, and $\mathbf{K}_{t,\sigma 2}$ are defined in Eqs. (3.2.39), (3.2.40), and (3.2.46), respectively.

In order to compute the integrals in Eqs. (3.2.35), (3.2.39), (3.2.40), and (3.2.46) (i.e., the internal nodal force and tangent stiffness matrix), we employ a type of numerical quadrature. As described in Reference [104], a single stack of 3 Gauss quadrature points is utilized along the thickness direction while one Gauss quadrature point is used along the length direction of the element. Such a quadrature scheme is called selective-reduced integration and recommended for the beam element to avoid shear locking problem [104].

3.2.4 Stress/Strain Postprocessing

The components of Green strain and second Piola-Kirchhoff (PK2) stresses are computed at the Gauss quadrature points. In order to determine the strain and stress components at other points in the element domain for postprocessing purposes, we assume a bilinear function, $\mathfrak{s}(\xi, \eta) = s_0 + s_1\eta + s_2\xi$, for the distribution of each component over the element domain. Then, the coefficients (s_0, s_1, and s_2) are calculated based on the known values at the quadrature points by using a linear least squares regression. Finally, the strain and stress

components at a node are determined using the function $\mathfrak{s}(\xi, \eta)$ with ξ and η coordinates of the node.

3.2.5 Time Discretization via HHT-α Method

Assembling the element forces/matrices, which is mathematically equivalent to mapping the region $\bar{\Omega}_0$ containing all nodal points of Ω_0, onto the disconnected set of elements (unassembled region) results in the following set of ordinary differential equations:

$$\mathbf{M}\ddot{\mathbf{u}} + \mathbf{f}^{damp} + \mathbf{f}^{int} = \mathbf{f}^{ext}. \tag{3.2.48}$$

Equations (3.2.48) are referred to as semi-discrete because they are discrete only in the spatial domain and need to be discretized and, thus, solved in the time domain as well. In the realm of structural dynamics most often Eq. (3.2.48) is solved numerically by using so-called direct time integration methods such as the Newmark family of methods [109–111]. According to direct time integration, the response history of interest is divided into steps and the numerical scheme is applied step-by-step to compute out into the future and, hence, trace out the trajectory of the solution [100, 112].

In the present study, we solved the assembled semi-discrete equations of motion, (3.2.48), by using the Hilber-Hughes-Taylor α (HHT-α) method [99] which is an improved version of the Newmark method. Contributions of the higher modes of the semi-discrete equations of motion to the dynamic response are often of little interest. In addition, these higher modes are typically inaccurate due to spatial discretization error. Therefore, the Newmark method provides algorithmic dissipation to damp out the high-frequency spurious re-

sponse. However, dissipation of the high-frequency spurious modes with the Newmark method also significantly degrades the order of accuracy. In this regard, HHT-α improves on the algorithmic dissipation of the high-frequency spurious modes in order to lessen the degree of accuracy degradation [104,111].

The HHT-α time integration algorithm applied to Eq. (3.2.48) is written as [101,111]:

$$\mathbf{M}\ddot{\mathbf{u}}^{n+1} + (1+\alpha_{HHT})\left(\mathbf{C}\dot{\mathbf{u}}^{n+1} + \mathbf{f}_{int}^{n+1} - \mathbf{f}_{ext}^{n+1}\right) - \alpha_{HHT}\left(\mathbf{C}\dot{\mathbf{u}}^{n} + \mathbf{f}_{int}^{n} - \mathbf{f}_{ext}^{n}\right) = \mathbf{0}, \tag{3.2.49}$$

$$\mathbf{u}^{n+1} = \tilde{\mathbf{u}}^{n+1} + \beta_{HHT}(\Delta t)^2\ddot{\mathbf{u}}^{n+1}, \tag{3.2.50a}$$

$$\dot{\mathbf{u}}^{n+1} = \tilde{\dot{\mathbf{u}}}^{n+1} + \gamma_{HHT}\Delta t\ \ddot{\mathbf{u}}^{n+1}, \tag{3.2.50b}$$

$$\tilde{\mathbf{u}}^{n+1} = \mathbf{u}^{n} + \Delta t\dot{\mathbf{u}}^{n} + \tfrac{1}{2}(\Delta t)^2(1-2\beta_{HHT})\ddot{\mathbf{u}}^{n}, \tag{3.2.51a}$$

$$\tilde{\dot{\mathbf{u}}}^{n+1} = \dot{\mathbf{u}}^{n} + (1-\gamma_{HHT})\Delta t\ \ddot{\mathbf{u}}^{n}, \tag{3.2.51b}$$

with $\mathbf{f}^{damp}$ in Eq. (3.2.48) given by $\mathbf{C}\dot{\mathbf{u}}$.

In Eqs. (3.2.49)-(3.2.51), α_{HHT}, β_{HHT}, and γ_{HHT} are the parameters controlling the characteristics of the HHT-α algorithm such as accuracy, numerical stability and the amount of algorithmic damping, Δt is the step size ($\Delta t = t^{n+1} - t^n$), superscripts $n+1$ and n refer to the "current" and "previous" time steps, respectively, $\mathbf{u}^n$ and $\mathbf{u}^{n+1}$ designate the approximations for the nodal degrees of freedom at successive time steps, $\mathbf{f}_{int}^{n+1}$ and $\mathbf{f}_{ext}^{n+1}$ refer to $\mathbf{f}_{int}(\mathbf{u}^{n+1}, t^{n+1})$ and $\mathbf{f}_{ext}(\mathbf{u}^{n+1}, t^{n+1})$, respectively. Equation (3.2.49) is the discrete equation of motion at the end of a time step. Equations (3.2.50) are called *correctors* while Eqs. (3.2.51) are referred to as *predictors* [111]. In the present

study, the parameter α_{HHT} is taken to be -0.05 with $\beta_{HHT} = 0.25(1-\alpha_{HHT})^2$ and $\gamma_{HHT} = 0.5(1-2\alpha_{HHT})$. For linear systems, HHT-α method is known to be unconditionally stable when $\alpha_{HHT} \in [-\frac{1}{3}, 0]$ [104].

We can describe the HHT-α solution procedure as follows. Mass matrix $\mathbf{M}$ is computed and the initial values $\mathbf{u}^0$ and $\dot{\mathbf{u}}^0$ (at $t = t^{n=0} = t^0 = 0$) are used to determine the forces $\mathbf{f}^0 = \mathbf{f}^0_{ext} - \mathbf{f}^0_{int} - \mathbf{f}^0_{damp}$ at time t^0. Then, $\ddot{\mathbf{u}}^0$ is computed via $\ddot{\mathbf{u}}^0 = \mathbf{M}^{-1}\mathbf{f}^0$. Equation (3.2.50a) is solved for $\ddot{\mathbf{u}}$ at time step $n+1$, i.e., $\ddot{\mathbf{u}}^{n+1}$, and it is inserted into Eq. (3.2.50b) to determine $\dot{\mathbf{u}}$ at time step $n+1$, i.e., $\dot{\mathbf{u}}^{n+1}$. Substituting the results, $\ddot{\mathbf{u}}^{n+1}$ and $\dot{\mathbf{u}}^{n+1}$, into Eq. (3.2.49) yields a set of nonlinear algebraic equations in the unknown $\mathbf{u}^{n+1}$:

$$\begin{aligned}\mathbf{r}^{n+1} =& \mathbf{M}\left[\frac{1}{\beta_{HHT}(\Delta t)^2}(\mathbf{u}^{n+1} - \tilde{\mathbf{u}}^{n+1})\right] + \\ & (1+\alpha_{HHT})\left[\mathbf{C}\left(\tilde{\dot{\mathbf{u}}}^{n+1} + \frac{\gamma_{HHT}}{\beta_{HHT}\Delta t}(\mathbf{u}^{n+1} - \tilde{\mathbf{u}}^{n+1})\right) + \mathbf{f}^{n+1}_{int} - \mathbf{f}^{n+1}_{ext}\right] - \\ & \alpha_{HHT}\left[\mathbf{C}\dot{\mathbf{u}}^n + \mathbf{f}^n_{int} - \mathbf{f}^n_{ext}\right].\end{aligned} \tag{3.2.52}$$

Equation (3.2.52) is a set of nonlinear algebraic equations in the unknown $\mathbf{u}^{n+1}$ and can be solved using the Newton-Raphson method which is an iterative "root finding" scheme. Accordingly, at the current time step $n+1$, an initial guess made for $\mathbf{u}^{n+1}$ is inserted into Eq. (3.2.52). Unless the guess is the correct one, dynamic equilibrium will not be satisfied and Eq. (3.2.52) will produce a nonzero *residual* vector $\mathbf{r}^{n+1} \equiv \mathbf{r}(\mathbf{u}^{n+1}, t^{n+1})$. Therefore, the purpose is to determine $\mathbf{u}^{n+1}$ which renders the nonlinear residual function $\mathbf{r}^{n+1}$ zero and, thus, maintains the conservation of momentum at each time step.

Taylor series expansion of the residual function $\mathbf{r}^{n+1}$, Eq. (3.2.52), about the value of $\mathbf{u}^{n+1}$ at the current Newton *iteration number* i can be expressed

as:

$$\mathbf{r}(\mathbf{u}_{i+1}^{n+1}, t^{n+1}) = \mathbf{r}(\mathbf{u}_{i}^{n+1}, t^{n+1}) + \frac{\partial \mathbf{r}(\mathbf{u}_{i}^{n+1}, t^{n+1})}{\partial \mathbf{u}} \Delta\mathbf{u} + \mathcal{O}(\Delta\mathbf{u}^2), \tag{3.2.53}$$

where $\Delta\mathbf{u}$ is the increment in nodal unknowns and given by:

$$\Delta\mathbf{u} = \mathbf{u}_{i+1}^{n+1} - \mathbf{u}_{i}^{n+1}. \tag{3.2.54}$$

The Jacobian matrix in Eq. (3.2.53) is called the "effective tangent stiffness" matrix in computational mechanics [104] and can be expressed using Eq. (3.2.52) as:

$$\begin{aligned}
\mathbf{K}_{eff} &= \frac{\partial \mathbf{r}(\mathbf{u}_{i}^{n+1}, t^{n+1})}{\partial \mathbf{u}} \\
&= \tfrac{1}{\beta_{HHT}(\Delta t)^2}\mathbf{M} + (1+\alpha_{HHT})\left[\tfrac{\gamma_{HHT}}{\beta_{HHT}\Delta t}\mathbf{C} + \tfrac{\partial \mathbf{f}_{int}^{n+1}}{\partial \mathbf{u}} - \tfrac{\partial \mathbf{f}_{ext}^{n+1}}{\partial \mathbf{u}}\right] \\
&= \tfrac{1}{\beta_{HHT}(\Delta t)^2}\mathbf{M} + (1+\alpha_{HHT})\left[\tfrac{\gamma_{HHT}}{\beta_{HHT}\Delta t}\mathbf{C} + \mathbf{K}_t - \mathbf{K}_{ext}\right],
\end{aligned} \tag{3.2.55}$$

where $\mathbf{K}_t$ and $\mathbf{K}_{ext}$ are called the tangent stiffness and external load stiffness matrices, respectively. In the present study, the external load stiffness matrix is zero, whereas the tangent stiffness matrix $\mathbf{K}_t$ is given by the assembly of Eq. (3.2.47). Linearizing Eq. (3.2.53) and rearranging yields:

$$\mathbf{K}_{eff}\ \Delta\mathbf{u} = \mathbf{r}(\mathbf{u}_{i+1}^{n+1}, t^{n+1}) - \mathbf{r}(\mathbf{u}_{i}^{n+1}, t^{n+1}), \tag{3.2.56}$$

or noting that $\mathbf{r}(\mathbf{u}_{i+1}^{n+1}, t^{n+1}) = 0$:

$$\Delta\mathbf{u} = -\mathbf{K}_{eff}^{-1}\ \mathbf{r}(\mathbf{u}_{i}^{n+1}, t^{n+1}). \tag{3.2.57}$$

Once the Jacobian matrix, Eq. (3.2.55), is computed, Eq. (3.2.57) is used to determine $\Delta\mathbf{u}$ which is then used to compute the updated values of nodal degrees of freedom $\mathbf{u}_{i+1}^{n+1}$ via Eq. (3.2.54). The updated values are subsequently inserted in Eq. (3.2.52) to compute the residual $\mathbf{r}^{n+1}$. The foregoing process is carried out in an iterative fashion until the convergence criterion is met. The converged solution $\mathbf{u}^{n+1}$ (along with $\dot{\mathbf{u}}^{n+1}$ and $\ddot{\mathbf{u}}^{n+1}$) obtained at the current time step $n+1$ is used in the predictors (i.e., Eqs. (3.2.51)) of the subsequent time step $n+2$. This step-by-step iterative scheme is carried out over the course of the simulation time. In the present study, we used the "residual error criterion" [104] to terminate Newton-Raphson iterations according to:

$$\|\mathbf{r}^{n+1}\|_{\ell_2} \leq \epsilon_{tol} \max\left(\|\mathbf{f}_{ext}^{n+1}\|_{\ell_2}, \|\mathbf{f}_{int}^{n+1}\|_{\ell_2}, \|\mathbf{f}_{kin}^{n+1}\|_{\ell_2}\right), \tag{3.2.58}$$

where Euclidean norm (ℓ_2 norm) of a vector $\mathbf{a}$ is defined as $\|\mathbf{a}\|_{\ell_2} = (\sum_i a_i^2)^{1/2}$ and ϵ_{tol} is the convergence tolerance which was taken to be 0.001.

3.2.6 Implementation of Time-Dependent Boundary Conditions

The cantilever beam is put into flapping motion through its clamped end as shown in Figure 3.1. As depicted in Figure 2.3, the clamped end of the beam is rigidly connected to the rocker link of a 4-bar crank-and-rocker mechanism. As such, the flapping angle θ_f which varies with time is directly related to the rocker angle θ_4 of the mechanism (see Figure 2.3). As can be noted from Figure 2.3b, there is a fixed angle between θ_f and θ_4 such that θ_f=$\theta_4 - \frac{2\pi}{3}$. The rocker angle θ_4 is a function of link lengths of the mechanism and the crank angle θ_2 as given by Eq. (B.5) in Appendix B. The crank angle θ_2 is a

function of the flapping frequency and time and is given by:

$$\theta_2 \equiv \omega_f \; t + \theta_{rot} \pmod{2\pi}, \tag{3.2.59}$$

where ω_f is the flapping frequency, t is the time, and θ_{rot} is a constant angle which is used to rotate the crank link so that the flapping angle is set to zero (i.e., the beam lines up with the reference line, see Figure 2.3b) when $t = 0$. In Eq. (3.2.59), modulo 2π is used to keep θ_2 in the range of $[0, 2\pi]$ in accordance with the kinematic analysis given in Appendix B.

The flapping motion of the beam is modeled by imposing time-dependent boundary conditions on all 3 degrees of freedom of node 1, which is coincident with the clamped boundary point of the beam, see Figure 3.1. The motion is imposed by considering the theoretical position of the boundary point (point E shown in Figure 2.3b) based upon the 4-bar mechanism kinematics. Accordingly, the degrees of freedom of node 1, $\mathbf{u}_1$, are prescribed as:

$$\begin{aligned} u_1 &= x_1 - X_1 = d\cos\theta_f - d - X_1 \\ v_1 &= y_1 - Y_1 = d\sin\theta_f - Y_1 \\ \theta_1 &= \theta_f, \end{aligned} \tag{3.2.60}$$

where, x_1 and y_1 are the current coordinates of node 1, X_1 and Y_1 are the initial coordinates of node 1, d is the offset distance (33.3 mm) as shown in Figure 3.1a. Note that as the flapping angle θ_f varies with time so do the u_1, v_1, and θ_1. Also note that, for a given time step t^{n+1}, the degrees of freedom of the boundary point (node 1) at that particular time step $n+1$, $\mathbf{u}_{1,i}^{n+1}$, are also known per Eqs. (3.2.60).

Prescribed displacements, Eqs. (3.2.60), are implemented into the com-

putational model by modifying Eq. (3.2.56). Implementation of the time-dependent boundary conditions as described in the following procedure is similar to the procedure reported by Attar and Gordnier [101], and its time-independent version can be found in Reference [105]. To begin with, we call the right hand side of Eq. (3.2.56) as $\mathbf{r}_{eff}$ and modify it according to:

$$\mathbf{r}_{eff,\diamond} = \mathbf{r}_{eff} - \mathbf{K}_{eff}\ \Delta\mathbf{u}_{\diamond}, \tag{3.2.61}$$

where $\Delta\mathbf{u}_{\diamond}$ involves the prescribed displacements at a given time step. Next, the entries of the vector $\mathbf{r}_{eff,\diamond}$ which correspond to the prescribed degrees of freedom are assigned the prescribed displacement values. Then, the effective tangent stiffness matrix $\mathbf{K}_{eff}$ is modified such that the entries of the row and column which correspond to a prescribed degree of freedom are assigned zeroes while the entry at the intersection of the row and column is given unity. Modification of $\mathbf{K}_{eff}$ in this manner is repeated for all prescribed degrees of freedom.

The premise of the foregoing modification process is as follows. At a given node either forces or degrees of freedom are known but not both. Likewise, prescribing the degrees of freedom at a node leaves the forces at the node unknown and *vice versa*. At the boundary node, we prescribe the degrees of freedom which leaves reaction forces at the node unknown. Aforementioned modification replaces the equations related to unknown reaction forces with trivial equations, which set nodal degrees of freedom to their prescribed values, while taking into account the contribution of prescribed degrees of freedom to the force vector. This procedure excludes the unknown reaction forces from computation and, thus, reduces the number of unknowns, and renders nodal

degrees of freedom as the only unknowns. If desired, the unknown reaction forces can be computed after nodal degrees of freedom are determined.

3.3 Experimental Model

In the present work, one-degree-of-freedom flapping motion is generated with a flapping test bed details of which is given in Section 2.2.1. Aluminum 6061-T6 beam specimens (see Section 2.3) are tested in ambient air at two flapping amplitudes 15° and 30°. The structural dynamic response is characterized based on surface bending strain and tip displacement data collected with electrical resistance strain gages and a high-speed camera. The details of bending strain and tip deformation measurements are given in Sections 2.4.1 and 2.4.2, respectively. The beam transverse tip displacements are calculated through comparison of the pixel data and the calibrated pixel width using the following equation:

$$v_{tip} = (y(t) - y_0)\, l_{pix}, \tag{3.3.1}$$

where $y(t)$ and y_0 are the current and initial y coordinates (see Figure 3.1a) of the beam tip as measured in units of pixels and $l_{pix} = 0.53$ [mm/pixel]. Note that y coordinate given in Eq. (3.3.1) corresponds to the horizontal coordinate in the image processing program window shown in Figure 2.12. The camera frame rate is reset for each flapping frequency such that 129 images are captured over one flapping cycle at all frequencies tested. Uncertainty in the tip displacement data is primarily due to bias error which is caused by the image resolution with least count of 0.53 mm.

Experiments are performed at flapping frequencies up to 19 Hz for flapping at 15° and up to 11 Hz for flapping at 30°, with increments as small as 0.1 Hz.

Each test is performed as many as three times and the results are found to be repeatable. Standard deviation data of experimental bending strain signal is listed in Table D.1 (in Appendix D) along with the associated uncertainties which are calculated using either Student's t-distribution with 95% confidence level of standard deviation. The experimental data points which are presented in Section 3.4 represent the average of the test results (without error bars). Each realization of the experiment is initiated with the beam at rest. Data collection is started once the desired flapping frequency is reached; a minimum of 3 s of data is taken.

For flapping at 30°, tests are not run above 11 Hz as doing so leads to the beam experiencing damage and eventual fracture. For frequencies of 11 Hz and below, the beam does not show any damage which is confirmed through testing the beam, after each frequency realization, for possible shifts in the first natural frequency which would indicate some level of damage. For flapping at 15° and higher frequencies (i.e., above 13 Hz), a reduction of 0.62 Hz is determined in the first natural frequency. Such a decrease in the natural frequency corresponds to a reduction of approximately $5 \sim 5.5$ GPa in the Young's modulus. Theoretical strain at the yield point is calculated as 3600 μ-strain based on the tensile yield strength of 248 MPa given for the material [89] (see Table 2.1). As can be seen in frequency response curve (given in Section 3.4), this value is achieved near primary resonance and therefore, despite the fact that there is no visual indication of damage (i.e., permanent deformation, fracture, etc.), it is likely that the beam undergoes slight yielding at flapping frequencies above 13 Hz for flapping at 15°. It is also likely that at high strain levels, in addition to some permanent stiffness reduction, the material exhibits some recoverable reduction in stiffness due to nonlinear elastic effects which are not modeled in

the simulation. This permanent and (possible) recoverable stiffness reduction may attribute to some of the observed disagreement (see Section 3.4) between simulation and experiment in the primary resonance region for flapping at 15°.

3.4 Comparison of Experimental and Numerical Results

3.4.1 Comparison of Beam Bending Strains

Frequency response curves obtained through experiment and simulation are shown in Figure 3.3 for flapping amplitudes of 15° and 30°. All results in this section, and in the sections to follow, will be presented in terms of a nondimensional flapping frequency $\omega_0 = \omega_f/\omega_1$ where ω_f is the flapping frequency and ω_1 is the beam first modal frequency. In Figure 3.3, the response of the beam is characterized by the standard deviation (S.D.) of the surface bending strain which is obtained on the beam midline 40 mm away from the clamped edge. The simulation data points shown in Figure 3.3 correspond to the beam response taken from $t = 35$ s to $t = 40$ s (i.e., for a duration of 5 s). The simulation results are generated by "marching up" the flapping frequency in a range starting at $\omega_0 = 0.034$ and ending at a point past the beam linear natural frequency, with frequency increments no larger than $\Delta\omega_0 = 0.034$. In regions of particular interest, smaller frequency increments (as small as $\Delta\omega_0 = 0.007$) are taken in both experiment and simulation. With the exception of a small region near the first natural frequency of the beam, where irregular, possibly chaotic solutions are observed (to be discussed below), the numerical solutions do not change when the initial conditions are modified to correspond to frequency "marching down." This result, which is demonstrated in Figure 3.3, does not necessarily indicate that only one stable solution branch exists for the

these forcing parameters but perhaps does point to small basin of attraction for these additional stable branches if they do exist. This idea will be explored further in Chapters 4 and 5.

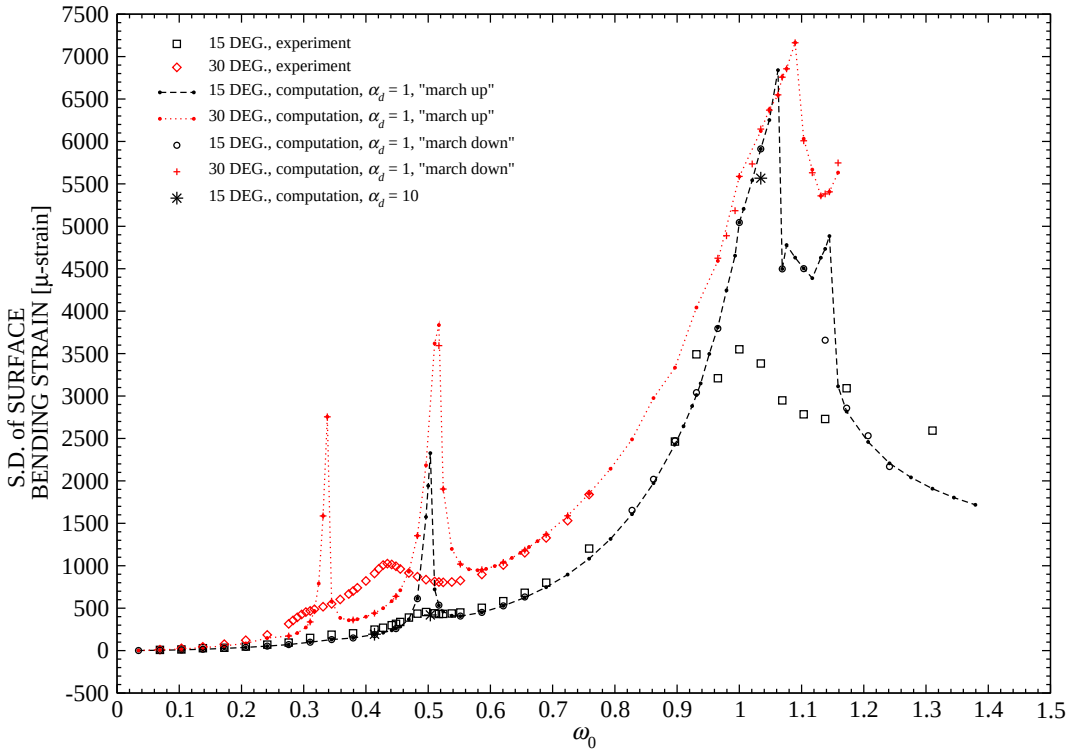

Figure 3.3: Experimental and simulation midline surface bending strains (standard deviation of strain signal) versus flapping frequency at flapping amplitudes of 15° and 30°. Effect of an increase in damping (from $\alpha_d = 1$ to $\alpha_d = 10$) on the response at $\omega_0 = 0.41$, 0.50, and 1.03 at 15° is also depicted. Data points corresponding to the frequency "march down" cases are plotted with hollow circles (for 15°) and plus signs (for 30°). Due to small uncertainty levels, and to improve clarity of presentation, error bars are not indicated on the experimental data points. See Table D.1 for experimental data values and associated uncertainty intervals.

The first characteristic to be observed in Figure 3.3 is that in both the experiment and simulation peak response occurs near the linear natural frequency. This result is in accordance with the lack of strong hysteretic effects, i.e., multiple stable solutions for a given set of flapping parameters as noted in

the previous paragraph. Also observe in Figure 3.3 that the simulation data show secondary resonance peaks in addition to the primary resonance peak near $\omega_0 = 1$. A superharmonic resonance peak of order 2 is observed at both flapping amplitude levels when the flapping frequency nears $\omega_0 = 1/2$, and another superharmonic resonance peak (of order 3) appears for flapping at 30° when ω_0 approaches a value of 1/3. Experimental data shown in Figure 3.3 are in good quantitative agreement with the computational data for flapping frequencies outside regions of (primary or secondary) resonance. The superharmonic resonance of order 2 for flapping at 15° is present in the experimental data but with smaller magnitude when compared with the simulation data. At 30°, experimental data reveal a broad peak centered around $\omega_0 = 0.43$ which extends over the region of superharmonic peaks given by the simulation data. While it may be coincidental, it is interesting that $\omega_0 = 0.43$ is approximately equal to the arithmetic mean of the second and third-order superharmonic resonance frequencies, $\omega_0 = 0.34$ and $\omega_0 = 0.52$, as determined in the simulations. As will be shown below (Figure 3.7), the experimental response frequency spectra in this region of secondary resonance ($0.31 \lessapprox \omega_0 \lessapprox 0.51$) contain dominant peaks at third-order harmonics of the forcing frequency. Hence it is likely that this region of secondary resonance is due to a third-order superharmonic resonance whereby the nonlinearity in the system is adjusting the free-vibration response such that it is 3 times the flapping frequency [22].

As mentioned in Section 3.2, the simulations use linear (Rayleigh) damping with nominal mass proportional coefficient of $\alpha_d = 1.0$. This linear approximation for the damping appears to be sufficient in regions away from the resonance peaks since, as shown in Figure 3.3, overall agreement between the experimental and computational data is good. Conversely, it is also demon-

strated in Figure 3.3 that discrepancy between the experimental and computational data is considerable when primary and secondary resonance regions are considered. In order to observe how the magnitude of the linear damping coefficient affects the response in the various flapping frequency regions (i.e., near and away from resonance) simulation is conducted with $\alpha_d = 10.0$. As shown in Figure 3.3, increasing the damping coefficient has no effect on the response at $\omega_0 = 0.41$ (away from any resonance peaks); decreases response amplitude considerably at $\omega_0 = 0.50$ (near superharmonic resonance) resulting in better agreement with experiment; and decreases the response amplitude slightly at $\omega_0 = 1.03$ (near primary resonance). It is our conclusion, and backed up by the relevant literature in this area [52,84], that for this problem the linear damping assumption appears to be incorrect in regions of resonance. To obtain better quantitative agreement with experiment in these regions it may be necessary to include interaction with the surrounding fluid or, at the very least, use a nonlinear damping model with empirically-determined coefficients. This topic is explored in Chapter 4. It is also possible that nonlinear elastic effects need to be included in the simulation in order to improve the agreement between experiment and simulation in the primary resonance region.

Shown in Figures 3.4-3.7 are the time histories and discrete Fourier transforms (DFTs) of surface bending strain obtained from both experiment and simulation. In the sequel the result of performing a DFT of a response signal will be referred to as a response spectrum. In both experiment and simulation the results presented correspond to data collected over 5 flapping cycles. It should be noted here that the abscissa of the time history plots presented in this chapter refers to the number of flapping cycles (through normalizing time by the flapping period) and is shifted to zero only for convenience. As

shown in Figure 3.4, for flapping at 15°, the evolution of the beam response with increasing flapping frequency appears to follow a similar pattern in both experimental and simulation results. At flapping frequencies below $\omega_0 \approx 0.21$, the response is periodic with a period equal to that of the flapping period. In the remainder of this chapter this type of 1-period or 1-cycle response will be denoted as "1T." As expected, the response results in a single dominant peak in the corresponding response spectrum shown in Figure 3.5a. As shown in Figure 3.4b-e, when the flapping frequency is increased between $\omega_0 = 0.31$ and $\omega_0 = 0.54$, local vibrations with varying number of local minima and maxima appear in the time histories, which are the result of strong higher harmonic content in the response spectra. In particular, the simulation response spectra for these forcing frequencies, shown in Figure 3.5b-e, display second harmonic content while experimental response spectra have additional content at the third and fourth harmonics. In addition, when local vibrations in the time history are present, the response is asymmetric in both the experiment and simulation. As shown in Figure 3.5e-g, flapping with frequency in the range $0.54 \lessapprox \omega_0 \lessapprox 0.90$ results in a 1T response with minimal local vibration and response spectra which are dominated by the first harmonic of the flapping frequency. As shown in Figure 3.5h and i, further increase of the flapping frequency to $\omega_0 = 1.0$ and $\omega_0 = 1.10$, which is in the range of the linear first modal frequency, results in simulation response spectra containing many components. In particular the spectrum for $\omega_0 = 1.10$, shown in Figure 3.5i, appears to have wide bands, concentrated near odd harmonics, indicating possible irregular dynamics. On the other hand the experimental response is less complex for these two flapping frequencies with a dynamic response similar to the data measured for flapping at $\omega_0 = 0.69$ and $\omega_0 = 0.90$ Finally, as shown

in Figures 3.4j and 3.5j, at $\omega_0 = 1.17$ both experiment and simulation have a comparable 1T response dominated by the first harmonic of the flapping frequency.

Figures 3.6 and 3.7 show the beam surface bending strain obtained at 30° in the temporal and frequency domains. While the overall agreement between experiment and simulation is good for flapping frequencies where the experiment could be realized (i.e., below $\omega_0 = 0.76$), the simulation does overestimate the experimental bending strain in regions of superharmonic resonance. As observed for flapping at 15°, strong higher harmonic content and the resulting local vibration are present in both experiment and simulation in regions of superharmonic resonance (see Figure 3.6c & g). The experimental data show a larger number of local maxima and minima compared to the simulation which, as shown in Figure 3.7, is likely due to the larger contribution (with the exception of $\omega_0 = 0.51$, Figure 3.7g) from higher harmonics. The relatively larger contribution from higher harmonics over a larger range of flapping frequencies is likely a contributor to the broader peak, when compared to the simulation result, observed for the experiment in the superharmonic resonance region. Finally, as was the case for flapping at 15°, the simulation predicts a very dynamically complex response at $\omega_0 = 1.10$ with a broadband response spectrum (Figure 3.7j) which is perhaps indicative of an irregular response.

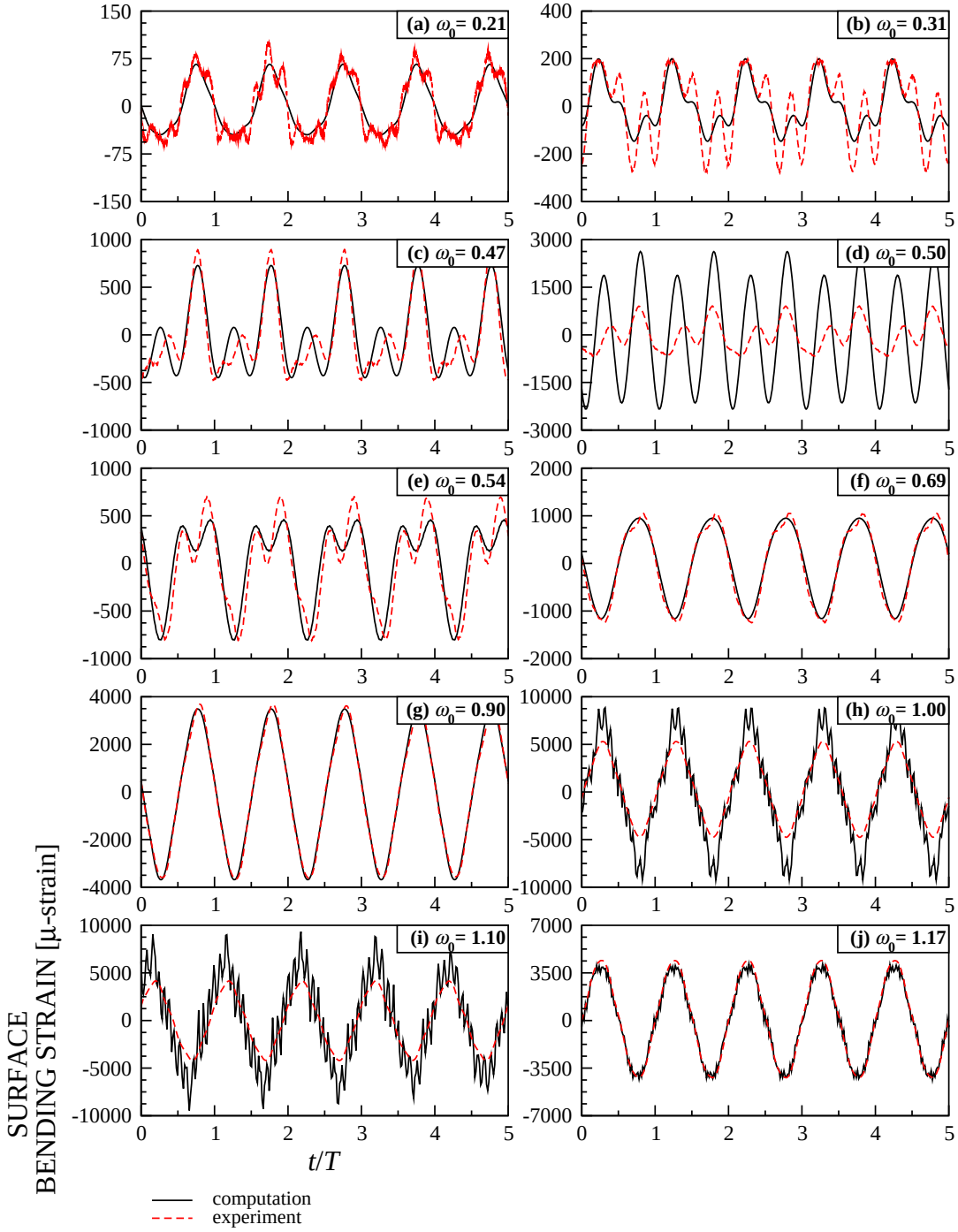

Figure 3.4: Time history of experimental and simulation surface bending strain obtained at 15° for normalized flapping frequencies ω_0 of: (a) 0.21, (b) 0.31, (c) 0.47, (d) 0.50, (e) 0.54, (f) 0.69, (g) 0.90, (h) 1.00, (i) 1.10, and (j) 1.17.

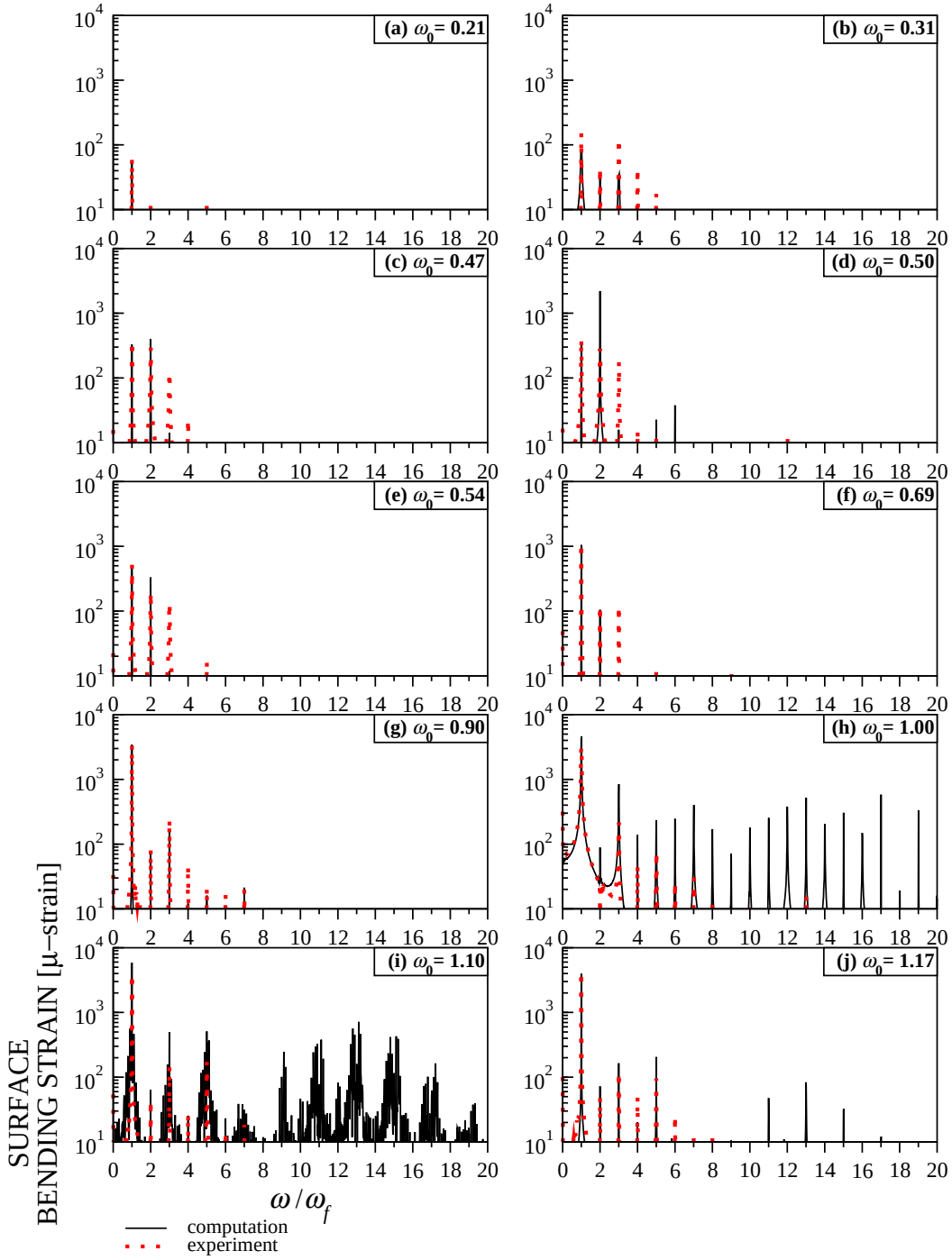

Figure 3.5: Discrete Fourier transform of experimental and simulation surface bending strain obtained at 15° for normalized flapping frequencies ω_0 of: (a) 0.21, (b) 0.31, (c) 0.47, (d) 0.50, (e) 0.54, (f) 0.69, (g) 0.90, (h) 1.00, (i) 1.10, and (j) 1.17.

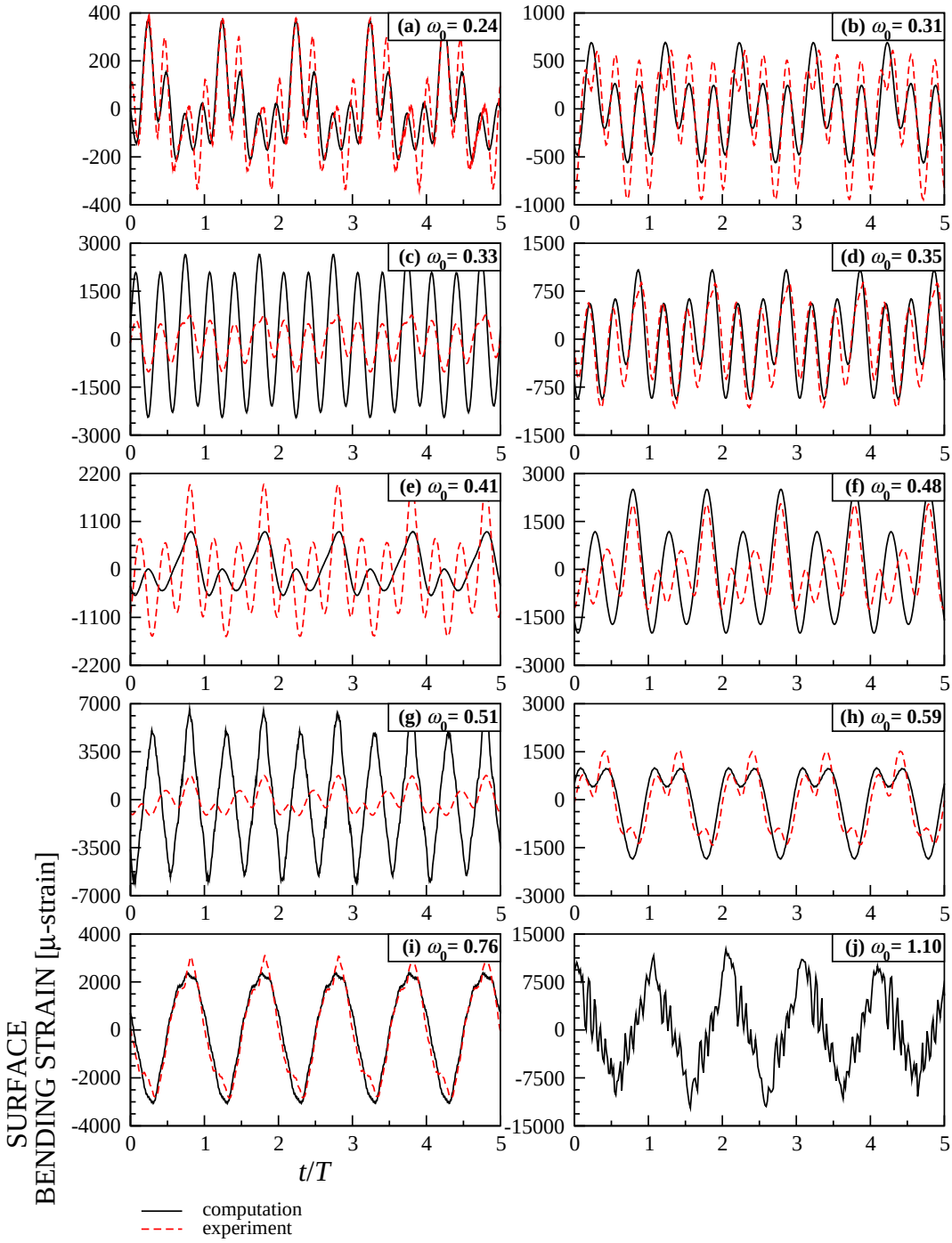

Figure 3.6: Time history of experimental and simulation surface bending strain obtained at 30° for normalized flapping frequencies ω_0 of: (a) 0.24, (b) 0.31, (c) 0.33, (d) 0.35, (e) 0.41, (f) 0.48, (g) 0.51, (h) 0.59, (i) 0.76, and (j) 1.10.

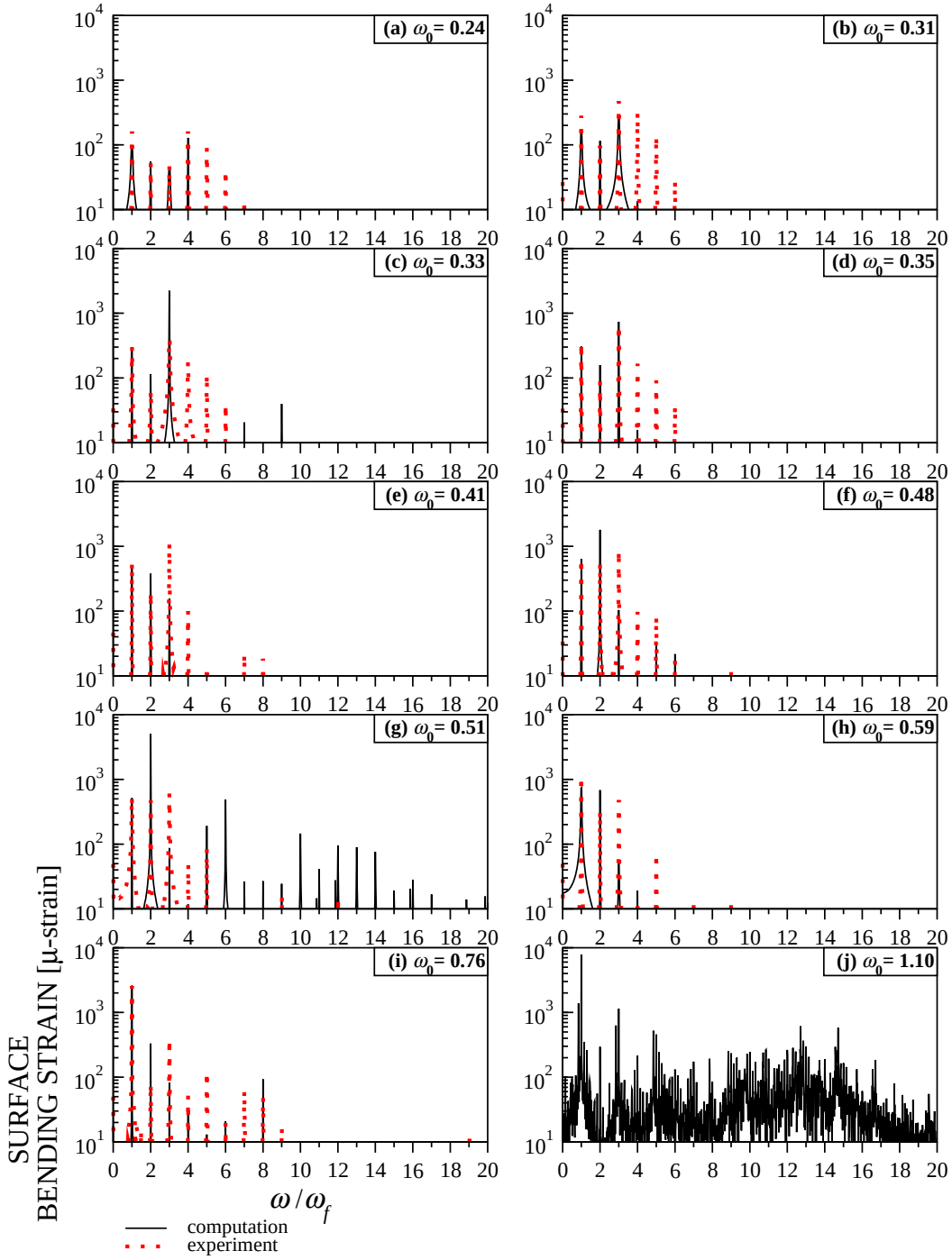

Figure 3.7: Discrete Fourier transform of experimental and simulation surface bending strain obtained at 30° for normalized flapping frequencies ω_0 of: (a) 0.24, (b) 0.31, (c) 0.33, (d) 0.35, (e) 0.41, (f) 0.48, (g) 0.51, (h) 0.59, (i) 0.76, and (j) 1.10.

3.4.2 Comparison of Beam Tip Displacements

Experimental and simulation transverse (y-coordinate as depicted in Figure 3.1a) tip displacements, v_{tip}, are compared in Figures 3.8 and 3.9 for flapping amplitudes of 15° and 30°, respectively. As shown in Figure 3.8, experimental and computational tip displacements (normalized by beam length) are in very good agreement for most of the flapping frequencies for flapping at 15°. The exception to this good quantitative agreement occurs for flapping at $\omega_0 = 0.48$, $\omega_0 = 0.97$, and $\omega_0 = 1.03$ (Figure 3.8c, g, and h, respectively), which correspond to secondary and primary resonance regions, where the simulation results have a more pronounced local vibration and asymmetry. Similarly, Figure 3.9 shows that the simulation tip displacements obtained for flapping at 30° are in good agreement with the experiment for flapping frequencies of $\omega_0 = 0.07$, 0.21, 0.62, and 0.76 (Figure 3.9a, b, e, and f, respectively) which are outside the superharmonic resonance regions (see Figure 3.3). As was the case for flapping at 15°, in region(s) of secondary resonance ($\omega_0 = 0.35$ and $\omega_0 = 0.48$; see Figure 3.9c and d, respectively) both the simulation and experiment show local vibration and response asymmetry but with differing degree.

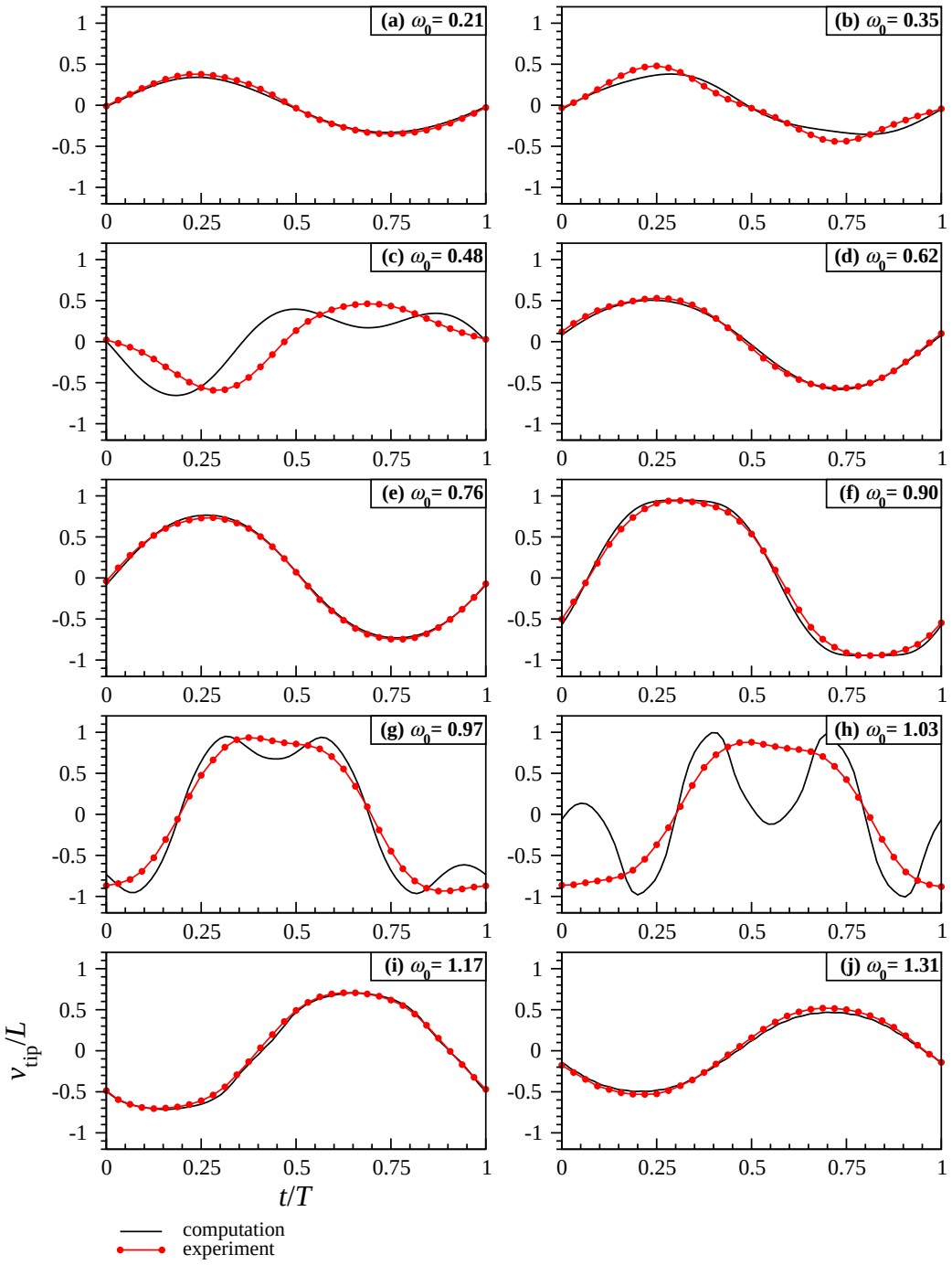

Figure 3.8: Time history of experimental and simulation transverse tip displacement (normalized by the beam length) obtained at 15° for normalized flapping frequencies ω_0 of: (a) 0.21, (b) 0.35, (c) 0.48, (d) 0.62, (e) 0.76, (f) 0.90, (g) 0.97, (h) 1.03, (i) 1.17, and (j) 1.31.

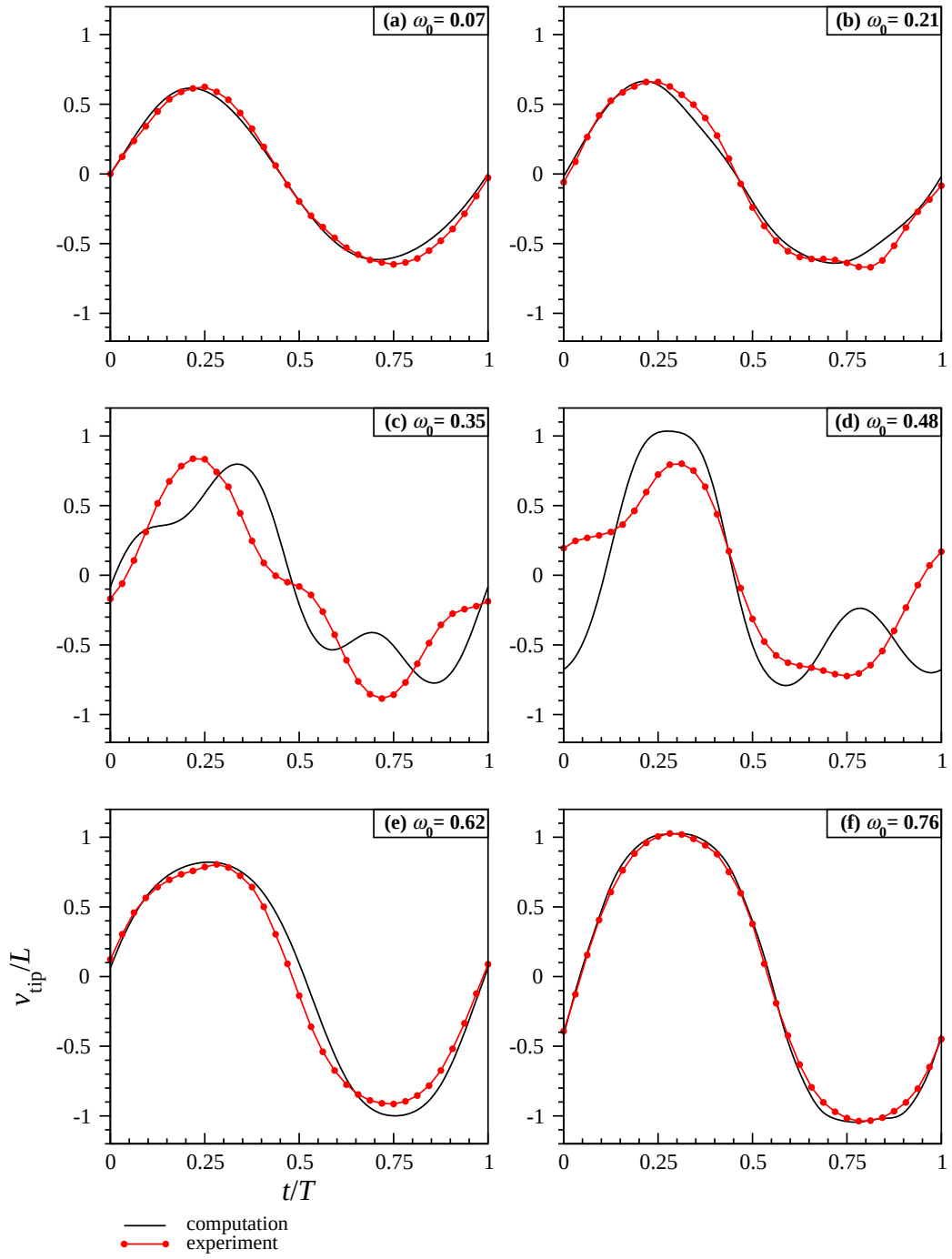

Figure 3.9: Time history of experimental and simulation transverse tip displacement (normalized by the beam length) obtained at 30° for normalized flapping frequencies ω_0 of: (a) 0.07, (b) 0.21, (c) 0.35, (d) 0.48, (e) 0.62, and (f) 0.76.

3.5 Numerical Experiments

In this section, additional simulation is performed to further explore the beam response characteristics. Of particular interest is the study of the types of bifurcations which are possible for this single equilibrium point problem. A similar numerical study was performed in Reference [30] for a beam without time-dependent boundary actuation.

3.5.1 Beam Response with Varying Flapping Frequency

In what follows, analysis of the beam tip response, as a function of flapping frequency, will be conducted through numerical experiment. This is accomplished by varying the flapping frequency ω_0 from 0.07 to 1.24 with increments as small as 0.007 for flapping at both 15° and 30°. The simulation parameters used to obtain the results presented in this section are the same as those used in Section 3.4.

Time history plots of transverse tip displacement of the beam obtained at 15° are given in Figures 3.10 and 3.11. Figure 3.10 shows tip displacement of time histories, over 10 flapping cycles, for ten different flapping frequencies ranging from $\omega_0 = 0.35$ to $\omega_0 = 1.24$. As shown in Figure 3.10b, the development of local vibration in the response, asymmetric on one extremum of the response signal, begins at $\omega_0 = 0.47$ as the frequency approaches the region of superharmonic resonance. These local vibrations are the result of significant contribution from the second harmonic of the flapping frequency, as observed in the response spectra given in Figure 3.12b-d. In the phase plane local vibration results in the emergence of a small loop from the main trajectory, as shown in Figure 3.13b-d. Within the superharmonic resonance

region, e.g., flapping at $\omega_0 = 0.50$ and $\omega_0 = 0.51$, the response spectra (Figure 3.12c and d) show significant contribution from harmonic orders as high as six. At transition frequencies between the primary and superharmonic resonance, local vibrations first disappear and then emerge again as shown in Figure 3.10d-f for the response at $\omega_0 = 0.51$, 0.54, and 0.91, respectively. It should also be mentioned that, for flapping at 15° with frequencies below the region of primary resonance, the beam response is 1T as evidenced from the single dot in the Poincaré sections given in Figure 3.15a-c. In the present work, Poincaré sections are constructed by sampling the tip motion data (velocity and displacement) in the phase plane at uniform time intervals equal to the period of flapping excitation.

A number of bifurcations in the response characteristics are found when the flapping frequency is varied within the region of primary resonance between $\omega_0 = 0.91$ and $\omega_0 = 1.14$. For flapping at $\omega_0 = 0.91$, where the response is 1T, local vibrations appear symmetrically at the extrema of the displacement signal (Figure 3.10f) and the phase projection contains two small loops in addition to the main loop (Figure 3.13f). Time history plots of tip displacement for flapping frequencies ranging from $\omega_0 = 0.98$ to 1.12 are given in Figure 3.11. As shown in Figure 3.11a, for a flapping frequency of $\omega_0 = 0.98$, slightly below the beam first modal frequency, the amplitude of the local vibration is large when compared to the result at $\omega_0 = 0.91$ (Figure 3.10f). Also the response which is periodic for flapping at $\omega_0 = 0.91$ evolves into a quasi-periodic response for flapping at $\omega_0 = 0.98$. As shown in Figure 3.15d, the Poincaré section of the response at $\omega_0 = 0.98$ contains a pair of closed curves which appear to form a strip resembling a Möbius band. The response becomes 1T again as the flapping frequency is increased to $\omega_0 = 1.00$. As shown in Figure 3.12h,

the corresponding response spectrum at $\omega_0 = 1.00$ contains sharp peaks which occur only at (odd and even) harmonics. Transition back to a quasi-periodic response is observed at $\omega_0 = 1.01$ as the Poincaré section (Figure 3.15f) is now a closed curve and the peaks in the response spectrum, which are again centered at the harmonics, have widened. As shown in Figure 3.14d-g, trajectories of tip motion at $\omega_0 = 1.08$, 1.09, 1.10, and 1.12 fill up a large sections of the phase projection and display an irregular, "wandering" characteristics. For flapping at $\omega_0 = 1.10$ and $\omega_0 = 1.12$ the Poincaré sections shown in Figure 3.15i and j contain clusters of points which appear to form fractal-like structures, while flapping at $\omega_0 = 1.09$ results in a circular ring structure (Figure 3.15h). The corresponding response spectra (Figure 3.12k-m) for these flapping frequencies show a further broadening of the peaks located at odd harmonics. Taking into consideration the phase projections, Poincaré sections, and response spectra, it appears that a region of narrow-band chaos occurs between $\omega_0 = 1.08$ and $\omega_0 = 1.12$. Increasing the flapping frequency above $\omega_0 = 1.12$ results in a 1T response, as can be observed in the results for $\omega_0 = 1.16$ and $\omega_0 = 1.24$ given in Figure 3.10 (i and j), Figure 3.12 (n and o), Figure 3.14 (h and i), and Figure 3.15 (k and l).

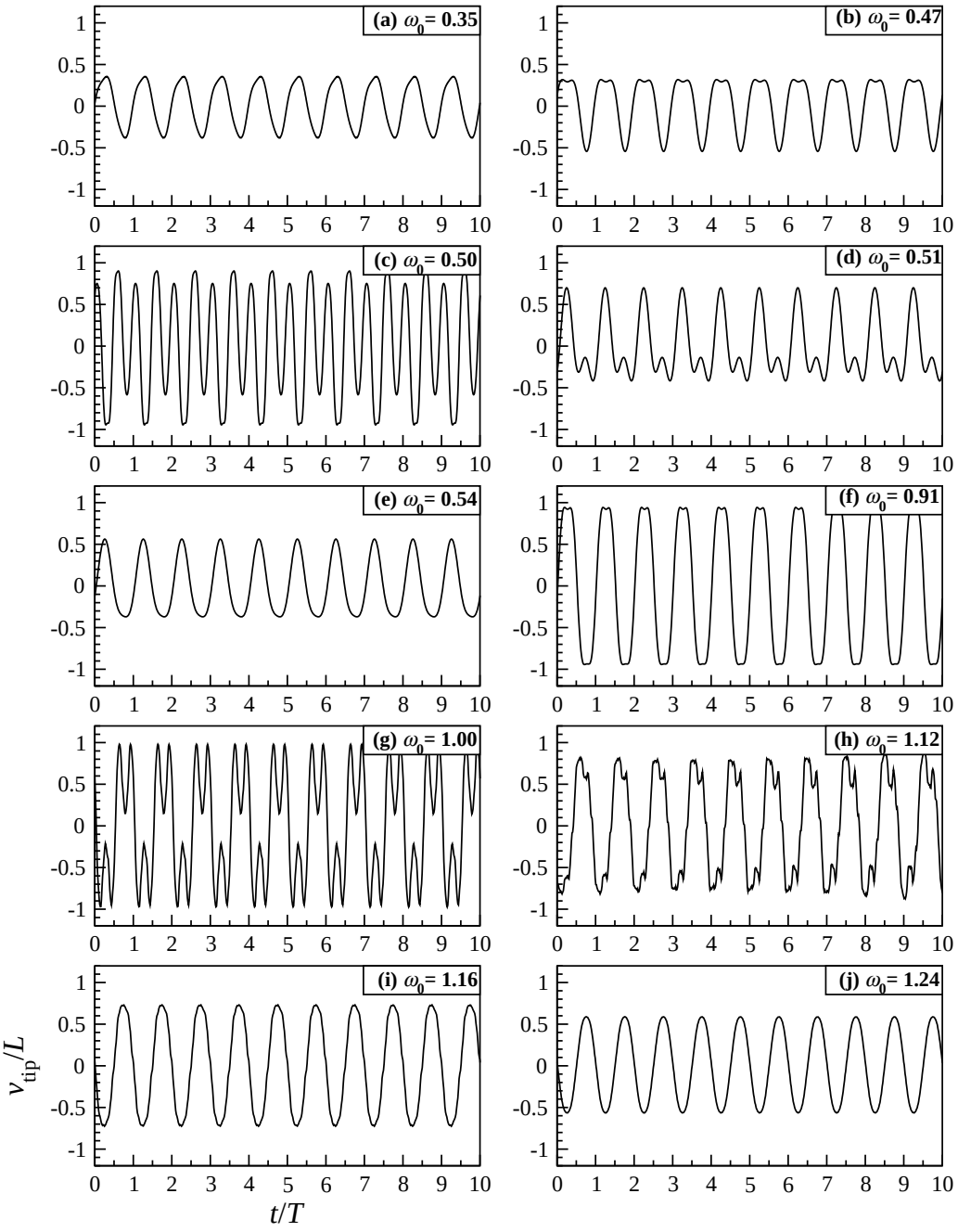

Figure 3.10: Time history of transverse tip displacement (normalized by the beam length) obtained at 15° for flapping frequencies ω_0 of: (a) 0.35, (b) 0.47, (c) 0.50, (d) 0.51, (e) 0.54, (f) 0.91, (g) 1.00, (h) 1.12, (i) 1.16, and (j) 1.24.

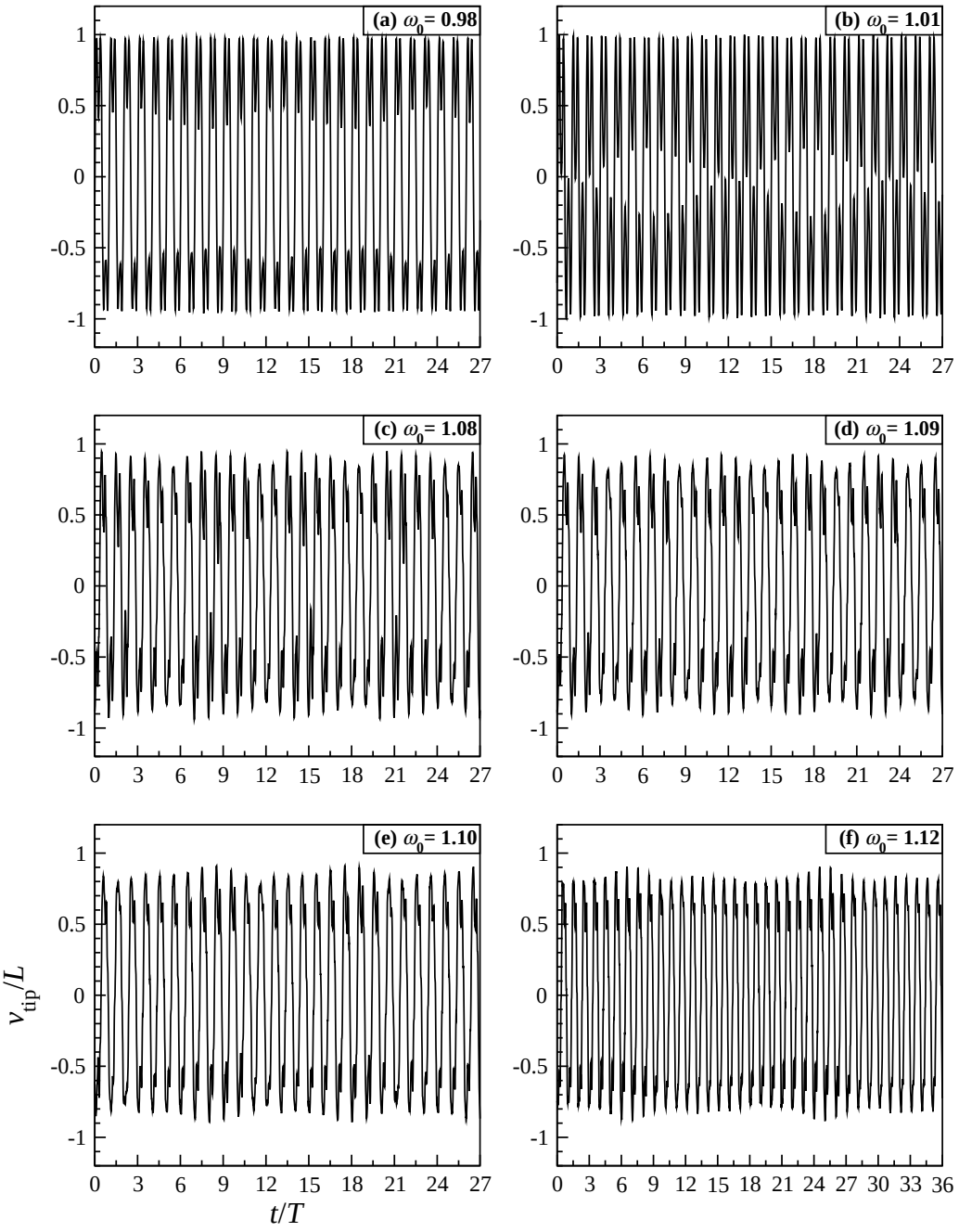

Figure 3.11: Time history of transverse tip displacement (normalized by the beam length) obtained at 15° for flapping frequencies ω_0 of: (a) 0.98, (b) 1.01, (c) 1.08, (d) 1.09, (e) 1.10, and (f) 1.12.

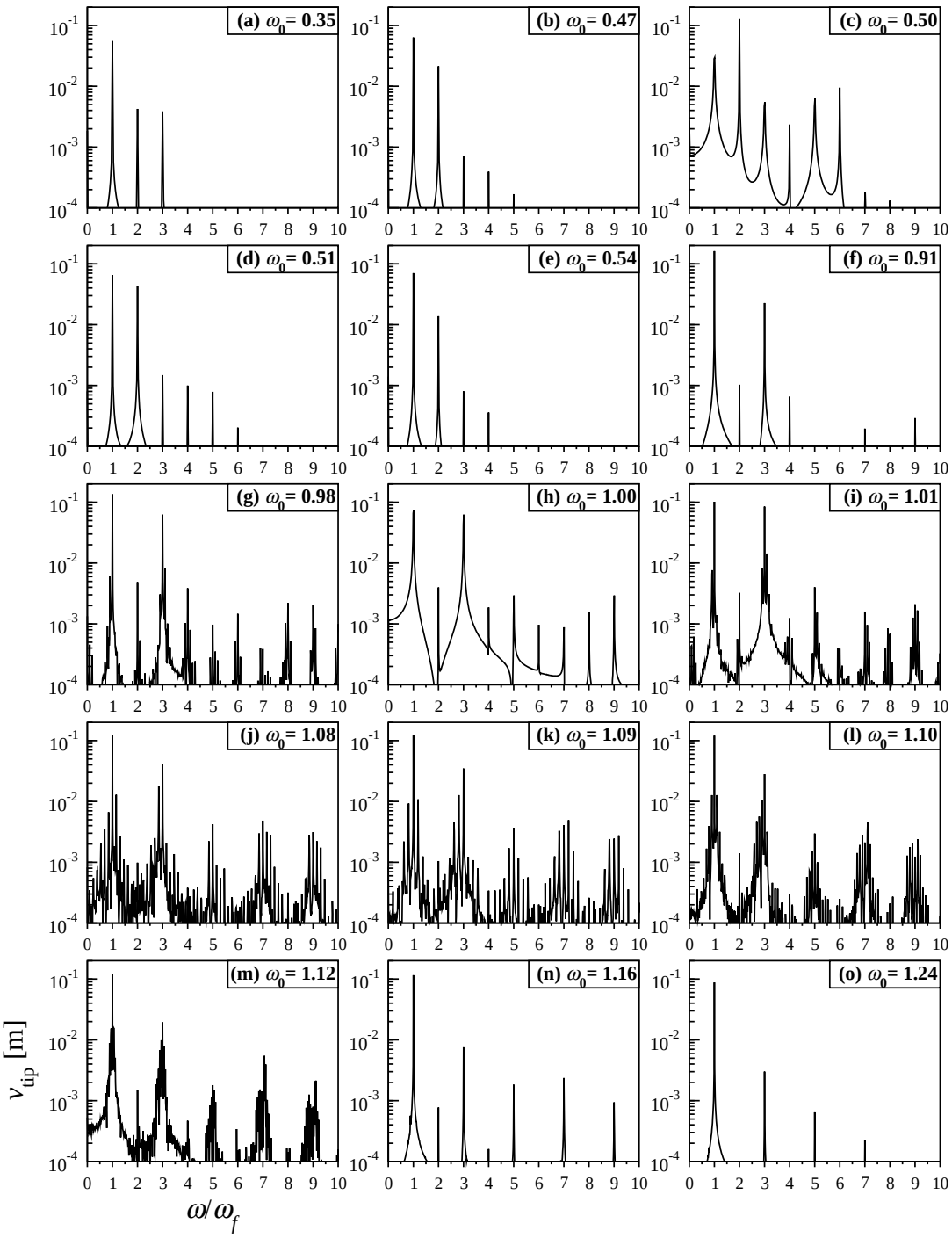

Figure 3.12: Discrete Fourier transform of transverse tip displacement (normalized by the beam length) at 15° for flapping frequencies ω_0 of: (a) 0.35, (b) 0.47, (c) 0.50, (d) 0.51, (e) 0.54, (f) 0.91, (g) 0.98, (h) 1.00, (i) 1.01, (j) 1.08, (k) 1.09, (l) 1.10, (m) 1.12, (n) 1.16, and (o) 1.24.

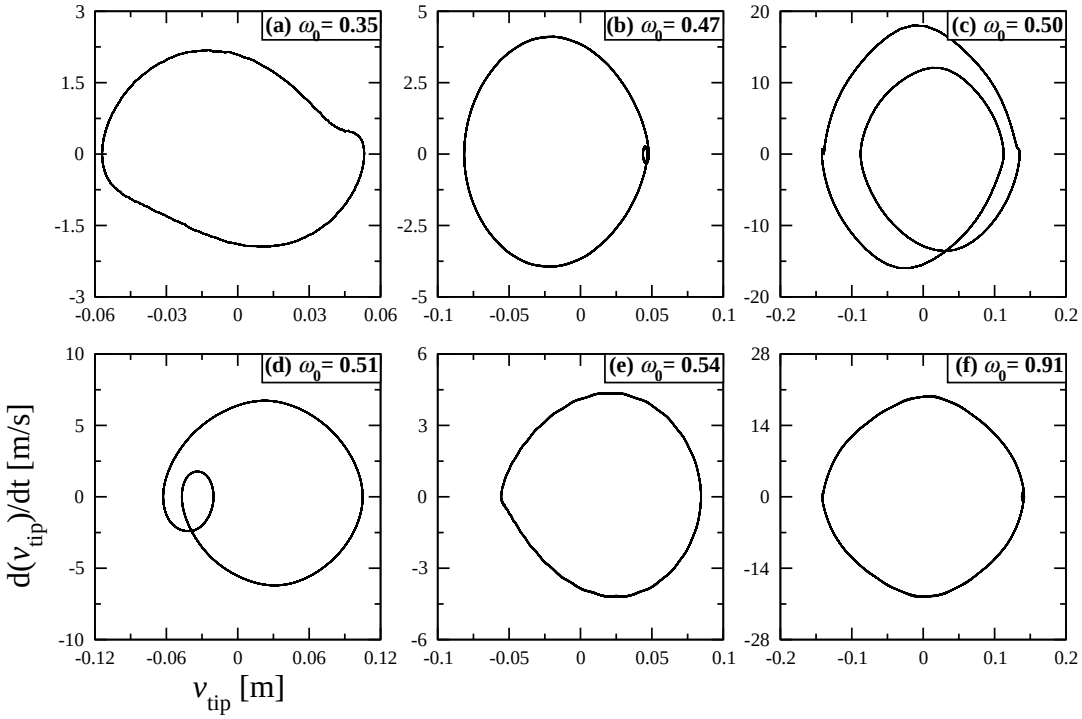

Figure 3.13: Phase projection of transverse tip motion at 15° for flapping frequencies ω_0 of: (a) 0.35, (b) 0.47, (c) 0.50, (d) 0.51, (e) 0.54, and (f) 0.91.

In Table 3.1, above-mentioned various response types and bifurcations which are encountered as ω_0 is increased for flapping at 15° are summarized. For the region below the superharmonic resonance of order 2, $\omega_0 \lessapprox 0.47$, the response is 1T symmetric as demonstrated in Figures 3.10a and 3.13a which show the response time history and phase projection for $\omega_0 = 0.35$. Within the superharmonic resonance region, $0.47 \lessapprox \omega_0 \lessapprox 0.51$, the response is asymmetric 1T with local vibrations occurring at one extremum of the response (Figure 3.10b-d) which are due to significant contribution from the second harmonic of the flapping frequency (Figure 3.12b-d), and result in a phase projection which contains an additional small loop (Figure 3.13b-d) off the main loop.

In the region $0.51 \lessapprox \omega_0 \lessapprox 0.98$ the response is found to be symmetric 1T.

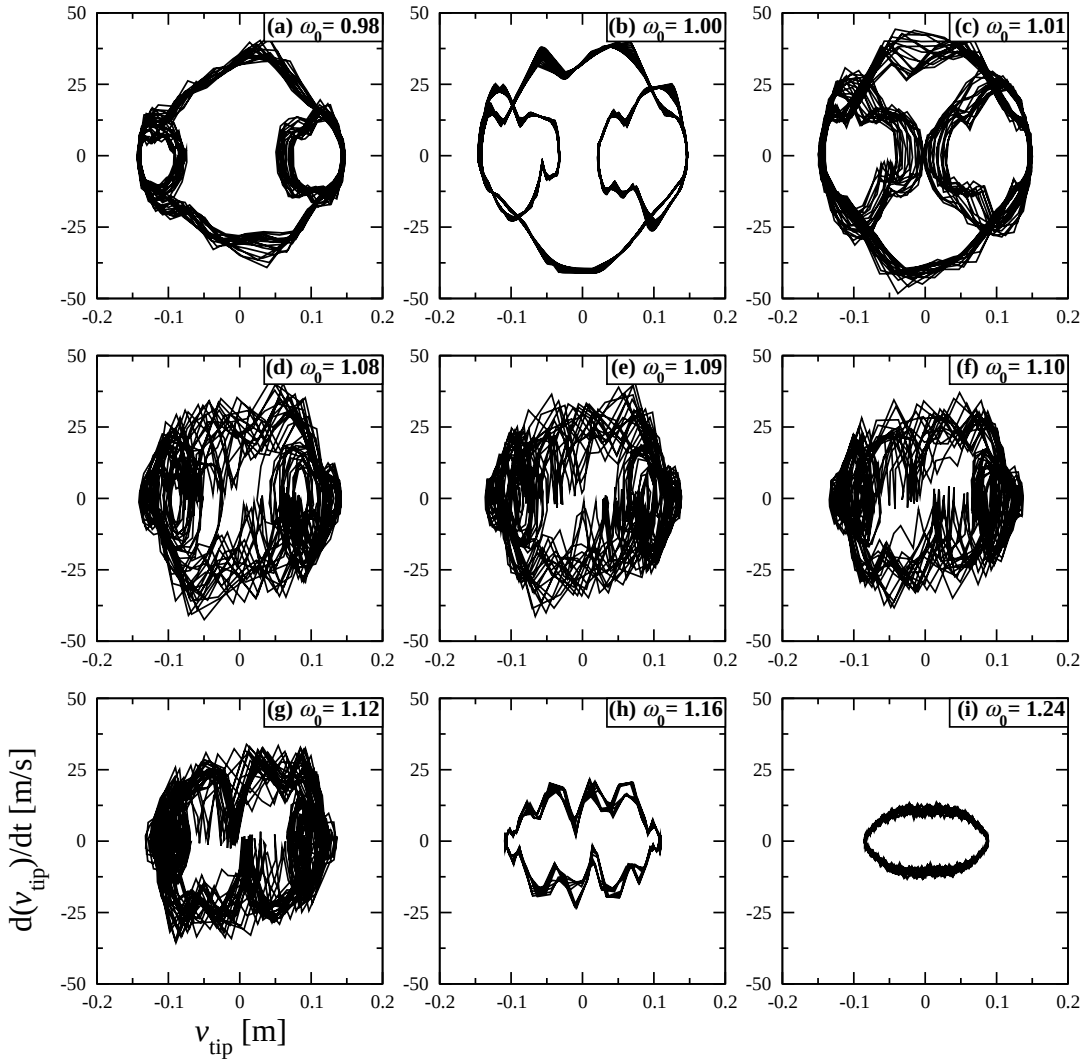

Figure 3.14: Phase projection of transverse tip motion at 15° for flapping frequencies ω_0 of: (a) 0.98, (b) 1.00, (c) 1.01, (d) 1.08, (e) 1.09, (f) 1.10, (g) 1.12, (h) 1.16, and (i) 1.24.

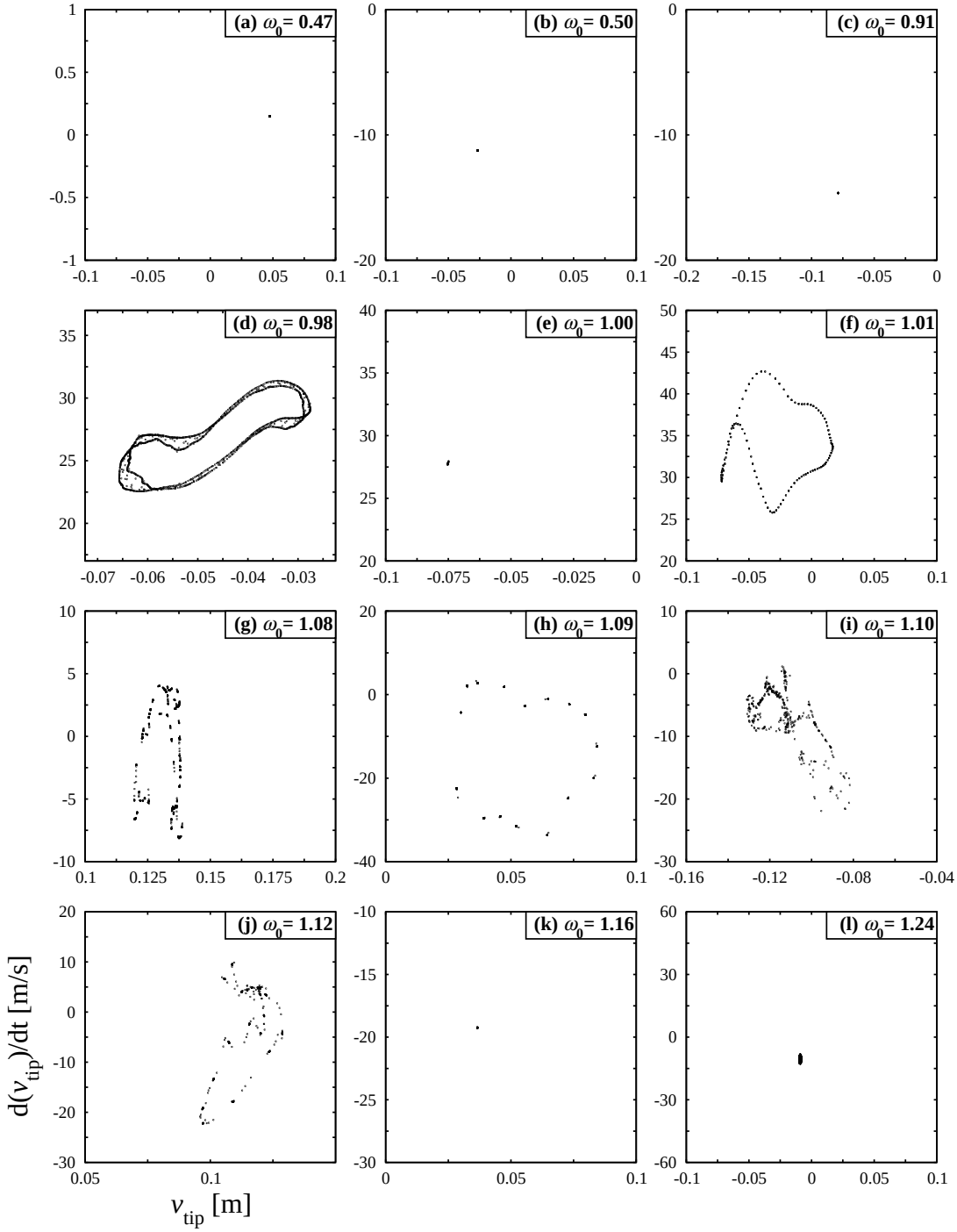

Figure 3.15: Poincaré section of transverse tip motion at 15° for flapping frequencies ω_0 of: (a) 0.47, (b) 0.50, (c) 0.91, (d) 0.98, (e) 1.00, (f) 1.01, (g) 1.08, (h) 1.09, (i) 1.10, (j) 1.12, (k) 1.16, and (l) 1.24.

As the frequency is increased within this region, the response changes from one without local vibration to one which contains local vibration at both extrema of the response. This is shown in Figure 3.10e and f and Figure 3.13e and f for $\omega_0 = 0.54$ and 0.91. A further increase in ω_0 results in two regions of quasi-periodic motion, $0.98 \lessapprox \omega_0 < 1.00$ and $1.00 < \omega_0 \lessapprox 1.08$, which are separated by a symmetric 1T response at $\omega_0 = 1.00$. As demonstrated in Figure 3.12g & i, Figure 3.14a & c, and Figure 3.15d & f for $\omega_0 = 0.98$ and 1.01, the quasi-periodic motion is characterized by diffuse phase projections, spectra which contain peaks at both even and odd harmonics, and two-dimensional Poincaré sections.

A small region of complex, possibly chaotic, response is found for $1.08 \lessapprox \omega_0 \lessapprox 1.12$. The response in this region, shown in Figures 3.12l and 3.14f for $\omega_0 = 1.10$, is characterized by a further broadening of the peaks in the response spectra when compared to the quasi-periodic response and trajectories which fill up a large portion of the phase projection. Finally, an increase in the flapping frequency beyond $\omega_0 \approx 1.12$ results in a symmetric 1T response for flapping at 15°.

Shown in Figures 3.16 and 3.17 are plots of the normalized tip displacement time histories obtained for flapping at 30°. The time histories of the transverse tip displacement at lower frequencies, which extend over the superharmonic resonance regions, are shown in Figure 3.16, while the time histories of the tip displacement at higher flapping frequencies in the primary resonance region (from $\omega_0 = 0.93$ to 1.17) are presented separately in Figure 3.17. As the characteristics of the response in the time domain are found to exhibit richer dynamics at higher frequencies, a longer time history (20 flapping-cycles versus 10) is shown in Figure 3.17. As shown in Figure 3.16c & g, the time histories

Table 3.1: List of various response types encountered as flapping frequency ω_0 is increased for flapping at 15°.

ω_0	Response type
$\omega_0 \lessapprox 0.47$	Symmetric, 1T periodic
$0.47 \lessapprox \omega_0 \lessapprox 0.51$	Asymmetric, 1T periodic
$0.51 \lessapprox \omega_0 \lessapprox 0.98$	Symmetric, 1T periodic
$0.98 \lessapprox \omega_0 < 1.00$	Quasi-periodic
$\omega_0 = 1.00$	Symmetric, 1T periodic
$1.00 < \omega_0 \lessapprox 1.08$	Quasi-periodic
$1.08 \lessapprox \omega_0 \lessapprox 1.12$	Irregular
$1.12 \lessapprox \omega_0 \lessapprox 1.24$	Symmetric, 1T periodic

of the response obtained at third and second order superharmonic resonance frequencies appear to be qualitatively similar and can easily be distinguished from those obtained at other flapping frequencies due to the large amount of local vibration in the signals. The peaks in the response spectrum shown in Figure 3.18b for flapping at $\omega_0 = 0.34$ demonstrates that the motion contains mainly odd harmonics for this flapping frequency, while the response spectrum for flapping at $\omega_0 = 0.52$, shown in Figure 3.18e, contains peaks at both (even and odd) integer and non-integer multiples of the excitation frequency. Trajectories of the tip motion at the superharmonic resonances are also markedly different, as noted in the phase portraits shown in Figure 3.19b & d for frequencies $\omega_0 = 0.34$ and 0.52, respectively. For the third-order superharmonic resonance ($\omega_0 = 0.34$), one can observe orbits which traverse regularly with accompanying local vibrations at both extrema of the displacement. The corresponding Poincaré section, Figure 3.20a, demonstrates that the response is 1T for flapping at $\omega_0 = 0.34$. On the other hand the trajectory of the tip motion for flapping at the second-order superharmonic resonance appear quite diffuse

(Figure 3.19d); even more pronounced diffusion in the trajectory is noticed in the corresponding Poincaré section shown in Figure 3.20c. The appearance of the Poincaré section of the response at $\omega_0 = 0.52$ alludes to a chaotic response which is also evidenced by the broadband response frequency spectrum with peaks at integer and non-integer multiples of the flapping frequency (see Figure 3.18e). Chaotic response occurring in a low frequency region in the neighborhood of the superharmonic resonance of order 2 was reported previously in Reference [113] for a system with multiple equilibrium points. As the frequency is increased between the secondary (superharmonic) resonances the local vibrations first diminish ($\omega_0 = 0.35$ and 0.41; Figure 3.16d & e, respectively) and then increase ($\omega_0 = 0.46$, Figure 3.16f) as the flapping frequency nears $\omega_0 = 0.52$. The tip response at these frequencies in found to be 1T with the first three harmonics of the flapping frequency dominating the spectra (see Figure 3.18c & d).

As is the case for flapping at 15°, transition from a 1T response (at $\omega_0 = 0.76$, for instance) to quasi-periodic motion ($\omega_0 = 0.90$) starts with the emergence of local vibrations in the response which occur at both extrema of the displacement signal (as opposed to occurrence at one extremum at lower frequencies). As shown in the phase projections given in Figure 3.19, the response trajectories gradually become more diffuse as the flapping frequency is increased above $\omega_0 = 0.90$. The response Poincaré section shown in Figure 3.20e for flapping at $\omega_0 = 0.90$ contains a collection of points which form a closed curve indicating a quasi-periodic motion. For flapping between $\omega_0 = 0.93$ and 1.05, the corresponding Poincaré sections shown in Figure 3.20f-h exhibit a fuzzy collection of points which amounts to a quasi-periodic response. At $\omega_0 = 1.09$, the response bifurcates back to a 1T response as the

Poincaré section reduces to a point (Figure 3.20i), the phase portrait becomes less diffuse (Figure 3.19j), and the response spectrum contains sharp peaks only at integer multiples of the forcing frequency (Figure 3.18l).

As shown in Figure 3.17g-j, time histories of tip displacement between $\omega_0 = 1.10$ and 1.17 appear to be erratic when compared to the response at the preceding frequencies. The tip motion phase projections for flapping at $\omega_0 = 1.10$ and 1.17, shown in Figure 3.19k & l, occupy a subset of the phase plane. As shown in Figure 3.18, when compared to the spectra at other flapping frequencies, the frequency spectra of the response for flapping at $\omega_0 = 1.10$ (Figure 3.18m) and $\omega_0 = 1.17$ (Figure 3.18o) are more broadband in nature indicating richer frequency content for the signals. The corresponding Poincaré sections (Figure 3.20) generate collections of points which appear to be ordered at $\omega_0 = 1.10$ (Figure 3.20j) and tend to uniformly fill up a portion of phase plane at $\omega_0 = 1.17$ (Figure 3.20l), which along with the response spectra appear to indicate chaotic dynamics [23].

The region between $\omega_0 = 1.10$ and 1.17 appears to be another transition region where the dynamics exhibit quasi-periodic characteristics. This quasi-periodic motion is captured in the Poincaré sections (Figure 3.20k) and response spectrum (Figure 3.18n) corresponding to $\omega_0 = 1.13$; the spectrum contains well-pronounced spikes occurring at even and odd harmonics and Poincaré section contains points forming an open (V-shape) pattern.

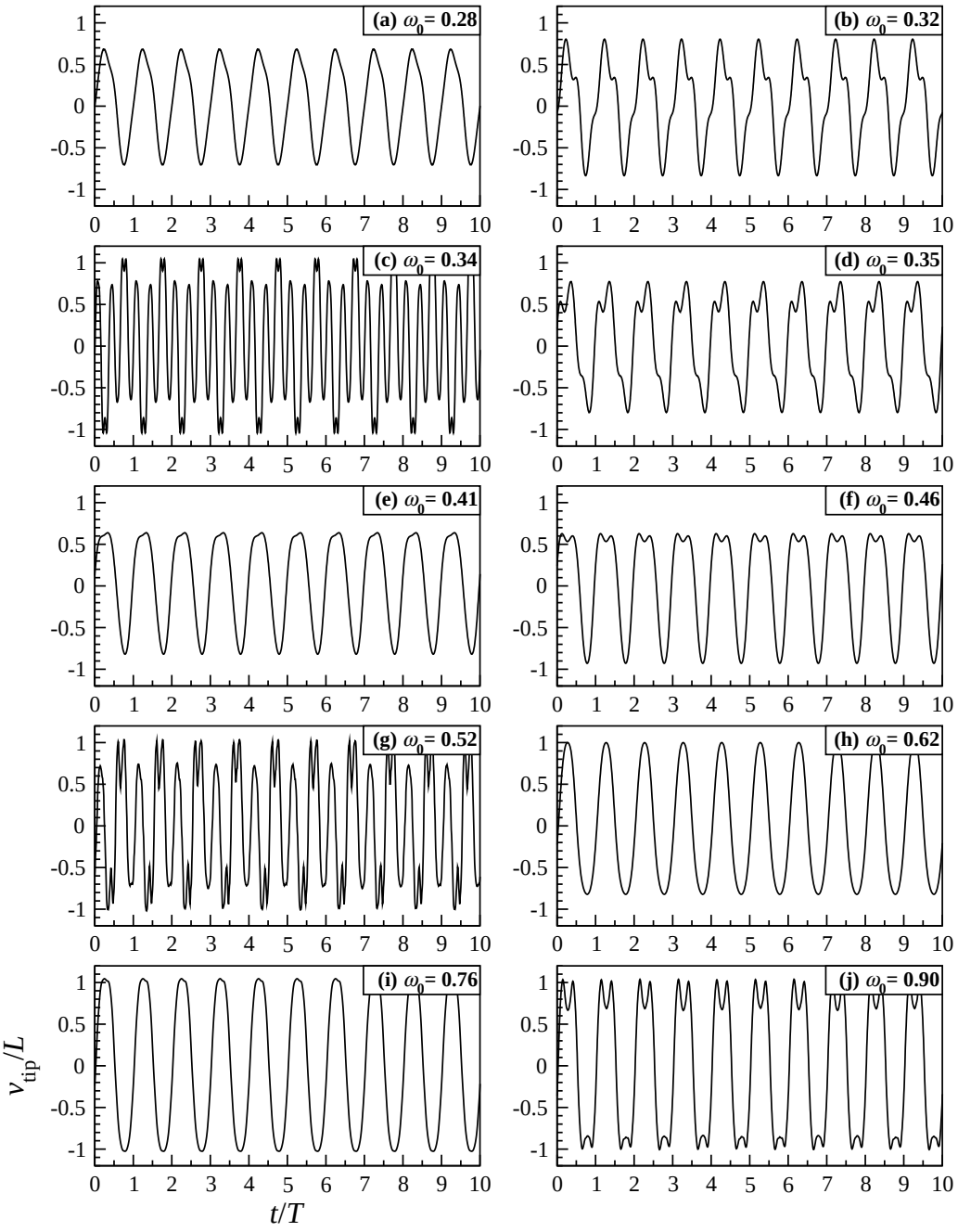

Figure 3.16: Time history of transverse tip displacement (normalized by the beam length) obtained at 30° for flapping frequencies ω_0 of: (a) 0.28, (b) 0.32, (c) 0.34, (d) 0.35, (e) 0.41, (f) 0.46, (g) 0.52, (h) 0.62, (i) 0.76, and (j) 0.90.

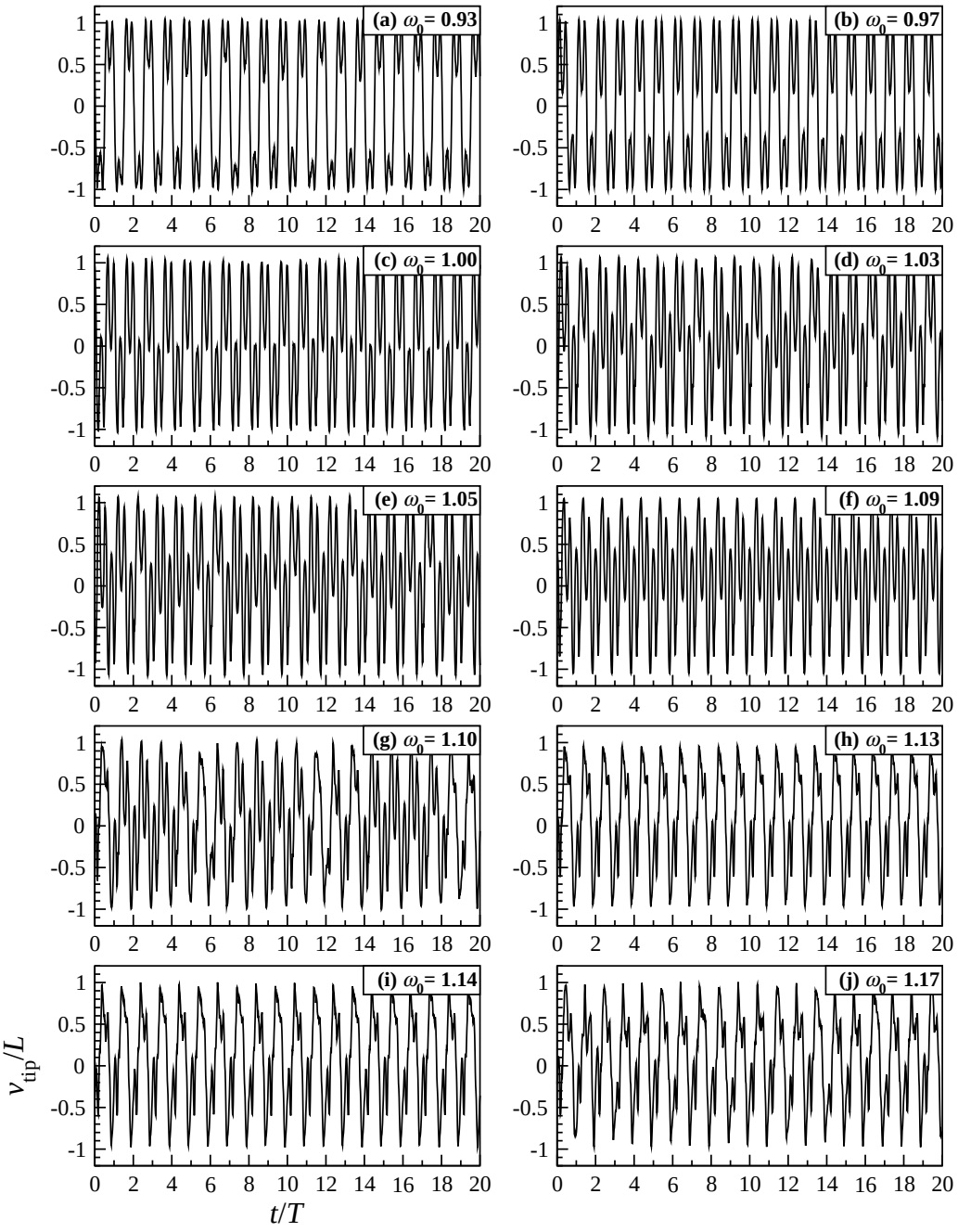

Figure 3.17: Time history of transverse tip displacement (normalized by the beam length) obtained at 30° for flapping frequencies ω_0 of: (a) 0.93, (b) 0.97, (c) 1.00, (d) 1.03, (e) 1.05, (f) 1.09, (g) 1.10, (h) 1.13, (i) 1.14, and (j) 1.17.

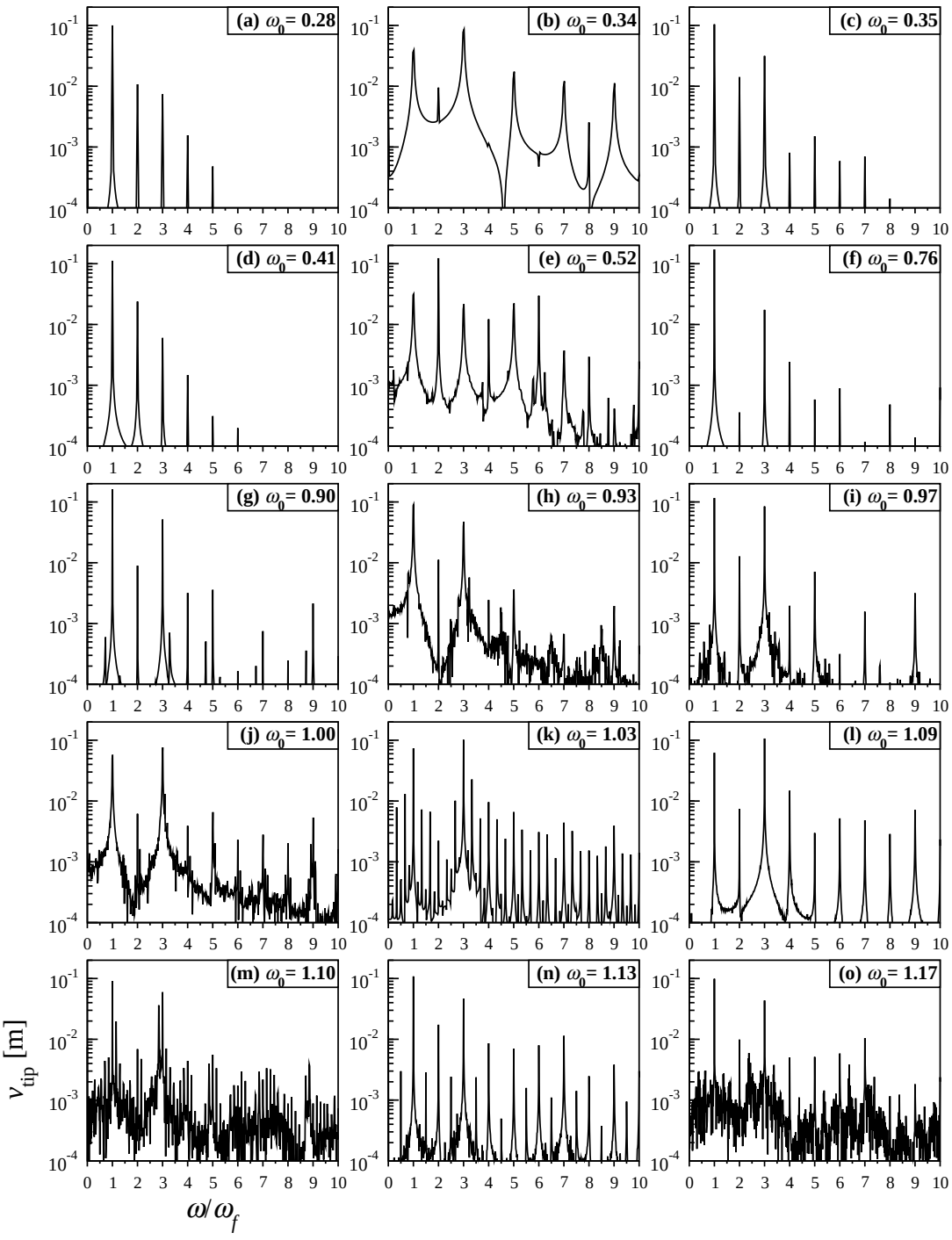

Figure 3.18: Discrete Fourier transform of transverse tip displacement (normalized by the beam length) at 30° for flapping frequencies ω_0 of: (a) 0.28, (b) 0.34, (c) 0.35, (d) 0.41, (e) 0.52, (f) 0.76, (g) 0.90, (h) 0.93, (i) 0.97, (j) 1.00, (k) 1.03, (l) 1.09, (m) 1.10, (n) 1.13, (o) 1.17.

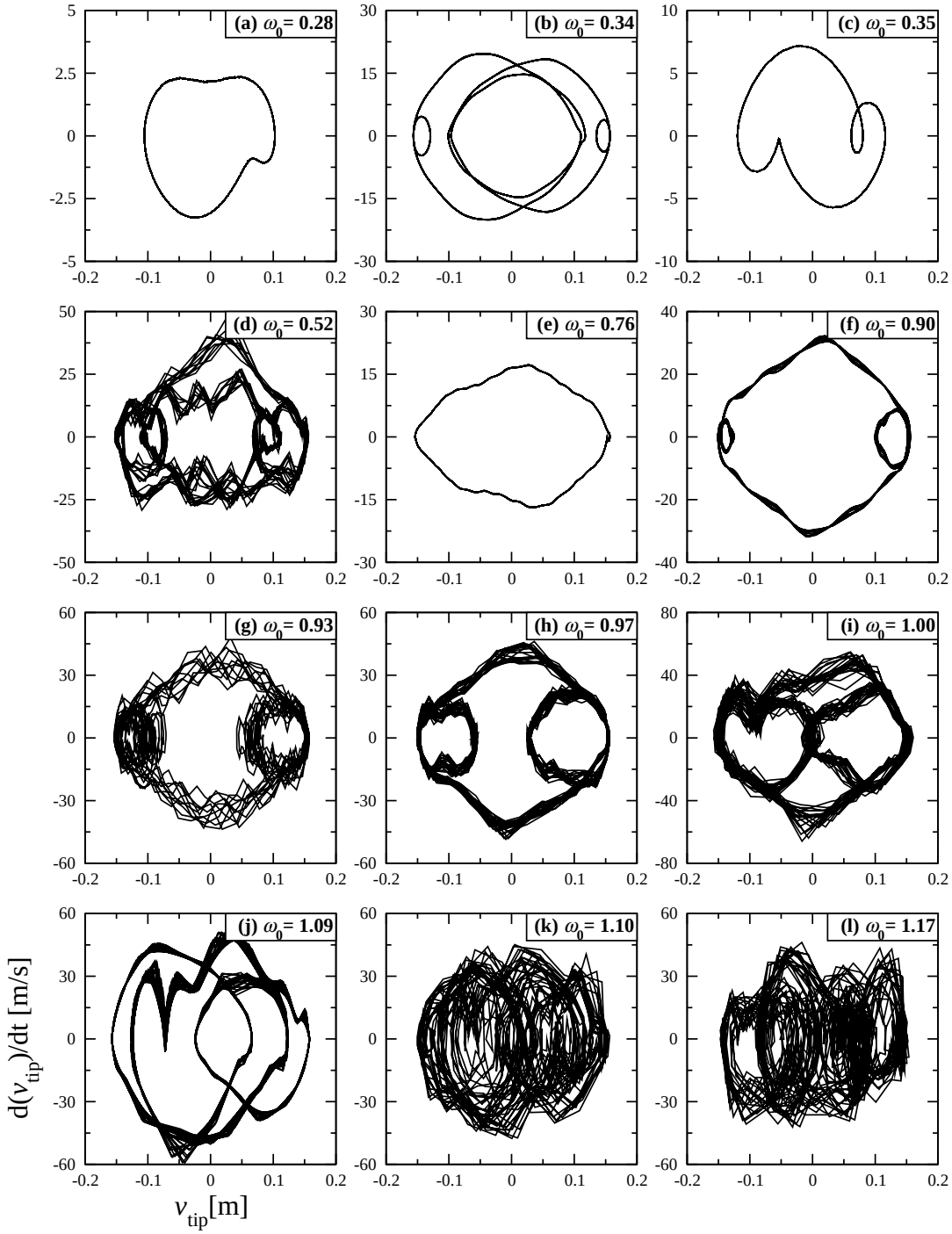

Figure 3.19: Phase projection of transverse tip motion at 30° for flapping frequencies ω_0 of: (a) 0.28, (b) 0.34, (c) 0.35, (d) 0.52, (e) 0.76, (f) 0.90, (g) 0.93, (h) 0.97, (i) 1.00, (j) 1.09, (k) 1.10, and (l) 1.17.

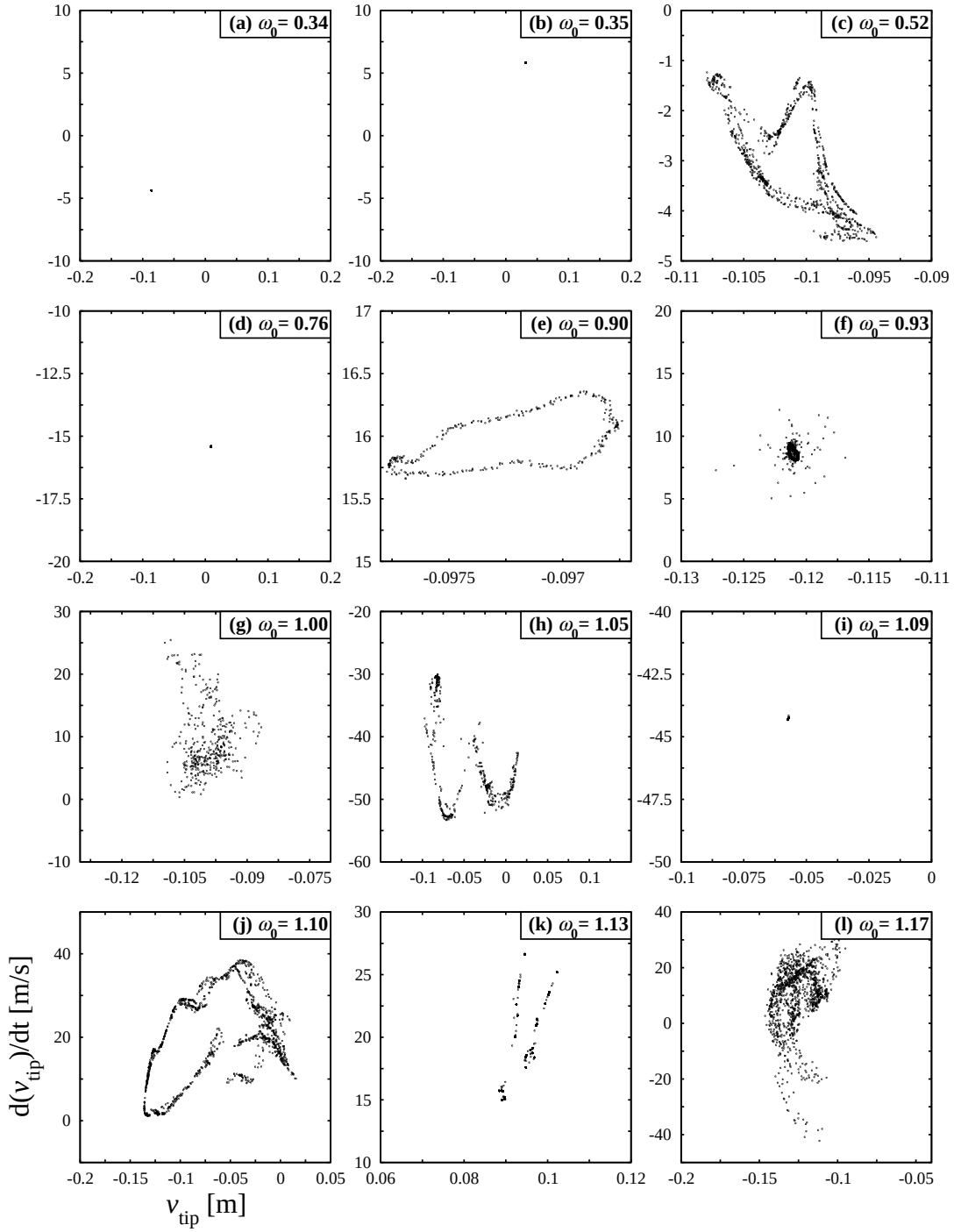

Figure 3.20: Poincaré section of transverse tip motion at 30° for flapping frequencies ω_0 of: (a) 0.34, (b) 0.35, (c) 0.52, (d) 0.76, (e) 0.90, (f) 0.93, (g) 1.00, (h) 1.05, (i) 1.09, (j) 1.10, (k) 1.13, and (l) 1.17.

Summary of above-mentioned response types and bifurcations which are encountered as ω_0 is increased for flapping at 30° are given in Table 3.2. Once again this table demonstrates that a number of bifurcations in response type occurs as ω_0 is increased. Flapping below the third-order superharmonic resonance ($\omega_0 \lessapprox 0.32$) results in a symmetric 1T response. From Figures 3.16c and 3.18b it can be seen that flapping in the third-order superharmonic resonance region results in a response which is asymmetric 1T with spectra dominated by odd harmonics. Conversely, Figures 3.16g, 3.18e, 3.19d, and 3.20c demonstrate that flapping within the second-order superharmonic resonance region $\omega_0 = 0.52$ results in more complex (possibly chaotic) response with spectra containing both even and odd harmonics and diffuse phase projections and Poincaré sections.

Overall for flapping at frequencies beyond the secondary resonance region, the transition in response characteristics are similar to what occurs for flapping at 15° with the only differences being the values of the flapping frequencies at which the various response types occur and a possible additional transition region for flapping beyond the linear first modal frequency. For example, when flapping at 15° quasi-periodic motion begins at $\omega_0 \approx 0.98$ whereas in the case of flapping at 30° transition to a quasi-periodic response occurs at $\omega_0 \approx 0.90$. Also, for flapping at 15° the initial regions of quasi-periodic motion near primary resonance are separated by a 1T symmetric response at $\omega_0 = 1.00$, while for flapping at 30° this frequency is determined to be $\omega_0 = 1.09$.

The possible additional transition region mentioned in the previous paragraph occurs for $1.10 \lessapprox \omega_0 \lessapprox 1.17$, where it is thought that small regions of chaotic response at the ends of this region (e.g., around $\omega_0 = 1.10$ and $\omega_0 = 1.17$) are separated by a region of quasi-periodic response. This is shown

in Figures 3.18m-o and 3.20j-l which depict the spectra and Poincaré sections for $\omega_0 = 1.10$, 1.13, and 1.17. From these figures it can be seen that the dynamics at both $\omega_0 = 1.10$ and 1.17 appear to be more complex than the dynamics at $\omega_0 = 1.13$ as the spectra at these two frequencies display a more broadband nature and the Poincaré sections are more diffuse. This additional transition region of quasi-periodic response is not found for flapping at 15°.

Table 3.2: List of various response types encountered as flapping frequency ω_0 is increased for flapping at 30°.

ω_0	Response type
$\omega_0 \lessapprox 0.28$	Symmetric, 1T periodic
$0.28 \lessapprox \omega_0 \lessapprox 0.34$	Asymmetric, 1T periodic
$\omega_0 \approx 0.34$	Symmetric, 1T periodic
$0.34 \lessapprox \omega_0 \lessapprox 0.52$	Asymmetric, 1T periodic
$\omega_0 \approx 0.52$	Irregular
$0.52 \lessapprox \omega_0 \lessapprox 0.90$	Symmetric, 1T periodic
$0.90 \lessapprox \omega_0 \lessapprox 1.05$	Quasi-periodic
$\omega_0 \approx 1.09$	Symmetric, 1T periodic
$\omega_0 \approx 1.10$	Irregular
$1.10 \lessapprox \omega_0 \lessapprox 1.17$	Quasi-periodic
$\omega_0 \approx 1.17$	Irregular

3.5.2 Beam Response with Varying Flapping Amplitude

In this section, we investigate the flapping beam's response (transverse tip displacement) as the flapping amplitude is increased from 1° to 30° with increments of 1°. While varying the flapping amplitude, the flapping frequency is kept constant at 3 selected values: $\omega_0 = 0.35$, $\omega_0 = 0.50$, and $\omega_0 = 1.10$. The former two frequencies correspond to flapping occurring in the secondary

resonance regions, whereas the latter coincides with the primary resonance region.

In Figure 3.21a-f, response spectra and phase projection trajectories of tip motion obtained at $\omega_0 = 0.35$ are given for three flapping amplitudes: 10°, 20°, and 26°. Data is not presented in these figures for flapping with amplitude less than 10° where the response spectra of the beam only contain the first harmonic. This first harmonic remains as the predominant response component at all flapping amplitudes considered when flapping at $\omega_0 = 0.35$. As shown in Figure 3.21a, peaks in the response spectra at the second and third harmonics begin to appear for flapping with amplitude of 10°. When the flapping amplitude reaches 20° (Figure 3.21b & e), the level of contribution to the response of the second and third harmonics becomes commensurate. Increasing the flapping amplitude to 26° (Figure 3.21c & f) results in a response which is dominated by both first and third-order harmonics.

Response spectra and phase projections for the beam flapping at $\omega_0 = 0.50$, which corresponds to the second-order superharmonic resonance, are shown in Figure 3.21g-l for three flapping amplitudes: 10°, 20°, and 30°. For all flapping amplitudes, flapping at this frequency results in a response which is dominated by the first and second harmonics. The second harmonic becomes significant as the amplitude increases above 5° and higher-order harmonics, up to order six, appear in the spectra for flapping amplitudes of 10° (Figure 3.21g) or higher. The higher harmonic components of the response grow in magnitude with increasing flapping amplitude (Figure 3.21h & i). As shown in Figure 3.21l, increasing the flapping amplitude past 27° results in phase projection trajectories which intermingle and become moderately more diffuse as the amplitude is increased. This modest diffusion in the phase trajectories is

likely a precursor to the chaotic dynamics noted in the previous section for flapping at $\omega_0 = 0.52$ and 30°.

Response time histories, spectra, and phase trajectories for flapping at $\omega_0 = 1.10$ are shown in Figure 3.22 for various flapping amplitudes. Increasing the flapping amplitude, for this flapping frequency, results in a more complex variation in the response characteristics when compared to the results obtained for flapping at lower frequencies (see Figure 3.21). As shown in Figure 3.22a, when flapping at amplitudes up to and including 10°, the beam response contains predominantly a single frequency (flapping frequency) component. As shown in Figure 3.22e, for flapping at 11°, a peak occurs in the response spectra at the third harmonic with smaller peaks also occurring at the 5th, 7th, and 9th harmonics. The peaks at the first, third, and seventh harmonics are rather broad with nonzero content contained in a band (centered at the harmonics) with a width which appears to be 1/2 of the flapping frequency. As Figure 3.22h demonstrates, for flapping at 11° phase trajectories of the tip motion show strong diffusion, albeit with the center of the main loop left unoccupied. By the time the flapping amplitude reaches 19°, response trajectories fill the entire subset of the phase projection (Figure 3.22i) and the corresponding response spectra (Figure 3.22f) contains strong content in wide bands centered about odd harmonics and a small peak at the second harmonic of the forcing frequency. Further increase of the flapping amplitude (up to 30°) does not alter the tip response on the phase projection; it remains densely occupied by the response trajectories. However, as shown in Figure 3.22g, when the flapping amplitude is increased to 28° the response spectra now consists of broad bands centered about both even and odd harmonics and further increase to flapping at 30° results in a Poincaré section which is an ordered cluster of

points (Figure 3.20j). Based upon these observations, it appears that the dynamics of the beam tip response is irregular for flapping at $\omega_0 = 1.10$ in this range of amplitudes (28-30°).

3.6 Chapter Summary

In this chapter, the structural dynamic characteristics of a flapping aluminum beam were investigated through both experiment and numerical simulation. Flapping was realized in the experiment through the use of a 4-bar crank-and-rocker mechanism while the computational model consisted of a nonlinear finite element model based upon an isoparametric degenerate-continuum approach using a total Lagrangian formulation.

Through comparison of temporal and frequency domain data, experimental and computational surface bending strains and tip displacement data are determined to be in good quantitative agreement for a majority of the flapping frequencies. Experimental frequency response curve for flapping at 15° was overestimated in the simulation for flapping frequencies corresponding to regions of secondary (superharmonic) and primary resonances. The experimental frequency response curve for flapping at 30° revealed a single broad peak at a nondimensional (by the beam first theoretical modal frequency) flapping frequency of $\omega_0 = 0.43$, which is thought to be due to a third-order superharmonic resonance. The discrepancy in the experiment and simulation results near primary and secondary resonance is primarily attributed to a nonlinear dependence of the damping force on the beam response and, subsequently, the use of a linear damping model in the simulation. In addition, large bending strain in the primary resonance region may have caused the experiment to

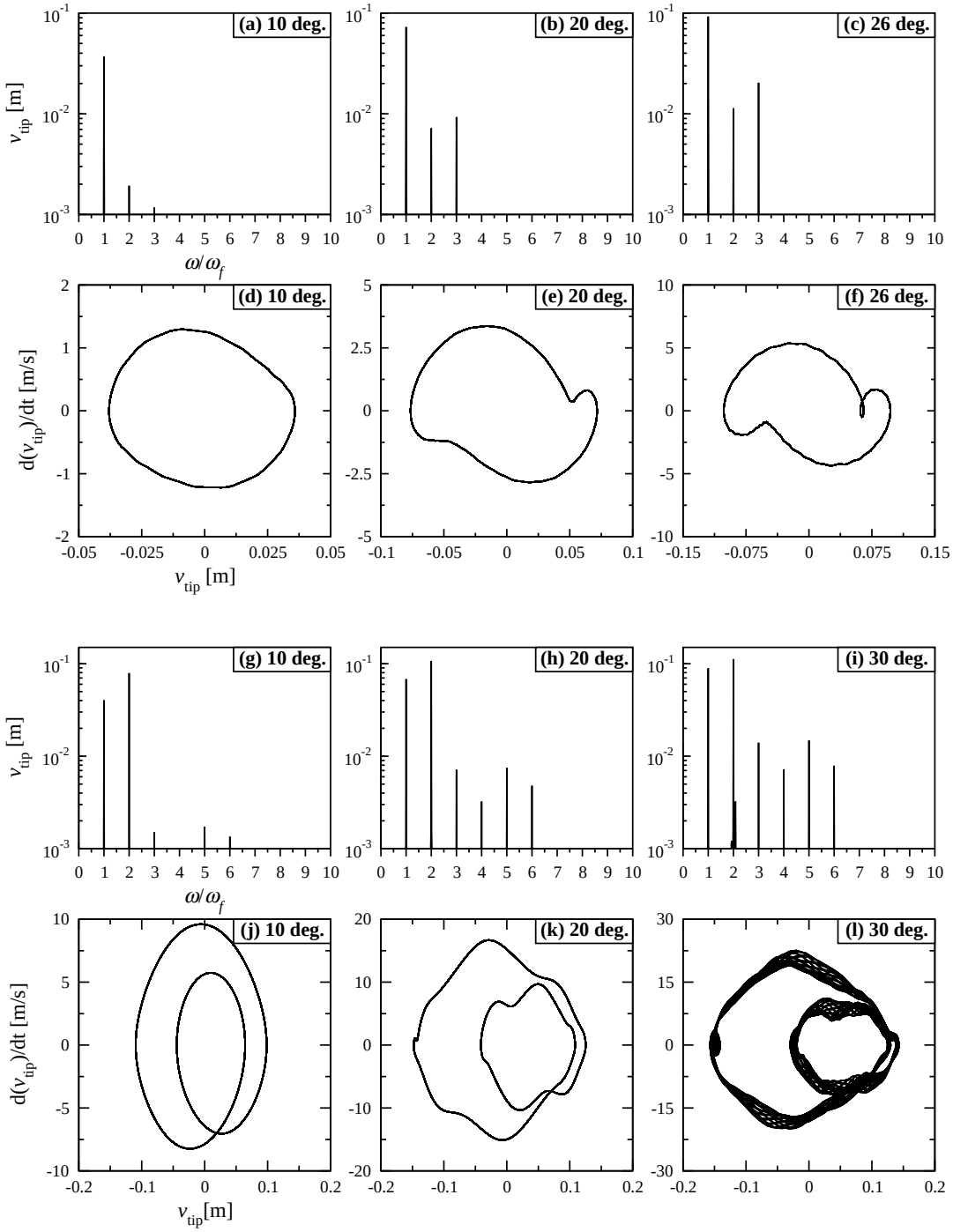

Figure 3.21: Discrete Fourier transform of transverse tip displacement at $\omega_0 = 0.35$ for flapping amplitudes of: (a) 10°, (b) 20°, (c) 26°; phase projection of transverse tip motion at $\omega_0 = 0.35$ for flapping amplitudes of: (d) 10°, (e) 20°, (f) 26°; discrete Fourier transform of transverse tip displacement at $\omega_0 = 0.50$ for flapping amplitudes of: (g) 10°, (h) 20°, (i) 30°; phase projection of transverse tip motion at $\omega_0 = 0.50$ for flapping amplitudes of: (j) 10°, (k) 20°, and (l) 30°.

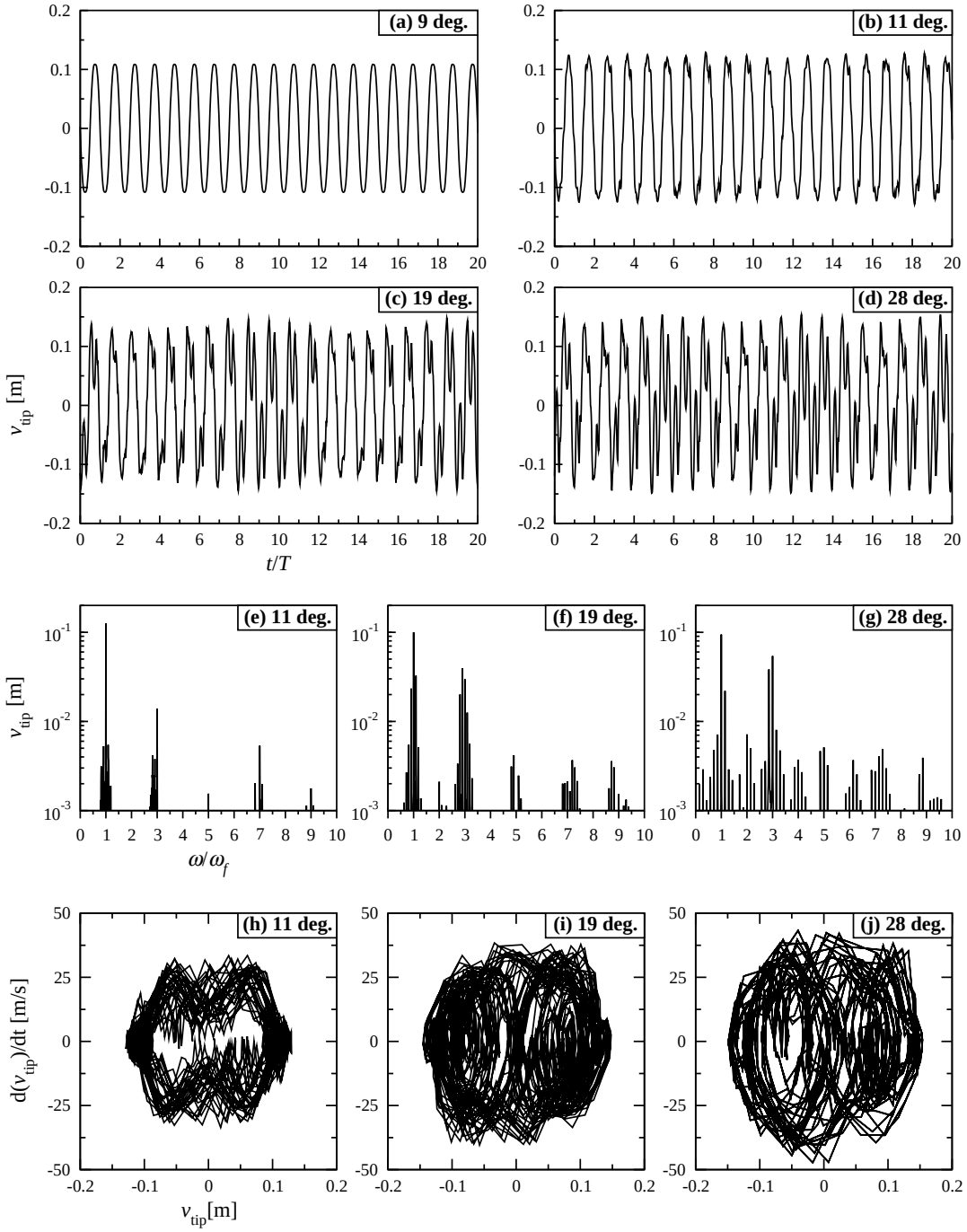

Figure 3.22: Time history of transverse tip displacement at $\omega_0 = 1.10$ for flapping amplitudes of: (a) 9°, (b) 11°, (c) 19°, (d) 28°; discrete Fourier transform of transverse tip displacement at $\omega_0 = 1.10$ for flapping amplitudes of: (e) 11°, (f) 19°, (g) 28°; phase projection of transverse tip motion at $\omega_0 = 1.10$ for flapping amplitudes of: (h) 11°, (i) 19°, and (j) 28°.

deviate from linear elastic material behavior which was not modeled in the simulation.

Additional numerical experiments were performed to investigate qualitative changes in the beam tip response dynamics as flapping frequency and amplitude were varied. For flapping at 15°, varying the flapping frequency resulted in a number of bifurcations. It was found that as the flapping frequency is increased from below the region of second order superharmonic resonance through the region of primary resonance, various transitions occur between symmetric 1-period response, quasi-periodic motions, and irregular (possibly chaotic) motions. Similar behavior is noted in the numerical experiments for flapping at 30° with notable difference being the existence of a small region of irregular response for flapping frequencies near the superharmonic resonance of order 2.

Finally, numerical experiments were performed at constant flapping frequencies ($\omega_0 = 0.35$, 0.50, and 1.10) with flapping amplitudes ranging from 1° to 30°. For flapping with $\omega_0 = 0.35$ the response was a 1-period motion for all flapping amplitudes while flapping with $\omega_0 = 0.50$ and $\omega_0 = 1.10$ resulted in a transition from 1-period, periodic motion to aperiodic motion at 28° and 11°, respectively.

CHAPTER 4

Effect of Nonlinear Damping on the Structural Dynamics of Flapping Beams

4.1 Scope of the Chapter

In this chapter,* the effects of nonlinear damping forces on the large amplitude structural dynamics of slender cantilever beams undergoing flapping motion in air are investigated through experiment and simulation. The aluminum beams are set into flapping motion through actuation at the beam base via a 4-bar crank-and-rocker mechanism. The beam strain response dynamics are investigated for two flapping amplitudes, 15° and 30°, and a range of flapping frequencies up to 1.3 times the first bending modal frequency. In addition to flapping at standard air pressure, flapping simulations and experiments are also performed at reduced air pressure (70% vacuum). In the simulations, linear and nonlinear, internal and external, damping force models in different functional forms are incorporated into a nonlinear, inextensible beam theory. The external nonlinear damping models are assumed to depend, parametrically, on ambient air density, beam width, and an empirically determined constant. Periodic solutions to the model equation are obtained numerically with a 1-mode Galerkin method and a high order time-spectral scheme. The effect of different damping forces on the stability of the computed periodic solutions are analyzed with the aid of Floquet theory. The strain-frequency

*The material presented in this chapter was published in *International Journal of Non-Linear Mechanics*, 65: 148-163, 2014.

response curves obtained with the various damping models suggest that, when compared to the linear viscous and nonlinear internal damping models, the nonlinear external damping models better represent the experimental damping forces in regions of primary and secondary resonances. In addition to providing improved correlation with experimental strain response amplitudes over the tested range of flapping frequencies, the nonlinear (external) damping models yield stable periodic solutions for each flapping frequency which is consistent with the experimental observations described in detail in Chapter 3. Changes in both the experimental ambient pressure and flapping amplitude result in some variation in the nondimensional parameters (which contain a constant determined from experiment) associated with each of the nonlinear external damping models. This result likely indicates an incomplete description of the model parameter dependence and/or nonlinear functional form of the damping force.

In Section 4.2 the features of the experimental apparatus relevant to the present chapter are discussed in summary. Section 4.3 describes the theoretical model; the equation of motion, boundary conditions, and their transformation are given. In Section 4.4, the governing equations are solved in spatial and temporal domains using the Galerkin's method and a time-spectral scheme, respectively. The linear and nonlinear damping models are presented in Section 4.5. Section 4.6 is devoted to the stability analysis of the periodic response using the Floquet theory. Results and discussion are given in Section 4.7. The chapter concludes with a summary of the work in Section 4.8.

4.2 Experimental Model

In the present research, the flapping beam experiments were conducted by using the same test bed which was utilized in the study presented in Chapter 3. Details of the flapping test bed can be found in Section 2.2.1. Aluminum 6061-T6 beam specimens (see Section 2.3) are tested in ambient air and reduced air pressures, at two flapping amplitudes 15° and 30°. The structural dynamic response is characterized based on the surface bending strain sampled with electrical resistance strain gages (see Section 2.4.1 for more information). In order to perform the flapping tests at reduced air pressure, a vacuum chamber, which is large enough to accommodate the test bed and data acquisition peripherals, was constructed from a clear acrylic cylinder. Experiments in the vacuum chamber were carried out at 21 inHg vacuum, i.e., 70% vacuum. Additional details of the vacuum chamber are given in Section 2.5. The beams were tested at flapping frequencies ranging from 1 Hz to 19 Hz with increments as small as 0.1 Hz. Tests at each flapping frequency were repeated a maximum of three times and determined to be repeatable. The experimental bending strain data obtained in ambient and reduced (70% vacuum) air pressures are listed in Tables D.1 and D.2, respectively, in Appendix D together with the estimated confidence intervals.

A general procedure for conducting the experiments can be summarized as follows (also see Section 2.6). A test at a particular flapping frequency is initiated with the beam at rest. The data collection is triggered soon after the target flapping frequency is reached and stabilized. A minimum of 3 s of strain data is collected at a sampling frequency of 2000 Hz. Immediately after the data acquisition stops, the motor is set to decelerate and brought to a halt.

The same procedure is repeated for the data collection at the next frequency level. The repetition of a test at a particular flapping frequency is realized once the entire frequency range of interest is investigated. For the tests conducted under 70% vacuum, the chamber door is sealed and the pump is run until the desired level of reduced pressure (i.e., 21 inHg vacuum) is reached. Then, the aforementioned procedure is followed for data acquisition at a particular flapping frequency.

4.3 Theoretical Model

4.3.1 Equation of Motion and Boundary Conditions

In order to simplify the implementation of the nonlinear damping models presented in this chapter and to facilitate the asymptotic analysis to be presented in the next chapter, we will now introduce a simpler nonlinear beam model than what was used in Chapter 3. The method of spatial discretization is also simplified in order to significantly reduce the number of degrees of freedom in the resulting numerical model.

The equation of motion of the flapping beam is based upon Semler *et al.*'s [114] derivation which was proposed to model the nonlinear dynamics of cantilevered pipes conveying fluid. The nonlinear slender beam model accounts for large curvature and axial inertia effects, and uses the assumption of an *inextensible* beam centerline (which allows longitudinal displacement u to be written in terms of transverse displacement v). The motion is assumed to be planar, and shear deformation and rotary inertia effects of the beam cross section are neglected. The schematic diagram of the flapping beam problem is given in Figure 4.1. In the context of the present study, terms in the original

partial differential equation which represent the forces due to fluid motion and gravity are excluded. A general dissipative force density (i.e., force per unit length along the beam) f_d, which will take on different functional forms, is included in the equation. Hence, denoting the transverse displacement y by $v(s,t)$, and the curvilinear coordinate measured along the centerline by s, one can write the equation of motion as:

$$\begin{aligned}&\rho A_c \ddot{v} + f_d(v,\dot{v}) + EI\left[v''''(1+v'^2) + 4v'v''v''' + v''^3\right] - \\ &v''\left[\int_s^L \int_0^s \rho A_c(\dot{v}'^2 + v'\ddot{v}')\,\mathrm{d}s\,\mathrm{d}s\right] + \\ &v'\int_0^s \rho A_c(\dot{v}'^2 + v'\ddot{v}')\,\mathrm{d}s = 0,\end{aligned} \tag{4.3.1}$$

where ρ, A_c, EI, and L are mass density, cross sectional area, flexural rigidity, and length of the beam, respectively, and primes and overdots denote partial differentiation with respect to s and t, respectively [i.e., $\dot{(\ )} \equiv \partial(\ )/\partial t$, $(\ )' \equiv \partial(\ )/\partial s$]. In Eq. (4.3.1), terms in the brackets multiplied by EI represent linear and nonlinear flexural restoring forces, whereas the terms under integral signs represent nonlinear inertia forces produced through the expression of the axial inertia using the inextensibility assumption. It should be noted that damping forces acting in the in-plane direction are neglected in this work.

In the present study, the experimental actuation of the cantilevered beam is realized in the simulation through the prescription of a set of time-dependent boundary conditions. These boundary conditions can be stated as:

$$v = d\sin(\theta_f), \qquad v' = \theta_f \qquad at \quad s = 0, \tag{4.3.2a}$$

$$v'' = 0, \qquad v''' = 0 \qquad at \quad s = L, \tag{4.3.2b}$$

where d and θ_f are rigid link length (offset distance, $d = 33.3$ mm) and flapping angle, respectively (see Figure 4.1). Equations (4.3.2a) imply that transverse displacement and rotation of the beam's clamped-end are equal to the transverse displacement of the clamping point of the rigid link and flapping angle, respectively. The flapping angle θ_f is a time-dependent function which is defined by the kinematics of 4-bar crank-and-rocker mechanism (see Appendix B).

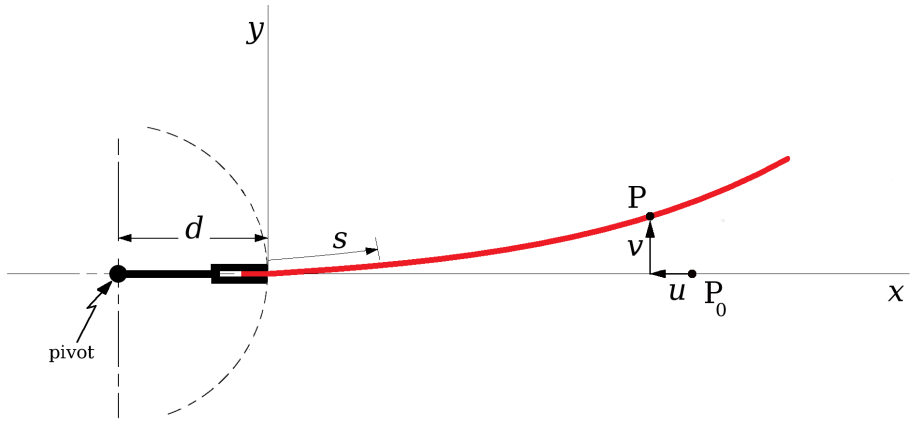

Figure 4.1: Schematic diagram of the flapping cantilever beam. Displacement of a representative point from initial configuration P_0 to current configuration P and longitudinal and transverse displacements (u and v) are illustrated.

4.3.2 Transformation of Governing Equations

In this work the numerical solution is based upon a 1-mode Galerkin-Kantorovich approach. In order to apply this method, which assumes separation in the spatial and temporal dependence of the solution, the nonhomogeneous boundary conditions are first rendered homogeneous [115, 116]. To this end, we assume

a two-part solution of the form:

$$v(s,t) = \zeta(s,t) + g(s,t), \tag{4.3.3}$$

where $g(s,t)$ is found so as to render the boundary conditions for the variable $\zeta(s,t)$ homogeneous [41, 115]:

$$g(s,t) = d\sin(\theta_f) + s\theta_f. \tag{4.3.4}$$

It should be noted that, in general, g in Eq. (4.3.3) is not unique which for nonlinear problems could influence the final answer [117]. However in this particular case: (1) simulations which numerically calculate $g(s,t)$ seem to confirm the uniqueness of g [118] and, (2) the transformation is used in the context of a numerical solution (method of weighted residuals, e.g., Galerkin's method) and hence can be viewed as just another choice which is made in the context of the approximate solution.

The foregoing transformation, after Eqs. (4.3.3) and (4.3.4) are inserted into Eqs. (4.3.1) and (4.3.2), leads to a boundary-value problem composed of a nonhomogeneous partial differential equation for the dependent variable $\zeta(s,t)$ and homogeneous boundary conditions. Noting that $g'' = g''' = g'''' = 0$,

the transformed governing equations become:

$$\rho A_c(\ddot{\zeta}+\ddot{g})+f_d(\zeta,\dot{\zeta},g,\dot{g})+$$
$$EI\Big[\zeta''''+\zeta''''\zeta'^2+2\zeta''''\zeta'g'+\zeta''''g'^2+4\zeta'\zeta''\zeta'''+4g'\zeta''\zeta'''+\zeta''^3\Big]-$$
$$\zeta''\int_s^L\int_0^s \rho A_c\big[\dot{\zeta}'^2+2\dot{\zeta}'\dot{g}'+\dot{g}'^2+\zeta'\ddot{\zeta}'+\zeta'\ddot{g}'+g'\ddot{\zeta}'+g'\ddot{g}'\big]\,\mathrm{d}s\,\mathrm{d}s+$$
$$(\zeta'+g')\int_0^s \rho A_c\big[\dot{\zeta}'^2+2\dot{\zeta}'\dot{g}'+\dot{g}'^2+\zeta'\ddot{\zeta}'+\zeta'\ddot{g}'+g'\ddot{\zeta}'+g'\ddot{g}'\big]\,\mathrm{d}s=0, \quad (4.3.5)$$

and

$$\zeta(0,t)=\zeta'(0,t)=\zeta''(L,t)=\zeta'''(L,t)=0. \quad (4.3.6)$$

4.4 Method of Solution

4.4.1 Spatial Discretization via Galerkin's Method

In order to eliminate the spatial dependence of the problem, we consider an approximate solution to Eqs. (4.3.5) and (4.3.6) of the form:

$$\zeta(s,t)\cong\sum_{i=1}^{n}a_i(t)\phi_i(s), \quad (4.4.1)$$

where $a_i(t)$ are the generalized coordinates to be determined, $\phi_i(s)$ are the trial functions taken as the transverse natural eigenmodes of a cantilever Euler-Bernoulli beam, and n is the total number of modes considered in the approximation. Equation (4.4.1) is inserted into Eq. (4.3.5) and Galerkin's method

is applied, *viz.*:

$$\int_0^L \phi_j \Bigg(\rho A_c \big(\textstyle\sum \ddot{a}_i \phi_i + \ddot{g}\big) + f_d(a_i, \dot{a}_i, \phi_i, g, \dot{g}) + \\ EI \Big[\textstyle\sum a_i \phi_i'''' + \big(\sum a_i \phi_i''''\big)\big(\sum a_i \phi_i'\big)^2 + 2g'\big(\sum a_i \phi_i''''\big)\big(\sum a_i \phi_i'\big) + \\ g'^2 \textstyle\sum a_i \phi_i'''' + 4\big(\sum a_i \phi_i'\big)\big(\sum a_i \phi_i''\big)\big(\sum a_i \phi_i'''\big) + \\ 4g'\big(\sum a_i \phi_i''\big)\big(\sum a_i \phi_i'''\big) + \big(\sum a_i \phi_i''\big)^3 \Big] - \\ \textstyle\sum a_i \phi_i'' \int_s^L \int_0^s \rho A_c \Big[\big(\sum \dot{a}_i \phi_i'\big)^2 + 2\dot{g}' \sum \dot{a}_i \phi_i' + \dot{g}'^2 + \\ \big(\sum a_i \phi_i'\big)\big(\sum \ddot{a}_i \phi_i'\big) + \ddot{g}' \sum a_i \phi_i' + g' \sum \ddot{a}_i \phi_i' + g'\ddot{g}' \Big] \, \mathrm{d}s \, \mathrm{d}s + \\ \textstyle\sum a_i \phi_i' \int_0^s \rho A_c \Big[\big(\sum \dot{a}_i \phi_i'\big)^2 + 2\dot{g}' \sum \dot{a}_i \phi_i' + \dot{g}'^2 + \\ \big(\sum a_i \phi_i'\big)\big(\sum \ddot{a}_i \phi_i'\big) + \ddot{g}' \sum a_i \phi_i' + g' \sum \ddot{a}_i \phi_i' + g'\ddot{g}' \Big] \, \mathrm{d}s + \\ g' \int_0^s \rho A_c \Big[\big(\sum \dot{a}_i \phi_i'\big)^2 + 2\dot{g}' \sum \dot{a}_i \phi_i' + \dot{g}'^2 + \big(\sum a_i \phi_i'\big)\big(\sum \ddot{a}_i \phi_i'\big) + \\ \ddot{g}' \sum a_i \phi_i' + g' \sum \ddot{a}_i \phi_i' + g'\ddot{g}' \Big] \, \mathrm{d}s \Bigg) \, \mathrm{d}s = 0, \qquad i, j = 1, 2, \ldots, n. \tag{4.4.2}$$

where in Eq. (4.4.2) the limits of summations are omitted for clarity. Invoking the orthonormality of eigenmodes (i.e., $\int_0^L \phi_i \phi_j ds = \delta_{ij}$, where δ_{ij} is the Kronecker delta) in Eq. (4.4.2) yields a set of n nonlinear, coupled, ordinary (time dependent) differential equations for the modal displacements $a_i(t)$.

A convergence study conducted to determine the number of eigenmodes needed in the analysis suggests that a 1-mode approximation is sufficient for the range of flapping amplitudes and frequencies tested (see Figure F.1 in Appendix F). The convergence study is undertaken for both geometrically linear and nonlinear beam models. In both of these models the velocity-

3^{rd} power damping model is used. From the results it can be noted that it appears that for this particular problem, when flapping is taking place in the superharmonic resonance region the effect of geometric nonlinearity is small.

Considering a one-mode approximation (i.e., $n = 1$) in Eq. (4.4.2), invoking orthonormality and choosing characteristic length and time scales of L and $\left(\frac{EI}{\rho A_c L^4}\right)^{-1/2}$, respectively, e.g.:

$$\begin{aligned} &a = \bar{a}L, \quad s = \bar{s}L, \quad d = \bar{d}L, \quad \bar{g} = g(\bar{s}, \bar{d}, \bar{\omega}_f, \bar{t}), \\ &t = \bar{t}\Big(\frac{EI}{\rho A_c L^4}\Big)^{-1/2}, \quad \omega_f = \bar{\omega}_f\Big(\frac{EI}{\rho A_c L^4}\Big)^{1/2}, \end{aligned} \tag{4.4.3}$$

we arrive at a 1-mode modal equation in terms of the normal coordinate $\bar{a}(\bar{t})$ (subscript on a suppressed). In Eq. (4.4.3), ω_f denotes the flapping frequency, and a variable with an overbar represents the corresponding nondimensional variable. Note also that from this point onward, primes and superposed dots operating on nondimensional variables will be used to represent partial differentiation with respect to nondimensional coordinate $\bar{s}$ and nondimensional time $\bar{t}$, respectively; i.e., $\dot{(\bar{\ })} \equiv \partial(\bar{\ })/\partial\bar{t}$, $(\bar{\ })' \equiv \partial(\bar{\ })/\partial\bar{s}$. Finally, dividing through the modal equation by EI/L^2 and rearranging, one obtains:

$$\begin{aligned} &\ddot{\bar{a}}\big[M_1 + M_2(\bar{t}) + M_3(\bar{t})\bar{a} + M_4\bar{a}^2\big] + \bar{f}_d + A_1(\bar{t})\bar{a} + 2A_2(\bar{t})\bar{a}^2 + A_3\bar{a}^3 + \\ &B_1(\bar{t})\bar{a} + 2B_2(\bar{t})\dot{\bar{a}} + 2B_3(\bar{t})\bar{a}\dot{\bar{a}} + B_4(\bar{t})\bar{a}^2 + B_5(\bar{t})\dot{\bar{a}}^2 + B_6\bar{a}\dot{\bar{a}}^2 + C(\bar{t}) = 0, \end{aligned} \tag{4.4.4}$$

where M_i, A_i, B_i and C are comprised of spatial integrals which are given in Appendix E and $\bar{f}_d$ is the modal damping force. These integrals are evaluated numerically using a composite Simpson's 1/3 integration with 20 intervals.

Equation (4.4.4) can be expressed in standard form as:

$$\ddot{\bar{a}} + \frac{\bar{f}_{KM}(\bar{a}, \dot{\bar{a}})}{H(\bar{a})} + \frac{\bar{f}_d(\bar{a}, \dot{\bar{a}})}{H(\bar{a})} = 0, \tag{4.4.5}$$

with,

$$H(\bar{a}) = M_1 + M_2(\bar{t}) + M_3(\bar{t})\bar{a} + M_4\bar{a}^2,$$

and where $\bar{f}_{KM}$ denotes the generalized forces induced by curvature (nonlinear and linear) and nonlinear inertia.

Alternatively, Eq. (4.4.5) can be expressed as a system two first-order differential equations as:

$$\begin{aligned} \dot{x_1} &= x_2, \\ \dot{x_2} &= -\frac{\bar{f}_{KM}(x_1, x_2)}{H(x_1)} - \frac{\bar{f}_d(x_1, x_2)}{H(x_1)}, \end{aligned} \tag{4.4.6}$$

where $x_1 = \bar{a}$ and $x_2 = \dot{\bar{a}}$ or, in matrix form,

$$\dot{\mathbf{x}} + \mathbf{r} = \mathbf{0}, \tag{4.4.7}$$

where,

$$\mathbf{x} = \begin{Bmatrix} x_1 \\ x_2 \end{Bmatrix}, \quad \dot{\mathbf{x}} = \begin{Bmatrix} \dot{x_1} \\ \dot{x_2} \end{Bmatrix}, \quad \mathbf{r} = \begin{Bmatrix} -x_2 \\ \frac{\bar{f}_{KM}(x_1,x_2)}{H(x_1)} + \frac{\bar{f}_d(x_1,x_2)}{H(x_1)} \end{Bmatrix}, \quad \mathbf{0} = \begin{Bmatrix} 0 \\ 0 \end{Bmatrix}.$$

4.4.2 Temporal Discretization via Time-Domain Fourier Pseudospectral Scheme

As in this chapter we are interested in characterizing the periodic solution, Eq. (4.4.7) is discretized in the time domain with a time-domain Fourier pseudospectral method [119–121] which is equivalent to a spectral collocation [122]. This method has also been called high dimensional harmonic balance (HDHB) in the literature, which is the terminology we will adopt here for brevity.

In classical harmonic balance (HB) methods for computing time-periodic solutions, one assumes a solution in the form of a Fourier series, the coefficients of which are found based on the uniqueness theorem of trigonometric series [123] or, equivalently, through Galerkin projection. When the problem to be investigated happens to be a nonlinear dynamical system with many degrees of freedom, the implementation of the classical HB formulation typically becomes very cumbersome. Also in some cases terms in the governing equation may not admit Fourier series representations (as is the case here due to mathematical form of the boundary actuation). As such, a number of modifications of the classical method have been developed including the HDHB method used here.

In the HDHB method, the unknown Fourier coefficients are written in terms of time-domain variables at uniformly spaced intervals over one period of oscillation via a discrete Fourier transformation matrix. The resulting set of algebraic equations are then solved for the time-domain variables which, if the underlying dynamical equations are nonlinear, requires the use of a root finding scheme. Also, since the HDHB method casts the problem into the time domain, implementation of the HDHB formulation into an existing time-

marching code is generally very convenient.

In order to apply the HDHB method, the solution to Eq. (4.4.7) is assumed to be smooth and periodic with period $T = 2\pi/\bar{\omega}_f$ and thus can be expressed in the form of a truncated Fourier series expansion. Accordingly, the state variables in Eq. (4.4.7) can be expanded in Fourier series as:

$$\mathbf{x}(t) \approx \hat{\mathbf{x}}^0 + \sum_{n=1}^{N_H} [\hat{\mathbf{x}}^{2n-1} \cos(n\bar{\omega}_f \bar{t}) + \hat{\mathbf{x}}^{2n} \sin(n\bar{\omega}_f \bar{t})], \tag{4.4.8}$$

and,

$$\mathbf{r}(t) \approx \hat{\mathbf{r}}^0 + \sum_{n=1}^{N_H} [\hat{\mathbf{r}}^{2n-1} \cos(n\bar{\omega}_f \bar{t}) + \hat{\mathbf{r}}^{2n} \sin(n\bar{\omega}_f \bar{t})], \tag{4.4.9}$$

with,

$$\begin{aligned}
\hat{\mathbf{r}}^0 &= \frac{1}{T} \int_0^T \mathbf{r}(\bar{t})\, \mathrm{d}\bar{t}, \\
\hat{\mathbf{r}}^{2n-1} &= \frac{2}{T} \int_0^T \mathbf{r}(\bar{t}) \cos(n\bar{\omega}_f \bar{t})\, \mathrm{d}\bar{t}, \\
\hat{\mathbf{r}}^{2n} &= \frac{2}{T} \int_0^T \mathbf{r}(\bar{t}) \sin(n\bar{\omega}_f \bar{t})\, \mathrm{d}\bar{t},
\end{aligned} \tag{4.4.10}$$

where, $\hat{\mathbf{x}}^n$ and $\hat{\mathbf{r}}^n$ $(n = 0, 1, 2, \ldots, N_H)$ are the Fourier coefficients and N_H is the number of harmonics retained in the Fourier expansions. Inserting Eqs. (4.4.8), (4.4.9), and (4.4.10) into Eq. (4.4.7), and collecting terms associated with each harmonic (i.e., $\cos(n\bar{\omega}_f \bar{t})$ and $\sin(n\bar{\omega}_f \bar{t})$; $n = 0, 1, 2, \ldots, N_H$) results in a system of equations for the Fourier coefficients:

$$\bar{\omega}_f \mathbf{A} \hat{\mathbf{X}} + \hat{\mathbf{R}} = \mathbf{0}, \tag{4.4.11}$$

where,

$$\hat{\mathbf{X}} = \begin{bmatrix} \hat{x}_1^0 & \cdots & \hat{x}_{N_K}^0 \\ \vdots & \hat{x}_k^n & \vdots \\ \hat{x}_1^{2N_H} & \cdots & \hat{x}_{N_K}^{2N_H} \end{bmatrix}, \quad \hat{\mathbf{R}} = \begin{bmatrix} \hat{r}_1^0 & \cdots & \hat{r}_{N_K}^0 \\ \vdots & \hat{r}_k^n & \vdots \\ \hat{r}_1^{2N_H} & \cdots & \hat{r}_{N_K}^{2N_H} \end{bmatrix},$$

$$\mathbf{A} = \begin{bmatrix} 0 & & & & \\ & \mathbf{J}_1 & & & \\ & & \mathbf{J}_2 & & \\ & & & \ddots & \\ & & & & \mathbf{J}_{N_K} \end{bmatrix}, \quad \mathbf{J}_k = \begin{bmatrix} 0 & k \\ -k & 0 \end{bmatrix} \quad (k = 1, 2, \ldots, N_K),$$

with N_K the total number of states which is twice the number of modes used in Eq. (4.4.1) ($N_K = 2$ here). Equation (4.4.11) is a system of $N_T = (2N_H+1)N_K$ equations which can be solved for the N_T unknown Fourier coefficients $\hat{\mathbf{x}}^n$. In order to solve the system (4.4.11), one needs to derive expressions for $\hat{\mathbf{r}}^n$ in terms of the Fourier coefficients $\hat{\mathbf{x}}^n$ by using Eq. (4.4.10). This is the procedure followed in the classical harmonic balance technique and is very cumbersome since $\hat{\mathbf{r}}^n$ are the nonlinear functions of the $\hat{\mathbf{x}}^n$. As a novel extension of the classical harmonic balance method, the HDHB technique circumvents this difficulty [124, 125].

In the HDHB method, the N_T Fourier coefficients $\hat{\mathbf{x}}^n$ are written in terms of the time-domain variables $\tilde{\mathbf{x}}^n$ at N_T equally spaced intervals over one period of oscillation via a discrete Fourier transform operator $\mathbb{F}$:

$$\hat{\mathbf{X}} = \mathbb{F}\tilde{\mathbf{X}}, \qquad \hat{\mathbf{R}} = \mathbb{F}\tilde{\mathbf{R}}, \tag{4.4.12}$$

where,

$$\tilde{\mathbf{X}} = \begin{bmatrix} x_1(\bar{t}_0) & \cdots & x_{N_K}(\bar{t}_0) \\ \vdots & x_k(\bar{t}_n) & \vdots \\ x_1(\bar{t}_{2N_H}) & \cdots & x_{N_K}(\bar{t}_{2N_H}) \end{bmatrix},$$

$$\tilde{\mathbf{R}} = \begin{bmatrix} r_1(\bar{t}_0) & \cdots & r_{N_K}(\bar{t}_0) \\ \vdots & r_k(\bar{t}_n) & \vdots \\ r_1(\bar{t}_{2N_H}) & \cdots & r_{N_K}(\bar{t}_{2N_H}) \end{bmatrix}, \tag{4.4.13}$$

with $\bar{t}_n = (2\pi n)/(N_T\bar{\omega}_f)$ $(n = 0, 1, 2, \ldots, 2N_H)$. The transformation operator $\mathbb{F}$ is given by:

$$\mathbb{F} = \frac{2}{N_T} \begin{bmatrix} 1/2 & 1/2 & \cdots & 1/2 \\ \cos(\bar{t}_0) & \cos(\bar{t}_1) & \cdots & \cos(\bar{t}_{2N_H}) \\ \sin(\bar{t}_0) & \sin(\bar{t}_1) & \cdots & \sin(\bar{t}_{2N_H}) \\ \cos(2\bar{t}_0) & \cos(2\bar{t}_1) & \cdots & \cos(2\bar{t}_{2N_H}) \\ \sin(2\bar{t}_0) & \sin(2\bar{t}_1) & \cdots & \sin(2\bar{t}_{2N_H}) \\ \vdots & \vdots & & \vdots \\ \cos(N_H\bar{t}_0) & \cos(N_H\bar{t}_1) & \cdots & \cos(N_H\bar{t}_{2N_H}) \\ \sin(N_H\bar{t}_0) & \sin(N_H\bar{t}_1) & \cdots & \sin(N_H\bar{t}_{2N_H}) \end{bmatrix} \tag{4.4.14}$$

The time-domain solution array $\tilde{\mathbf{X}}$, and forcing array $\tilde{\mathbf{R}}$, can be related to the HB Fourier coefficients via the inverse transform operator $\mathbb{F}^{-1}$, namely:

$$\tilde{\mathbf{X}} = \mathbb{F}^{-1}\hat{\mathbf{X}}, \qquad \tilde{\mathbf{R}} = \mathbb{F}^{-1}\hat{\mathbf{R}} \tag{4.4.15}$$

and Eq. (4.4.11) can be rewritten by using Eq. (4.4.12) as:

$$\bar{\omega}_f \mathbf{A}\mathbb{F}\tilde{\mathbf{X}} + \mathbb{F}\tilde{\mathbf{R}} = \mathbf{0}. \tag{4.4.16}$$

Multiplying both sides of Eq. (4.4.16) by $\mathbb{F}^{-1}$ we get the HDHB system of equations:

$$\bar{\omega}_f \mathbf{D}\tilde{\mathbf{X}} + \tilde{\mathbf{R}} = \mathbf{0}, \tag{4.4.17}$$

where the time derivative operator $\mathbf{D}$ is given by $\mathbf{D} = \mathbb{F}^{-1}\mathbf{A}\mathbb{F}$. Note that solving the system (4.4.17) does not require one to express $\hat{\mathbf{r}}^n$ in terms of the Fourier coefficients $\hat{\mathbf{x}}^n$ since the problem is cast into the time domain. In this work Eq. (4.4.17) is solved for $\tilde{\mathbf{X}}$ using a standard Newton-Raphson method with the Jacobian evaluated analytically. The details of the HDHB method and its implementation can be found in References [121, 124, 125]. A convergence study for HDHB solution is conducted with different values of N_H and the results are given in Appendix G. Based upon the convergence study it is determined that retaining 100 harmonics (i.e., $N_H = 100$, 201 equally spaced points in time over $\bar{t} \in [0, 200T/201]$) in the Fourier series approximations provides more than enough accuracy and is the resolution which is used for all simulation results presented in this chapter.

One of the objectives of the present study is to address the question of what effect the damping mechanism has on the stability, and existence, of periodic solutions. As such, once $\tilde{\mathbf{X}}$ is found, Eq. (4.4.12) is used to compute the Fourier coefficients which are then used in conjunction with Floquet theory to determine the stability of the periodic solution. This is accomplished through computation of the monodromy matrix, and its eigenvalues, via a

time-integration of the linearized (about the periodic solution) equations of motion. Further details of Floquet theory and stability analysis are given in Section 4.6. Also, the reader is referred to the References [126–128] for additional information on this topic. The numerical time-integration used to compute the monodromy matrix utilizes a 4^{th} order Runge-Kutta time integration with 100 timesteps per period.

4.5 Linear and Nonlinear Damping Models

In this section, the explicit functional forms for different damping models $f_d(v, \dot{v})$ considered in the equation of motion, Eq. (4.3.1), are given and the corresponding modal forces $\bar{f}_d$ are derived. Four different damping models which aim to represent energy dissipation mechanisms of different origins are studied. These include linear viscous damping $f_{d,vis}$, stress-dependent material damping $f_{d,mat}$, velocity-3^{rd} power damping $f_{d,vel}$, and displacement-2^{nd} power damping $f_{d,disp}$. In contrast to the linear viscous model, the latter three are nonlinear damping models. It should be noted that the total damping force f_d for both the velocity-3^{rd} power damping and displacement-2^{nd} power damping includes $f_{d,vis}$. As will be described below, the unknown parameter in both $f_{d,vel}$ and $f_{d,disp}$ is computed through comparison of the simulation results with experiment. These simulations include the linear damping term whose coefficient is known via small (free) vibration experiments.

Linear viscous damping is the most widely assumed form of dissipation operative in various nonconservative systems. This is due to its mathematical convenience and its fairly good agreement with physical observation. It simulates, in a simple linear manner, the impeding force acting on a body creeping

through a viscous fluid in a laminar flow regime as observed in a dashpot. The damping force is assumed to be proportional to the relative velocity between the body whose motion is hampered and the surrounding medium. That is:

$$f_{d,vis} = c_{vis}\dot{v}. \tag{4.5.1}$$

In the present study the viscous damping constant, c_{vis}, is approximated experimentally based upon the linear (i.e., small amplitude) free vibration response of the cantilevered beam tested in air. In this regard, the source of the measured dissipation can attributed to both the beam material itself (material damping or internal damping) and the surrounding air medium (external damping).

The second type of damping which is investigated is internal (material) damping. Using a carefully-designed experimental setup, Crawley and van Schoor [129] proposed a material damping model based upon the empirical data obtained from the free-free vibration response of aluminum beam samples. They showed that at vibration frequencies below the so-called Zener relaxation frequency [130], the average material damping in the aluminum beam samples increases exponentially with increasing maximum stress level in the samples. According to the proposed *stress-dependent nonlinear damping* model, the functional dependence of internal damping on the stress is given by [129]:

$$\xi_{mat} = \alpha \exp[\beta\ \sigma_{max}/\sigma_y], \tag{4.5.2}$$

where ξ_{mat} is the damping ratio, σ_{max} is the maximum bending stress and σ_y is the nominal yield stress of aluminum. The model parameters in Eq. (4.5.2)

are given in Reference [129] as $\alpha = 7.73 \times 10^{-4}$ and $\beta = 4.06$.

In situations where a solid body is exposed to high relative velocities, the damping force can be expected to depend nonlinearly on the relative velocity [85, 131, 132]. In such cases nonlinear damping models involving quadratic or higher powers of the relative velocity would be appropriate to model the damping force induced by the surrounding medium. As such, fluid damping force experienced by a solid body is known to be contributed by normal and shear stresses (form and friction drag) and is traditionally modeled as quadratic velocity damping model. In the case of air damping acting on the flapping beam, the skin friction drag is expected to be negligible, whereas damping due to normal stresses and convected shed vortices is expected be significant. To account for the damping due to separated flow conditions and convected vortices, a nonlinear damping model other than the quadratic velocity model would be more appropriate. Accordingly, we consider the *velocity-*3^{rd} *power damping* of the following form:

$$f_{d,vel} = c_{vel}\dot{v}^3 = (\rho_a b \eta_{vel})\dot{v}^3, \tag{4.5.3}$$

where, c_{vel} is the velocity-3^{rd} power damping coefficient which is a function of beam geometry and fluid properties. We assume c_{vel} to be the product of the air density ρ_a, beam width b and an empirically determined parameter η_{vel} which has dimensions of time/length.

The final dissipation model which is investigated in this study is the *displacement* 2^{nd} *power damping*. This type of dissipation model has been associated with the nonlinear damping of aluminum plates subjected to different levels of sound pressure [86, 87]. Accordingly, the damping force density takes

the following form:

$$f_{d,disp} = c_{disp} v^2 \dot{v} = (\rho_a b \eta_{disp}) v^2 \dot{v}, \tag{4.5.4}$$

where c_{disp} is the displacement-2^{nd} power damping coefficient which is again assumed to be the product of ambient air density, beam width and an empirically determined parameter η_{disp} which has dimensions of 1/(length×time).

The generalized damping forces associated with the above-mentioned models should be derived so that Eq. (4.4.4) can be used. In order to determine the modal damping force $\bar{f}_{d,vis}$ corresponding to the linear viscous damping model, Eq. (4.5.1), along with Eqs. (4.3.3) and (4.3.4), is substituted for $f_d(\zeta, \dot{\zeta}, g, \dot{g})$ in Eq. (4.3.5). Applying Galerkin's method with a 1-mode approximation in Eq. (4.4.1), nondimensionalizing with Eqs. (4.4.3), and dividing through by ρA_c, one obtains:

$$\ddot{\bar{a}} I_1 + 2\xi_{vis}\bar{\omega}_N (I_1 \dot{\bar{a}} + I_{31}) + \ldots = 0, \tag{4.5.5}$$

where,

$$\xi_{vis} = c_{vis}/(2\omega_N \rho A_c),$$

ω_N ($\omega_N = 1.875^2 \sqrt{\frac{EI}{\rho A_c L^4}}$) is the first bending mode frequency of the cantilever beam, and I_{31} is defined in Appendix E. In Eq. (4.5.5), the first term is recognized as the linear inertial modal force, the ellipsis denote the terms which are not shown for the sake of brevity and the remaining terms represent the damping force $\bar{f}_{d,vis}$, i.e.:

$$\bar{f}_{d,vis} = 2\xi_{vis}\bar{\omega}_N (I_1 \dot{\bar{a}} + I_{31}). \tag{4.5.6}$$

The generalized damping force $\bar{f}_{d,mat}$ is obtained by replacing ξ_{vis} in Eq. (4.5.5) with the expression for ξ_{mat} which is given in Eq. (4.5.2). However, one needs to first determine the maximum bending stress, which varies during flapping, in terms of the transverse displacement $v(s,t)$ [114]:

$$\begin{aligned}\sigma_{max} &= \kappa Eh = \left(v''/\sqrt{1-v'^2}\right) Eh \\ &= \frac{a\phi'' + g''}{\sqrt{1 - a^2\phi'^2 - 2a\phi' g' + g'^2}} Eh, \end{aligned} \tag{4.5.7}$$

where κ is the curvature and h represents half of the beam thickness. Substituting Eq. (4.5.7) into Eq. (4.5.2), expanding the exponential function in a three term Taylor series and evaluating ϕ' and ϕ'' at the beam root (i.e., $s = 0$) where the maximum bending stress occurs results in (after nondimensionalization) the following expression for ξ_{mat}:

$$\xi_{mat} = \alpha[1 + \Psi + (1/2)\Psi^2 + (1/6)\Psi^3], \tag{4.5.8}$$

with the nondimensional parameter Ψ given as:

$$\Psi = \beta \frac{Eh}{L\sigma_y} \frac{\bar{\phi}(0)''\bar{a}}{\sqrt{1-\bar{g}'^2}}. \tag{4.5.9}$$

Thus, the generalized damping force corresponding to the stress-dependent nonlinear damping model can be written as:

$$\bar{f}_{d,mat} = 2\xi_{mat}\bar{\omega}_N(I_1\dot{\bar{a}} + I_{31}). \tag{4.5.10}$$

The generalized damping force $\bar{f}_{d,vel}$ can be determined in a similar manner

which yields:

$$\bar{f}_{d,vel} = \bar{\eta}_{vel}(\dot{\bar{a}}^3 I_{32} + 3\dot{\bar{a}}^2 I_{33} + 3\dot{\bar{a}} I_{34} + I_{35}), \tag{4.5.11}$$

with,

$$\bar{\eta}_{vel} = \eta_{vel}\rho_a b(EI)^{1/2}(\rho A_c)^{-3/2}.$$

Similarly, one can determine $\bar{f}_{d,disp}$ as:

$$\bar{f}_{d,disp} = \bar{\eta}_{disp}(\dot{\bar{a}}\bar{a}^2 I_{32} + \bar{a}^2 I_{33} + 2\dot{\bar{a}}\bar{a} I_{36} + \dot{\bar{a}} I_{37} + 2\bar{a} I_{38} + I_{39}), \tag{4.5.12}$$

with the dimensionless variable given by,

$$\bar{\eta}_{disp} = \eta_{disp}\rho_a b L^4 (EI\rho A_c)^{-1/2}.$$

The integrals $I_{32}, I_{33}, \ldots, I_{39}$ in Eqs. (4.5.11) and (4.5.12) are defined in Appendix E.

We would like to reiterate that when either the displacement-2^{nd} power or velocity-3^{rd} power damping models are used in the simulations, the linear viscous damping force is also included such that the total damping force acting on the beam is $\bar{f}_{d,vis} + \bar{f}_{d,vel}$ (or $\bar{f}_{d,vis} + \bar{f}_{d,disp}$).

4.6 Stability Analysis via Floquet Theory

One of the objectives of the present study is to address the question of what effect the damping mechanism has on the stability and existence of periodic solutions. The stability of periodic response can be assessed with the aid of Floquet theory. In a general sense, it is related to transforming a linear system of ordinary differential equations (ODEs) with periodic coefficients into an

equivalent linear system of ODEs with constant coefficients [126]. Accordingly, the dynamic stability information can be deduced from the eigenvalues of the matrix of constant coefficients which is referred to as the monodromy matrix [126–128].

In the present section, overbar notation is omitted for convenience and all variables remain in dimensionless form. We begin with the governing equations (4.4.7) which is a set of first-order nonlinear ODEs but focus on the *linearized* equations which govern the disturbance (perturbation) superimposed on the periodic solution to Eqs. (4.4.7). Let $\mathbf{x}_0(t)$ be a periodic solution (with period $T = 2\pi/\omega_f$) to the system (4.4.7), expressed in terms of the Fourier coefficients $\hat{\mathbf{x}}^n$ $(n = 0, 1, 2, \ldots, N_H)$. In order to assess the stability of a periodic solution of system (4.4.7), a small disturbance $\boldsymbol{\delta}(t)$ is superimposed on the periodic response to yield the disturbed solution:

$$\mathbf{x}(t) = \mathbf{x}_0(t) + \boldsymbol{\delta}(t). \tag{4.6.1}$$

Inserting the perturbed solution (4.6.1) into the governing equations (4.4.7), assuming that $\mathbf{r}(t)$ is at least twice continuously differentiable, expanding the result in a Taylor series about $\mathbf{x}_0(t)$, and dropping the second- and higher-order terms in $\boldsymbol{\delta}(t)$ we obtain a *linearized system of ODEs governing the evolution of disturbance*. That is:

$$\dot{\boldsymbol{\delta}}(t) = -\mathbf{J}(t)\boldsymbol{\delta}(t), \tag{4.6.2}$$

where,

$$\mathbf{J}(t) = \mathbf{J}(\mathbf{x}_0(t)) = \frac{\partial \mathbf{r}}{\partial \mathbf{x}}(\mathbf{x}_0(t)), \tag{4.6.3}$$

is the Jacobian matrix of $\mathbf{r}(t)$ evaluated at the periodic solution $\mathbf{x}_0(t)$. Note

that since $\mathbf{x}_0(t)$ is periodic with period T, $\mathbf{J}(t)$ is also periodic with period T per Eq. (4.6.3) and, as a consequence, Eqs. (4.6.2) represent a set of linear ODEs with *periodic coefficients*. At this point we make use of the Floquet theory [126, 133] to determine if the solution to Eq. (4.6.2) (i.e., disturbance $\boldsymbol{\delta}(t)$) gets amplified or approaches zero as $t \to \infty$. According to the Floquet theory, every fundamental system of solutions $\boldsymbol{\Delta}(t)$ of Eqs. (4.6.2) can be represented as the product of a periodic matrix with period T and a solution matrix for a system with constant coefficients; that is [126, 133]:

$$\boldsymbol{\Delta}(t) = \mathbf{P}(t)e^{\mathbf{B}t}, \tag{4.6.4}$$

where, $\mathbf{P}(t)$ and $\mathbf{B}$ are square matrices, $\mathbf{P}(t+T) = \mathbf{P}(t)$ for all t and $\mathbf{B}$ is a constant. By a fundamental system of solutions $\boldsymbol{\Delta}(t)$ of Eqs. (4.6.2) we mean a square matrix such that the columns of $\boldsymbol{\Delta}(t)$ are linearly independent solutions of Eqs. (4.6.2). If $\boldsymbol{\Delta}(t)$ is a fundamental system of solutions of Eqs. (4.6.2), $\boldsymbol{\Delta}(t+T)$ is also a fundamental system of solutions since $\mathbf{J}(t)$ is periodic with period T. Therefore, there is a nonsingular (i.e., $\det \boldsymbol{\mathcal{M}} \neq 0$) constant matrix $\boldsymbol{\mathcal{M}}$ such that $\boldsymbol{\Delta}(t+T)$ can be expressed as a linear combination of $\boldsymbol{\Delta}(t)$, viz.:

$$\boldsymbol{\Delta}(t+T) = \boldsymbol{\Delta}(t)\boldsymbol{\mathcal{M}}. \tag{4.6.5}$$

Also, $\det \boldsymbol{\mathcal{M}} \neq 0$ implies that there exists a nonunique matrix $\mathbf{B}$ such that $\boldsymbol{\mathcal{M}} = e^{\mathbf{B}T}$. For the matrix $\mathbf{B}$, let $\mathbf{P}(t) = \boldsymbol{\Delta}(t)e^{-\mathbf{B}t}$ per Eq. (4.6.4). Then,

$$\mathbf{P}(t+T) = \boldsymbol{\Delta}(t+T)e^{-\mathbf{B}(t+T)} = \boldsymbol{\Delta}(t+T)e^{-\mathbf{B}T}e^{-\mathbf{B}t} = \boldsymbol{\Delta}(t)e^{-\mathbf{B}t} = \mathbf{P}(t), \tag{4.6.6}$$

which proves the Floquet theory (4.6.4) [126].

A monodromy matrix of the system (4.6.2) is a nonsingular constant matrix $\boldsymbol{\mathcal{M}}$ associated with fundamental system of solutions $\boldsymbol{\Delta}(t)$ of (4.6.2) through the relation (4.6.5). The eigenvalues ρ of $\boldsymbol{\mathcal{M}}$ are called *characteristic multipliers* of (4.6.2) and any μ such that $\rho = e^{\mu T}$ is called a *characteristic exponent* of (4.6.2). We shall usually specify the initial condition $\boldsymbol{\Delta}(0) = \mathbf{I}$, where $\mathbf{I}$ is the identity matrix, set $t = 0$ in Eq. (4.6.5) and compute the monodoromy matrix as [126, 127]:

$$\boldsymbol{\mathcal{M}} = \boldsymbol{\Delta}(T), \tag{4.6.7}$$

which follows from Eq. (4.6.5) with $\boldsymbol{\Delta}(0) = \mathbf{I}$, where $\mathbf{I}$ is the identity matrix.

The characteristic multipliers ρ (or characteristic exponents μ) of $\boldsymbol{\mathcal{M}}$ are used to deduce the stability of periodic solutions of Eqs. (4.4.7). As such, if all characteristic multipliers of $\boldsymbol{\mathcal{M}}$ have moduli less than one (i.e., $|\rho| < 1$) or, equivalently, if all characteristic exponents have negative real parts, all solutions of Eq. (4.6.2), i.e., the disturbances, approach zero as $t \to \infty$. Then, the periodic solutions of Eqs. (4.4.7) are referred to as *asymptotically stable*.

The monodromy matrix in the present study is computed numerically as follows. The Fourier coefficients of a periodic solution whose stability is to be checked are first used to compute the Jacobian $\mathbf{J}(t)$ in Eq. (4.6.2) analytically. The computed Jacobian is then utilized in a classical $4th$-order Runge-Kutta scheme which is used to integrate Eq. (4.6.2) for each state over one period of the solution. Prior to integration, the corresponding state is initialized to 1 in accordance with Eq. (4.6.7). The solution of each state corresponds to a particular column in the monodromy matrix. A total of 100 points per period, with equal stepsize, are considered in the numerical integration. Finally once $\boldsymbol{\mathcal{M}}$ has been computed, its eigenvalues are then determined.

4.7 Results and Discussion

4.7.1 Bending Strain *vs.* Flapping Frequency Results

The effect of change in the surrounding air pressure on the response of flapping beams is observed to be similar at both tested flapping amplitudes, 15° and 30°. Figures 4.2 and 4.3 show the experimental bending strain data obtained at 15° in air (101.3 kPa) and 70% vacuum (30.3 kPa), respectively. Note that ω_0 denotes the flapping frequency normalized by the first-mode bending frequency of the cantilever beam; i.e., $\omega_0 = \omega_f/\omega_N$. Through comparison of the two figures, it can be noted that the vibration amplitudes at second and third-order superharmonic resonance frequencies (i.e., at $\omega_0 = 0.33$ and $\omega_0 = 0.50$) amplify considerably as the surrounding air pressure is decreased. On the other hand, the vibration amplitudes at frequencies other than the resonant frequencies do not vary with a change in ambient pressure. Similar behavior can be noted by comparing Figures 4.4 and 4.5, which show the experimental bending strain data obtained at 30° in air and 70% vacuum, respectively. When compared to flapping at 15°, the experiments conducted for flapping at 30° have much broader secondary resonance peaks (at $\omega_0 = 0.31$ and $\omega_0 = 0.43$). These peaks do become slightly more pronounced as the ambient pressure is reduced.

The first mode damping ratio of the cantilever beam is measured as 0.013 based on the small amplitude free vibration response in air. This experimentally-determined damping ratio, $\xi_{vis} = 0.013$, is used for the linear viscous damping force, $f_{d,vis}$, throughout the study. In Figure 4.2, the frequency response curve obtained with the linear viscous model is compared against the experimental data obtained at a flapping amplitude of 15°. Overall the viscous model es-

timation is in good agreement with the experiments at flapping frequencies up to $\omega_0 \approx 0.83$. The exception to this result is in regions of secondary resonances, $\omega_0 \approx 0.33$ and $\omega_0 \approx 0.50$. In regions of secondary resonance, the bending strain amplitude is severely overestimated, e.g. for $\omega_0 = 0.50$ the simulation overestimates the strain by an order of magnitude. In addition to the current simulation results, the result (labeled ATFEM in the figure) found using the time-marching, nonlinear finite element model solution discussed in Chapter 3, which contains the same linear viscous damping model used in the current work, is shown in Figure 4.2 (and Figure 4.4). While the nonlinear finite element model includes both in-plane and out-of-plane deformation, one can see that the current Galerkin 1-mode solution of the inextensible beam theory gives comparable results.

The response curves obtained with the displacement-2^{nd} power damping ($f_{d,disp}$) and velocity-3^{rd} power damping ($f_{d,vel}$) models are also included in Figure 4.2. The values of the damping parameters η_{disp} and η_{vel} are chosen through an (approximate) minimization of the following error measure:

$$\mathfrak{e} = \sum_{i=1}^{N} \left(\frac{\epsilon_i^{exp} - \epsilon_i^{model}}{\epsilon_i^{exp}} \right)^2, \tag{4.7.1}$$

where N is the number experimental data points for $\omega_0 \in [0.3, 0.6]$ and ϵ_{exp} and ϵ_{model} are the experimental and model (including $f_{d,vis}$) values of bending strain (standard deviation of dynamic bending strain signal). Note that Eq. (4.7.1) implies the sum of the squares of the normalized (by the experimental value) differences between the experimental and model values at the same flapping frequency [52,62]. For additional methods, in both frequency and time domains, for parameter estimation in linear and nonlinear structural dynamics

please see the review article by Kerschen [134].

For flapping at 15° in air, the values found are 0.45 $\mathrm{m}^{-1} \cdot \mathrm{s}$ and 3600 $\mathrm{m}^{-1} \cdot \mathrm{s}^{-1}$ for η_{vel} and η_{disp}, respectively. The values for the error measure $\mathfrak{e}$, for various values of the damping parameters, are given in Table 4.1 for flapping at 15° and 30° in both air and 70% vacuum.

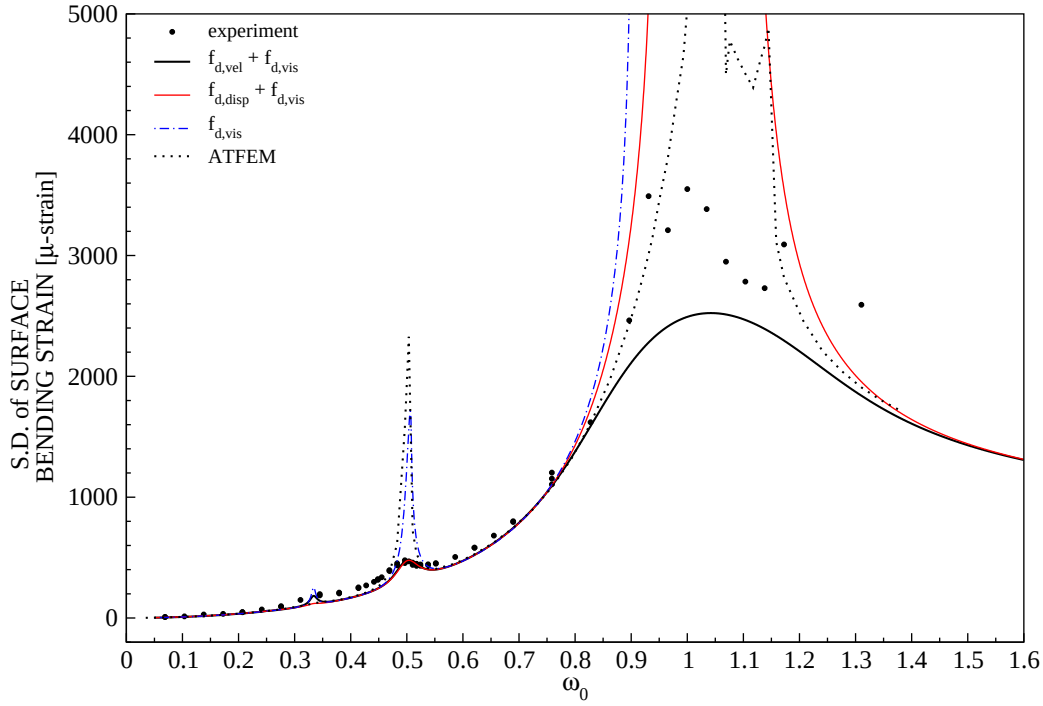

Figure 4.2: Experimental frequency response of the beam bending strain along with theoretical response curves obtained with different damping models (with, $\bar{\eta}_{vel} = 0.30$, $\bar{\eta}_{disp} = 3.61$, $\xi_{vis} = 0.013$) for flapping at 15°, in air. The curve labeled ATFEM represents the solution obtained with time-marching, nonlinear finite element model presented in Chapter 3.

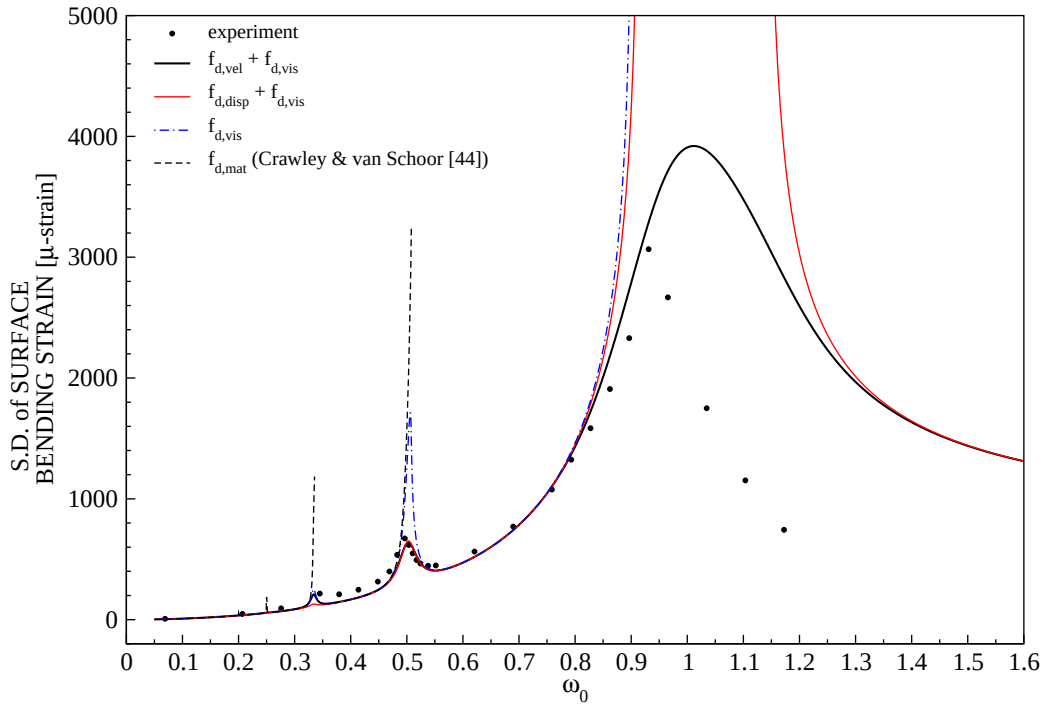

Figure 4.3: Experimental frequency response of the beam bending strain along with theoretical response curves obtained with different damping models (with, $\bar{\eta}_{vel} = 0.14$, $\bar{\eta}_{disp} = 1.87$, $\xi_{vis} = 0.013$) for flapping 15°, in 70% vacuum (21 inHg vacuum).

As shown in Figure 4.2, for flapping in air at 15°, the results obtained with both nonlinear damping models show good agreement with the experiments for frequencies well beyond the range over which they are fitted. It is noted, however, that the displacement-based model, $f_{d,disp}$, does not give any indication of superharmonic resonance peak at $\omega_0 = 0.33$ and, similar to the linear viscous model, fails to provide a realistic damping force in the primary resonance region. Conversely, the model $f_{d,vel}$ yields better predictions for both secondary resonance peaks and also for the primary resonance behavior of the beam.

The frequency response of the beam bending strain obtained at 15° in 70% vacuum is shown in Figure 4.3. In addition to the response curves of linear and nonlinear damping models, the data obtained with a model which only includes the nonlinear stress-dependent material damping force $f_{d,mat}$ is also given in the figure. The material damping model estimates follow a similar trend as the linear viscous model $f_{d,vis}$ with the secondary resonance peaks greatly overestimated. Moreover, the HDHB numerical scheme does not converge in the resonance regions when the material damping model is employed alone. The experiments in the present study are not run under the same vacuum conditions (0.133 kPa) as the experiments conducted by Crawley and van Schoor [129] and the results presented in Figure 4.3 suggest that the contribution of the internal damping to the overall damping force is trivial even under 70% vacuum.

Table 4.1: List of nonlinear damping parameters η_{vel} [$\mathrm{m}^{-1} \cdot \mathrm{s}$] and η_{disp} [$\mathrm{m}^{-1} \cdot \mathrm{s}^{-1}$] along with the associated error measure $\mathfrak{e}$ [see Eq. (4.7.1)] used to determine the best damping parameter estimate for flapping at 15° and 30°, in both air and 70% vacuum (21 inHg vacuum).

15°							
In air				In 70% vacuum			
η_{vel}	$\mathfrak{e}$	η_{disp}	$\mathfrak{e}$	η_{vel}	$\mathfrak{e}$	η_{disp}	$\mathfrak{e}$
0.30	0.751	2800	0.815	0.45	0.525	5400	0.538
0.35	0.690	3000	0.792	0.60	0.450	5800	0.528
0.40	0.663	3300	0.773	0.65	0.440	6100	0.526
0.45	0.656	3500	0.768	0.70	0.436	6200	0.524
0.50	0.663	3600	0.767	0.75	0.437	6400	0.525
0.55	0.679	3800	0.769	0.80	0.440	6600	0.526
30°							
In air				In 70% vacuum			
η_{vel}	$\mathfrak{e}$	η_{disp}	$\mathfrak{e}$	η_{vel}	$\mathfrak{e}$	η_{disp}	$\mathfrak{e}$
0.30	3.247	2000	5.601	0.90	3.502	6400	5.892
0.50	2.507	3000	4.307	1.50	2.634	7000	5.348
0.55	2.472	3600	4.184	1.80	2.577	9000	4.558
0.60	2.456	3800	4.166	1.90	2.575	10000	4.420
0.70	2.454	4000	4.153	2.00	2.577	12000	4.310
0.80	2.470	4600	4.120	2.10	2.583	14000	4.270

In the simulation, the reduced pressure condition is modeled through a change in the air density ρ_a, in Eqs. (4.5.4) and (4.5.3), which is assumed to be directly proportional to the air pressure. As such, in order to simulate 70% vacuum conditions, ρ_a is set to 0.36 $\mathrm{kg/m}^3$ which corresponds to 30% of the air density at 101.3 kPa. In Figure 4.3, the response curves for the nonlinear damping models $f_{d,disp}$ and $f_{d,vel}$ are obtained using parameter values η_{disp} and η_{vel} which are determined based upon the aforementioned error minimization procedure. The values of the damping parameters η_{disp} and η_{vel} in 70% vacuum are determined to be 6200 $\mathrm{m}^{-1} \cdot \mathrm{s}^{-1}$ and 0.70 $\mathrm{m}^{-1} \cdot \mathrm{s}$, respectively. Figure 4.3

reveals that the velocity-3^{rd} power damping model provides a slightly better prediction of the strain response when compared to the displacement-2^{nd} power model. In particular, it is able to better predict the response near the secondary ($\omega_0 \approx 0.33$) and primary ($\omega_0 \approx 0.93$) resonance regions. It should be noted that *a posteriori* measurement of the natural frequency of the beam after flapping in the primary resonance region (ω_0=0.97, 1.03, 1.10, and 1.17), for reduced air pressure, show some reduction in the natural frequency likely indicating some (unmodeled) yielding behavior.

Shown in Figures 4.4 and 4.5 are the experimental and theoretical frequency response data obtained for flapping at 30° in air and 70% vacuum, respectively. The most notable result, which can be observed in both figures, is that the experimental data form a broad "hump" over the range of frequencies encompassing the second and third-order superharmonic resonance frequencies. Close examination of the data collected in 70% vacuum (Figure 4.5) reveals that, in addition to being amplified in magnitude, the local peaks in this hump, which correspond to third and second-order superharmonics, occur at slightly higher values of the flapping frequency when flapping takes place at reduced air pressure.

As can be seen in Figure 4.4, once again simulation which includes only the linear viscous damping force $f_{d,vis}$ severely overestimates the strain amplitude in the regions of secondary resonance. In addition, as the secondary resonance frequencies are approached the simulation fails to converge, likely indicating either a breakdown in the beam model assumptions or the absence of a periodic solution. It also appears that the location of the secondary resonance peaks are overestimated by as much as 0.725 Hz ($\omega_0 = 0.05$). In addition the simulation results obtained with only material damping once again indi-

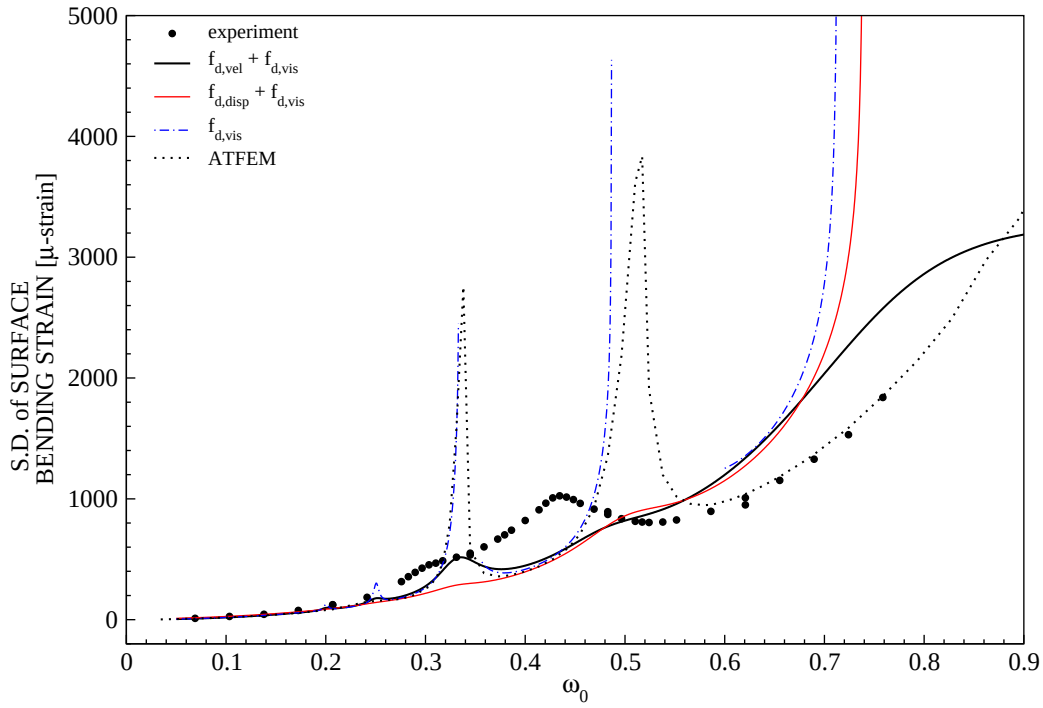

Figure 4.4: Experimental frequency response of the beam bending strain along with theoretical response curves obtained with different damping models (with, $\bar{\eta}_{vel} = 0.46$, $\bar{\eta}_{disp} = 4.02$, $\xi_{vis} = 0.013$) for flapping at 30°, in air. The curve labeled ATFEM represents the solution obtained with time-marching, nonlinear finite element model presented in Chapter 3.

cate minimal contribution to the overall damping force, similar to what was observed for flapping at 15°.

Also shown in Figure 4.4 are the theoretical curves obtained with the nonlinear external damping models. Damping parameters η_{vel} in air and in 70% vacuum are determined, according to Eq. (4.7.1), as 0.70 and 1.90 $\mathrm{m}^{-1} \cdot \mathrm{s}$, respectively. However, a qualitative agreement between the experiment and model could not be established for the displacement-2^{nd} power model by using the aforementioned error minimization scheme. The error values decrease as η_{disp} is increased until the model curve "flattens out" and the secondary resonant peak (obvious from the experiment) disappears. Therefore, the values of

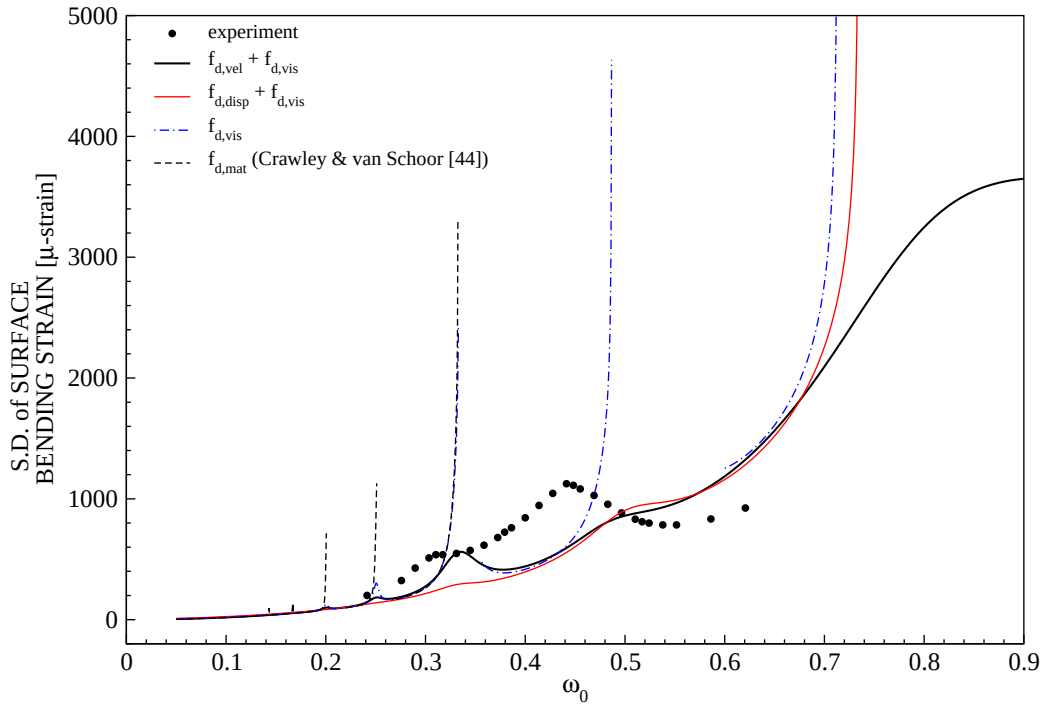

Figure 4.5: Experimental frequency response of the beam bending strain along with theoretical response curves obtained with different damping models (with, $\bar{\eta}_{vel} = 0.38$, $\bar{\eta}_{disp} = 3.61$, $\xi_{vis} = 0.013$) for 30°, in 70% vacuum (21 inHg vacuum).

the η_{disp} in air and in 70% vacuum are determined besed upon visual judgment as 4000 and 12000 $\mathrm{m}^{-1} \cdot \mathrm{s}^{-1}$, respectively. Unlike flapping at 15°, for flapping at 30° the nonlinear damping models fail to match, either qualitatively or quantitatively, the experimental strain response characteristics in regions of secondary resonance. While a previous study performed on a clamped beam by Mei and Prasad [86] indicated the ability of the nonlinear displacement-2^{nd} power damping model to predict broadening of resonance peaks, here it is observed that neither this damping model nor the velocity-3^{rd} power damping model are able to predict significant broadening of the strain response in the superharmonic resonance region. Similar observations can be made for flapping at 30° in a 70% vacuum, for which results are shown in Figure 4.5.

4.7.2 Discussion of Bending Strain *vs.* Flapping Frequency Results

Shown in Table 4.2 are the nonlinear damping parameters η_{vel} and η_{disp}, determined using the specified procedure, for the two flapping amplitudes and ambient pressure values. These are shown along with the values of the corresponding nondimensional parameters $\bar{\eta}_{vel}$ and $\bar{\eta}_{disp}$. While of the same order of magnitude, it is obvious that these nondimensional parameters do vary with both atmospheric pressure and flapping amplitude. In the absence of other unmodeled physics, if either of these damping models were to represent the dissipation mechanism exactly, both in terms of the physical parameter dependence and functional form, then the given nondimensional parameters should be invariant to changes in both air pressure and flapping amplitude. While there are likely other unmodeled (non-dissipative) effects which contribute to this result, it is also not surprising that a simple damping mechanism with only one empirical parameter is found incapable of providing a universal model. However the results for 15° do indicate that such models are able to accurately predict response characteristics given sufficient data to determine the parameter values. This would be particularly useful in cases where limited measurements are used to determine the parameter value which are then used in a simulation which can predict other quantities which are difficult or impossible to measure.

It should be noted that in Reference [39] it was reported that the damping coefficient of velocity-3^{rd} power damping model determined empirically at one level of excitation was able to accurately predict the beam response at another level of excitation. The velocity-3^{rd} power damping parameter value reported in [39] was $\bar{\eta}_{vel} = 0.128$ which is comparable to the optimal values determined

Table 4.2: List of nonlinear damping parameters η_{vel} $[\mathrm{m}^{-1} \cdot \mathrm{s}]$ and η_{disp} $[\mathrm{m}^{-1} \cdot \mathrm{s}^{-1}]$ along with the corresponding nondimensional parameters $\bar{\eta}_{vel}$ and $\bar{\eta}_{disp}$ obtained for flapping at 15° and 30°, in both air and 70% vacuum (21 inHg vacuum).

	15°		30°	
	In air	In 70% vacuum	In air	In 70% vacuum
η_{vel}	0.45	0.70	0.70	1.90
η_{disp}	3600	6200	4000	12000
$\bar{\eta}_{vel}$	0.30	0.14	0.46	0.38
$\bar{\eta}_{disp}$	3.61	1.87	4.02	3.61

in the present study ($\bar{\eta}_{vel} = 0.30$ and 0.46 for flapping at 15° and 30°, respectively). However the authors did not mention whether it was determined that this coefficient was the best, in terms of a consistent error measure, for the additional level of excitation or if it only gave acceptable results. Also, referring back to Table 4.1, one can see that the errors do not differ significantly for the various parameter values and hence a simulation with a parameter determined at one set of flapping conditions would likely provide reasonably accurate results at a different set of conditions.

An additional observation which can be made from the strain-frequency curves, is that the response does not appear to display any bistability characteristics. This result is also consistent with the stability analysis, to be presented in the next section, which indicates that a single stable periodic response exists for a given flapping frequency. This is the case regardless of the damping model used. Such a beam response characteristic was also noted in the work of Zaretzky and Crespo da Silva [39], which also utilized an inextensible beam model to study the dynamic response of beams subjected base excitation. Zaretzky and Crespo da Silva [39] attributed the absence of bistability in the system, which is often present for other forced beam configu-

rations, to the opposing softening and hardening effects of the nonlinear inertia and curvature, respectively. This topic will be discussed further in Chapter 5.

Finally, the lack of accuracy noted in the simulation results for flapping at 30° (Figures 4.4 and 4.5), regardless of the damping model used, likely indicates that additional unmodeled physics need to be considered in order to improve the theoretical predictions at this flapping amplitude. While for the flapping frequencies examined *a posteriori* testing did not reveal any appreciable reduction in the beam natural frequencies, and hence no apparent inelastic effects, it is possible that some slight nonlinear elastic behavior is present at such large vibration amplitudes. In addition, improved (qualitative and quantitative) prediction may require consideration of friction damping in the actuation mechanism and/or more complete nonlinear forms of external damping, including a possible fully-coupled aeroelastic model.

4.7.3 Effect of Nonlinear Damping on Stability of Periodic Solutions and Strain Spectra

In order to show the effect of nonlinear damping on the stability of periodic response, moduli of the characteristic multipliers, $|\rho_1|$ and $|\rho_2|$, of the monodromy matrix are plotted against the dimensionless flapping frequency in Figures 4.6 and 4.7 for 15° and 30°, respectively. Data obtained only with the linear viscous damping model $f_{d,vis}$ are also included in both figures. It can be observed in the figures that the moduli of each pair of characteristic multipliers obtained with nonlinear damping models, $f_{d,vel}$ and $f_{d,disp}$, under both surrounding air pressures remain less than unity. Therefore one can conclude that, according to Floquet theory, the periodic flapping motion under the effect of the studied nonlinear damping models remain asymptotically sta-

ble. This is consistent with the experimental results reported in Chapter 3 where it was noted that all measured experimental trajectories were periodic. Moreover, Figure 4.6 shows that the periodic flapping motion under the effect of linear viscous damping at 15° appears to be stable until the frequency of $\omega_0 = 1.06$, beyond which the numerical solution diverges. This result is also consistent with the time-marching simulations carried out in Chapter 3 where it was determined that when linear viscous damping was used all solutions were periodic for $\omega_0 \leq 1.0$. In these simulations it was found that *quasi-periodic* trajectories occurred for the frequency interval $1.0 < \omega_0 \lessapprox 1.08$ and *irregular* trajectories occurred for $1.08 \lessapprox \omega_0 \lessapprox 1.12$. The response curve obtained with the time-marching nonlinear finite element solution is given in Figure 4.2 (labeled ATFEM).

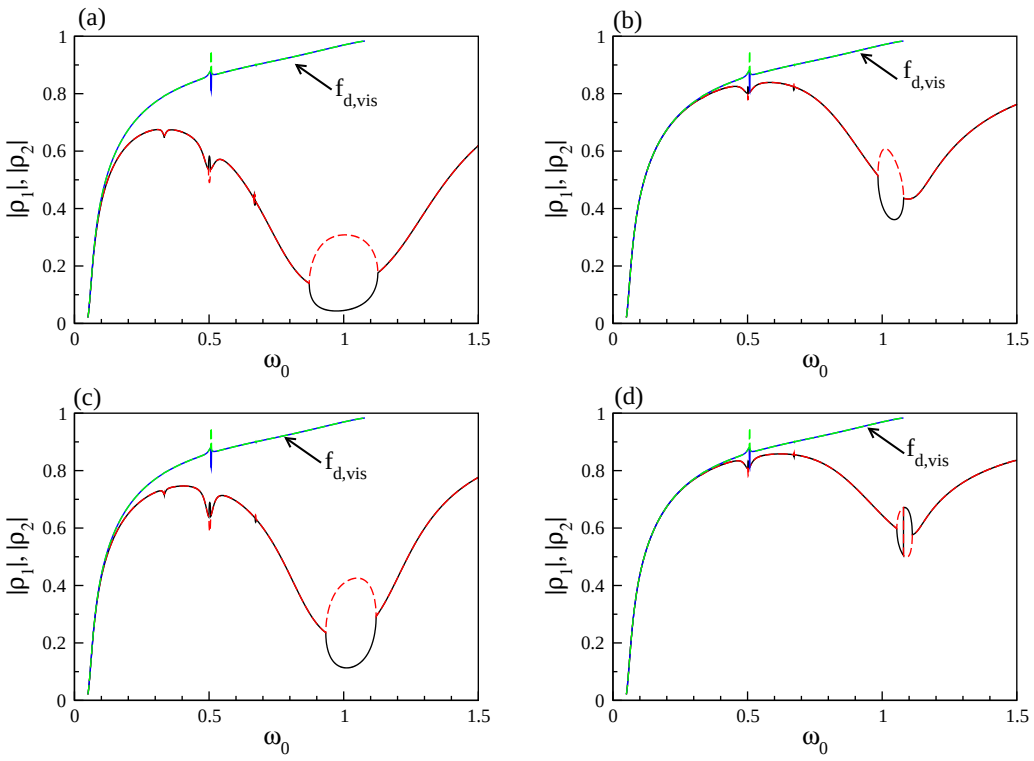

Figure 4.6: Change of characteristic multiplier moduli of the monodromy matrix as a function of dimensionless flapping frequency for 15° with: (a) velocity-3rd power damping model ($\bar{\eta}_{vel} = 0.30$) in air, (b) displacement-2nd power damping ($\bar{\eta}_{disp} = 3.61$) in air, (c) velocity-3rd power damping model ($\bar{\eta}_{vel} = 0.14$) in 70% vacuum, and (d) displacement-2nd power damping ($\bar{\eta}_{disp} = 1.87$) in 70% vacuum. The data curves only obtained with the viscous damping model ($\xi_{vis} = 0.013$) are also included in the subfigures.

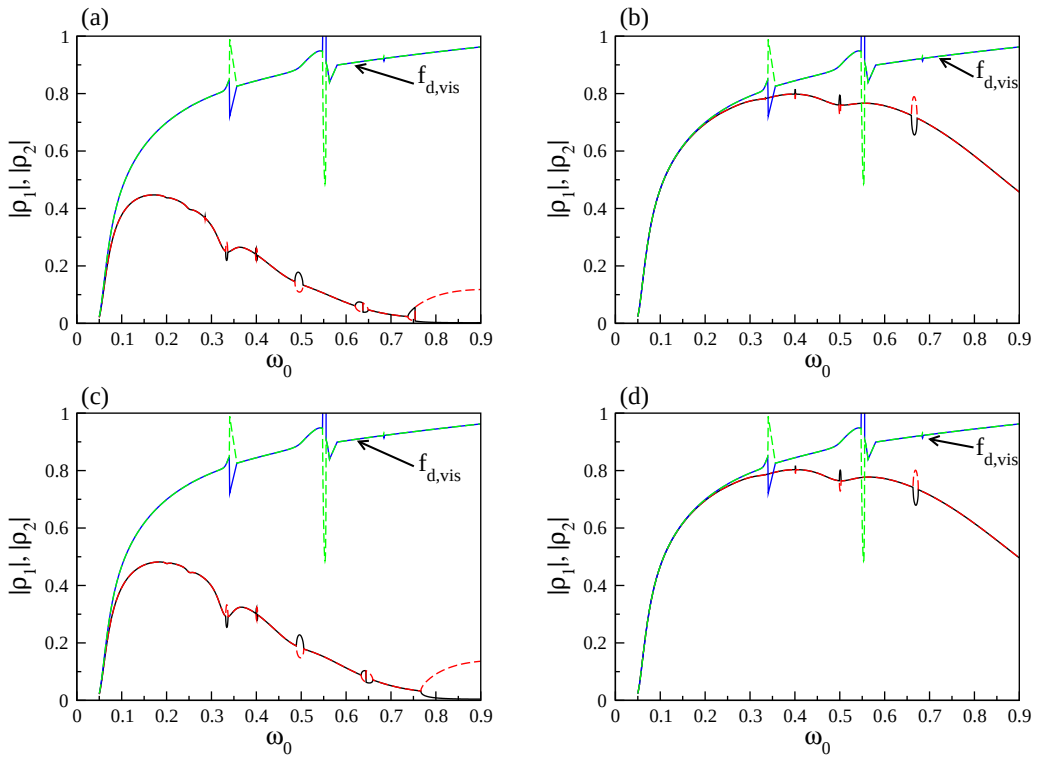

Figure 4.7: Change of characteristic multiplier moduli of the monodromy matrix as a function of dimensionless flapping frequency for 30° with: (a) velocity-3rd power damping model ($\bar{\eta}_{vel} = 0.46$) in air, (b) displacement-2nd power damping ($\bar{\eta}_{disp} = 4.02$) in air, (c) velocity-3rd power damping model ($\bar{\eta}_{vel} = 0.38$) in 70% vacuum, and (d) displacement-2nd power damping ($\bar{\eta}_{disp} = 3.61$) in 70% vacuum. The data curves only obtained with the viscous damping model ($\xi_{vis} = 0.013$) are also included in the subfigures.

As shown in Figure 4.7, for flapping at 30° the periodic solution obtained with the viscous damping model $f_{d,vis}$ loses stability at $\omega_0 = 0.55$ where the modulus of one of the characteristic multipliers becomes greater than unity. While not shown, the real and imaginary parts of the characteristic multipliers indicate that the periodic solution loses stability through one of the real parts leaving the unit circle at +1. The unstable periodic solutions exist over a small range of frequencies, beyond which the periodic solution regains stability. Also note in Figure 4.7 that at a frequency of $\omega_0 = 0.34$, the modulus of one of the characteristic multipliers associated with the periodic solution obtained with linear viscous damping approaches unity. This result is also consistent with the data presented in Chapter 3 which indicate that the flapping beam response becomes *irregular* at $\omega_0 \approx 0.52$ and *asymmetric-periodic* at $\omega_0 \approx 0.34$. The frequency response curve obtained at 30° with the time-marching nonlinear finite element solution, labeled ATFEM, is also plotted in Figure 4.4. Hence the time-spectral, 1-mode Galerkin results presented here, coupled with the Floquet analysis, both corroborate the previous results and provide some insight into the nature of the bifurcations which occur when a linear viscous damping model is assumed.

Finally, in order to ascertain how the various damping models effect the modal amplitude frequency spectra, in Figures 4.8 and 4.9 the amplitude of each harmonic (i.e., $\sqrt{(\hat{\mathbf{x}}^0)^2}$, and $\sqrt{(\hat{\mathbf{x}}^{2n-1})^2 + (\hat{\mathbf{x}}^{2n})^2}$ with $n = 1, \ldots, 100$) is plotted against the corresponding harmonic number for different damping models at four selected frequencies ω_0, which are representative of resonant and non-resonant frequencies, at 15° and 30°, respectively. From both of these figures it is obvious that the different damping models have a definite quantitative effect on the spectra, but the overall qualitative characteristics

of the various spectra are relatively unchanged with the different damping models.

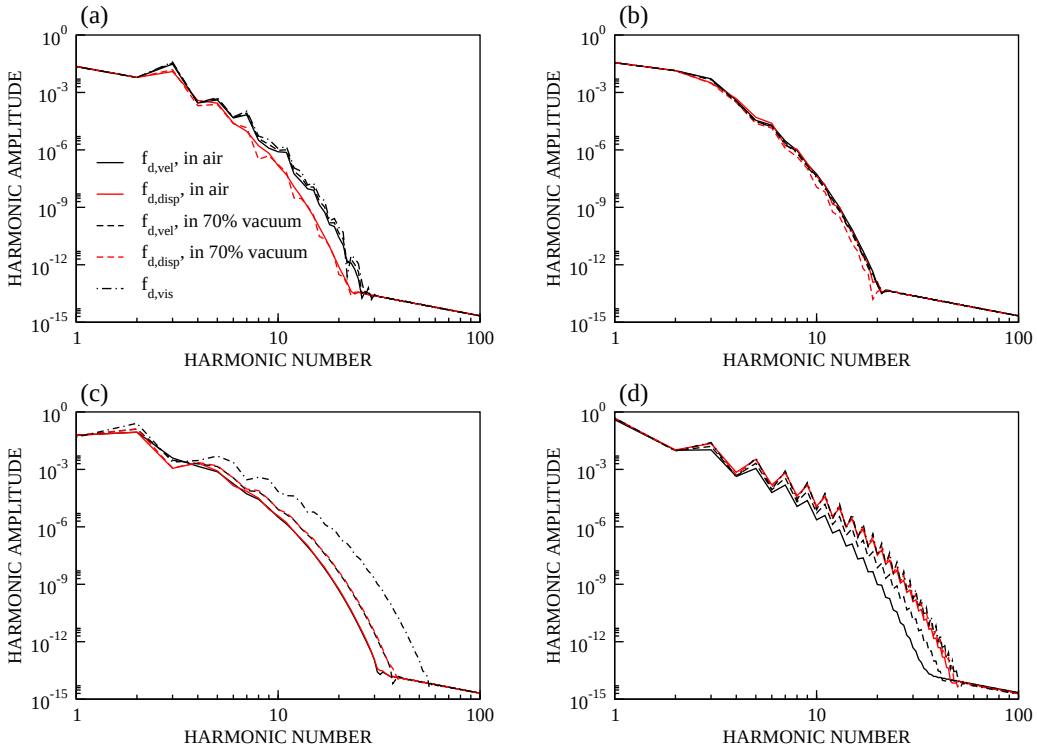

Figure 4.8: Response harmonic amplitudes versus harmonic number for different damping models and ambient pressures at 15°, at dimensionless flapping frequencies: (a) $\omega_0 = 0.33$, (b) $\omega_0 = 0.40$, (c) $\omega_0 = 0.50$, and (d) $\omega_0 = 0.90$.

4.8 Chapter Summary

In this chapter, the effect of linear and nonlinear damping mechanisms on the large amplitude structural dynamic response of slender aluminum cantilever beams set in flapping motion are studied both experimentally and through simulation. The experiments utilize a robust flapping mechanism (test-bed) which enables the appended beam to be tested at different flapping amplitudes and frequencies. The experiments (and simulations) are conducted at two

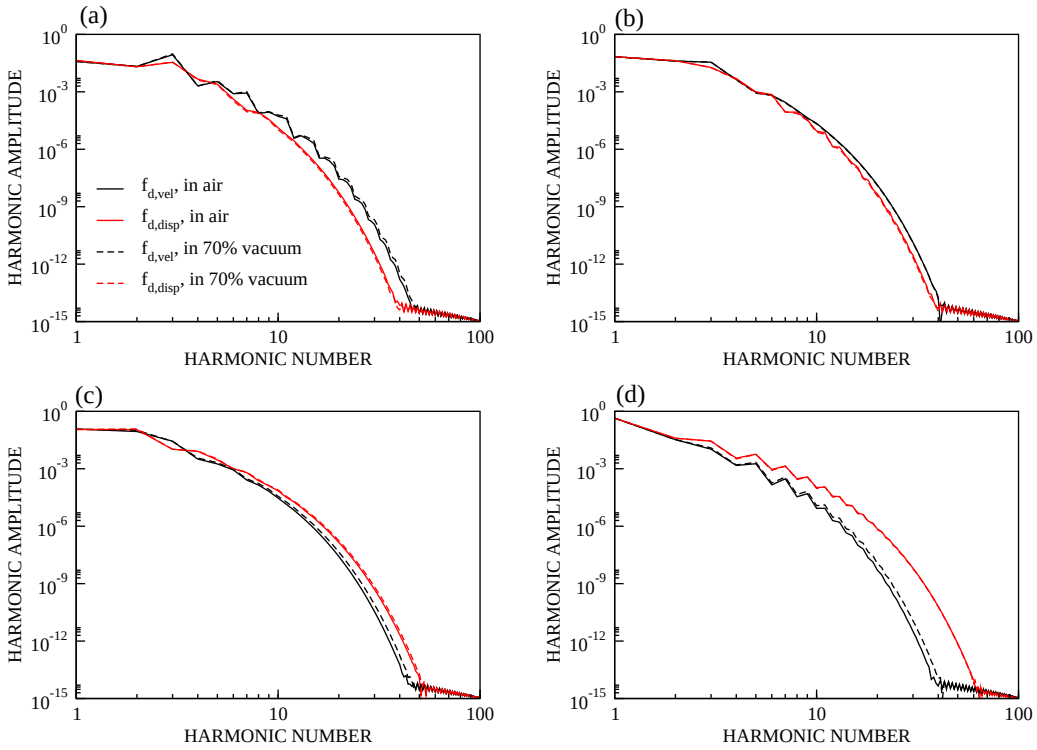

Figure 4.9: Response harmonic amplitudes versus harmonic number for different damping models and ambient pressures at 30°, at dimensionless flapping frequencies: (a) $\omega_0 = 0.33$, (b) $\omega_0 = 0.40$, (c) $\omega_0 = 0.50$, and (d) $\omega_0 = 0.80$.

flapping amplitudes 15° and 30°, in a range of flapping frequencies up to 1.3 times the first modal frequency in air. In order to separate the effects of air (external) damping from those of the material (internal) damping, the experiments are also performed under reduced pressure (70% vacuum). The simulation framework consists of a nonlinear, inextensible beam theory and various forms of linear and nonlinear damping models. Numerical solution of these model equations is obtained, in the spatial domain, through the use of a one-mode Galerkin method and, in the time domain, via a high-order Fourier pseudospectral scheme. In addition the simulation results were used, along with Floquet theory, to analyze the stability of periodic solutions and possible response bifurcation characteristics.

The linear damping model used in the simulation consisted of a simple viscous damping force, with a coefficient obtained via experiment, while the nonlinear damping models consisted of a internal (material) stress-dependent damping model and two nonlinear external models. These two nonlinear external damping models contained nonlinearities of the forms $\dot{v}^3$ and $v^2\dot{v}$, where v and $\dot{v}$ are the beam displacement and velocity, respectively. Both of the nonlinear external damping models were assumed to depend linearly on air density, beam width and an empirically determined constant. This constant was found through a least-squares error procedure based upon the experimental strain-frequency response curves and simulations with the assumed damping model form.

The results indicate that the nonlinear external damping models are able to better represent the damping forces acting on the flapping beam, when compared to the linear viscous and nonlinear internal mechanisms, for all testing conditions. In particular, for flapping at 15°, each of the nonlinear external damping models enabled simulation to accurately predict the strain-frequency response curves outside of the region in which the constant was determined. In the primary resonance region, the velocity-cubed damping model appeared to better predict the response. For flapping at 30° the broadening/merging of the secondary resonance region noted in the experiments was not accurately predicted in the simulation, perhaps indicating additional unmodeled physics such as nonlinear elasticity, friction damping in the mechanism and/or beam-mechanism dynamic interaction.

Changes in both ambient pressure and flapping amplitude resulted in variations in the nondimensional constants associated with the nonlinear external damping mechanisms. While these changes could be brought about through

unmodeled physics not related to damping, it is likely that this result is also partially due to incomplete parameter dependence and/or nonlinear forms. Finally, in addition to giving poor estimates of the damping forces operating at large amplitudes of flapping, the simulations which utilize a linear viscous damping model suggest that the periodic response loses stability at some frequencies. This result, while consistent with previous time-marched nonlinear finite element results, does not correspond with the experimental evidence which suggests that all trajectories are periodic for the flapping amplitudes and frequencies which are tested. This inconsistency in the simulation results is removed when either of the two nonlinear external damping models are used.

CHAPTER 5

Perturbation Analysis of the Nonlinear Response of Flapping Beams to Resonant Excitations

5.1 Scope of the Chapter

In this chapter,* the effect of excitation and damping parameters on the superharmonic and primary resonance responses of a slender cantilever beam undergoing flapping motion is analytically investigated. The problem is cast into mathematical form using a nonlinear inextensible beam model which is subjected to time-dependent boundary conditions and linear or nonlinear damping forces. The flapping excitation is assumed to be nonharmonic, composed of two sine waves with different amplitudes. We employ a combination of Galerkin and perturbation methods to arrive at the frequency-response relationships associated with the second- and third-order superharmonic and primary resonances. The resonance solutions of the spatially-discretized equation of motion, which involves both quadratic and cubic nonlinear terms (due to curvature, damping, and flapping excitation), are constructed in the form of first-order uniform asymptotic expansions via the method of multiple time scales. The effect of excitation and damping parameters on the steady-state resonance responses and their stability is described quantitatively with the aid of approximate analytical expressions. The critical excitation amplitudes leading to bistable solutions are identified. For the second-order superharmonic

*The material presented in this chapter has been submitted (February 2015) for publication in *Acta Mechanica*.

resonance, the critical excitation amplitude is determined to be dependent on the first harmonic amplitude in the case of nonlinear damping. The third-order superharmonic resonance is determined to be independent of the second harmonic excitation amplitude regardless of the damping types considered. The perturbation solutions are compared with numerical time-spectral solutions for different flapping amplitudes. The first-order perturbation solution is determined to be in very good agreement with the numerical solution up to 5° while above this amplitude differences in the two solutions develop, which are attributed to phase estimation accuracy.

In Section 5.2, the spatial solution of the governing equation and the resulting unimodal equation are presented in brief. The assumptions made on the flapping actuation and its implementation into the mathematical model are also given. In Section 5.3 first order approximate solutions of the problem in the case of superharmonic and primary resonances are determined using the method of multiple time scales. Section 5.4 is devoted to pertinent results, frequency-response curve analyses, and comparison of the results with the time-spectral numerical solutions. Finally, conclusions are given in Section 5.5.

5.2 Problem Formulation

In this section we will present the formulation of the governing modal equation which is to be solved, in the next section, by the method of multiple time scales. Here, we will also provide the details of how flapping actuation is considered in the mathematical model. We note that the contents of subsections §§ 5.2.1 and 5.2.2 are inherited from Chapter 4 and given here to allow for the chapter

to be self-contained.

5.2.1 Governing Equations

In this study, we consider a nonlinear slender beam model which assumes that the beam centerline is *inextensible* and takes into account large curvature and axial inertia effects. The model is based upon the derivation proposed by Semler *et al.* [114] and has been used before in various applications [135, 136]. The beam motion is considered to be planar and shear deformation and rotary inertia effects of the beam cross section are neglected. Denoting the transverse displacement by $v(s,t)$, the curvilinear coordinate measured along the centerline by s, and a general dissipative force density (i.e., force per unit length along the beam) by f_d, one obtains the equation of motion as:

$$\begin{aligned}
&\rho A_c \ddot{v} + f_d(v,\dot{v}) + EI\left[v''''(1+v'^2) + 4v'v''v''' + v''^3\right] - \\
&v''\left[\int_s^L \int_0^s \rho A_c(\dot{v}'^2 + v'\ddot{v}')\,\mathrm{d}s\,\mathrm{d}s\right] + \\
&v'\int_0^s \rho A_c(\dot{v}'^2 + v'\ddot{v}')\,\mathrm{d}s = 0,
\end{aligned} \tag{5.2.1}$$

where ρ, A_c, EI, and L are mass density, cross sectional area, flexural rigidity, and length of the beam, respectively, and a prime and a superimposed dot denotes differentiation with respect to s and t, respectively; i.e., $\dot{(\ )} \equiv \partial(\ )/\partial t$, $(\ )' \equiv \partial(\ )/\partial s$. In Eq. (5.2.1), terms in the brackets multiplied by EI represent linear and nonlinear flexural restoring forces, whereas the integral terms represent nonlinear inertia forces produced through the expression of the axial inertia using the inextensibility assumption. We note that damping forces acting in the in-plane direction are neglected in this work.

The flexible beam is set into flapping motion via its clamped end which

is secured to an undulating rigid pendulum of length d. The time-dependent boundary conditions can be stated as:

$$v = d\sin(\theta_f), \qquad v' = \theta_f \qquad at \quad s = 0, \tag{5.2.2a}$$

$$v'' = 0, \qquad v''' = 0 \qquad at \quad s = L, \tag{5.2.2b}$$

where d and θ_f are rigid pendulum length and flapping angle, respectively. Equations (5.2.2a) imply that the transverse displacement and rotation of the beam's clamped-end are equal to the transverse displacement of the clamping point of the rigid pendulum and flapping angle, respectively. The flapping angle θ_f is a time-dependent function which is defined by the kinematics of flapping mechanism.

5.2.2 Transformation and Spatial Discretization of Governing Equations

The approximate solution of the distributed-parameter system, Eqs. (5.2.1) and (5.2.2), is obtained by reducing it to a discrete one through spatial discretization based on the Galerkin method. To this end, we assume a two-part solution of the following form [41, 115, 116]:

$$v(s,t) = \zeta(s,t) + g(s,t), \tag{5.2.3}$$

where the shifting function $g(s,t)$ is determined so as to render the boundary conditions for the variable $\zeta(s,t)$ homogeneous:

$$g(s,t) = d\sin(\theta_f) + s\theta_f. \tag{5.2.4}$$

After Eqs. (5.2.3) and (5.2.4) are inserted into Eqs. (5.2.1) and (5.2.2), we obtain the transformed boundary-value problem which is composed of a nonhomogeneous partial differential equation in the dependent variable $\zeta(s,t)$ and homogeneous boundary conditions. Noting that $g'' = g''' = g'''' = 0$, the transformed governing equations become:

$$\begin{aligned}
&\rho A_c(\ddot{\zeta} + \ddot{g}) + f_d(\zeta, \dot{\zeta}, g, \dot{g}) + \\
&EI\Big[\zeta'''' + \zeta''''\zeta'^2 + 2\zeta''''\zeta' g' + \zeta''''g'^2 + 4\zeta'\zeta''\zeta''' + 4g'\zeta''\zeta''' + \zeta''^3\Big] - \\
&\zeta'' \int_s^L \int_0^s \rho A_c\big[\dot{\zeta}'^2 + 2\dot{\zeta}'\dot{g}' + \dot{g}'^2 + \zeta'\ddot{\zeta}' + \zeta'\ddot{g}' + g'\ddot{\zeta}' + g'\ddot{g}'\big]\,\mathrm{d}s\,\mathrm{d}s + \\
&(\zeta' + g') \int_0^s \rho A_c\big[\dot{\zeta}'^2 + 2\dot{\zeta}'\dot{g}' + \dot{g}'^2 + \zeta'\ddot{\zeta}' + \zeta'\ddot{g}' + g'\ddot{\zeta}' + g'\ddot{g}'\big]\,\mathrm{d}s = 0, \qquad (5.2.5)
\end{aligned}$$

and

$$\zeta(0,t) = \zeta'(0,t) = \zeta''(L,t) = \zeta'''(L,t) = 0. \qquad (5.2.6)$$

According to the Galerkin procedure, the solution of Eqs. (5.2.5) and (5.2.6) is assumed to be:

$$\zeta(s,t) \cong \sum_{i=1}^{n} a_i(t)\phi_i(s), \qquad (5.2.7)$$

where $a_i(t)$ are the generalized coordinates to be determined, $\phi_i(s)$ are the trial functions which are taken as the transverse natural eigenmodes of a cantilevered beam, and n is the total number of modes considered in the approximation. Multiplying Eq. (5.2.5) by $\phi_j(s)$, considering a 1-mode approximation (i.e., $n = 1$), invoking orthonormality of eigenmodes (i.e., $\int_0^L \phi_i\phi_j ds = \delta_{ij}$, where δ_{ij} is the Kronecker delta), choosing L and $\left(\frac{EI}{\rho A_c L}\right)^{-1/2}$ as the characteristic length and time scales, respectively, and making the variables dimen-

sionless:

$$a = \bar{a}L, \quad s = \bar{s}L, \quad d = \bar{d}L, \quad \bar{g} = g(\bar{s}, \bar{d}, \bar{\omega}_f, \bar{t}),$$
$$t = \bar{t}\Big(\frac{EI}{\rho A_c L^4}\Big)^{-1/2}, \quad \omega_f = \bar{\omega}_f\Big(\frac{EI}{\rho A_c L^4}\Big)^{1/2}, \tag{5.2.8}$$

we arrive at a 1-mode modal equation in terms of the normal coordinate $\bar{a}(\bar{t})$ (subscript on a suppressed).

In Eq. (5.2.8), a variable with an overbar represents the corresponding nondimensional variable and ω_f denotes the flapping frequency in radians per second. Note also that, from this point onward, primes and superposed dots operating on nondimensional variables will be used to represent partial differentiation with respect to nondimensional coordinate $\bar{s}$ and nondimensional time $\bar{t}$, respectively; i.e., $\dot{(\bar{\ })} \equiv \partial(\bar{\ })/\partial\bar{t}$, $(\bar{\ })' \equiv \partial(\bar{\ })/\partial\bar{s}$. Finally, dividing through the modal equation by EI/L^2 and rearranging, one obtains:

$$\ddot{\bar{a}}\big[M_1 + M_2(\bar{t}) + M_3(\bar{t})\bar{a} + M_4\bar{a}^2\big] + \bar{f}_d + A_1(\bar{t})\bar{a} + 2A_2(\bar{t})\bar{a}^2 + A_3\bar{a}^3 +$$
$$B_1(\bar{t})\bar{a} + 2B_2(\bar{t})\dot{\bar{a}} + 2B_3(\bar{t})\bar{a}\dot{\bar{a}} + B_4(\bar{t})\bar{a}^2 + B_5(\bar{t})\dot{\bar{a}}^2 + B_6\bar{a}\dot{\bar{a}}^2 + C(\bar{t}) = 0, \tag{5.2.9}$$

where M_i, A_i, B_i and C are comprised of spatial integrals which are given in Appendix E, and $\bar{f}_d$ is the modal damping force.

In the present work, we consider two different damping models: linear viscous damping $\bar{f}_{d,l}$ and nonlinear velocity-3rd power damping $\bar{f}_{d,nl}$. The latter is obtained by adding a cubic velocity term to the linear viscous damping model. Accordingly, the modal damping forces can be expressed as:

$$\bar{f}_{d,l} = 2\zeta_{vis}\bar{\omega}_N(I_1\dot{\bar{a}} + I_{31}), \tag{5.2.10}$$

$$\bar{f}_{d,nl} = 2\zeta_{vis}\bar{\omega}_N(I_1\dot{\bar{a}} + I_{31}) + \bar{\eta}_{vel}(\dot{\bar{a}}^3 I_{32} + 3\dot{\bar{a}}^2 I_{33} + 3\dot{\bar{a}} I_{34} + I_{35}), \qquad (5.2.11)$$

where ζ_{vis} is the viscous damping ratio, $\bar{\eta}_{vel}$ a dimensionless nonlinear damping coefficient, $\bar{\omega}_N$ is the dimensionless first mode bending (natural) frequency of the beam, and I_1, I_{31} - I_{35} are given in Appendix E.

5.2.3 Flapping Actuation

The flapping angle $\theta_f(t)$ is dependent upon the flapping frequency and amplitude while its actual functional form is dictated by the kinematics of the actuation mechanism. In the case of a 4-bar crank-and-rocker based actuation, which is the case considered in Chapters 3 and 4, the actual functional form of $\theta_f(t)$ is so complex that using it in a perturbation analysis without simplification is not feasible. Therefore, a compromise between retaining both generality and simplicity in flapping actuation can be achieved by assuming $\theta_f(t)$ as a nonharmonic periodic function composed of two sine waves. To this end, we approximate $\theta_f(t)$ as:

$$\theta_f(t) = \beta_1 \sin(\omega_f t) + \beta_2 \sin(2\omega_f t). \qquad (5.2.12)$$

Assuming that $\sin\theta_f \approx \theta_f$ and using Eq. (5.2.12), Eq. (5.2.4) can be rewritten as:

$$g(s,t) = (d+s)\left[\beta_1 \sin(\omega_f t) + \beta_2 \sin(2\omega_f t)\right]. \qquad (5.2.13)$$

Inserting Eq. (5.2.13) into the relevant integrals given in Appendix E and nondimensionalizing, one can rewrite the integrals $I1 - I39$ as listed in Appendix H. Using the integral definitions given in Appendix H and such well-known trigonometric identities as $\cos^4\theta = \frac{1}{8}[\cos(4\theta) + 4\cos(2\theta) + 3]$, and omit-

ting, for convenience, the overbar notation for the remainder of this chapter, one can rewrite the modal equation (5.2.9) as:

$$f_i + f_d + f_b + f_s + f_t = 0, \tag{5.2.14}$$

where f_i, f_b, f_s, f_t, and f_d are given in Appendix I. Note that depending on type of the damping model considered, the modal damping force f_d shall be either $f_{d,l}$ or $f_{d,nl}$ where subscripts "l" and "nl" denote linear and nonlinear, respectively.

5.3 Multiple Time Scales Solution

In this section, the steady-state response of system (5.2.14) to resonant excitations when $\omega_f \approx \frac{1}{2}\omega_N$, $\omega_f \approx \frac{1}{3}\omega_N$, and $\omega_f \approx \omega_N$ is investigated by using the method of multiple scales. In the method of multiple scales, a type of perturbation method, one obtains an approximate analytical solution in the form of a uniformly-valid asymptotic series (expansion) in a parameter [137–140]. The method will lead to a set of first-order nonlinear ordinary differential equations which govern the evolution of the amplitude and phase of the superharmonic or harmonic response (modulated response associated with the resonance) under investigation. It should be noted that much of the mathematical manipulations in this section (and the next) was accomplished with the aid of the symbolic computing software Mathematica (Wolfram Research, Champaign, IL).

Toward this end we introduce a "bookkeeping" parameter ϵ, which is solely a mathematical artifice to group (order) terms of comparable degrees of ap-

proximation in a systematic and convenient fashion [141], and let:

$$a = \epsilon x, \tag{5.3.1}$$

in Eq. (5.2.14) and seek a second-order uniform approximate solution in the form:

$$x(t;\epsilon) = x_0(T_0, T_2) + \epsilon^2 x_2(T_0, T_2) + \ldots. \tag{5.3.2}$$

In Eq. (5.3.2), T_0 is a "fast" time scale which allows one to trace rapid evolutions occurring at frequencies ω_N and ω_f, while T_2 is a "slow" time scale which enables one to follow slow variations associated with the modulations in the amplitude and phase caused by the nonlinearity, damping, and resonances. The time scales are defined as:

$$T_0 = t, \quad T_2 = \epsilon^2 t. \tag{5.3.3}$$

Using the chain rule, one can transform time derivatives as:

$$\begin{aligned}
\frac{\mathrm{d}(\ )}{\mathrm{d}t} &= \frac{\partial(\ )}{\partial T_0} + \epsilon^2 \frac{\partial(\ )}{\partial T_2} = D_0(\ ) + \epsilon^2 D_2(\ ), \\
\frac{\mathrm{d}^2(\ )}{\mathrm{d}t^2} &= \frac{\partial^2(\ )}{\partial T_0^2} + 2\epsilon^2 \frac{\partial^2(\ )}{\partial T_0 \partial T_2} + \epsilon^4 \frac{\partial^2(\ )}{\partial T_2^2} = D_0^2(\ ) + 2\epsilon^2 D_0 D_2(\ ) + \epsilon^4 D_2^2(\ ).
\end{aligned} \tag{5.3.4}$$

Eqs. (5.3.1)-(5.3.4) can be used to express a, $\dot{a}$, and $\ddot{a}$ as:

$$\begin{aligned}
a =& \epsilon x_0 + \epsilon^3 x_2 + \mathcal{O}(\epsilon^5), \\
\dot{a} =& \epsilon D_0 x_0 + \epsilon^3 D_0 x_2 + \epsilon^3 D_2 x_0 + \mathcal{O}(\epsilon^5), \\
\ddot{a} =& \epsilon D_0^2 x_0 + \epsilon^3 D_0^2 x_2 + 2\epsilon^3 D_0 D_2 x_0 + \mathcal{O}(\epsilon^5).
\end{aligned} \tag{5.3.5}$$

5.3.1 The Case of $\omega_f \approx \frac{1}{2}\omega_N$

In this section, we analyze the response of system (5.2.14) when the flapping frequency ω_f is in the neighborhood of $\frac{1}{2}\omega_N$ (i.e., second-order superharmonic resonance). The damping force acting on the beam is assumed to be nonlinear in the form given by Eq. (5.2.11). Analysis of the case with linear viscous damping (i.e., with Eq. (5.2.10)) can be carried out in a manner similar to what is presented herein by setting $\bar{\eta}_{vel} = 0$. We employ the following ordering scheme for the boundary excitation and damping:

$$\beta_1 = \epsilon b_1, \quad \beta_2 = \epsilon^3 b_2, \tag{5.3.6}$$

$$\zeta_{vis} = \epsilon^2 \hat{\zeta}_{vis}, \tag{5.3.7}$$

and,

$$\bar{\eta}_{vel} = \epsilon^0 \hat{\eta}_{vel}. \tag{5.3.8}$$

Substituting Eqs. (5.3.5) and (5.3.6)-(5.3.8) into Eq. (5.2.14) (with $f_d = f_{d,nl}$ via Eq. (I.6)), dividing through the resulting equation by ϵ, equating the coefficients of ϵ^0 and ϵ^2 on both sides, and noting that $K_{I1} = 1$ and $K_{I8} = \omega_N^2$, we obtain:

$$D_0^2 x_0 + \omega_N^2 x_0 = -b_1 K_{I28} \omega_f^2 \sin(\omega_f t), \tag{5.3.9}$$

and,

$$
\begin{aligned}
&D_0^2 x_2 + \omega_N^2 x_2 = \\
&-\big[2b_1 K1_{I31}\hat{\zeta}_{vis}\omega_f\omega_N\cos(\omega_f t) + \tfrac{1}{4}b_1^3\omega_f^2\sin(\omega_f t)(K_{I29}+3K_{I30}) + \\
&4b_2 K_{I28}\omega_f^2\sin(2\omega_f t) + \tfrac{1}{4}b_1^3\omega_f^2\sin(3\omega_f t)(K_{I29}-K_{I30}) + \\
&\tfrac{3}{4}b_1^3 K_{I35}\hat{\eta}_{vel}\omega_f^3\cos(\omega_f t) + \tfrac{1}{4}b_1^3 K_{I35}\hat{\eta}_{vel}\omega_f^3\cos(3\omega_f t) + \\
&x_0 b_1^2\big(-\tfrac{1}{2}\omega_f^2\cos(2\omega_f t)(K_{I15}+2K_{I16}-K_{I17}+K_{I18}+K_{I19}) + \\
&\tfrac{1}{2}\omega_f^2(-K_{I15}+2K_{I16}+K_{I17}+K_{I18}+K_{I19}) + \tfrac{1}{2}K_{I9}(1-\cos(2\omega_f t))\big) + \\
&x_0^2 b_1\big(\sin(\omega_f t)(2K_{I10}+4K_{I11}) + \omega_f^2\sin(\omega_f t)(K_{I24}-K_{I23})\big) + \\
&D_0 x_0\big(2\hat{\zeta}_{vis}\omega_N + b_1^2 K_{I20}\omega_f\sin(2\omega_f t) + \tfrac{3}{2}b_1^2 K_{I34}\hat{\eta}_{vel}\omega_f^2(1+\cos(2\omega_f t))\big) + \\
&x_0^3\big(K_{I12}+4K_{I13}+K_{I14}\big) + x_0 D_0 x_0\big(2b_1\omega_f\cos(\omega_f t)(K1_{I22}-K1_{I21})\big) + \\
&(D_0 x_0)^2\big(b_1 K_{I27}\sin(\omega_f t) + 3b_1 K1_{I33}\hat{\eta}_{vel}\omega_f\cos(\omega_f t)\big) + (D_0 x_0)^3\big(K_{I32}\hat{\eta}_{vel}\big) + \\
&x_0(D_0 x_0)^2\big(K_{I26}-K_{I25}\big) + 2D_0 D_2 x_0 + D_0^2 x_0\big(\tfrac{1}{2}b_1^2 K_{I7}(1-\cos(2\omega_f t))\big) + \\
&x_0 D_0^2 x_0\big(b_1\sin(\omega_f t)(-K_{I3}+K_{I5}+K_{I6})\big) + x_0^2 D_0^2 x_0\big(K_{I4}-K_{I2}\big)\big].
\end{aligned}
\tag{5.3.10}
$$

The homogeneous and particular solutions of Eq. (5.3.9) can be expressed as:

$$
x_{0h} = \alpha(T_2)\sin(\omega_N T_0 + \phi(T_2)) = A(T_2)\mathrm{e}^{\mathrm{i}\omega_N T_0} + \bar{A}(T_2)\mathrm{e}^{-\mathrm{i}\omega_N T_0}, \tag{5.3.11}
$$

and,

$$
x_{0p} = \frac{b_1 K_{I28}\omega_f^2}{\omega_f^2-\omega_N^2}\sin(\omega_f T_0) = \Lambda\mathrm{e}^{\mathrm{i}\omega_f T_0} + \bar{\Lambda}\mathrm{e}^{-\mathrm{i}\omega_f T_0}, \tag{5.3.12}
$$

respectively, where,

$$A(T_2) = \alpha(T_2)\frac{1}{2\mathrm{i}}\mathrm{e}^{\mathrm{i}\phi(T_2)}, \tag{5.3.13}$$

and,

$$\Lambda = \frac{1}{2\mathrm{i}}\frac{b_1 K_{I28}\omega_f^2}{\omega_f^2 - \omega_N^2} = \frac{1}{2\mathrm{i}}\Lambda_1, \tag{5.3.14}$$

with,

$$\Lambda_1 = \frac{b_1 K_{I28}\omega_f^2}{\omega_f^2 - \omega_N^2}. \tag{5.3.15}$$

In Eqs. (5.3.11) and (5.3.12), $\bar{A}$ and $\bar{\Lambda}$ denote complex conjugate of A and Λ, respectively. Combining homogeneous and particular solutions, Eqs. (5.3.11) and (5.3.12), the general solution of Eq. (5.3.9) can be stated as:

$$x_0 = A(T_2)\mathrm{e}^{\mathrm{i}\omega_N T_0} + \bar{A}(T_2)\mathrm{e}^{-\mathrm{i}\omega_N T_0} + \Lambda\mathrm{e}^{\mathrm{i}\omega_f T_0} + \bar{\Lambda}\mathrm{e}^{-\mathrm{i}\omega_f T_0} \tag{5.3.16}$$

Inserting Eq. (5.3.16) into (5.3.10), replacing the trigonometric expressions with their complex exponential counterparts, and collecting the terms, we get the following expression:

$$\begin{aligned} D_0^2 x_2 + \omega_N^2 x_2 =& \mathrm{e}^{\mathrm{i}\omega_N T_0}\{\ldots\} + \mathrm{e}^{-\mathrm{i}\omega_N T_0}\{\ldots\} + \\ & \mathrm{e}^{\mathrm{i}\omega_f T_0}\{\ldots + \mathrm{e}^{\mathrm{i}2\omega_N T_0}(\ldots) + \mathrm{e}^{-\mathrm{i}2\omega_N T_0}(\ldots)\} + \\ & \mathrm{e}^{-\mathrm{i}\omega_f T_0}\{\ldots + \mathrm{e}^{-\mathrm{i}2\omega_N T_0}(\ldots) + \mathrm{e}^{\mathrm{i}2\omega_N T_0}(\ldots)\} + \\ & \mathrm{e}^{\mathrm{i}2\omega_f T_0}\{2\mathrm{i}b_2 K_{I28}\omega_f^2 + \mathrm{e}^{\mathrm{i}\omega_N T_0}(\ldots) + \mathrm{e}^{-\mathrm{i}\omega_N T_0}(\ldots)\} + \\ & \mathrm{e}^{-\mathrm{i}2\omega_f T_0}\{-2\mathrm{i}b_2 K_{I28}\omega_f^2 + \mathrm{e}^{-\mathrm{i}\omega_N T_0}(\ldots) + \mathrm{e}^{\mathrm{i}\omega_N T_0}(\ldots)\} + \\ & \mathrm{e}^{\mathrm{i}3\omega_f T_0}\{\ldots\} + \mathrm{e}^{-\mathrm{i}3\omega_f T_0}\{\ldots\} + \mathrm{e}^{\mathrm{i}3\omega_N T_0}\{\ldots\} + \mathrm{e}^{-\mathrm{i}3\omega_N T_0}\{\ldots\}. \end{aligned} \tag{5.3.17}$$

In Eq. (5.3.17), in addition to the terms proportional to $\mathrm{e}^{\pm \mathrm{i}\omega_N T_0}$, the terms proportional to $\mathrm{e}^{\pm \mathrm{i}2\omega_f T_0}$ produce secular terms in x_2 when $2\omega_f \approx \omega_N$. We only consider one of the complex conjugates of these secular terms and express Eq. (5.3.17) as:

$$
\begin{aligned}
&D_0^2 x_2 + \omega_N^2 x_2 = \\
&\mathrm{e}^{\mathrm{i}\omega_N T_0}\Big\{\tfrac{1}{2}\Big[-A\Big(4\Lambda\bar{\Lambda}\big(\omega_f^2(2K_{I2} - K_{I25} + K_{I26} - 2K_{I4} + 3\mathrm{i}K_{I32}\hat{\eta}_{vel}\omega_N) + \\
&3(K_{I12} + 4K_{I13} + K_{I14})\big) + 4\omega_N^2(\mathrm{i}\hat{\zeta}_{vis} + \Lambda\bar{\Lambda}(K_{I2} - K_{I4})) + b_1^2\big(K_{I9} + \\
&\omega_f^2(-K_{I15} + 2K_{I16} + K_{I17} + K_{I18} + K_{I19} + 3\mathrm{i}K_{I34}\hat{\eta}_{vel}\omega_N) - \omega_N^2 K_{I7}\big) - \\
&\mathrm{i}b_1\big[(\Lambda - \bar{\Lambda})\big(-4(K_{I10} + 2K_{I11}) - 6\mathrm{i}K1_{I33}\hat{\eta}_{vel}\omega_f^2\omega_N + \\
&\omega_f^2(2K1_{I21} - 2K1_{I22} + 2K_{I23} - 2K_{I24} - K_{I3} + K_{I5} + K_{I6})\big) + \\
&2\omega_f\omega_N(\Lambda + \bar{\Lambda})(K1_{I21} - K1_{I22} + K_{I27}) - \omega_N^2(\Lambda - \bar{\Lambda})(K_{I3} - K_{I5} - K_{I6})\big]\Big) - \\
&2A^2\bar{A}\big(3(K_{I12} + 4K_{I13} + K_{I14}) + \omega_N^2(3K_{I2} - K_{I25} + K_{I26} - 3K_{I4}) + \\
&3\mathrm{i}K_{I32}\hat{\eta}_{vel}\omega_N^3\big) - 4\mathrm{i}\omega_N A'\Big]\Big\} + \mathrm{e}^{\mathrm{i}2\omega_f T_0}\{2\mathrm{i}b_2 K_{I28}\omega_f^2\} + \text{c.c.} + \text{N.S.T.},
\end{aligned}
\tag{5.3.18}
$$

where, c.c. stands for the complex conjugate of the preceding terms and N.S.T. represents the terms that do not produce secular terms.

We can express the nearness of ω_f to $\frac{1}{2}\omega_N$ by introducing a detuning parameter σ as follows:

$$
2\omega_f = \omega_N + \epsilon^2\sigma. \tag{5.3.19}
$$

At this point, one can write $2\omega_f T_0$ with the aid of Eq. (5.3.19) as:

$$
2\omega_f T_0 = (\omega_N + \epsilon^2\sigma)T_0 = \omega_N T_0 + \epsilon^2 T_0\sigma = \omega_N T_0 + \sigma T_2. \tag{5.3.20}
$$

Using Eq. (5.3.20), we can show $\mathrm{e}^{\mathrm{i}2\omega_f T_0} = \mathrm{e}^{\mathrm{i}\omega_N T_0}\mathrm{e}^{\mathrm{i}\sigma T_2}$ and eliminate the secular terms from Eq. (5.3.18) if the following equation is satisfied:

$$\begin{aligned}
&\tfrac{1}{2}\Big[-A\Big(4\Lambda\bar{\Lambda}\big(\omega_f^2(2K_{I2} - K_{I25} + K_{I26} - 2K_{I4} + 3\mathrm{i}K_{I32}\hat{\eta}_{vel}\omega_N)+ \\
&3(K_{I12} + 4K_{I13} + K_{I14})\big) + 4\omega_N^2(\mathrm{i}\hat{\zeta}_{vis} + \Lambda\bar{\Lambda}(K_{I2} - K_{I4})) + b_1^2\big(K_{I9}+ \\
&\omega_f^2(-K_{I15} + 2K_{I16} + K_{I17} + K_{I18} + K_{I19} + 3\mathrm{i}K_{I34}\hat{\eta}_{vel}\omega_N) - \omega_N^2 K_{I7}\big)- \\
&\mathrm{i}b_1\big[(\Lambda - \bar{\Lambda})\big(-4(K_{I10} + 2K_{I11}) - 6\mathrm{i}K1_{I33}\hat{\eta}_{vel}\omega_f^2\omega_N+ \\
&\omega_f^2(2K1_{I21} - 2K1_{I22} + 2K_{I23} - 2K_{I24} - K_{I3} + K_{I5} + K_{I6})\big)+ \\
&2\omega_f\omega_N(\Lambda + \bar{\Lambda})(K1_{I21} - K1_{I22} + K_{I27}) - \omega_N^2(\Lambda - \bar{\Lambda})(K_{I3} - K_{I5} - K_{I6})\big]\Big)- \\
&2A^2\bar{A}\big(3(K_{I12} + 4K_{I13} + K_{I14}) + \omega_N^2(3K_{I2} - K_{I25} + K_{I26} - 3K_{I4})+ \\
&3\mathrm{i}K_{I32}\hat{\eta}_{vel}\omega_N^3\big) - 4\mathrm{i}\omega_N A'\Big] + \mathrm{e}^{\mathrm{i}\sigma T_2}(2\mathrm{i}b_2 K_{I28}\omega_f^2) = 0.
\end{aligned} \tag{5.3.21}$$

Substituting for A and Λ from Eqs. (5.3.13) and (5.3.14) into solvability condition, Eq. (5.3.21), multiplying through the resulting equation by $\mathrm{i}\mathrm{e}^{-\mathrm{i}\phi}$, noticing that $\mathrm{e}^{\mathrm{i}(\sigma T_2 - \phi)} = \cos(\sigma T_2 - \phi) + \mathrm{i}\sin(\sigma T_2 - \phi)$, separating real and imaginary parts, and rearranging yields:

$$
\begin{aligned}
&\alpha\phi' = \\
&\tfrac{1}{\omega_N}\{2b_2K_{I28}\omega_f^2\cos(\sigma T_2-\phi)+ \\
&\tfrac{1}{4}b_1^2K_{I9}\alpha + b_1K_{I10}\Lambda_1\alpha + 2b_1K_{I11}\Lambda_1\alpha+ \\
&\tfrac{3}{4}K_{I12}\Lambda_1^2\alpha + 3K_{I13}\Lambda_1^2\alpha + \tfrac{3}{4}K_{I14}\Lambda_1^2\alpha - \tfrac{1}{4}b_1^2K_{I15}\omega_f^2\alpha+ \\
&\tfrac{1}{2}b_1^2K_{I16}\omega_f^2\alpha + \tfrac{1}{4}b_1^2K_{I17}\omega_f^2\alpha + \tfrac{1}{4}b_1^2K_{I18}\omega_f^2\alpha + \tfrac{1}{4}b_1^2K_{I19}\omega_f^2\alpha- \\
&\tfrac{1}{2}b_1K1_{I21}\Lambda_1\omega_f^2\alpha + \tfrac{1}{2}b_1K1_{I22}\Lambda_1\omega_f^2\alpha - \tfrac{1}{2}b_1K_{I23}\Lambda_1\omega_f^2\alpha+ \\
&\tfrac{1}{2}b_1K_{I24}\Lambda_1\omega_f^2\alpha + \tfrac{1}{4}b_1K_{I3}\Lambda_1\omega_f^2\alpha - \tfrac{1}{4}b_1K_{I5}\Lambda_1\omega_f^2\alpha - \tfrac{1}{4}b_1K_{I6}\Lambda_1\omega_f^2\alpha+ \\
&\tfrac{1}{2}K_{I2}\Lambda_1^2\omega_f^2\alpha - \tfrac{1}{4}K_{I25}\Lambda_1^2\omega_f^2\alpha + \tfrac{1}{4}K_{I26}\Lambda_1^2\omega_f^2\alpha - \tfrac{1}{2}K_{I4}\Lambda_1^2\omega_f^2\alpha + \tfrac{3}{8}K_{I12}\alpha^3+ \\
&\tfrac{3}{2}K_{I13}\alpha^3 + \tfrac{3}{8}K_{I14}\alpha^3\} - \tfrac{1}{4}b_1^2K_{I7}\omega_N\alpha + \tfrac{1}{4}b_1K_{I3}\Lambda_1\omega_N\alpha - \tfrac{1}{4}b_1K_{I5}\Lambda_1\omega_N\alpha- \\
&\tfrac{1}{4}b_1K_{I6}\Lambda_1\omega_N\alpha + \tfrac{1}{4}K_{I2}\Lambda_1^2\omega_N\alpha - \tfrac{1}{4}K_{I4}\Lambda_1^2\omega_N\alpha + \tfrac{3}{8}K_{I2}\omega_N\alpha^3- \\
&\tfrac{1}{8}K_{I25}\omega_N\alpha^3 + \tfrac{1}{8}K_{I26}\omega_N\alpha^3 - \tfrac{3}{8}K_{I4}\omega_N\alpha^3,
\end{aligned}
\tag{5.3.22}
$$

and,

$$
\begin{aligned}
\alpha' = &-2b_2K_{I28}\tfrac{\omega_f^2}{\omega_N}\sin(\sigma T_2-\phi) - \hat{\zeta}_{vis}\omega_N\alpha - \tfrac{3}{4}b_1^2K_{I34}\hat{\eta}_{vel}\alpha- \\
&\tfrac{3}{2}b_1K1_{I33}\hat{\eta}_{vel}\Lambda_1\omega_f^2\alpha - \tfrac{3}{4}K_{I32}\hat{\eta}_{vel}\Lambda_1^2\omega_f^2\alpha - \tfrac{3}{8}K_{I32}\hat{\eta}_{vel}\omega_N^2\alpha^3.
\end{aligned}
\tag{5.3.23}
$$

To this end we introduce the following transformation which will remove the explicit dependence on the variable T_2:

$$
\gamma = \sigma T_2 - \phi, \tag{5.3.24}
$$

and,

$$\gamma' = \sigma - \phi'. \tag{5.3.25}$$

Using Eqs. (5.3.24) and (5.3.25), Eqs. (5.3.22) and (5.3.23) can be transformed into an autonomous system:

$$\begin{aligned}\alpha' = &- 2b_2 K_{I28}\frac{\omega_f^2}{\omega_N}\sin\gamma - \alpha\big[\hat{\zeta}_{vis}\omega_f + \tfrac{3}{4}b_1^2 K_{I34}\hat{\eta}_{vel}\omega_f^2 + \tfrac{3}{2}b_1 K1_{I33}\hat{\eta}_{vel}\Lambda_1\omega_f^2 + \\ &\tfrac{3}{4}K_{I32}\hat{\eta}_{vel}\Lambda_1^2\omega_f^2\big] - \tfrac{3}{8}K_{I32}\hat{\eta}_{vel}\omega_N^2\alpha^3,\end{aligned} \tag{5.3.26}$$

$$\begin{aligned}\alpha\gamma' = &\alpha\sigma - \tfrac{1}{\omega_N}\{2b_2 K_{I28}\omega_f^2\cos\gamma + \\ &\tfrac{1}{4}b_1^2 K_{I9}\alpha + b_1 K_{I10}\Lambda_1\alpha + 2b_1 K_{I11}\Lambda_1\alpha + \\ &\tfrac{3}{4}K_{I12}\Lambda_1^2\alpha + 3K_{I13}\Lambda_1^2\alpha + \tfrac{3}{4}K_{I14}\Lambda_1^2\alpha - \tfrac{1}{4}b_1^2 K_{I15}\omega_f^2\alpha + \\ &\tfrac{1}{2}b_1^2 K_{I16}\omega_f^2\alpha + \tfrac{1}{4}b_1^2 K_{I17}\omega_f^2\alpha + \tfrac{1}{4}b_1^2 K_{I18}\omega_f^2\alpha + \tfrac{1}{4}b_1^2 K_{I19}\omega_f^2\alpha - \\ &\tfrac{1}{2}b_1 K1_{I21}\Lambda_1\omega_f^2\alpha + \tfrac{1}{2}b_1 K1_{I22}\Lambda_1\omega_f^2\alpha - \tfrac{1}{2}b_1 K_{I23}\Lambda_1\omega_f^2\alpha + \\ &\tfrac{1}{2}b_1 K_{I24}\Lambda_1\omega_f^2\alpha + \tfrac{1}{4}b_1 K_{I3}\Lambda_1\omega_f^2\alpha - \tfrac{1}{4}b_1 K_{I5}\Lambda_1\omega_f^2\alpha - \tfrac{1}{4}b_1 K_{I6}\Lambda_1\omega_f^2\alpha + \\ &\tfrac{1}{2}K_{I2}\Lambda_1^2\omega_f^2\alpha - \tfrac{1}{4}K_{I25}\Lambda_1^2\omega_f^2\alpha + \tfrac{1}{4}K_{I26}\Lambda_1^2\omega_f^2\alpha - \tfrac{1}{2}K_{I4}\Lambda_1^2\omega_f^2\alpha + \tfrac{3}{8}K_{I12}\alpha^3 + \\ &\tfrac{3}{2}K_{I13}\alpha^3 + \tfrac{3}{8}K_{I14}\alpha^3\} + \tfrac{1}{4}b_1^2 K_{I7}\omega_N\alpha - \tfrac{1}{4}b_1 K_{I3}\Lambda_1\omega_N\alpha + \tfrac{1}{4}b_1 K_{I5}\Lambda_1\omega_N\alpha + \\ &\tfrac{1}{4}b_1 K_{I6}\Lambda_1\omega_N\alpha - \tfrac{1}{4}K_{I2}\Lambda_1^2\omega_N\alpha + \tfrac{1}{4}K_{I4}\Lambda_1^2\omega_N\alpha - \tfrac{3}{8}K_{I2}\omega_N\alpha^3 + \\ &\tfrac{1}{8}K_{I25}\omega_N\alpha^3 - \tfrac{1}{8}K_{I26}\omega_N\alpha^3 + \tfrac{3}{8}K_{I4}\omega_N\alpha^3.\end{aligned} \tag{5.3.27}$$

Finally, we substitute detuning parameter σ for the flapping frequency ω_f via Eq. (5.3.19), use Eq. (5.3.15), rewrite Eqs. (5.3.26) and (5.3.27) by expanding in a series and keeping only the order $\mathcal{O}(\epsilon^0)$ terms, and arrive at

the modulation (evolution) equations:

$$\alpha' = -\tfrac{1}{2}b_2 K_{I28}\omega_N \sin\gamma - \alpha\big[\hat{\zeta}_{vis}\omega_N + \tfrac{3}{16}b_1^2 K_{I34}\hat{\eta}_{vel}\omega_N^2 - \tfrac{1}{8}b_1^2 K1_{I33}K_{I28}\hat{\eta}_{vel}\omega_N^2 + \tfrac{1}{48}b_1^2 K_{I32}K_{I28}^2\hat{\eta}_{vel}\omega_N^2\big] - \tfrac{3}{8}K_{I32}\hat{\eta}_{vel}\omega_N^2\alpha^3, \tag{5.3.28}$$

and,

$$\begin{aligned}\alpha\gamma' =& \frac{1}{144\omega_N}\Big\{-72b_2K_{I28}\omega_N^2\cos\gamma + \alpha\big[144\omega_N\sigma + 12b_1^2(4K_{I10}K_{I28} + 8K_{I11}K_{I28} - \\ & K_{I12}K_{I28}^2 - 4K_{I13}K_{I28}^2 - K_{I14}K_{I28}^2 - 3K_{I9}) + b_1^2\omega_N^2(9K_{I15} - 18K_{I16} - \\ & 9K_{I17} - 9K_{I18} - 9K_{I19} - 6K1_{I21}K_{I28} + 6K1_{I22}K_{I28} - 6K_{I23}K_{I28} + \\ & 6K_{I24}K_{I28} - 6K_{I2}K_{I28}^2 + K_{I25}K_{I28}^2 - K_{I26}K_{I28}^2 + 15K_{I28}K_{I3} + 6K_{I28}^2K_{I4} - \\ & 15K_{I28}K_{I5} - 15K_{I28}K_{I6} + 36K_{I7})\big] + \alpha^3\big[-54(K_{I12} + 4K_{I13} + K_{I14}) - \\ & 18\omega_N^2(3K_{I2} - K_{I25} + K_{I26} - 3K_{I4})\big]\Big\}.\end{aligned} \tag{5.3.29}$$

In order to determine the periodic response, we note that α and γ are constants at the steady-state and $\alpha' = 0$ and $\gamma' = 0$. Then, it follows from Eqs. (5.3.28) and (5.3.29) that the steady-state amplitude α and phase γ correspond to the solutions of the following pair of equations:

$$b_2\sin\gamma = \alpha\big[\hat{\zeta}_{vis}\Gamma_1 + b_1^2\hat{\eta}_{vel}(\Gamma_7 + \Gamma_8 + \Gamma_9)\big] + \hat{\eta}_{vel}\Gamma_{10}\alpha^3 \tag{5.3.30}$$

and,

$$b_2\cos\gamma = \Gamma_2[\alpha(\sigma\Gamma_3 + b_1^2\Gamma_4 + b_1^2\Gamma_5) + \alpha^3\Gamma_6], \tag{5.3.31}$$

where Γ_1 - Γ_{10} are given in Appendix J. Squaring Eq. (5.3.30) and (5.3.31),

and adding the results yields the frequency-response equation:

$$\mathfrak{F}(\alpha,\sigma) = \Big[\alpha\big[\hat{\zeta}_{vis}\Gamma_1 + b_1^2\hat{\eta}_{vel}(\Gamma_7+\Gamma_8+\Gamma_9)\big] + \hat{\eta}_{vel}\Gamma_{10}\alpha^3\Big]^2 + \Gamma_2^2[\alpha(\sigma\Gamma_3 + b_1^2\Gamma_4 + b_1^2\Gamma_5) + \alpha^3\Gamma_6]^2 - b_2^2 = 0. \tag{5.3.32}$$

The frequency-response function $\mathfrak{F}(\alpha,\sigma)$ relates the amplitude of the free oscillation term α to detuning σ (or ω_f) for a given set of parameters. This relationship can be depicted by plotting the frequency-response curve which can be obtained by solving Eq. (5.3.32) for α or σ. $\mathfrak{F}(\alpha,\sigma)$ is a sixth-order polynomial function in the variable α; therefore, it is easier to solve Eq. (5.3.32) for σ which then becomes a quadratic equation. Solving Eq. (5.3.32) for σ yields:

$$\sigma_{1,2} = \frac{-b_1^2(\Gamma_4+\Gamma_5) - \Gamma_6\alpha^2}{\Gamma_3} \pm \sqrt{\frac{1}{\Gamma_2^2\Gamma_3^2\alpha^2}\Big[b_2^2 - \mathfrak{G}^2\alpha^2 - 2\Gamma_{10}\hat{\eta}_{vel}\mathfrak{G}\alpha^4 - \Gamma_{10}^2\hat{\eta}_{vel}^2\alpha^6\Big]}, \tag{5.3.33}$$

where,

$$\mathfrak{G} = \Gamma_1\hat{\zeta}_{vis} + b_1^2\hat{\eta}_{vel}(\Gamma_7+\Gamma_8+\Gamma_9). \tag{5.3.34}$$

The perturbation solution of Eq. (5.2.14) is given by Eqs. (5.3.1) and (5.3.2) and, to the first-order approximation, it can be expressed at the second-order superharmonic resonance via Eq. (5.3.16) as:

$$x(t) \approx x_0(T_0,T_2) = \alpha(T_2)\sin[\omega_N T_0 + \phi(T_2)] + \frac{b_1 K_{I28}\omega_f^2}{\omega_f^2 - \omega_N^2}\sin(\omega_f T_0). \tag{5.3.35}$$

Using Eqs. (5.3.3), (5.3.20), and (5.3.24) one can write:

$$\omega_N T_0 + \phi(T_2) = (2\omega_f T_0 - \sigma T_2) + (\sigma T_2 - \gamma) = 2\omega_f t - \gamma. \tag{5.3.36}$$

Substituting Eq. (5.3.36) into (5.3.35) yields the perturbation solution we sought:

$$x(t) = \alpha \sin(2\omega_f t - \gamma) + \frac{b_1 K_{I28} \omega_f^2}{\omega_f^2 - \omega_N^2} \sin(\omega_f t) + \mathcal{O}(\epsilon^2). \tag{5.3.37}$$

In Eq. (5.3.37), α and γ are given by the modulation equations (5.3.30) and (5.3.31). In order to determine α and γ; one first solves the frequency response equation (5.3.32) (a cubic equation in α^2) for α, then substitutes the result into Eq. (5.3.30) to determine γ.

5.3.2 The Case of $\omega_f \approx \frac{1}{3}\omega_N$

The response of system (5.2.14) in the vicinity of third-order superharmonic resonance, i.e., when $\omega_f \approx \frac{1}{3}\omega_N$, can be investigated by following the same analysis manner as given in Section 5.3.1. To this end, we proceed with the steps given in Eqs. (5.3.6)-(5.3.16) with only difference being in the order-ϵ^2 equation. We note in equation for x_2 (i.e., order-ϵ^2 equation) that in addition to the terms proportional to $\mathrm{e}^{\pm \mathrm{i}\omega_N T_0}$, the terms proportional to $\mathrm{e}^{\pm \mathrm{i}3\omega_f T_0}$ produce secular terms in x_2 when $3\omega_f \approx \omega_N$. We only consider one of the complex conjugates of these secular terms and introduce a detuning parameter σ which quantifies the nearness of flapping frequency to $\frac{1}{3}\omega_N$:

$$3\omega_f = \omega_N + \epsilon^2 \sigma. \tag{5.3.38}$$

At this point, we express $3\omega_f T_0$ as:

$$3\omega_f T_0 = (\omega_N + \epsilon^2 \sigma) T_0 = \omega_N T_0 + \epsilon^2 T_0 \sigma = \omega_N T_0 + \sigma T_2, \tag{5.3.39}$$

and, using Eq. (5.3.39), write $\mathrm{e}^{\mathrm{i}3\omega_f T_0} = \mathrm{e}^{\mathrm{i}\omega_N T_0}\mathrm{e}^{\mathrm{i}\sigma T_2}$ and eliminate the secular terms if:

$$\Big\{\tfrac{1}{2}\Big[-A\Big(4\Lambda\bar{\Lambda}\big(3(K_{I12}+4K_{I13}+K_{I14})+$$
$$\omega_f^2(2K_{I2}-K_{I25}+K_{I26}-2K_{I4}+3\mathrm{i}K_{I32}\hat{\eta}_{vel}\omega_N)\big)+4\omega_N^2(\mathrm{i}\hat{\zeta}_{vis}+\Lambda\bar{\Lambda}(K_{I2}-K_{I4}))+$$
$$b_1^2\big(K_{I9}+\omega_f^2(-K_{I15}+2K_{I16}+K_{I17}+K_{I18}+K_{I19}+3\mathrm{i}K_{I34}\hat{\eta}_{vel}\omega_N)-\omega_N^2K_{I7}\big)-$$
$$\mathrm{i}b_1\big[(\Lambda-\bar{\Lambda})\big(-4(K_{I10}+2K_{I11})+$$
$$\omega_f^2(2K1_{I21}-2K1_{I22}+2K_{I23}-2K_{I24}-K_{I3}+K_{I5}+K_{I6}-6\mathrm{i}K1_{I33}\hat{\eta}_{vel}\omega_N)\big)+$$
$$2\omega_f\omega_N(\Lambda+\bar{\Lambda})(K1_{I21}-K1_{I22}+K_{I27})-\omega_N^2(\Lambda-\bar{\Lambda})(K_{I3}-K_{I5}-K_{I6})\big]\Big)-$$
$$2A^2\bar{A}\big(3(K_{I12}+4K_{I13}+K_{I14})+\omega_N^2(3K_{I2}-K_{I25}+K_{I26}-3K_{I4})+3\mathrm{i}K_{I32}\hat{\eta}_{vel}\omega_N^3\big)-$$
$$4\mathrm{i}\omega_N A'\Big]+\mathrm{e}^{\mathrm{i}\sigma T_2}\big[\tfrac{1}{4}b_1^2K_{I9}\Lambda+(\mathrm{i}b_1K_{I10}+2\mathrm{i}b_1K_{I11})\Lambda^2-(K_{I12}+4K_{I13}+K_{I14})\Lambda^3+$$
$$(\tfrac{1}{4}K_{I15}+\tfrac{1}{2}K_{I16}-\tfrac{1}{4}K_{I17}+\tfrac{1}{4}K_{I18}+\tfrac{1}{4}K_{I19}-\tfrac{1}{2}K_{I20}-\tfrac{1}{4}K_{I7})b_1^2\Lambda\omega_f^2+$$
$$(\mathrm{i}K1_{I21}-\mathrm{i}K1_{I22}-\tfrac{1}{2}\mathrm{i}K_{I23}+\tfrac{1}{2}\mathrm{i}K_{I24}-\tfrac{1}{2}\mathrm{i}K_{I27}+\tfrac{1}{2}\mathrm{i}K_{I3}-\tfrac{1}{2}\mathrm{i}K_{I5}-\tfrac{1}{2}\mathrm{i}K_{I6})b_1\Lambda^2\omega_f^2+$$
$$(-K_{I2}-K_{I25}+K_{I26}+K_{I4})\Lambda^3\omega_f^2+\tfrac{1}{8}\mathrm{i}b_1^3\omega_f^2(K_{I29}-K_{I30})-\tfrac{1}{8}b_1^3K_{I35}\hat{\eta}_{vel}\omega_f^3-$$
$$\tfrac{3}{4}\mathrm{i}b_1^2K_{I34}\hat{\eta}_{vel}\Lambda\omega_f^3+\tfrac{3}{2}b_1K1_{I33}\hat{\eta}_{vel}\Lambda^2\omega_f^3+\mathrm{i}K_{I32}\hat{\eta}_{vel}\Lambda^3\omega_f^3\big]\Big\}=0, \tag{5.3.40}$$

Substituting for A and Λ from Eqs. (5.3.13) and (5.3.14) into solvability condition, Eq. (5.3.40), multiplying through the resulting equation by $\mathrm{i}\mathrm{e}^{-\mathrm{i}\phi}$, noticing that $\mathrm{e}^{\mathrm{i}(\sigma T_2-\phi)} = \cos(\sigma T_2-\phi)+\mathrm{i}\sin(\sigma T_2-\phi)$, separating real and imaginary parts, transforming the resulting equations into an autonomous system, replacing detuning σ for ω_f via Eq. (5.3.38), we obtain the modulation

equations:

$$\begin{aligned}\alpha' =&\Gamma_{19}\hat{\eta}_{vel}\alpha^3 + \Gamma_{11}\hat{\zeta}_{vis}\alpha + \frac{1}{\Gamma_{12}}\alpha(b_1^2\hat{\eta}_{vel}\Gamma_{20})+ \\ &\frac{1}{\Gamma_{12}}b_1^3\hat{\eta}_{vel}\Gamma_{21}\cos\gamma + \frac{1}{\Gamma_{12}}b_1^3(\Gamma_{13}+\Gamma_{14})\sin\gamma, \end{aligned} \tag{5.3.41}$$

and,

$$\begin{aligned}\alpha\gamma' =&\frac{1}{\Gamma_{12}}\alpha^3(\Gamma_{15}+\Gamma_{16}) + \frac{1}{\Gamma_{12}}\alpha[\sigma\Gamma_{12} + b_1^2(\Gamma_{17}+\Gamma_{18})]+ \\ &\frac{1}{\Gamma_{12}}b_1^3(\Gamma_{13}+\Gamma_{14})\cos\gamma - \frac{1}{\Gamma_{12}}b_1^3\hat{\eta}_{vel}\Gamma_{21}\sin\gamma, \end{aligned} \tag{5.3.42}$$

where Γ_{11}-Γ_{21} are given in Appendix J. At steady-state, $\alpha' = 0$ and $\gamma' = 0$. Then, the steady-state modulation equations can be obtained from Eqs. (5.3.41) and (5.3.42) as:

$$\begin{aligned}&\frac{-1}{\Gamma_{12}}b_1^3\hat{\eta}_{vel}\Gamma_{21}\cos\gamma + \frac{-1}{\Gamma_{12}}b_1^3(\Gamma_{13}+\Gamma_{14})\sin\gamma = \\ &\Gamma_{19}\hat{\eta}_{vel}\alpha^3 + \Gamma_{11}\hat{\zeta}_{vis}\alpha + \frac{1}{\Gamma_{12}}\alpha(b_1^2\hat{\eta}_{vel}\Gamma_{20}), \end{aligned} \tag{5.3.43}$$

and,

$$\begin{aligned}&\frac{-1}{\Gamma_{12}}b_1^3(\Gamma_{13}+\Gamma_{14})\cos\gamma + \frac{1}{\Gamma_{12}}b_1^3\hat{\eta}_{vel}\Gamma_{21}\sin\gamma = \\ &\frac{1}{\Gamma_{12}}\alpha^3(\Gamma_{15}+\Gamma_{16}) + \frac{1}{\Gamma_{12}}\alpha[\sigma\Gamma_{12} + b_1^2(\Gamma_{17}+\Gamma_{18})]. \end{aligned} \tag{5.3.44}$$

Squaring Eqs. (5.3.43) and (5.3.44), and adding the results gives the frequency-

response equation:

$$\begin{aligned}\mathfrak{F}(\alpha,\sigma) =&\alpha^6\Big(\frac{\Gamma_{15}^2+2\Gamma_{15}\Gamma_{16}+\Gamma_{16}^2}{\Gamma_{12}^2}+\Gamma_{19}^2\hat{\eta}_{vel}^2\Big)+\alpha^4\Big[2\Gamma_{11}\Gamma_{19}\hat{\zeta}_{vis}\hat{\eta}_{vel}+\\ &2b_1^2\Big(\frac{\Gamma_{15}\Gamma_{17}+\Gamma_{16}\Gamma_{17}+\Gamma_{15}\Gamma_{18}+\Gamma_{16}\Gamma_{18}}{\Gamma_{12}^2}+\frac{\Gamma_{19}\Gamma_{20}\hat{\eta}_{vel}^2}{\Gamma_{12}}\Big)+\\ &2\sigma\Big(\frac{\Gamma_{15}+\Gamma_{16}}{\Gamma_{12}}\Big)\Big]+\alpha^2\Big[b_1^4\Big(\frac{\Gamma_{17}^2+2\Gamma_{17}\Gamma_{18}+\Gamma_{18}^2+\Gamma_{20}^2\hat{\eta}_{vel}^2}{\Gamma_{12}^2}\Big)+\\ &2b_1^2\Big(\frac{\Gamma_{11}\Gamma_{20}\hat{\zeta}_{vis}\hat{\eta}_{vel}}{\Gamma_{12}}+\sigma\frac{\Gamma_{17}+\Gamma_{18}}{\Gamma_{12}}\Big)+\Gamma_{11}^2\hat{\zeta}_{vis}^2+\sigma^2\Big]-\\ &b_1^6\Big(\frac{\Gamma_{13}^2+2\Gamma_{13}\Gamma_{14}+\Gamma_{14}^2+\Gamma_{21}^2\hat{\eta}_{vel}^2}{\Gamma_{12}^2}\Big)=0.\end{aligned} \tag{5.3.45}$$

Solving Eq. (5.3.45) for σ yields:

$$\begin{aligned}\sigma_{1,2} =&\frac{-\alpha^2(\Gamma_{15}+\Gamma_{16})-b_1^2(\Gamma_{17}+\Gamma_{18})}{\Gamma_{12}}\pm\\ &\Big[\frac{1}{\alpha^2\Gamma_{12}^2}\Big(-b_1^4\alpha^2\Gamma_{20}^2\hat{\eta}_{vel}^2-2b_1^2\alpha^2\Gamma_{12}\Gamma_{20}\hat{\eta}_{vel}(\Gamma_{11}\hat{\zeta}_{vis}+\alpha^2\Gamma_{19}\hat{\eta}_{vel})-\\ &\alpha^2\Gamma_{12}^2(\Gamma_{11}\hat{\zeta}_{vis}+\alpha^2\Gamma_{19}\hat{\eta}_{vel})^2+b_1^6(\Gamma_{13}^2+2\Gamma_{13}\Gamma_{14}+\Gamma_{14}^2+\Gamma_{21}^2\hat{\eta}_{vel}^2)\Big)\Big]^{1/2}.\end{aligned} \tag{5.3.46}$$

To the first-order approximation, the perturbation solution of Eq. (5.2.14) at the third-order superharmonic resonance is given by Eq. (5.3.35). Using Eqs. (5.3.3), (5.3.39), and (5.3.24) we obtain:

$$\omega_N T_0+\phi(T_2)=(3\omega_f T_0-\sigma T_2)+(\sigma T_2-\gamma)=3\omega_f t-\gamma, \tag{5.3.47}$$

and inserting Eq. (5.3.47) into Eq. (5.3.35) yields:

$$x(t)=\alpha\sin(3\omega_f t-\gamma)+\frac{b_1 K_{I28}\omega_f^2}{\omega_f^2-\omega_N^2}\sin(\omega_f t)+\mathcal{O}(\epsilon^2), \tag{5.3.48}$$

where α and γ are given by Eqs. (5.3.43) and (5.3.44). Accordingly, Eq. (5.3.45) can be solved for α and then the result is substituted into Eqs. (5.3.43) and (5.3.44) to determine γ.

5.3.3 The Case of $\omega_f \approx \omega_N$

In this section, the focus is placed on the behavior of system (5.2.14) when $\omega_f \approx \omega_N$. The damping force acting on the beam is assumed to be governed by the nonlinear model Eq. (5.2.11). Introducing a small bookkeeping parameter ϵ, we employ the same ordering for the damping as given in Eqs. (5.3.7) and (5.3.8), whereas we consider the following ordering scheme for the excitation:

$$\beta_1 = \epsilon^3 b_1, \quad \beta_2 = \epsilon^5 b_2. \tag{5.3.49}$$

Note that the physical reasoning of employing the ordering for the excitation in Eq. (5.3.49) originates from the notion that a small-amplitude ("weak") excitation creates a relatively large-amplitude response in the primary resonance case.

Substituting Eqs. (5.3.5), (5.3.7), (5.3.8), and (5.3.49) into Eq. (5.2.14) (with $f_d = f_{d,nl}$ via Eq. (I.6)), dividing through the resulting equation by ϵ, equating the coefficients of ϵ^0 and ϵ^2 on both sides, using the definitions $K_{I1} = 1$ and $K_{I8} = \omega_N^2$, and rearranging we get:

$$D_0^2 x_0 + \omega_N^2 x_0 = 0, \tag{5.3.50}$$

and,

$$D_0^2 x_2 + \omega_N^2 x_2 =$$
$$-\big[b_1 K_{I28}\omega_f^2 \sin(\omega_f t) + 4b_2 K_{I28}\omega_f^2 \sin(2\omega_f t) + x_0^3(K_{I12} + 4K_{I13} + K_{I14}) +$$
$$2K_{I1}\hat{\zeta}_{vis}\omega_N D_0 x_0 + (-K_{I25} + K_{I26})x_0(D_0 x_0)^2 + K_{I32}\hat{\eta}_{vel}(D_0 x_0)^3 + 2K_{I1}D_0 D_2 x_0 +$$
$$x_0^2 D_0^2 x_0(-K_{I2} + K_{I4})\big]. \tag{5.3.51}$$

Solution of Eq. (5.3.50) is given by Eq. (5.3.11). Inserting Eq. (5.3.11) into (5.3.51), replacing the trigonometric expressions with their complex exponential counterparts, and collecting the terms yield:

$$D_0^2 x_2 + \omega_N^2 x_2 = \mathrm{e}^{\mathrm{i}\omega_f T_0}\{\ldots\} + \mathrm{e}^{-\mathrm{i}\omega_f T_0}\{\ldots\} + \mathrm{e}^{\mathrm{i}2\omega_f T_0}\{\ldots\} + \mathrm{e}^{-\mathrm{i}2\omega_f T_0}\{\ldots\} +$$
$$\mathrm{e}^{\mathrm{i}\omega_N T_0}\{\ldots\} + \mathrm{e}^{-\mathrm{i}\omega_N T_0}\{\ldots\} + \mathrm{e}^{\mathrm{i}3\omega_N T_0}\{\ldots\} + \mathrm{e}^{-\mathrm{i}3\omega_N T_0}\{\ldots\}. \tag{5.3.52}$$

In Eq. (5.3.52), in addition to the terms proportional to $\mathrm{e}^{\pm\mathrm{i}\omega_N T_0}$, the terms proportional to $\mathrm{e}^{\pm\mathrm{i}\omega_f T_0}$ produce secular terms in x_2 when $\omega_f \approx \omega_N$. We only consider one of the complex conjugates of these secular terms and rewrite it as:

$$D_0^2 x_2 + \omega_N^2 x_2 = \mathrm{e}^{\mathrm{i}\omega_f T_0}\{\tfrac{1}{2}\mathrm{i}b_1 K_{I28}\omega_f^2\} +$$
$$\mathrm{e}^{\mathrm{i}\omega_N T_0}\{A^2\bar{A}\big(-3K_{I12} - 12K_{I13} - 3K_{I14} + \omega_N^2(-3K_{I2} + K_{I25} - K_{I26} + 3K_{I4}) -$$
$$3\mathrm{i}K_{I32}\hat{\eta}_{vel}\omega_N^3\big) - 2\mathrm{i}\hat{\zeta}_{vis}\omega_N^2 A - 2\mathrm{i}\omega_N A'\} + \text{c.c.} + \text{N.S.T.}, \tag{5.3.53}$$

where, c.c. stands for the complex conjugate of the preceding terms and N.S.T.

stands for the terms that do not produce secular terms.

We express the nearness of flapping frequency to the primary resonance by introducing a detuning parameter σ:

$$\omega_f = \omega_N + \epsilon^2 \sigma, \tag{5.3.54}$$

and write:

$$\omega_f T_0 = (\omega_N + \epsilon^2 \sigma) T_0 = \omega_N T_0 + \epsilon^2 T_0 \sigma = \omega_N T_0 + \sigma T_2. \tag{5.3.55}$$

Using Eq. (5.3.55), one can show $\mathrm{e}^{\mathrm{i}\omega_f T_0} = \mathrm{e}^{\mathrm{i}(\omega_N T_0 + \sigma T_2)} = \mathrm{e}^{\mathrm{i}\omega_N T_0} \mathrm{e}^{\mathrm{i}\sigma T_2}$, and eliminate the secular terms in Eq. (5.3.53) according to:

$$\begin{aligned}\{A^2 \bar{A}\big(&-3K_{I12} - 12K_{I13} - 3K_{I14} + \omega_N^2(-3K_{I2} + K_{I25} - K_{I26} + 3K_{I4}) - \\ &3\mathrm{i}K_{I32}\hat{\eta}_{vel}\omega_N^3\big) - 2\mathrm{i}\hat{\zeta}_{vis}\omega_N^2 A - 2\mathrm{i}\omega_N A' + \mathrm{e}^{\mathrm{i}\sigma T_2}\tfrac{1}{2}\mathrm{i}b_1 K_{I28}\omega_f^2\} = 0.\end{aligned} \tag{5.3.56}$$

Substituting for A from Eq. (5.3.13) into solvability condition (5.3.56), multiplying through the resulting equation by $\mathrm{i}\mathrm{e}^{-\mathrm{i}\phi}$, noting that $\mathrm{e}^{\mathrm{i}(\sigma T_2 - \phi)} = \cos(\sigma T_2 - \phi) + \mathrm{i}\sin(\sigma T_2 - \phi)$, separating real and imaginary parts, transforming the ensuing equations into an autonomous set system, replacing detuning σ for ω_f via (5.3.54), and expanding in series to the order $\mathcal{O}(\epsilon^0)$ we arrive at the modulation equations:

$$\alpha' = \alpha\Gamma_{22}\hat{\zeta}_{vis} - \alpha^3\Gamma_{25}\hat{\eta}_{vel} - b_1\Gamma_{23}\sin\gamma, \tag{5.3.57}$$

and,

$$\alpha\gamma' = \alpha^3\Gamma_{24} + \alpha\sigma - b_1\Gamma_{23}\cos\gamma. \tag{5.3.58}$$

where $\Gamma_{22} - \Gamma_{25}$ are given in Appendix J. At steady-state $\alpha' = 0$ and $\gamma' = 0$, then it follows from Eqs. (5.3.57) and (5.3.58):

$$b_1\Gamma_{23}\sin\gamma = \alpha\Gamma_{22}\hat{\zeta}_{vis} + \alpha^3\Gamma_{25}\hat{\eta}_{vel}, \tag{5.3.59}$$

and,

$$b_1\Gamma_{23}\cos\gamma = \alpha^3\Gamma_{24} + \alpha\sigma. \tag{5.3.60}$$

Squaring Eqs. (5.3.59) and (5.3.60), and summing the results gives the frequency-response equation:

$$\mathfrak{F}(\alpha,\sigma) = \alpha^6(\Gamma_{24}^2+\Gamma_{25}^2\hat{\eta}_{vel}^2)+2\alpha^4(\sigma\Gamma_{24}+\Gamma_{22}\Gamma_{25}\hat{\zeta}_{vis}\hat{\eta}_{vel})+\alpha^2(\Gamma_{22}^2\hat{\zeta}_{vis}^2+\sigma^2)-b_1^2\Gamma_{23}^2 = 0. \tag{5.3.61}$$

Finally, solving Eq. (5.3.61) for σ yields:

$$\sigma_{1,2} = -\alpha^2\Gamma_{24} \pm \sqrt{-(\Gamma_{22}\hat{\zeta}_{vis} + \alpha^2\Gamma_{25}\hat{\eta}_{vel})^2 + \frac{b_1^2\Gamma_{23}^2}{\alpha^2}} \tag{5.3.62}$$

The perturbation solution of Eq. (5.2.14) is given by Eqs. (5.3.1) and (5.3.2) and, to the first-order approximation, it can be expressed at the primary resonance via Eq. (5.3.11) as:

$$x(t) \approx x_0(T_0, T_2) = \alpha(T_2)\sin[\omega_N T_0 + \phi(T_2)]. \tag{5.3.63}$$

Using Eqs. (5.3.3), (5.3.55), and (5.3.24) one can write:

$$\omega_N T_0 + \phi(T_2) = (\omega_f T_0 - \sigma T_2) + (\sigma T_2 - \gamma) = \omega_f t - \gamma, \tag{5.3.64}$$

and substituting Eq. (5.3.64) into (5.3.63) yields the first-order perturbation solution at the primary resonance:

$$x(t) = \alpha \sin(\omega_f t - \gamma) + \mathcal{O}(\epsilon^2), \tag{5.3.65}$$

where α and γ can be determined from Eqs. (5.3.61) and (5.3.59).

5.4 Results and Analyses

5.4.1 The Case of $\omega_f \approx \frac{1}{2}\omega_N$

The frequency-response function for the second-order superharmonic resonance with velocity-3rd power damping is given by Eqs. (5.3.32). It can be shown that setting $b_2 = 0$ in Eq. (5.3.32), leads to a quadratic equation in α^2. In order for this quadratic equation to have real solutions, the corresponding discriminant must be non-negative. This condition can be expressed as:

$$-4\Gamma_2^2\Big[\Gamma_1\Gamma_6\hat{\zeta}_{vis} + \hat{\eta}_{vel}\big(b_1^2(-\Gamma_{10}(\Gamma_4+\Gamma_5) + \Gamma_6(\Gamma_7+\Gamma_8+\Gamma_9)) - \Gamma_{10}\Gamma_3\sigma\big)\Big]^2 \geq 0. \tag{5.4.1}$$

Note that the condition given by Eq. (5.4.1) cannot hold true. Therefore, we conclude that for the existence of a free oscillation term leading to second-order superharmonic resonance, the excitation amplitude b_2 must be nonzero. In other words, flapping excitation in the form of a simple harmonic function will not trigger the second-order superharmonic resonance.

Second-order superharmonic frequency-response curves of the beam under the effect of nonlinear damping are depicted in Figure 5.1. These curves are obtained from Eq. (5.3.33) by varying either the excitation amplitude b_2 (Figure 5.1a) or nonlinear damping coefficient $\hat{\eta}_{vel}$ (Figure 5.1b) while keeping other relevant variables constant. One can note in Figure 5.1a that as the excitation amplitude b_2 is increased for a given nonlinear damping force, the frequency-response curves reveal a "hardening-spring" type nonlinearity indicated by Eq. (5.3.33) and bend toward the righthand side with increasing peak amplitudes α_p. The peak amplitude α_p in the frequency-response curve is observed where left and right branches meet at the same frequency; i.e., when $\sigma_1 = \sigma_2$, and this condition is satisfied if the radicand in Eq. (5.3.33) vanishes. Setting the radicand in Eq. (5.3.33) equal to zero and solving the resulting equation for α yields α_p. Substituting α_p into Eq. (5.3.33) with vanishing radicand then gives the corresponding peak frequency σ_p.

As can be noted in Figure 5.1a, there exists a minimum critical excitation amplitude b_2 above which the frequency-response curve bends over. Bending of the frequency-response curve reveals a frequency interval $\sigma \in [\sigma_{up}, \sigma_{down}]$ over which there are 3 amplitudes, α's, for a fixed σ. All three α's are real solutions and represent three equilibrium states. The frequency interval $\sigma \in [\sigma_{up}, \sigma_{down}]$ is referred to as "bistable" as there are two stable solutions; which of these two can be realized is determined by the initial conditions. In any experiment, the third real solution existing between the upper and lower solutions is unstable and cannot be realized due to ever present disturbances [142]. At both ends of the interval, i.e., at σ_{down} and σ_{up}, where the jump phenomenon is observed, one stable solution coalesce into the unstable solution which results in bifurcation (jump) to the other stable solution. This type of bifurcation is termed

saddle-node or *fold* bifurcation [143, 144].

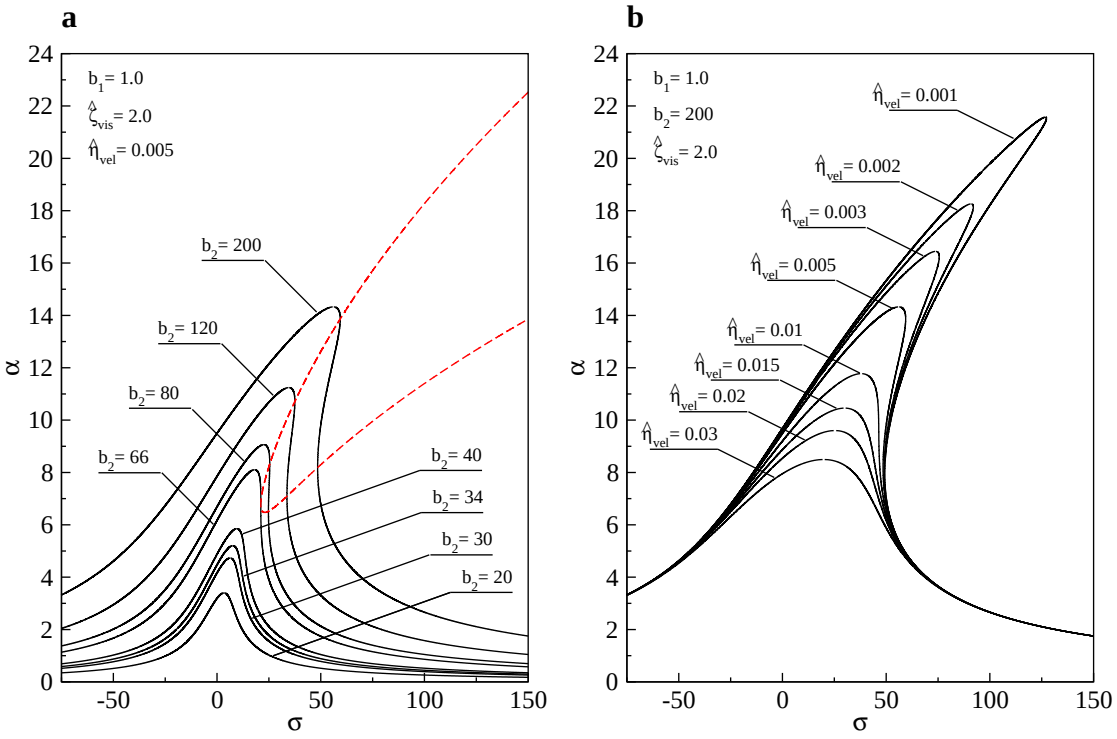

Figure 5.1: Frequency-response curves for the second-order superharmonic resonance and nonlinear damping with (a) different excitation amplitudes b_2, $\hat{\zeta}_{vis} = 2$, $\hat{\eta}_{vel} = 0.005$, and $b_1 = 1$; (b) different nonlinear damping coefficients $\hat{\eta}_{vel}$, $\hat{\zeta}_{vis} = 2$, $b_1 = 1$, and $b_2 = 200$. Dashed line in (a) represents the instability boundary.

The stability of steady-state (periodic) solutions can be determined by introducing small perturbations to the steady-state motions (amplitude α_0 and phase γ_0) and analyzing if those perturbations grow with time or not. To this end, we introduce small perturbations to the steady-state amplitude α_0 and phase γ_0:

$$\alpha(T_2) = \alpha_0 + \alpha_1(T_2),$$
$$\gamma(T_2) = \gamma_0 + \gamma_1(T_2), \tag{5.4.2}$$

Substituting Eqs. (5.4.2) into modulation equations, Eqs. (5.3.28) and (5.3.29), keeping only the linear terms in α_1 and γ_1, and noting that α_0 and σ_0 satisfy the steady-state modulation equations (5.3.30) and (5.3.31), we get:

$$\begin{Bmatrix} \alpha_1' \\ \gamma_1' \end{Bmatrix} = \mathbf{A} \begin{Bmatrix} \alpha_1 \\ \gamma_1 \end{Bmatrix} = \begin{bmatrix} A_{11} & A_{12} \\ A_{21} & A_{22} \end{bmatrix} \begin{Bmatrix} \alpha_1 \\ \gamma_1 \end{Bmatrix}, \tag{5.4.3}$$

where the elements of coefficient matrix $\mathbf{A}$ are given as:

$$A_{11} = \tfrac{1}{\Gamma_2\Gamma_3}\big[\Gamma_1\hat{\zeta}_{vis} + 3\alpha_0^2\Gamma_{10}\hat{\eta}_{vel} + b_1^2\hat{\eta}_{vel}(\Gamma_7 + \Gamma_8 + \Gamma_9)\big], \tag{5.4.4}$$

$$A_{12} = \tfrac{-1}{\Gamma_3}\big[\alpha_0(\sigma\Gamma_3 + b_1^2\Gamma_4 + b_1^2\Gamma_5) + \alpha_0^3\Gamma_6\big], \tag{5.4.5}$$

$$A_{21} = \tfrac{1}{\Gamma_3\alpha_0}\big[(\sigma\Gamma_3 + b_1^2\Gamma_4 + b_1^2\Gamma_5) + 3\alpha_0^2\Gamma_6\big], \tag{5.4.6}$$

$$A_{22} = \tfrac{1}{\Gamma_2\Gamma_3}\big[\Gamma_1\hat{\zeta}_{vis} + \alpha_0^2\Gamma_{10}\hat{\eta}_{vel} + b_1^2\hat{\eta}_{vel}(\Gamma_7 + \Gamma_8 + \Gamma_9)\big]. \tag{5.4.7}$$

The stability of the steady-state motion depends on the eigenvalues of the coefficient matrix $\mathbf{A}$. The eigenvalues λ of the coefficient matrix are given by the characteristic equation:

$$|\mathbf{A} - \lambda\mathbf{I}| = \lambda^2 - \mathrm{tr}(\mathbf{A})\lambda + \det(\mathbf{A}) = 0, \tag{5.4.8}$$

where $\mathrm{tr}(\mathbf{A})$ and $\det(\mathbf{A})$ are trace and determinant of the coefficient matrix, respectively.

The steady-state motions are unstable when the constant term in Eq. (5.4.8), i.e., $\det(\mathbf{A})$, is less than zero, and are stable otherwise. That is, for unstable

steady-state motions:

$$
\begin{aligned}
&\det(\mathbf{A}) = \\
&\Gamma_1^2\hat{\zeta}_{vis}^2 + 3\alpha_0^4\big(\Gamma_2^2\Gamma_6^2 + \Gamma_{10}^2\hat{\eta}_{vel}^2\big) + 2b_1^4\big(\Gamma_2^2\Gamma_4\Gamma_5 + \hat{\eta}_{vel}^2(\Gamma_7\Gamma_8 + \Gamma_7\Gamma_9 + \Gamma_8\Gamma_9)\big) + \\
&b_1^4\big(\Gamma_2^2\Gamma_4^2 + \Gamma_2^2\Gamma_5^2 + \hat{\eta}_{vel}^2(\Gamma_7^2 + \Gamma_8^2 + \Gamma_9^2)\big) + \Gamma_2^2\Gamma_3^2\sigma^2 + \\
&2b_1^2\big(\Gamma_2^2\Gamma_3\Gamma_4\sigma + \Gamma_2^2\Gamma_3\Gamma_5\sigma + \Gamma_1\hat{\zeta}_{vis}\hat{\eta}_{vel}(\Gamma_7 + \Gamma_8 + \Gamma_9)\big) + \\
&4\alpha_0^2\big(\Gamma_1\Gamma 10\hat{\zeta}_{vis}\hat{\eta}_{vel} + b_1^2[\Gamma_2^2\Gamma_4\Gamma_6 + \Gamma_2^2\Gamma_5\Gamma_6 + \Gamma_{10}\hat{\eta}_{vel}^2(\Gamma_7 + \Gamma_8 + \Gamma_9)] + \Gamma_2^2\Gamma_3\Gamma_6\sigma\big) < 0.
\end{aligned}
\tag{5.4.9}
$$

The region indicated by Eq. (5.4.9) coincides with the area enclosed by dashed curve in Figure 5.1a. The equation of this dashed curve, which marks the boundary points of the unstable solution branch of the response curves, is obtained by replacing the "<" sign in Eq. (5.4.9) by equality. The equation of the dashed curve can also be obtained by noting that the end points of unstable response branch coincide with the points at which the frequency-response curve has vertical tangents [22, 142]. $\mathfrak{F}(\alpha, \sigma)$ has vertical tangents in the α-σ plane at points where derivative of σ with respect to α vanishes; i.e., $\frac{\mathrm{d}\sigma}{\mathrm{d}\alpha} = -\left(\frac{\partial\mathfrak{F}}{\partial\alpha}\right) / \left(\frac{\partial\mathfrak{F}}{\partial\sigma}\right) = 0$. The vanishing derivative leads to:

$$
\begin{aligned}
&3\alpha^4(\Gamma_2^2\Gamma_6^2 + \Gamma_{10}^2\hat{\eta}_{vel}^2) + 4\alpha^2\big(b_1^2(\Gamma_2^2\Gamma_4\Gamma_6 + \Gamma_2^2\Gamma_5\Gamma_6) + \mathfrak{G}\Gamma_{10}\hat{\eta}_{vel} + \Gamma_2^2\Gamma_3\Gamma_6\sigma\big) + \\
&b_1^4(\Gamma_2^2\Gamma_4^2 + 2\Gamma_2^2\Gamma_4\Gamma_5 + \Gamma_2^2\Gamma_5^2) + b_1^2(2\Gamma_2^2\Gamma_3\Gamma_4\sigma + 2\Gamma_2^2\Gamma_3\Gamma_5\sigma) + \Gamma_2^2\Gamma_3^2\sigma^2 + \mathfrak{G}^2 = 0.
\end{aligned}
\tag{5.4.10}
$$

The curve given by Eq. (5.4.10) represents the locus of vertical tangents of the frequency-response curve and is the same equation as (5.4.9) with equal sign.

As mentioned above, the frequency-response curve does not exhibit bista-

bility ("bending over") unless the excitation amplitude b_2 exceeds a threshold value. On the verge of bending, the frequency-response curve has an inflection point at which the second derivative of σ with respect to α vanishes; i.e., $\frac{\mathrm{d}^2\sigma}{\mathrm{d}\alpha^2} = -\left(\frac{\partial^2\mathfrak{F}}{\partial\alpha^2}\right) / \left(\frac{\partial^2\mathfrak{F}}{\partial\sigma^2}\right) = 0$. When the equation given by the vanishing second derivative is solved for σ, one obtains the value of σ at the inflection point:

$$\sigma = \frac{-1}{2\Gamma_2^2\Gamma_3\Gamma_6}\Big[2\Gamma_1\Gamma_{10}\hat{\zeta}_{vis}\hat{\eta}_{vel} + 3\alpha^2(\Gamma_2^2\Gamma_6^2 + \Gamma_{10}^2\hat{\eta}_{vel}^2) + 2b_1^2\big(\Gamma_2^2\Gamma_6(\Gamma_4+\Gamma_5) + \Gamma_{10}\hat{\eta}_{vel}^2(\Gamma_7+\Gamma_8+\Gamma_9)\big)\Big]. \tag{5.4.11}$$

Equation (5.4.11) also satisfies the equation of the locus of vertical tangents; therefore, inserting Eq. (5.4.11) into Eq. (5.4.10) yields:

$$-\frac{\Gamma_2^2\Gamma_6^2 + \Gamma_{10}^2\hat{\eta}_{vel}^2}{4\Gamma_2^2\Gamma_6^2}\left[-12\alpha^2\Gamma_{10}\hat{\eta}_{vel}\mathfrak{G} - 4\mathfrak{G}^2 + 3\alpha^4(\Gamma_2^2\Gamma_6^2 - 3\Gamma_{10}^2\hat{\eta}_{vel}^2)\right] = 0. \tag{5.4.12}$$

Solving Eq. (5.4.12) for α, and only considering the real positive root, yields the critical response amplitude at the inflection point of the frequency-response curve:

$$\alpha_{cr}(b_1, \hat{\zeta}_{vis}, \hat{\eta}_{vel}) = \sqrt{\frac{6\Gamma_{10}\hat{\eta}_{vel}\mathfrak{G} + 2\sqrt{3}\sqrt{\Gamma_2^2\Gamma_6^2\mathfrak{G}^2}}{3\Gamma_2^2\Gamma_6^2 - 9\Gamma_{10}^2\hat{\eta}_{vel}^2}}. \tag{5.4.13}$$

Substituting Eq. (5.4.13) into Eq. (5.4.11) gives the response frequency at the inflection point:

$$\sigma_{cr}(b_1, \hat{\zeta}_{vis}, \hat{\eta}_{vel}) = \frac{-1}{2\Gamma_2^2\Gamma_3\Gamma_6}\Big[2\Gamma_1\Gamma_{10}\hat{\zeta}_{vis}\hat{\eta}_{vel} + 3\alpha_{cr}^2(\Gamma_2^2\Gamma_6^2 + \Gamma_{10}^2\hat{\eta}_{vel}^2) + 2b_1^2\big(\Gamma_2^2\Gamma_6(\Gamma_4+\Gamma_5) + \Gamma_{10}\hat{\eta}_{vel}^2(\Gamma_7+\Gamma_8+\Gamma_9)\big)\Big]. \tag{5.4.14}$$

Inserting Eqs. (5.4.13) and (5.4.14) into the frequency-response function Eq. (5.3.32) and solving the resulting equation for b_2 yields the critical excitation amplitude for which bistability occurs:

$$b_{2,cr}(b_1,\hat{\zeta}_{vis},\hat{\eta}_{vel}) = \Big[\big[\alpha_{cr}\big(\hat{\zeta}_{vis}\Gamma_1 + b_1^2\hat{\eta}_{vel}(\Gamma_7+\Gamma_8+\Gamma_9)\big) + \hat{\eta}_{vel}\Gamma_{10}\alpha_{cr}^3\big]^2 + \Gamma_2^2[\alpha_{cr}(\sigma_{cr}\Gamma_3 + b_1^2\Gamma_4 + b_1^2\Gamma_5) + \alpha_{cr}^3\Gamma_6]^2\Big]^{1/2}. \tag{5.4.15}$$

Jump-up and jump-down frequencies, σ_{up} and σ_{down}, and the corresponding response amplitudes α_{up} and α_{down} can be determined by solving Eqs. (5.3.32) and (5.4.10) simultaneously. Considering only real and positive roots we obtain:

$$\begin{aligned}
&\sigma_{up}(b_1,b_2,\hat{\zeta}_{vis},\hat{\eta}_{vel}) = \\
&\frac{1}{b_2^2\Gamma_2^2\Gamma_3\Gamma_6}\Big[b_2^2\big[\Gamma_1\Gamma_{10}\hat{\zeta}_{vis}\hat{\eta}_{vel} + b_1^2\big(-\Gamma_2^2\Gamma_6(\Gamma_4+\Gamma_5) + \Gamma_{10}\hat{\eta}_{vel}^2(\Gamma_7+\Gamma_8+\Gamma_9)\big)\big] + \\
&\quad b_2^2(-3\Gamma_2^2\Gamma_6^2 + \Gamma_{10}^2\hat{\eta}_{vel}^2)\sigma_{one} + \\
&\quad 2\big(\Gamma_1\hat{\zeta}_{vis} + b_1^2(\Gamma_7+\Gamma_8+\Gamma_9)\hat{\eta}_{vel}\big)^2(\Gamma_2^2\Gamma_6^2 + \Gamma_{10}^2\hat{\eta}_{vel}^2)\sigma_{one}^2 + \\
&\quad 4\Gamma_{10}\hat{\eta}_{vel}\big(\Gamma_1\hat{\zeta}_{vis} + b_1^2(\Gamma_7+\Gamma_8+\Gamma_9)\hat{\eta}_{vel}\big)(\Gamma_2^2\Gamma_6^2 + \Gamma_{10}^2\hat{\eta}_{vel}^2)\sigma_{one}^3 + \\
&\quad 2(\Gamma_{10}^2\Gamma_2^2\Gamma_6^2\hat{\eta}_{vel}^2 + \Gamma_{10}^4\hat{\eta}_{vel}^4)\sigma_{one}^4\Big],
\end{aligned} \tag{5.4.16}$$

$$\alpha_{up}(b_1,b_2,\hat{\zeta}_{vis},\hat{\eta}_{vel}) = \sqrt{\sigma_{one}}\ , \tag{5.4.17}$$

and,

$$\sigma_{down}(b_1, b_2, \hat{\zeta}_{vis}, \hat{\eta}_{vel}) =$$
$$\frac{1}{b_2^2\Gamma_2^2\Gamma_3\Gamma_6}\Big[b_2^2\big[\Gamma_1\Gamma_{10}\hat{\zeta}_{vis}\hat{\eta}_{vel} + b_1^2\big(-\Gamma_2^2\Gamma_6(\Gamma_4+\Gamma_5) + \Gamma_{10}\hat{\eta}_{vel}^2(\Gamma_7+\Gamma_8+\Gamma_9)\big)\big] +$$
$$b_2^2(-3\Gamma_2^2\Gamma_6^2 + \Gamma_{10}^2\hat{\eta}_{vel}^2)\sigma_{two} +$$
$$2\big(\Gamma_1\hat{\zeta}_{vis} + b_1^2(\Gamma_7+\Gamma_8+\Gamma_9)\hat{\eta}_{vel}\big)^2(\Gamma_2^2\Gamma_6^2 + \Gamma_{10}^2\hat{\eta}_{vel}^2)\sigma_{two}^2 +$$
$$4\Gamma_{10}\hat{\eta}_{vel}\big(\Gamma_1\hat{\zeta}_{vis} + b_1^2(\Gamma_7+\Gamma_8+\Gamma_9)\hat{\eta}_{vel}\big)(\Gamma_2^2\Gamma_6^2 + \Gamma_{10}^2\hat{\eta}_{vel}^2)\sigma_{two}^3 +$$
$$2(\Gamma_{10}^2\Gamma_2^2\Gamma_6^2\hat{\eta}_{vel}^2 + \Gamma_{10}^4\hat{\eta}_{vel}^4)\sigma_{two}^4\Big], \tag{5.4.18}$$

$$\alpha_{down}(b_1, b_2, \hat{\zeta}_{vis}, \hat{\eta}_{vel}) = \sqrt{\sigma_{two}}\ , \tag{5.4.19}$$

where σ_{one} and σ_{two} are the first two real roots ($\sigma_{one} < \sigma_{two}$) of the sixth-order equation:

$$b_2^4 + 4\sigma^4(\Gamma_2^2\Gamma_6^2 + \Gamma_{10}^2\hat{\eta}_{vel}^2)\big(\Gamma_1\hat{\zeta}_{vis} + b_1^2(\Gamma_7+\Gamma_8+\Gamma_9)\hat{\eta}_{vel} + \Gamma_{10}\hat{\eta}_{vel}\sigma\big)^2 +$$
$$4b_2^2\sigma^2\big[-\Gamma_2^2\Gamma_6^2\sigma + \Gamma_{10}\hat{\eta}_{vel}\big(\Gamma_1\hat{\zeta}_{vis} + b_1^2(\Gamma_7+\Gamma_8+\Gamma_9)\hat{\eta}_{vel} + \Gamma_{10}\hat{\eta}_{vel}\sigma\big)\big] = 0. \tag{5.4.20}$$

For the damping and excitation conditions $\hat{\zeta}_{vis} = 2$, $\hat{\eta}_{vel} = 0.005$, and $b_1 = 1$ given in Figure 5.1a, we use Eqs. (5.4.13)-(5.4.15) and determine the inflection point response amplitude and detuning as $\alpha_{cr} = 6.77$ and $\sigma_{cr} = 21.10$, while critical excitation amplitude b_2 as $b_{2,cr} = 65.97$. Using Eqs. (5.4.16)-(5.4.19), one can also determine jump frequencies and amplitudes for the case, for example, $b_2 = 120$ given in Figure 5.1a as $\sigma_{up} = 33.71$, $\alpha_{up} = 7.09$, $\sigma_{down} = 37.51$, and $\alpha_{down} = 10.71$.

In Figure 5.1b, the effect of the nonlinear damping force on the 2nd-order superharmonic frequency-response is depicted. For a given excitation amplitude b_1 and b_2, the influence of decreasing nonlinear damping is observed to amplify the peak response in the vicinity of resonance peak, as expected. As indicated by the figure, one can also determine a critical nonlinear damping coefficient for which bistable response occurs via inserting Eqs. (5.4.13) and (5.4.14) into Eq. (5.3.32) and solving the resulting equation for $\hat{\eta}_{vel}$.

Figure 5.2 is obtained from Eq. (5.3.33) with $\hat{\eta}_{vel} = 0$ and illustrates the effect of excitation amplitude b_2 and damping on the 2nd-order superharmonic frequency-response when linear viscous damping is considered as the only operative dissipation mechanism. Comparing Figures 5.1 and 5.2, we note that the nonlinear damping widens the response curves and results in broadening of the 2nd-order superharmonic resonance peak. By following the analysis steps detailed above, one can determine peak values, critical values, and jump values for the case with linear viscous damping.

Variation of critical excitation amplitude $b_{2,cr}$ with $\hat{\zeta}_{vis}$, $\hat{\eta}_{vel}$, and b_1 is shown in Figure 5.3. Note that when damping is considered to be linear viscous (i.e., $\hat{\eta}_{vel} = 0$), $b_{2,cr}$ is not dependent on b_1 and is a function of $\hat{\zeta}_{vis}$ only.

At this point it is pertinent to compare the analytical results presented in Figure 5.3 with those obtained from the experiments and numerical simulations given in previous chapters. In Chapters 3 and 4, the results were obtained based on the 4-bar crank-and-rocker mechanism excitation at two flapping amplitudes, 15° and 30°. The coefficients b_1 and b_2 corresponding to flapping at 15° and 30° produced by the 4-bar mechanism can be determined by sampling the actual functional form of the flapping angle (see Appendix B, Eq. (B.5)) and subsequently performing a discrete Fourier transform. The excitation

amplitudes b_1 and b_2 corresponding to various flapping amplitudes produced by the 4-bar mechanism are listed in Table 5.1. Accordingly, for flapping at 15°, $b_1 = 0.261564$ and $b_2 = 0.00109996$; and for flapping at 30°, $b_1 = 0.51302$ and $b_2 = 0.0123805$.

When damping is in the form of a linear viscous model with $\hat{\zeta}_{vis} = 0.013$ ($\hat{\eta}_{vel} = 0$), $b_{2,cr}$ is calculated, from Eq. (5.4.15), to be 0.0178105 for both amplitudes $b_1 = 0.261564$ and $b_1 = 0.51302$ given for 15° and 30°, respectively. Note that the amplitudes $b_2 = 0.00109996$ and $b_2 = 0.0123805$ given for 15° and 30° are both less than the critical value $b_{2,cr} = 0.0178105$. Therefore, for the case of linear viscous damping ($\hat{\zeta}_{vis} = 0.013$, $\hat{\eta}_{vel} = 0$), the second-order superharmonic response at 15° and 30° leads to one stable solution and does not show bistability which corroborates the observations in Figures 3.3, 4.2, and 4.4. When nonlinear damping is considered with $\hat{\eta}_{vel} = 0.3$ ($\hat{\zeta}_{vis} = 0.013$), Eq. (5.4.15) does not yield a real value for both $b_1 = 0.261564$ (15°) and $b_1 = 0.51302$ (30°), meaning that, for nonlinear damping ($\hat{\eta}_{vel} = 0.3$, $\hat{\zeta}_{vis} = 0.013$), no inflection point forms and thus the second-order superharmonic response always leads to one stable solution. This also confirms the observations made in Figures 4.2 and 4.4.

Finally, it can be deduced from Eqs. (5.3.33) that the effect of increasing excitation amplitude b_1 is determined to be only a shifting of the response curve to the right when damping is in the form of a linear viscous model ($\hat{\eta}_{vel} = 0$). However, when nonlinear damping is considered, increasing the excitation amplitude b_1, which is then coupled with $\hat{\eta}_{vel}$, not only shifts the response curve to the right but also amplifies the effect of nonlinear damping force in a way to diminish the peak amplitude and the hardening-spring type nonlinearity.

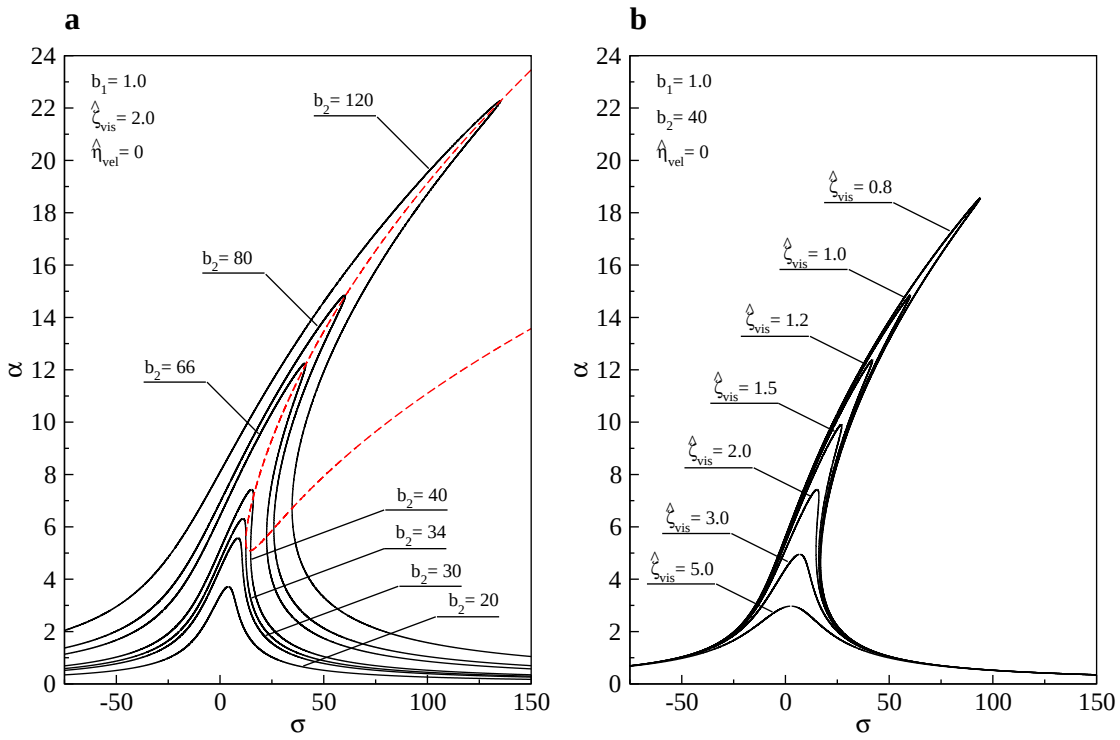

Figure 5.2: Frequency-response curves for the second-order superharmonic resonance and linear viscous damping with (a) different excitation amplitudes b_2, $\hat{\zeta}_{vis} = 2$, and $b_1 = 1$; (b) different damping coefficients $\hat{\zeta}_{vis}$, $b_1 = 1$, and $b_2 = 40$. Dashed line in (a) represents the instability boundary.

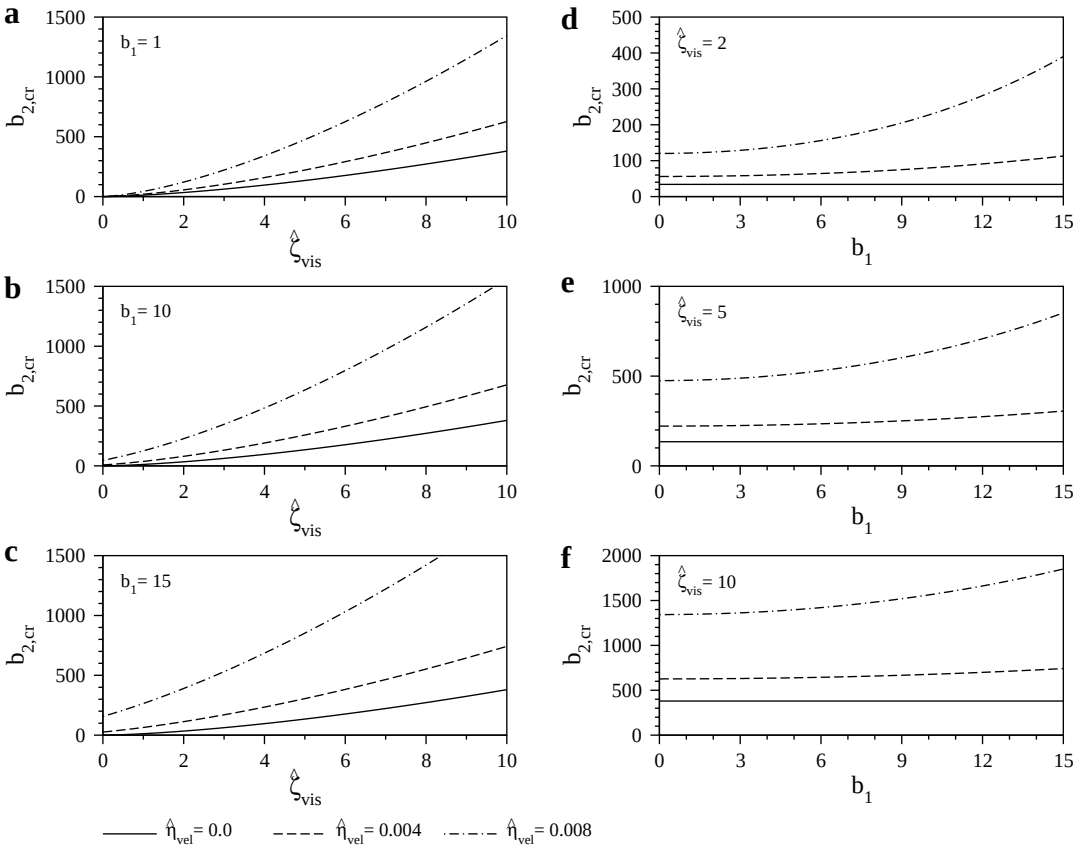

Figure 5.3: For the second-order superharmonic resonance case, variation of $b_{2,cr}$ with $\hat{\zeta}_{vis}$ for different values of $\hat{\eta}_{vel}$ at: (a) $b_1 = 1$, (b) $b_1 = 10$, (c) $b_1 = 15$; and with b_1 for different values of $\hat{\eta}_{vel}$ at: (d) $\hat{\zeta}_{vis} = 2$, (e) $\hat{\zeta}_{vis} = 5$, (f) $\hat{\zeta}_{vis} = 10$.

5.4.2 The Case of $\omega_f \approx \frac{1}{3}\omega_N$

The frequency response function Eqs. (5.3.45) shows that the third-order superharmonic resonance is independent of the excitation amplitude b_2. If b_1 is set equal to zero in Eq. (5.3.45), quadratic polynomial equations in α^2 are obtained. Discriminants of the resulting quadratic equations can be expressed as:

$$-4\Gamma_{11}^2(\Gamma_{15}^2 + \Gamma_{16}^2)\hat{\zeta}_{vis}^2/\Gamma_{12}^2, \tag{5.4.21}$$

and,

$$-4\big(\Gamma_{11}(\Gamma_{15}+\Gamma_{16})\hat{\zeta}_{vis}-\Gamma_{12}\Gamma_{19}\hat{\eta}_{vel}\sigma\big)^2/\Gamma_{12}^2, \tag{5.4.22}$$

for the cases with linear and nonlinear damping, respectively. For the existence of real solutions α, Eqs. (5.4.21) and (5.4.22) must be nonnegative for positive damping, which clearly does not hold true. Therefore, for the existence of the free oscillation term leading to third-order superharmonic resonance, b_1 must be nonzero as could be expected.

Third-order superharmonic frequency-response curves obtained for nonlinear and linear viscous damping cases are given in Figures 5.4 and 5.5 for the beam under the effect of nonlinear and linear damping forces, respectively. In Figure 5.4a, the excitation amplitude b_1 is varied for fixed damping parameters with $\hat{\zeta}_{vis}=2$ and $\hat{\eta}_{vel}=0.005$. The effect of increasing b_1 is observed to be threefold: increasing the peak response amplitude α_p, augmenting nonlinearity and bending the curve to the right, and shifting the curve to the right. One can also determine a critical excitation amplitude $b_{1,cr}$ above which α becomes multivalued for a given σ.

At this point, we determine locus of vertical tangents of Eq. (5.3.45) which is the curve determining the border separating stable solution branches from the unstable ones. This curve is plotted as a red dashed line in Figure 5.4a for $\hat{\zeta}_{vis}=2$ and $\hat{\eta}_{vel}=0.005$. As is done in the previous section, we take the derivative of the frequency-response function with respect to α, set the result

equal to zero, and obtain the equation of the stability border curve as:

$$
\begin{aligned}
&3\alpha^4\Big(\frac{\Gamma_{15}^2+2\Gamma_{15}\Gamma_{16}+\Gamma_{16}^2}{\Gamma_{12}^2}+\Gamma_{19}^2\hat{\eta}_{vel}^2\Big)+\\
&2\alpha^2\Big[2\Gamma_{11}\Gamma_{19}\hat{\zeta}_{vis}\hat{\eta}_{vel}+2b_1^2\Big(\frac{\Gamma_{15}\Gamma_{17}+\Gamma_{16}\Gamma_{17}+\Gamma_{15}\Gamma_{18}+\Gamma_{16}\Gamma_{18}}{\Gamma_{12}^2}+\frac{\Gamma_{19}\Gamma_{20}\hat{\eta}_{vel}^2}{\Gamma_{12}}\Big)+\\
&2\sigma\Big(\frac{\Gamma_{15}+\Gamma_{16}}{\Gamma_{12}}\Big)\Big]+b_1^4\Big(\frac{\Gamma_{17}^2+2\Gamma_{17}\Gamma_{18}+\Gamma_{18}^2+\Gamma_{20}^2\hat{\eta}_{vel}^2}{\Gamma_{12}^2}\Big)+\\
&2b_1^2\Big(\frac{\Gamma_{11}\Gamma_{20}\hat{\zeta}_{vis}\hat{\eta}_{vel}}{\Gamma_{12}}+\sigma\frac{\Gamma_{17}+\Gamma_{18}}{\Gamma_{12}}\Big)+\Gamma_{11}^2\hat{\zeta}_{vis}^2+\sigma^2=0,
\end{aligned}
\tag{5.4.23}
$$

where b_1 is obtained via solving Eq. (5.3.45).

Critical point values α_{cr}, σ_{cr}, and $b_{1,cr}$ can be calculated in a manner outlined previously. To summarize, we begin with solving the equation given by the vanishing second derivative of Eq. (5.3.45) with respect to α for σ. The resulting expression for σ must also satisfy Eq. (5.4.23). Solving the latter equation for α and only considering the real positve root yields the critical response amplitude α_{cr}, while inserting α_{cr} into the expression for σ obtained in the previous step gives σ_{cr}. Finally, substituting α_{cr} and σ_{cr} into Eq. (5.3.45) and solving the result for b_1 leads to the critical excitation amplitude $b_{1,cr}$. For the case illustrated in Figure 5.4a, critical values are calculated as $\alpha_{cr}=7.47$, $\sigma_{cr}=41.35$, and $b_{1,cr}=14.74$.

Figure 5.4b shows the effect of the nonlinear damping parameter on the response curves for a given excitation amplitude $b_1=21$. Increasing $\hat{\eta}_{vel}$ results in decreasing peak amplitude which is then accompanied with single-valued stable solutions when the threshold value for $\hat{\eta}_{vel}$ is exceeded. Comparing Figure 5.4b with Figure 5.5b, one can note that nonlinear damping gives rise to broader response curves than those obtained with linear viscous damping.

In Figures 5.6a and 5.6b, variation of critical excitation amplitude $b_{1,cr}$ with damping coefficients $\hat{\zeta}_{vis}$ and $\hat{\eta}_{vel}$ are depicted, respectively. According to Figure 5.6a, the influence of $\hat{\zeta}_{vis}$ on the $b_{1,cr}$ resembles "logarithmic growth" for a given $\hat{\eta}_{vel}$. Whereas, the effect of increasing $\hat{\eta}_{vel}$ on the $b_{1,cr}$ appears to be similar to "exponential growth" for a constant value of $\hat{\zeta}_{vis}$. The region under each of the curves in both figures gives the damping and excitation parameter combinations resulting in single-valued solutions.

To compare the analytical results given in Figure 5.6 with those obtained from the experiment and numerical simulation in Chapters 3 and 4, critical excitation amplitude is calculated for the cases linear viscous damping ($\hat{\zeta}_{vis} = 0.013$, $\hat{\eta}_{vel} = 0$) and nonlinear damping ($\hat{\eta}_{vel} = 0.3$, $\hat{\zeta}_{vis} = 0.013$). As such, for the case of linear viscous damping, the critical amplitude is determined to be $b_{1,cr} = 0.86294$ which is greater than both $b_1 = 0.261564$ and $b_1 = 0.51302$ given for 15° and 30°, respectively. Hence, the approximate analytical solution confirms the observations made in Figures 3.3, 4.2, and 4.4 that the third-order superharmonic resonance leads to one stable solution and does not reveal bistability for flapping at 15° and 30°, under linear viscous damping. For the case of nonlinear damping, $b_{1,cr}$ is determined to be nonreal which amounts to the fact that no inflection point can be determined on the frequency-response curve and thus the third-order superharmonic response leads to one stable solution at both 15° and 30°. This result agrees with the observations in Figure 4.2 and 4.4.

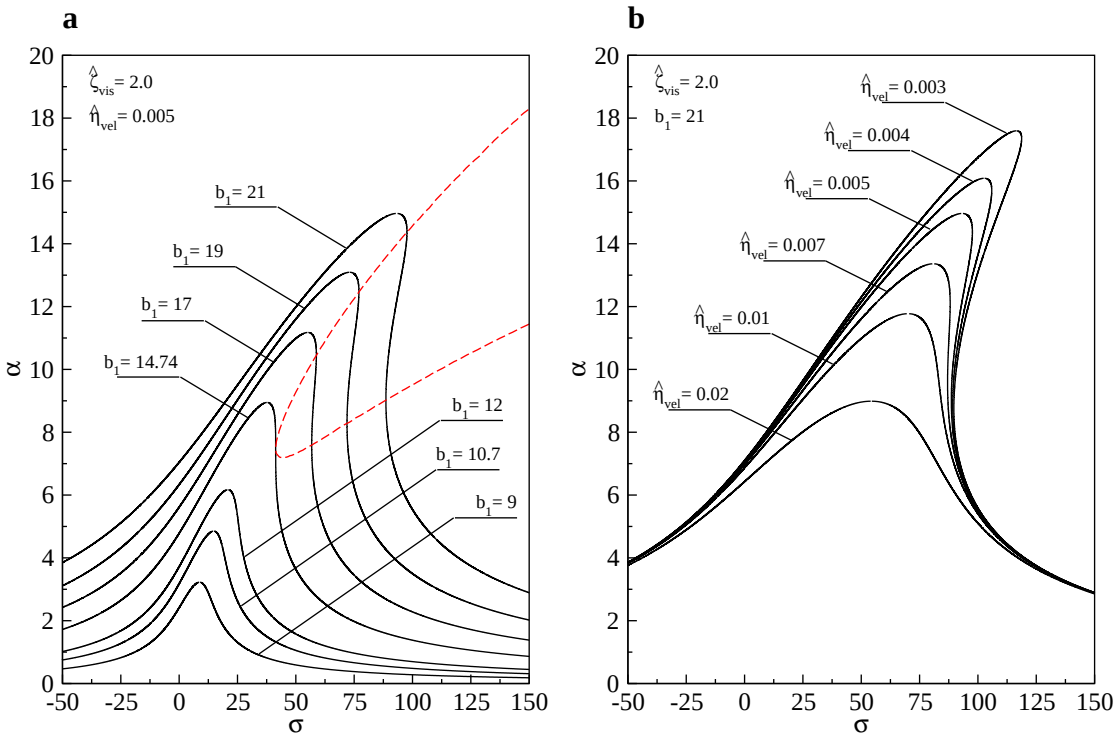

Figure 5.4: Frequency-response curves for the third-order superharmonic resonance and nonlinear damping with (a) different excitation amplitudes b_1, $\hat{\zeta}_{vis} = 2$, and $\hat{\eta}_{vel} = 0.005$; (b) different nonlinear damping coefficients $\hat{\eta}_{vel}$, $\hat{\zeta}_{vis} = 2$, and $b_1 = 21$. Dashed line in (a) represents the instability boundary.

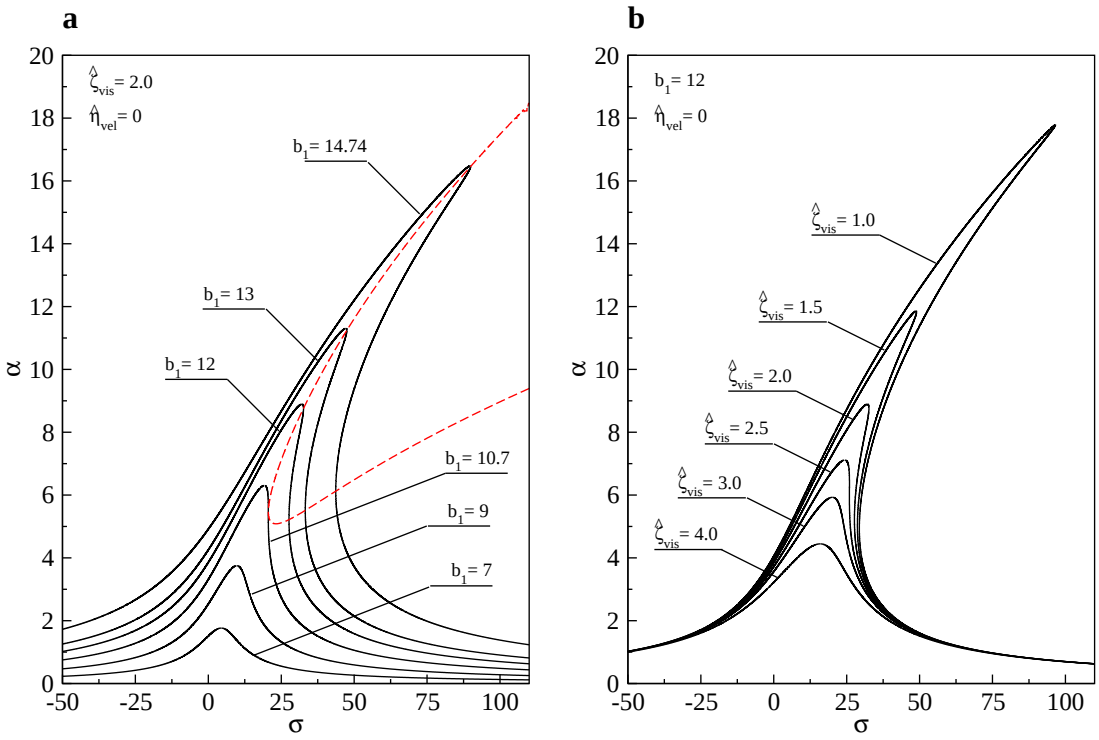

Figure 5.5: Frequency-response curves for the third-order superharmonic resonance and linear viscous damping with (a) different excitation amplitudes b_1 and $\hat{\zeta}_{vis} = 2$; (b) different damping coefficients $\hat{\zeta}_{vis}$ and $b_1 = 12$. Dashed line in (a) represents the instability boundary.

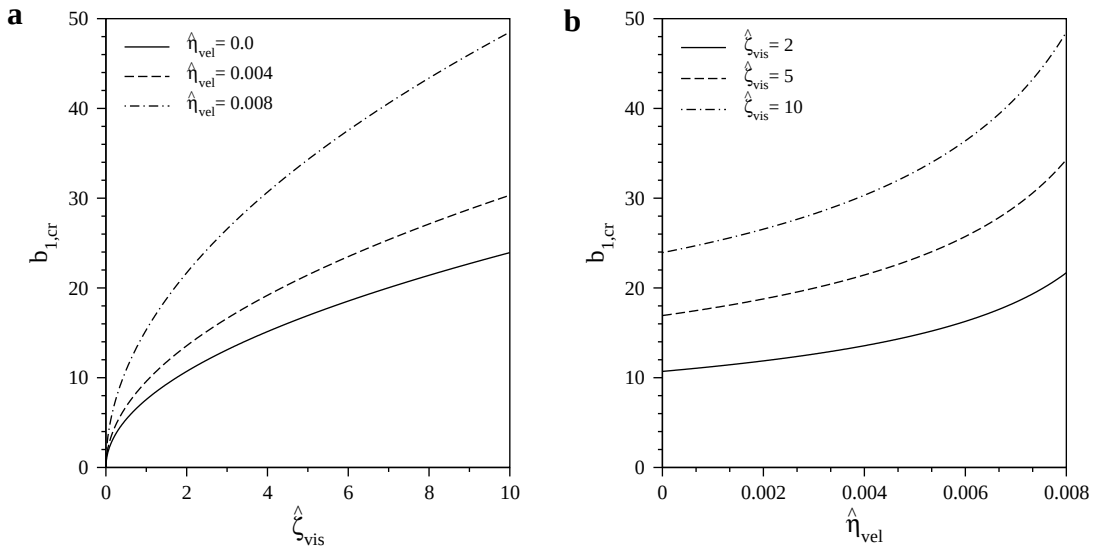

Figure 5.6: Variation of $b_{1,cr}$ for the third-order superharmonic resonance: (a) with $\hat{\zeta}_{vis}$ for $\hat{\eta}_{vel} = 0$, $\hat{\eta}_{vel} = 0.004$, and $\hat{\eta}_{vel} = 0.008$; (b) with $\hat{\eta}_{vel}$ for $\hat{\zeta}_{vis} = 2$, $\hat{\zeta}_{vis} = 5$, and $\hat{\zeta}_{vis} = 10$.

5.4.3 The Case of $\omega_f \approx \omega_N$

The frequency-response function Eq. (5.3.61) obtained for the primary resonance case show that the resonance response is not dependent on b_2. Moreover, if we let $b_1 = 0$ in Eq. (5.3.61), the discriminant of the resulting quadratic equation can be shown to be negative, which is then contrary to the existence of real solutions α. Therefore, it can be concluded that for the existence of primary resonance, b_1 must be nonzero.

Equation (5.3.62) is used to plot primary resonance frequency-response curves as shown in Figures 5.7 and 5.8 for nonlinear and linear damping, respectively. It can be inferred from Figure 5.7a that increasing the excitation amplitude b_1 for a given nonlinear damping force only results in bending of the response curves to the right. Accordingly, a threshold value $b_{1,cr}$ which needs to be exceeded for bistability to occur can be determined.

The locus of vertical tangents of the frequency-response function Eq. (5.3.61) is given:

$$3\alpha^4(\Gamma_{24}^2+\Gamma_{25}^2\hat{\eta}_{vel}^2)+4\alpha^2(\Gamma_{24}\sigma+\Gamma_{22}\Gamma_{25}\hat{\zeta}_{vis}\hat{\eta}_{vel})+\Gamma_{22}^2\hat{\zeta}_{vis}^2+\sigma^2=0, \quad (5.4.24)$$

and is plotted in Figure 5.7a as a red dashed line. Likewise, the critical values of α, σ, and b_1 above which bistability occurs are given as:

$$\alpha_{cr}=\sqrt{\frac{2\hat{\zeta}_{vis}\Gamma_{22}(\sqrt{3}\Gamma_{24}+3\Gamma_{25}\hat{\eta}_{vel})}{3\Gamma_{24}^2-9\Gamma_{25}^2\hat{\eta}_{vel}^2}}, \quad (5.4.25)$$

$$\sigma_{cr}=-\frac{\Gamma_{22}\Gamma_{25}\hat{\zeta}_{vis}\hat{\eta}_{vel}}{\Gamma_{24}}-\frac{3\alpha_{cr}^2(\Gamma_{24}^2+\Gamma_{25}^2\hat{\eta}_{vel}^2)}{2\Gamma_{24}}, \quad (5.4.26)$$

and,

$$b_{1,cr}=\sqrt{\frac{1}{\Gamma_{23}^2}\Big[\alpha_{cr}^6(\Gamma_{24}^2+\Gamma_{25}^2\hat{\eta}_{vel}^2)+2\alpha_{cr}^4(\sigma_{cr}\Gamma_{24}+\Gamma_{22}\Gamma_{25}\hat{\zeta}_{vis}\hat{\eta}_{vel})+\alpha_{cr}^2(\Gamma_{22}^2\hat{\zeta}_{vis}^2+\sigma_{cr}^2)\Big]}. \quad (5.4.27)$$

Using Eqs. (5.4.25)-(5.4.27), critical point values for the primary resonance response curves given in Figure 5.7a can be calculated as $\sigma_{cr}=20.80$, $\alpha_{cr}=6.76$, and $b_{1,cr}=65.65$.

In Figure 5.7b, the effect of varying the nonlinear damping coefficient on the primary resonance response is illustrated for a given excitation $b_1=200$. Due to nonlinear coupling of α and $\hat{\eta}_{vel}$, as noted in Eq. (5.3.62), increasing $\hat{\eta}_{vel}$ results in broader resonance peaks which tend to broaden as the peak amplitude decreases. The primary resonance response curves only considering the linear viscous damping are given in Figure 5.8. We note, by comparing Figure 5.7b with Figure 5.8b, that the effect of increasing linear damping $\hat{\zeta}_{vis}$

for a given excitation mainly results in diminishing of the peak amplitudes with less of the broadening distortion which was observed in the case of nonlinear damping.

The dependence of the critical excitation amplitude $b_{1,cr}$ on damping coefficients $\hat{\zeta}_{vis}$ and $\hat{\eta}_{vel}$ is depicted in Figure 5.9. The excitation and damping parameter combinations falling into the regions under the curves lead to stable, single-valued response amplitudes for frequencies in the vicinity of primary resonance.

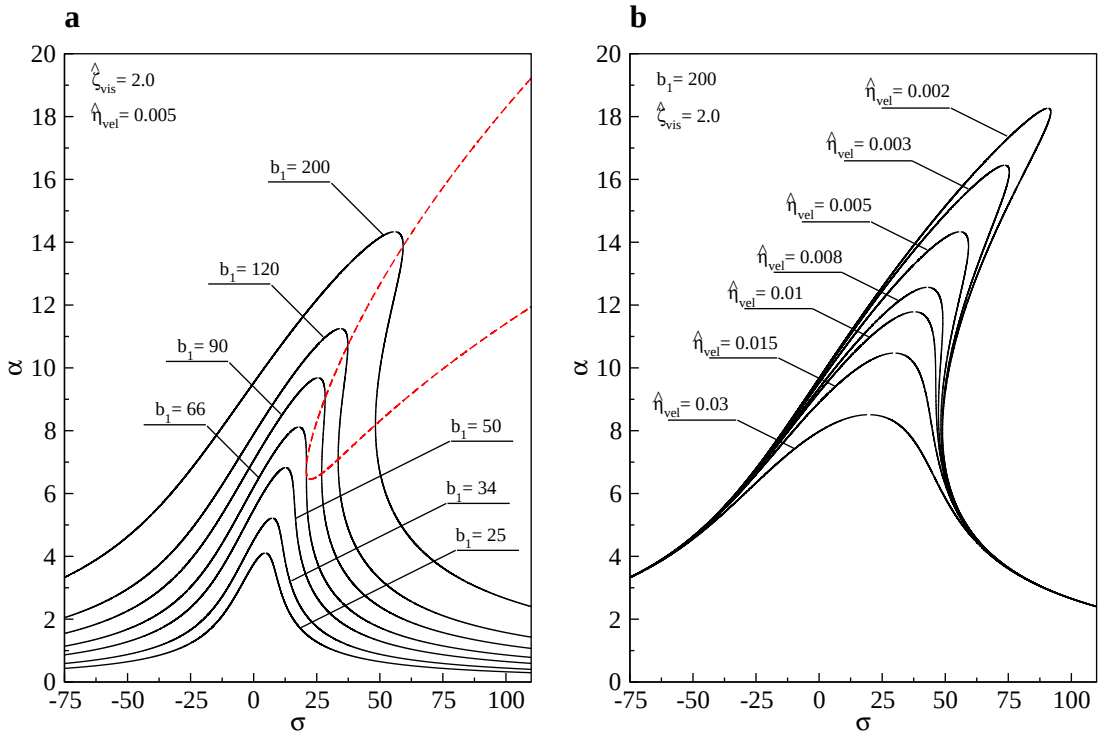

Figure 5.7: Frequency-response curves for the primary resonance and nonlinear damping with (a) different excitation amplitudes b_1, $\hat{\zeta}_{vis} = 2$, and $\hat{\eta}_{vel} = 0.005$; (b) different nonlinear damping coefficients $\hat{\eta}_{vel}$, $\hat{\zeta}_{vis} = 2$, and $b_1 = 200$. Dashed line in (a) represents the instability boundary.

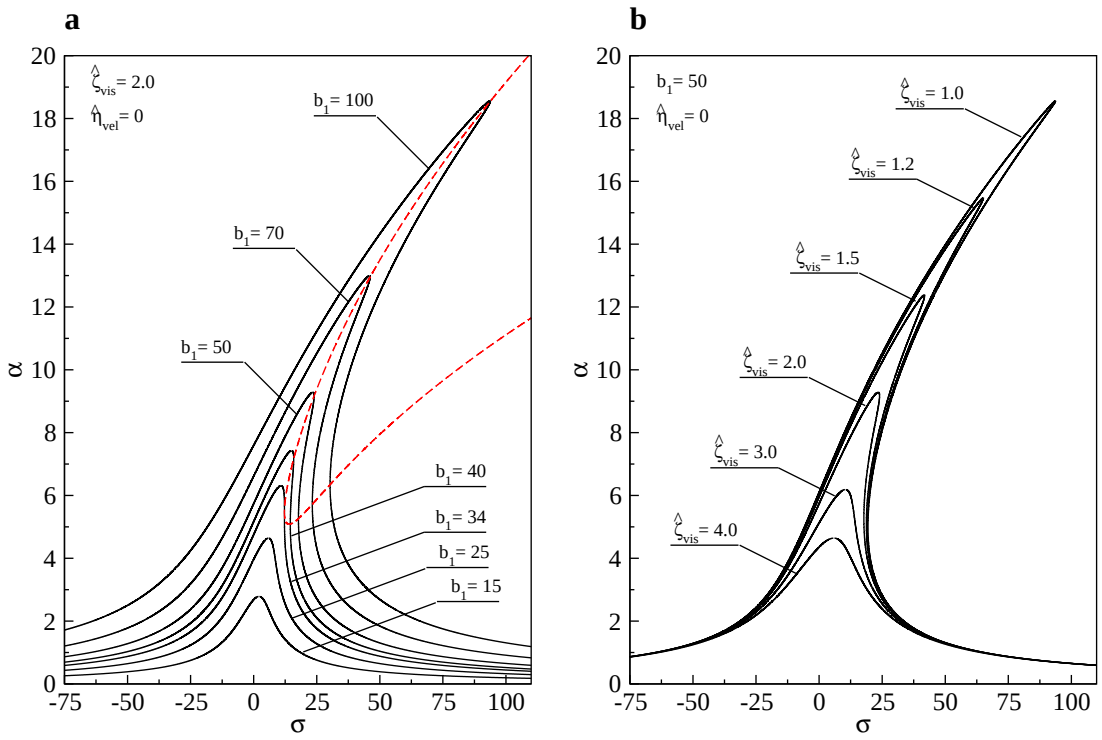

Figure 5.8: Frequency-response curves for the primary resonance and linear viscous damping with (a) different excitation amplitudes b_1 and $\hat{\zeta}_{vis} = 2$; (b) different damping coefficients $\hat{\zeta}_{vis}$ and $b_1 = 50$. Dashed line in (a) represents the instability boundary.

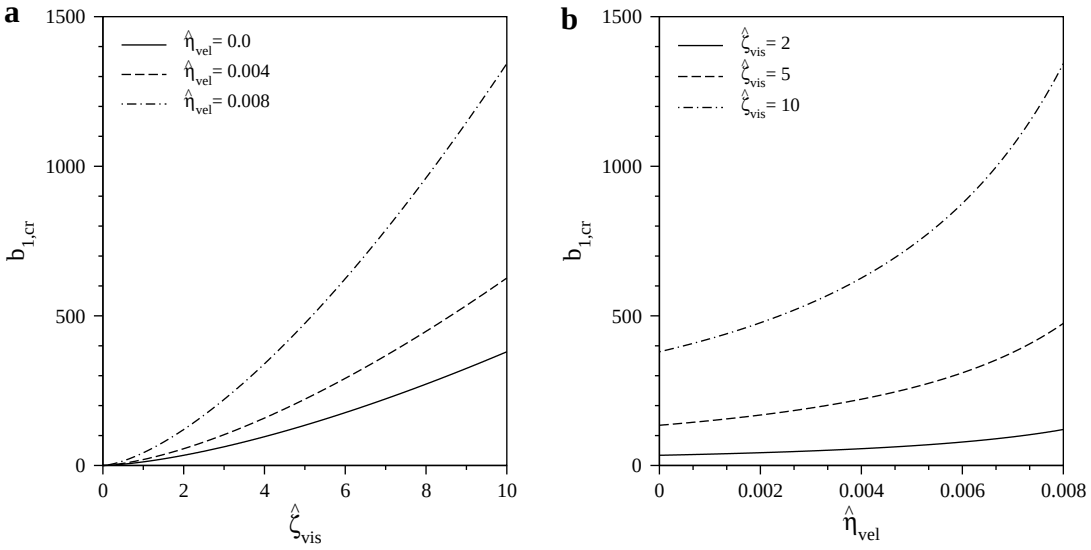

Figure 5.9: Variation of $b_{1,cr}$ for the primary resonance: (a) with $\hat{\zeta}_{vis}$ for $\hat{\eta}_{vel} = 0$, $\hat{\eta}_{vel} = 0.004$, and $\hat{\eta}_{vel} = 0.008$; (b) with $\hat{\eta}_{vel}$ for $\hat{\zeta}_{vis} = 2$, $\hat{\zeta}_{vis} = 5$, and $\hat{\zeta}_{vis} = 10$.

5.4.4 Comparison with High-Fidelity Time-Spectral Solution

In this section, first-order perturbation solutions are compared with those obtained with a numerical solution obtained through a time-spectral method [119–122, 135]. The flapping excitation amplitudes b_1 and b_2 used in this comparison study are determined from the functional form of the "actual" flapping angle $\theta_f(t)$. By actual flapping angle, it is meant to be the flapping angle generated by a flapping test-bed which is constructed based upon a 4-bar crank-and-rocker mechanism. Details of the flapping test-bed and the actual functional form of the flapping angle can be found in Chapter 2. The coefficients b_1 and b_2 are determined by sampling (in time) the flapping angle and then performing a discrete Fourier transform. A list of excitation amplitudes corresponding to different flapping amplitudes $\theta_{f,max}$ (i.e., maximum flapping angle) is given in Table 5.1. The damping parameter values, $\zeta_{vis} = 0.013$ and

$\bar{\eta}_{vel} = 0.3$ used in this section correspond to the values determined in Chapter 4.

Table 5.1: List of flapping excitation amplitudes b_1 and b_2 corresponding to flapping amplitude $\theta_{f,max}$ produced by a flapping test-bed based upon 4-bar crank-and-rocker mechanism.

$\theta_{f,max}$ [DEG.]	b_1	b_2
1	0.0174739	-5.37256×10^{-6}
3	0.0524088	-0.0000228282
5	0.0874119	-0.0000307847
7	0.1222730	0.0000116216
10	0.1745860	0.0002066910
15	0.2615640	0.0010999600
30	0.5130200	0.0123805000

Equation (5.2.14) is solved in the time domain with a time-spectral solution which has 61 collocation points (e.g., 30 harmonics) and comparison with the first-order multiple scales solutions is made by setting the perturbation parameter ϵ to 1, thereby obtaining formal solutions [141]. Based upon a convergence study, we determined that retaining 30 harmonics in the Fourier series approximations in the time-spectral solution provides sufficient accuracy. Maximum value of the response $a(t)$ over one cycle of flapping is used to compare the perturbation solutions with the time-spectral solutions (referred to as numerical solution in what follows) at different flapping amplitudes and damping conditions for a range of normalized flapping frequencies ω_0 ($\omega_0 = \omega_f/\omega_N$) in the vicinity of resonances.

In Figure 5.10, the maximum response, a_{max}, obtained from Eq. (5.3.37) in the vicinity of second-order superharmonic resonance is compared with that given by the numerical solution at different flapping amplitudes. Solutions obtained with the two methods are in agreement with comparable accuracy

at a given flapping amplitude when damping is assumed to be linear and nonlinear as shown in Figure 5.10a and b, respectively. At 1°, the response can be assumed to be linear and first-order multiple scales solution corroborates the numerical solution. No visible resonance peak is observed at 1° since b_2 is very close to zero (see Table 5.1). One can observe that, regardless of damping type, the first-order perturbation solution is in very good quantitative agreement with numerical solution up to 5°. As the flapping amplitude is increased beyond 5°, the perturbation solution overestimates the numerical solution. As the primary difference in the resonance peaks given by the two methods obtained at 10° and 15° is a vertical offset in the figures, this suggests that the discrepancy between the solutions is due to a difference between the amplitudes α estimated by the two methods. In other words, the phases γ's (see Eq. (5.3.37)) predicted by the perturbation and numerical methods are comparable.

In Figure 5.11, the maximum response obtained via perturbation solution Eq. (5.3.48) in the neighborhood of third-order superharmonic resonance is compared against that obtained by the numerical method. Similar to the case of second-order superharmonic resonance, both methods yield comparable solutions up to 5°. At flapping amplitudes of 5° and above, the perturbation solution overestimates the numerical solution. In particular there is a marked difference between the solutions on righthand side of the resonance peak. We attribute this result to the discrepancy between the phases γ estimated by the two methods. Toward this end, we note that there are higher order terms (ϵ^4, ϵ^6,...) which multiply $\cos(3\omega_f t)$, $\sin(3\omega_f t)$, *etc.*; e.g., the term $2aK_{I9}\beta_1\beta_2\cos(3\omega_f t)$ in Eq. (I.2). They are all taken into account in the numerical solution but are not included in the perturbation solution. Similar issues

related to third-order superharmonic resonance was noted in Reference [71].

Figure 5.12 shows comparison of the perturbation solution with the numerical solution in the vicinity of primary resonance. The first-order perturbation solution a_{max} presented in the figure is based upon Eq. (5.3.65). We note in Figure 5.12a that, when the dissipation mechanism is modeled as linear viscous damping, the time-spectral numerical scheme does not converge over a range of frequencies in the primary resonance region. One can also observe in Figure 5.12a that the perturbation solution reveals bending of resonance peak to the right at flapping amplitudes greater than 1°. Regardless of the damping model considered, the solutions obtained via both methods are in good agreement at 1°. In the case of nonlinear damping, Figure 5.12b, both methods reveal broad resonance peaks whose amplitude is comparable at $\omega_0 = 1.0$ for flapping at 3°, 5°, and 10°. In Figure 5.12b, we notice that at higher flapping amplitudes (3°-15°), the perturbation solution overestimates the numerical solution at frequencies below $\omega_0 \approx 1.0$ and underestimates the numerical solution at frequencies above $\omega_0 \approx 1.0$. Once again this would indicate the discrepancy in the phase γ predicted by the two methods. A higher order perturbation solution would likely diminish this error.

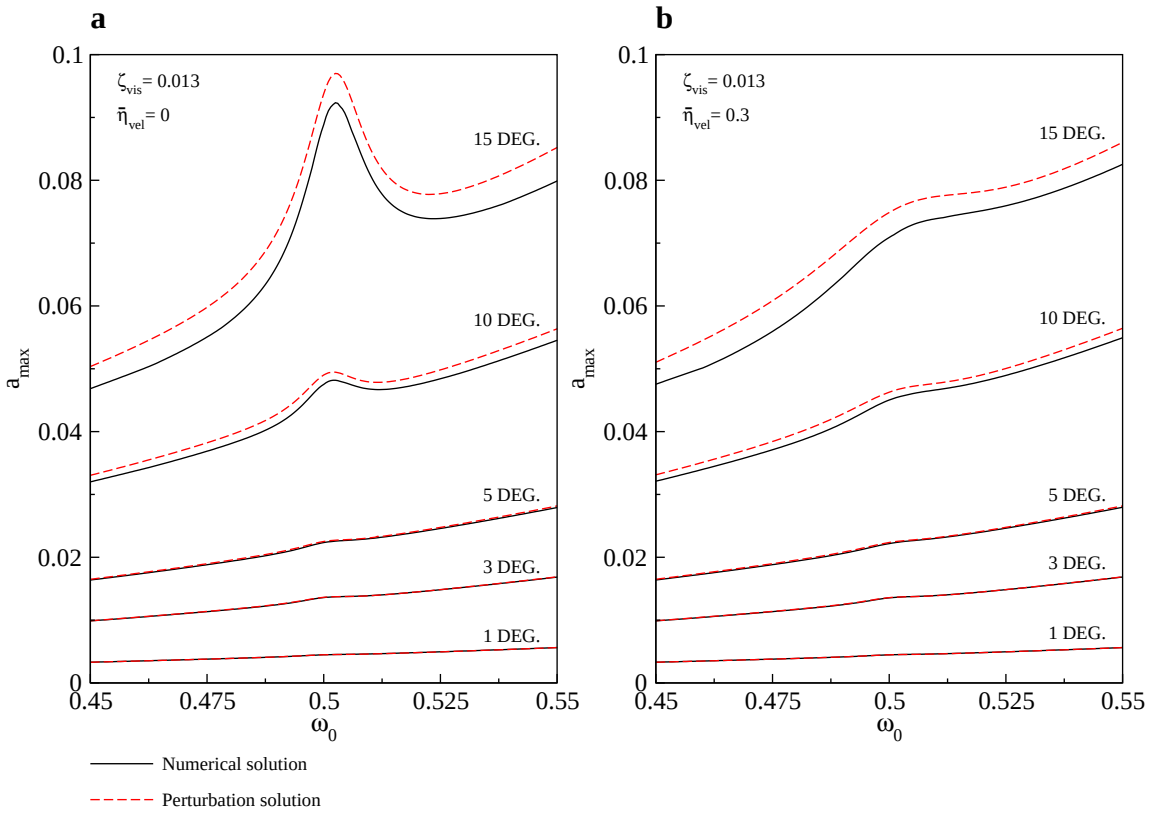

Figure 5.10: Comparison of perturbation solution with the time-spectral numerical solution for the case of second-order superharmonic resonance with (a) linear viscous damping and (b) nonlinear velocity 3rd power damping.

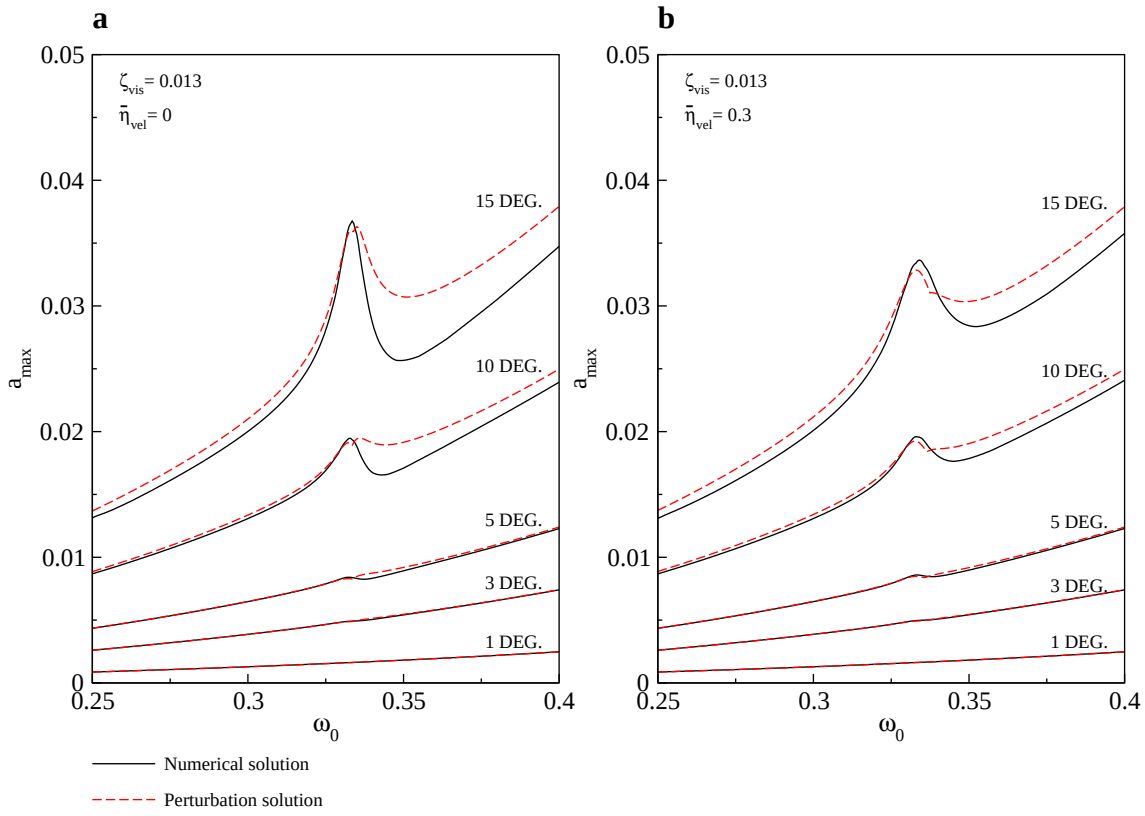

Figure 5.11: Comparison of perturbation solution with the time-spectral numerical solution for the case of third-order superharmonic resonance with (a) linear viscous damping and (b) nonlinear velocity 3rd power damping..

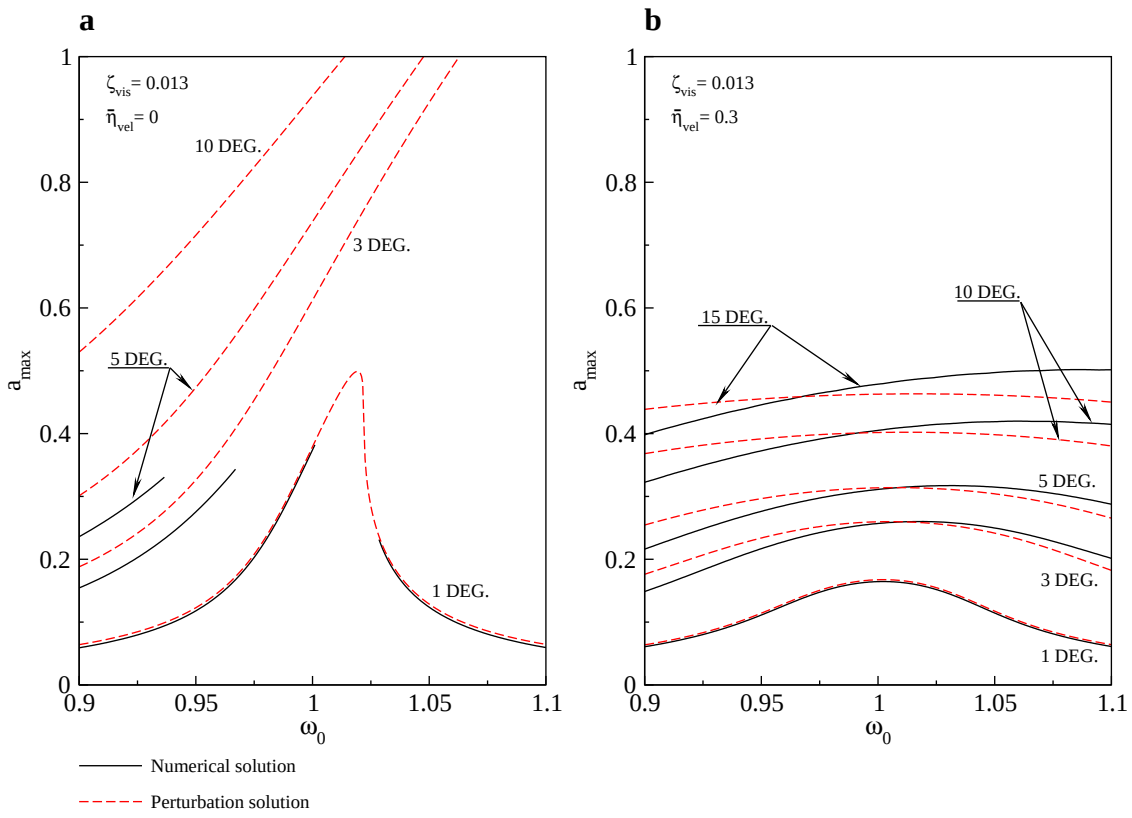

Figure 5.12: Comparison of perturbation solution with the time-spectral numerical solution for the case of primary resonance with (a) linear viscous damping and (b) nonlinear velocity 3rd power damping..

5.5 Chapter Summary

In this chapter, the effect of excitation and damping parameters on the second- and third-order superharmonic and primary resonance responses of a slender cantilever beam set into flapping motion is analytically studied via method of multiple time scales. The flapping excitation is assumed to be composed of two sine waves of the fundamental and second harmonics. Linear viscous and nonlinear velocity 3rd-power damping models are considered as the dissipative forces acting on the beam. Modulation equations governing the amplitude

and phase of the superharmonic and harmonic oscillations are derived and used to construct first-order approximation of steady-state solutions and their stability. In order to assess the accuracy of first-order perturbation solutions, the resonance curves obtained at different flapping amplitudes are compared with those obtained with high fidelity time-spectral numerical method.

Analysis of the frequency-response equations revealed that in order for the existence of free oscillation term leading to second-order and third-order superharmonic resonances, the excitation amplitudes associated with the second and fundamental harmonics, b_2 and b_1, respectively, must be nonzero. This also means that flapping excitation in the form of a simple harmonic function does not trigger the second-order superharmonic resonance. Likewise, it was shown that for the existence of primary resonance, amplitude of the fundamental harmonic of the excitation, b_1, must be nonzero.

The frequency-response curves for the second-order superharmonic resonance case show that there exists a minimum excitation amplitude $b_{2,cr}$ above which bistable solutions exist. When damping is considered to be linear viscous, $b_{2,cr}$ is a function of the linear viscous damping coefficient ζ_{vis} only and is not dependent on the amplitude b_1. However, when nonlinear damping is considered, $b_{2,cr}$ is a function of b_1 and damping coefficients ζ_{vis} and η_{vel}. The analytical results for $b_{2,cr}$ are found to be consistent with the experimental and numerical results presented in Chapters 3 and 4. The effect of increasing excitation amplitude b_1 is determined to be only shifting the response curve to the right in the case of linear damping. When damping is nonlinear, increasing excitation amplitude b_1, which is then coupled with η_{vel}, not only shifts the response curve but also amplifies the effect of the nonlinear damping force in a manner to diminish the peak amplitude and the hardening-spring type

nonlinearity. Comparing the response curves obtained with different types of damping models, we noted that the nonlinear damping widens the response curve and results in large frequency bandwidth in the vicinity of the 2nd-order superharmonic resonance peak.

The third-order superharmonic resonance was determined to be independent of the excitation amplitude b_2 for the first order approximation. The effect of increasing b_1 was determined to be threefold regardless of the damping models considered: increasing the peak response amplitude, augmenting nonlinearity and increasing the region of bistability, and shifting the curve to the right. Influence of ζ_{vis} on the critical excitation amplitude $b_{1,cr}$ was determined to resemble a "logarithmic growth" for a given η_{vel}. On the other hand, the effect of increasing η_{vel} on the $b_{1,cr}$ appears to be similar to "exponential growth" for a constant value of ζ_{vis}. Similar to the case of second order superharmonic resonance, the analytical results for $b_{1,cr}$ are found to be in agreement with the numerical and experimental results presented in Chapters 3 and 4.

With regards to primary resonance, due to the nonlinear coupling of response amplitude and η_{vel} revealed by the frequency-response equation, increasing the nonlinear damping coefficient η_{vel} resulted in broader resonance peaks which tend to flatten out as the peak amplitude decreases. On the other hand, for the case with linear viscous damping only, the effect of increasing ζ_{vis} for a given excitation merely gave rise to diminishing of the peak amplitudes without broadening distortion.

The frequency-response curves obtained at different flapping amplitudes up to 15° are compared with those given by a time-spectral numerical method. In the case of second-order superharmonic resonance, regardless of the damping

type, the first-order perturbation solution is determined to be in very good agreement with the numerical solution up to 5°. As the flapping amplitude is increased beyond 5°, perturbation solution overestimates the numerical solution. Regarding the third-order superharmonic resonance curves, both methods yield comparable solutions up to 5° and perturbation solution overestimates the numerical solution at 5° and above. For third-order superharmonic resonance, a marked difference between the solutions is noted at frequencies which are larger than the resonance frequency is attributed to the discrepancy between the phases estimated by the two methods. This discrepancy in the phase prediction is also thought to exist in the primary resonance case for flapping larger than 1°.

CHAPTER 6

Concluding Remarks

6.1 Scope of the Chapter

In this chapter we will attempt to summarize and tie together the results of this dissertation and relate them to the research goal. Towards this end, in Section 6.2 the main results of the dissertation will be given and discussed in the context of how each adds to the current state of the art along with how the results can be used to further both theoretical and experimental research in this area. Section 6.3 summarizes individual chapter results and can be considered as a supplement to the more detailed summaries given in Sections 3.6, 4.8 and 5.5. Finally, in Section 6.4 recommendations for future research are discussed with additional material given in Appendix I for one of these topics.

6.2 Summary of Main Results

The nonlinear dynamics of a single flapping (aluminum) beam configuration, actuated at its base through a 4-bar crank-and-rocker mechanism has been investigated through experiment, numerical and approximate analytical methods. Experimental results, in the form of both bending strain and tip deflection data, indicate that for the tested flapping amplitudes (15° and 30°) and frequencies (up to, and slightly beyond, the first modal frequency) investigated, the dynamic response of the beam is planar and regular (time periodic) in both

ambient and reduced air pressure environments. Results also indicate that superharmonic resonances are present and that for a given flapping frequency and amplitude there exists only a single stable solution. The knowledge that the response is both planar and periodic is beneficial in a number of different areas including the design of control laws, choice of theoretical models and numerical algorithms for simulation, and methods to be used for approximate analytical solution. The existence of superharmonic resonances is also important as it may be possible to utilize such a characteristic to improve an efficiency metric such as the ratio of input power to output response (e.g., tip deflection, bending strain, etc.) by flapping in a region of superharmonic resonance.

Numerical simulation using a high fidelity computational model (nonlinear finite element beam model) determined that while the experimental response could be predicted quite well away from resonances, thus validating a number of simulation assumptions (e.g., planar response and linear elasticity assumptions, ignoring actuation mechanism/beam interaction). However, near the resonance conditions (both superharmonic and primary), the simulation was unable to predict the quantitative and qualitative characteristics of the experimental response. Being interesting from a nonlinear dynamics perspective, in this single equilibrium point system a number of response bifurcations occur resulting in aperiodic responses. While for the experimental conditions present in this work these aperiodic solutions did not exist, these simulation results are important in that they indicate the existence of such solutions which could perhaps be realized under different experimental conditions.

In order to explore the abovementioned differences in simulation and experiment at resonance conditions, a reduced order model (inextensible beam;

1-mode Galerkin discretization; time-spectral temporal discretization) for the beam dynamics was used in conjunction with various simple (1 or 2 parameter) nonlinear damping models. The main conclusion from this work was that a single parameter velocity-cubed (damping force $\propto \dot{v}^3$) external damping model best matched the experimental results. Other damping models investigated included a 2-parameter internal damping mechanism and a 1-parameter displacement-squared model (damping force $\propto v^2\dot{v}$). In addition, it was found that changing the experimental conditions (flapping conditions and surrounding air pressure) resulted in a change in the empirical parameter of the model. While the constant was of the same order of magnitude for the various conditions, this lack of invariance is likely due to an incomplete parameter dependence and/or functional form for the damping model. Overall the results indicate that the simple damping model used should be of sufficient accuracy to be utilized in circumstances when low-order simulations are required, e.g., when real-time simulation is necessary. While fully coupled aeroelastic simulation would provide more accurate results without the need for empirically determined constants, parameter studies and control applications require computational efficiency which is still only afforded through the use of low-dimensional or analytical solutions. The results do indicate, however, that in cases where flapping amplitude is large, higher fidelity solution (e.g., aeroelastic simulation) may be required in order to, at least, qualitatively predict the response near resonance conditions.

As mentioned in the previous paragraph, approximate analytical solutions can provide the efficiency necessary for applications requiring real-time computation. In addition, analytical solutions can give direct insight into the parameter dependence for various response characteristics. As such, a first or-

der multiple scale perturbation solution was found for second and third order superharmonic resonances and primary resonance. As noted above, experimental and simulation results indicate that bistability does not occur for the experimentally realized beam configuration. Our analytical results corroborate this while giving conditions for which bistability will occur. In addition, our analytical solution shows that in order for second order superharmonic resonance to occur, the boundary actuation mechanism must contain the second harmonic of flapping frequency. This result confirms numerical simulation, not shown in this thesis, whereby second order superharmonic resonance was non-existent when the flapping actuation was a pure sine wave. This result can be used to design an actuation mechanism which attempts to either utilize, or negate, the second order superharmonic resonance response.

In summary, in this thesis various aspects of the complex problem of flapping beam dynamics have been explored and characterized. While there are many additional areas which could be explored, some of which are mentioned in Section 6.4, the main results of this dissertation detailed above should prove to be beneficial for various applications which have configurations similar to (or which can be approximated by) the studied flapping beam configuration.

6.3 Chapter Summaries

In Chapter 3, the structural dynamics of a slender aluminum beam in flapping motion was investigated through experiment and numerical simulation. The experimental and computational surface bending strain and tip displacement data were comparatively analyzed in time and frequency domains. For the majority of tested flapping frequencies, the simulation was determined

to be in good quantitative agreement with the experiment. For flapping at 15°, the experimental frequency response curve was noted to overestimate the simulation frequency response curve at flapping frequencies in the vicinity of superharmonic and primary resonances. On the other hand the experimental frequency response curve for flapping at 30° showed a broad peak at $\omega_0 = 0.43$ (43% of the first natural frequency), which is thought to be due to the third-order superharmonic resonance. The discrepancy between the experimental and simulation results was primarily attributed to a non-linear dependence of the dissipative forces on the beam response and, subsequently, to the use of linear viscous damping model in the simulation. Qualitative changes in the beam tip response dynamics were investigated as the flapping frequency and amplitude were varied in the simulations. For flapping at 15°, it was found that as the flapping frequency is increased from below the region of superharmonic resonance through the region of primary resonance, various transitions occur between symmetric 1-period response, quasi-periodic motions and irregular motions. The simulations carried out at 30° revealed observations similar to those made at 15°, while a small region of irregular response at frequencies corresponding to the second-order superharmonic resonance was noted as well. The numerical simulations performed for a range of flapping amplitudes up to 30° revealed a transition from 1-period periodic motion to aperiodic motion at 28° and 11° for flapping at $\omega_0 = 0.50$ and $\omega_0 = 1.10$, respectively.

In Chapter 4, the effect of non-linear damping on the structural dynamics of flapping beams was investigated via experiment and numerical simulation. The results showed that the non-linear damping models better represent the damping forces acting on the flapping beam when compared to the linear viscous and non-linear internal damping models. For flapping at 15°, each of

the non-linear external damping models yielded more accurate predictions for the experimental frequency response curves outside of the frequency region in which the damping coefficient was determined. In the region of primary resonance, the velocity 3rd-power damping model was determined to better predict the experimental response. For flapping at 30°, the broadening of the experimental frequency-response curve in the secondary resonance region was not accurately captured by the simulation, perhaps indicating unmodeled physics related to non-linear elasticity, friction damping in the mechanism, or beam-mechanism dynamic interaction. The non-dimensional coefficients of non-linear damping models were determined to vary with changing ambient pressure and flapping amplitude. While these changes could be because of unmodeled physics not related to damping, it is likely that this result is due to incomplete coefficient dependence and/or non-linear functional forms of the damping models. The simulations which utilize a linear viscous damping model suggested that the periodic response loses stability at some frequencies. On the other hand, the simulations with the non-linear damping models corroborated the experimental evidence and predicted stable periodic response for the tested flapping frequencies and amplitudes.

In Chapter 5, the effect of excitation and damping parameters on the second- and third-order superharmonic and primary resonance responses of flapping beams is studied via the method of multiple scales. The flapping excitation is assumed to be composed of two sine waves of the fundamental and second harmonics with amplitudes of b_1 and b_2, respectively. Linear viscous and non-linear velocity third power damping models, with coefficients ζ_{vis} and η_{vel}, are considered as the dissipative forces acting on the beam. Analysis of the frequency-response equations revealed that in order for the existence free

oscillation term leading to second- and third-order superharmonic resonances, the excitation amplitudes b_2 and b_1, respectively, must be nonzero. There exist a minimum excitation amplitude $b_{2,cr}$ above which the second-order superharmonic frequency-response curve reveals bistable solutions. When damping is considered to be linear viscous, $b_{2,cr}$ is a function of ζ_{vis} only whereas it is a function of b_1, ζ_{vis} , and η_{vel} when non-linear damping is considered. Comparison of the response curves obtained with different damping models showed that the non-linear damping widens the curve and results in large frequency bandwidth in the vicinity of second-order superharmonic resonance peak. At third-order superharmonic resonance, the effect of increasing b_1 was determined to be threefold regardless of the damping model considered: increasing the peak response amplitude, augmenting non-linearity and increasing the region of bistability, and shifting the curve to the right. The primary resonance frequency-response equation revealed that due to the non-linear coupling of response amplitude and η_{vel}, increasing η_{vel} resulted in broader resonance peaks which tend to flatten out as the peak amplitude decreases.

The frequency-response curves obtained at different flapping amplitudes up to 15° are compared with those given by a time-spectral numerical method. In the case of second-order superharmonic resonance, regardless of the damping type, the first-order perturbation solution is determined to be in very good agreement with the numerical solution up to 5°. As the flapping amplitude is increased beyond 5°, perturbation solution overestimates the numerical solution. Regarding the third-order superharmonic resonance curves, both methods yield comparable solutions up to 5° and perturbation solution overestimates the numerical solution at 5° and above. For third-order superharmonic resonance, a marked difference between the solutions is noted at frequencies

which are larger than the resonance frequency is attributed to the discrepancy between the phases estimated by the two methods. This discrepancy in the phase prediction is also thought to exist in the primary resonance case for flapping larger than 1°.

6.4 Recommendations for Future Work

6.4.1 Characterization of Air Damping

In Chapter 4 we demonstrated, based on the experimental evidence, that the non-linear damping models better represent the physical damping forces acting on the cantilever beam undergoing large amplitude flapping motion when compared to the linear viscous model. In particular, we determined that the velocity 3rd-power damping model provides the best estimate for the experimental frequency-response curves. That the damping forces are linearly dependent on the air density was found to be appropriate as evidenced from the results obtained at different air pressures. However, the prediction accuracy for the response amplitude worsened as the flapping amplitude is increased from 15° to 30°. Discrepancies observed between the experiment and simulation were primarily attributed to incomplete description of the model parameter dependence and/or non-linear functional form of the damping force.

The simulations were performed using a theoretical model which incorporates simple non-linear damping models of the forms $c_{vel}\dot{v}^3$ or $c_{disp}v^2\dot{v}$ into a non-linear inextensible beam theory. The variables on which the damping coefficients are dependent are not identified clearly as these coefficients are determined from the experimental data through an error minimization scheme. As mentioned earlier, such simple analytical models for damping have been

used to compensate for the inability, or unwillingness, to solve the true fluid-structure interaction problem. In this regard, a future work would aim at identifying the dependence of the damping coefficients on the all-important flapping variables such as flapping amplitude and frequency by using computational fluid dynamics (CFD) tools. If the computational cost of the CFD model can be kept at a reasonable level, the dependence of damping coefficients on the flapping variables can be identified parametrically in a practical manner. The experimental data can then be used for validation purposes.

In future work, the fluid motion around the flapping beam can be regarded as an incompressible viscous flow. In order to limit the computational expense, the flow domain can be modeled two dimensional and the flapping beam can be thought of as an undulating rigid filament in the planar fluid domain. This type of simplified fluid-structure interaction models have been used recently in the studies concerning the fluid forces acting on cantilever beams and plates [52, 57, 59]. In this regard, the oscillating rigid filament represents any cross section of the slender beam structure. The functional form determined for the fluid force acting on the rigid filament can then be substituted for the *damping force per unit length*, f_d, in the equation of motion, (4.3.1), given for the inextensible beam. A class of two-dimensional incompressible Navier-Stokes schemes such as the vorticity-stream function formulation [145] can be implemented for the numerical solution. The fluid forces acting on the oscillating rigid filament can be computed for a range oscillation amplitudes and frequencies. The force data computed for a range of amplitudes and frequencies can be fitted to a function which happens to be the functional form of the damping force per unit length of the flapping beam.

In addition to the work suggested above, future work which is an immediate

extension of the research presented this dissertation would be to use a different mathematical model for air damping while staying in the framework given in Chapter 4. The ideas related to this later work are developed in Appendix K.

6.4.2 Compliant Clamp and Flapping Mechanism

The efficient utilization of flapping energy which is drawn from a limited energy source is of prime importance. As a means of efficient energy utilization in the applications of flapping beams, excitation in the vicinity of superharmonic and primary resonances is considered and studied in detail in Chapter 5. Other possible strategies for maximizing the energy efficiency in the flapping beam applications would be the use of compliant flapping mechanisms and/or compliant clamps at the beam base.

The flapping mechanism can be employed to reduce energy consumption in flapping-wing MAVs. Flapping mechanisms with spring-supported revolute joints and links have been designed to better utilize torque input [146–148]. These so-called compliant mechanisms have shown that judicious use of elastic energy storage elements can increase energy efficiency by reducing the torque variation over a flapping cycle and peak torque requirement of the motor. In addition to energy efficiency concerns, miniaturization of MAV and ease of manufacturing process have led to compliant mechanisms [149]. Accordingly, the entire mechanism can expeditiously be manufactured from a single piece of plastic material via injection molding without creating any revolute joints or friction surfaces.

A rubber-like protein, *resilin*, has been known to exist in certain regions of the insect cuticle in the form of highly elastic structure [150]. The elastic "cushions" inserted between wing axillae, wing-hinge ligaments, and elastic

"patches" at the wing base are well-known resilin rich structures in the winged insects [150, 151]. It has been reported that the greatly increased movement of the wings is produced by the spring action in the wing base assisted by an elastic tensioning element in the thorax [152]. Recently, Mahjoubi and Byl [153] showed that adjusting stiffness of the wing joint can be used to regulate lift and thrust forces in flapping-wing MAVs.

Motivated by increasing the energy efficiency, the effect of compliant clamp or mechanism on the structural dynamics of flapping beams can be studied in a future work. As such, a pair of highly elastic patches of certain thickness can be inserted between the beam and clamping surface. With this setting the problem can be viewed as a special version of the vibration of cantilever beams on partial elastic foundation [154–157]. The approach of the study would be similar to the one presented in Chapter 4. The equations of motion for the cantilever beam with elastically-supported clamp edge can be derived by using the Hamilton's principle. The length of the beam which is sandwiched between the elastic patches inside the clamp can be modeled as a beam span with partial elastic foundation.

6.4.3 Passive Twisting with Laminated Composite Flapping Beam

The occurrence of twisting deformation (torsion) in insect wings has been known since the early high-speed cinematographic data collected from insect species and is regarded as having a key role in hovering flight of insects [158, 159]. Insects have very limited, if any, control over the deformation of their wings. Therefore, it appears that passively inducing twisting deformation in flapping beams would have potential benefits from an aerodynamics perspective and remains as a fruitful research area for a future work.

A certain class of fiber-reinforced polymeric composite laminates is known to exhibit *bending-twisting coupling* [160]. This behavior of the composites has been utilized in forward-swept wing aircrafts to suppress undesired aerodynamic twisting and termed as aeroelastic tailoring [161]. Symmetric, angle-ply laminates with stacking sequences $[\pm\theta]_s$ (where θ represents ply orientation with respect to the x-axis of laminate coordinate system, subscript s stands for "symmetric") belong to the above-mentioned class of laminated composite materials. Accordingly, a beam made out of a symmetric angle-ply laminate not only bends in the spanwise direction but it also twists at the same time about its longitudinal axis.

In a future work, symmetric angle-ply laminated composite beams of different stacking configurations can be studied. As such, the effect of aerodynamic loads on passive twisting behavior of the flapping beams can be investigated at different flapping frequencies and amplitudes by performing experiments in atmospheric and reduced air pressures.

Bibliography

[1] J. Chung and H. H. Yoo. Dynamic analysis of a rotating cantilever beam by using the finite element method. *Journal of Sound and Vibration*, 249:147–164, 2002.

[2] J. B. Kosmatka and P. P. Friedmann. Vibration analysis of composite turbopropellers using a nonlinear beam-type finite-element approach. *AIAA Journal*, 27:1606–1614, 1989.

[3] D. Younesian and E. Esmailzadeh. Non-linear vibration of variable speed rotating viscoelastic beams. *Nonlinear Dynamics*, 60:193–205, 2010.

[4] H. Arvin and F. Bakhtiari-Nejad. Non-linear modal analysis of a rotating beam. *International Journal of Non-linear Mechanics*, 46:877–897, 2011.

[5] M. Abolghasemi and M. A. Jalali. Attractors of a rotating viscoelastic beam. *International Journal of Non-linear Mechanics*, 38:739–751, 2003.

[6] D. Wang and M. Meng. Frequency analysis of a flexible rotor manipulator. In *Proceedings of the IEEE Canadian Conference on Electrical and Computer Engineering*, 1403-1407, Edmonton, Canada, May 9-12, 1999.

[7] P. J. Murtagh, B. Basu, and B. M. Broderick. Along-wind response of a wind turbine tower with blade coupling subjected to rotationally sampled wind loading. *Engineering Structures*, 27:1209–1219, 2005.

[8] W. Shyy, M. Berg, and D. Ljungqvist. Flapping and flexible wings for biological and micro air vehicles. *Progress in Aerospace Sciences*, 35:455–505, 1999.

[9] A. G. Norris, A. N. Palazotto, and R. G. Cobb. Structural dynamic characterization of an insect wing. In *51st AIAA/ASME/ASCE/AHS/ASC Structures, Structural Dynamics, and Materials Conference*, AIAA-2010-2790, Orlando, FL, Apr 12-15, 2010.

[10] A. Barut, M. Das, and E. Madenci. Nonlinear deformations of flapping wings on a micro air vehicle. In *47th AIAA/ASME/ASCE/AHS/ASC Structures, Structural Dynamics, and Materials Conference*, AIAA-2006-1662, Newport, RI, May 1-4, 2006.

[11] P. Wu, P. Ifju, and B. Stanford. Flapping wing structural deformation and thrust correlation study with flexible membrane wings. *AIAA Journal*, 48(9):2111–2122, 2010.

[12] R. E. Gordnier, S. K. Chimakurthi, C. E. S. Cesnik, and P. J. Attar. High-fidelity aeroelastic computations of a flapping wing with spanwise flexibility. *Journal of Fluids and Structures*, 40:86–104, 2013.

[13] P. Valdivia y Alvarado and K. Youcef-Toumi. Design of machines with compliant bodies for biomimetic locomotion in liquid environments. *Journal of Dynamic Systems, Measurement, and Control*, 128(1):3–13, 2006.

[14] P. L. Nguyen, V. P. Do, and B. R. Lee. Dynamic modeling and experiment of a fish robot with a flexible tail fin. *Journal of Bionic Engineering*, 10:39–45, 2013.

[15] V. Kopman and M. Porfiri. Design, modeling, and characterization of a miniature robotic fish for research and education in biomimetics and bioinspiration. *IEEE/ASME Transactions on Mechatronics*, 18:471–483, 2013.

[16] V. Kopman, J. Laut, F. Acquaviva, A. Rizzo, and M. Porfiri. Dynamic modeling of a robotic fish propelled by a compliant tail. *IEEE Journal of Oceanic Engineering*, 40:209–221, 2015.

[17] J. A. Dunnmon, S. C. Stanton, B. P. Mann, and E. H. Dowell. Power extraction from aeroelastic limit cycle oscillations. *Journal of Fluids and Structures*, 27:1182–1198, 2011.

[18] A. Erturk and G. Delporte. Underwater thrust and power generation using flexible piezoelectric composites: an experimental investigation toward self-powered swimmer-sensor platforms. *Smart Materials and Structures*, 20:125013(1–11), 2011.

[19] Y. Cha, H. Kim, and M. Porfiri. Energy harvesting from underwater base excitation of a piezoelectric composite beam. *Smart Materials and Structures*, 22(11):115026(1–14), 2013.

[20] J. Young, J. C. S. Lai, and M. F. Platzer. A review of progress and challenges in flapping foil power generation. *Progress in Aerospace Sciences*, 67:2–28, 2014.

[21] Q. Xiao and Q. Zhu. A review on flow energy harvesters based on flapping foils. *Journal of Fluids and Structures*, 46:174–191, 2014.

[22] A. H. Nayfeh and D. T. Mook. *Nonlinear Oscillations*. John Wiley & Sons Inc., New York, NY, 1979.

[23] F. C. Moon. *Chaotic and Fractal Dynamics: An Introduction for Applied Scientists and Engineers*. John Wiley & Sons Inc., New York, 1992.

[24] S. H. Strogatz. *Nonlinear Dynamics and Chaos: With Applications to Physics, Biology, Chemistry, and Engineering*. Addison-Wesley Pub., Reading, MA, 1994.

[25] F. C. Moon. Experiments on chaotic motions of a forced nonlinear oscillator: strange attractors. *Journal of Applied Mechanics*, 47:638–644, 1980.

[26] D. M. Tang and E. H. Dowell. On the threshold force for chaotic motions for a forced buckled beam. *Journal of Applied Mechanics*, 55:190–196, 1988.

[27] P. J. Holmes and F. C. Moon. Strange attractors and chaos in nonlinear mechanics. *Journal of Applied Mechanics*, 50:1021–1032, 1983.

[28] F. C. Moon and S. W. Shaw. Chaotic vibrations of a beam with nonlinear boundary conditions. *International Journal of Non-Linear Mechanics*, 18(6):465–477, 1983.

[29] N. S. Abhyankar, E. K. Hall, II, and S. V. Hanagud. Chaotic vibrations of beams: numerical solution of partial differential equations. *Journal of Applied Mechanics*, 60:167–174, 1993.

[30] E. K. Hall, II and S. V. Hanagud. Chaos in a single equilibrium point system: finite deformations. *Nonlinear Dynamics*, 2:157–170, 1991.

[31] W.-Y. Tseng and J. Dugundji. Nonlinear vibrations of a buckled beam under harmonic excitation. *Journal of Applied Mechanics*, 38:467–476, 1971.

[32] D. H. Hodges, X. Shang, and C. E. S. Cesnik. Finite element solution of nonlinear intrinsic equations for curved composite beams. *Journal of the American Helicopter Society*, 41:313–321, 1996.

[33] L. N. Virgin. *Introduction to Experimental Nonlinear Dynamics: A Case Study in Mechanical Vibration*. Cambridge University Press, New York, NY, 2000.

[34] P. Malatkar. *Nonlinear Vibrations of Cantilever Beams and Plates*. Ph.D. thesis, Virginia Polytechnic Institute and State University, 2003.

[35] P. F. Pai and A. H. Nayfeh. Non-linear non-planar oscillations of a cantilever beam under lateral base excitations. *International Journal of Non-Linear Mechanics*, 25(5):455–474, 1990.

[36] A. H. Nayfeh and P. F. Pai. Non-linear non-planar parametric responses of an inextensional beam. *International Journal of Non-Linear Mechanics*, 24(2):139–158, 1989.

[37] H. N. Arafat, A. H. Nayfeh, and C.-M. Chin. Nonlinear nonplanar dynamics of parametrically excited cantilever beams. *Nonlinear Dynamics*, 15:31–61, 1998.

[38] L. D. Zavodney and A. H. Nayfeh. The non-linear response of a slender beam carrying a lumped mass to a principal parametric excitation: theory and experiment. *International Journal of Non-Linear Mechanics*, 24(2):105–125, 1989.

[39] C. L. Zaretzky and M. R. M. Crespo da Silva. Experimental investigation of non-linear modal coupling in the response of cantilever beams. *Journal of Sound and Vibration*, 174(2):145–167, 1994.

[40] W. Zhang, F. Wang, and M. Yao. Global bifurcations and chaotic dynamics in nonlinear nonplanar oscillations of a parametrically excited cantilever beam. *Nonlinear Dynamics*, 40:251–279, 2005.

[41] R. D. Mindlin and L. E. Goodman. Beam vibrations with time-dependent boundary conditions. *Journal of Applied Mechanics*, 17(4):377–380, 1950.

[42] G. Herrmann. Forced motions of Timoshenko beams. *Journal of Applied Mechanics*, 22:53–56, 1955.

[43] J. G. Berry and P. M. Naghdi. On the vibration of elastic bodies having time-dependent boundary conditions. *Quarterly of Applied Mathematics*, 14:43–50, 1956.

[44] K. S. Aravamudan and P. N. Murthy. Non-linear vibration of beams with time-dependent boundary conditions. *International Journal of Non-Linear Mechanics*, 8:195–212, 1973.

[45] S. M. Lin and S. Y. Lee. The forced vibration and boundary control of pretwisted Timoshenko beams with general time dependent elastic boundary conditions. *Journal of Sound and Vibration*, 254:69–90, 2002.

[46] E. A. Paraskevopoulos, C. G. Panagiotopoulos, and G. D. Manolis. Imposition of time-dependent boundary conditions in FEM formulations for elastodynamics: critical assessment of penalty-type methods. *Computational Mechanics*, 45:157–166, 2010.

[47] B. Stanford, P. Beran, and M. Kurdi. Model reduction strategies for nonlinear beams subjected to large rotary actuations. *The Aeronautical Journal*, 113(1150):751–762, 2009.

[48] M. Kimber, S. V. Garimella, and A. Raman. Local heat transfer coefficients induced by piezoelectrically actuated vibrating cantilevers. *Journal of Heat Transfer*, 129:1168–1176, 2007.

[49] S. F. Sufian, M. Z. Abdullah, and J. J. Mohamed. Effect of synchronized piezoelectric fans on microelectronic cooling performance. *International Communications in Heat and Mass Transfer*, 43:81–89, 2013.

[50] B. J. Lazan. *Damping of Materials and Members in Structural Mechanics*. Pergamon Press, Oxford, 1968.

[51] C. W. Bert. Material damping: an introductory review of mathematical models, measures and experimental techniques. *Journal of Sound and Vibration*, 29(2):129–153, 1973.

[52] M. Aureli, M. E. Basaran, and M. Porfiri. Nonlinear finite amplitude vibrations of sharp-edged beams in viscous fluids. *Journal of Sound and Vibration*, 331:1624–1654, 2012.

[53] J. R. Morison, M. P. O'Brien, J. W. Johnson, and S. A. Schaaf. The force exerted by surface waves on piles. *Petroleum Transactions of AIME*, 189:149–154, 1950.

[54] T. Sarpkaya. Resistance in unsteady flow: search for an in-line force model. *International Journal of Offshore and Polar Engineering*, 10(4):249–254, 2000.

[55] A. L. Facci and M. Porfiri. Nonlinear hydrodynamic damping of sharp-edged cantilevers in viscous fluids undergoing multi-harmonic base excitation. *Journal of Applied Physics*, 112:124908(1–9), 2012.

[56] T. Sarpkaya. On the force decompositions of Lighthill and Morison. *Journal of Fluids and Structures*, 15:227–233, 2001.

[57] R. A. Bidkar, M. Kimber, A. Raman, A. K. Bajaj, and S. V. Garimella. Nonlinear aerodynamic damping of sharp-edged flexible beams oscillating at low Keulegan-Carpenter numbers. *Journal of Fluid Mechanics*, 634:269–289, 2009.

[58] G. K. Batchelor. *An Introduction to Fluid Dynamics*. Cambridge University Press, Cambridge, 2000.

[59] M. A. Jones. The separated flow of an inviscid fluid around a moving flat plate. *Journal of Fluid Mechanics*, 496:405–441, 2003.

[60] T. Sarpkaya. Hydrodynamic damping, flow-induced oscillations, and biharmonic response. *Journal of Offshore Mechanics and Arctic Engineering*, 117(4):232–238, 1995.

[61] J. E. Sader. Frequency response of cantilever beams immersed in viscous fluids with applications to the atomic force microscope. *Journal of Applied Physics*, 84:64–76, 1998.

[62] M. Aureli and M. Porfiri. Low frequency and large amplitude oscillations of cantilevers in viscous fluids. *Applied Physics Letters*, 96:164102(1–3), 2010.

[63] K. C. Hall and S. R. Hall. Minimum induced power requirements for flapping flight. *Journal of Fluid Mechanics*, 323:285–315, 1996.

[64] K. Sibilski, J. Pietrucha, and M. Zlocka. The comparative evaluation of power requirements for fixed, rotary, and flapping wings micro air vehicles. In *AIAA Atmospheric Flight Mechanics Conference and Exhibit*, AIAA-2007-6498, Hilton Head, SC, Aug 20-23, 2007.

[65] K. H. Low and C. W. Chong. Parametric study of the swimming performance of a fish robot propelled by a flexible caudal fin. *Bioinspiration & Biomimetics*, 5(4):046002(1–12), 2010.

[66] Y.-J. Park, U. Jeong, J. Lee, S.-R. Kwon, H.-Y. Kim, and K.-J. Cho. Kinematic condition for maximizing the thrust of a robotic fish using a compliant caudal fin. *IEEE Transactions on Robotics*, 28(6):1216–1227, 2012.

[67] S. Timoshenko, D. H. Young, and W. Weaver, Jr. *Vibration Problems in Engineering*. John Wiley & Sons Inc., New York, 1974.

[68] G. Schmidt and A. Tondl. *Non-linear Vibrations*. Cambridge University Press, New York, 1986.

[69] A. H. Nayfeh. *Nonlinear Interactions: Analytical, Computational, and Experimental Methods*. John Wiley & Sons Inc., New York, NY, 2000.

[70] Z. Rahman and T. D. Burton. Large amplitude primary and superharmonic resonances in the Duffing oscillator. *Journal of Sound and Vibration*, 110(3):363–380, 1986.

[71] A. Hassan. On the third superharmonic resonance in the Duffing oscillator. *Journal of Sound and Vibration*, 172(4):513–526, 1994.

[72] H.-H. Dai, X.-K. Yue, and J.-P. Yuan. A time domain collocation method for obtaining the third superharmonic solutions to the Duffing oscillator. *Nonlinear Dynamics*, 73:593–609, 2013.

[73] C. T. Bolsman, J. F. L. Goosen, and F. van Keulen. Insect-inspired wing actuation structures based on ring-type resonators. In *Proceedings of the SPIE - Active and Passive Smart Structures and Integrated Systems Conference*, 692811(1-12), San Diego, CA, Mar 10-13, 2008.

[74] S. S. Baek, K. Y. Ma, and R. S. Fearing. Efficient resonant drive of flapping-wing robots. In *The 2009 IEEE/RSJ International Conference on Intelligent Robot and Systems*, 2854-2860, St. Louis, USA, Oct 11-15, 2009.

[75] H. Masoud and A. Alexeev. Resonance of flexible flapping wings at low Reynolds number. *Physical Review E*, 81:056304(1–5), 2010.

[76] M. Vanella, T. Fitzgerald, S. Preidikman, E. Balaras, and B. Balachandran. Influence of flexibility on the aerodynamic performance of a hovering wing. *The Journal of Experimental Biology*, 212:95–105, 2009.

[77] S. Ramananarivo, R. Godoy-Diana, and B. Thiria. Rather than resonance, flapping wing flyers may play on aerodynamics to improve performance. *PNAS (Proceedings of the National Academy of Sciences of the USA)*, 108(15):5964–5969, 2011.

[78] J. Zhu and C. Zhou. The aerodynamic performance of flexible wing in plunge. *Journal of Mechanical Science and Technology*, 28(7):2687–2695, 2014.

[79] H.-C. Chung, K. L. Kummari, S. J. Croucher, N. J. Lawson, S. Guo, R. W. Whatmore, and Z. Huang. Development of piezoelectric fans for flapping wing application. *Sensors and Actuators A: Physical*, 149(1):136–142, 2009.

[80] G. J. Lindholm and R. G. Cobb. Closed-loop control of a constrained, resonant-flapping micro air vehicle. *AIAA Journal*, 52(8):1616–1623, 2014.

[81] H. A. Sodano, D. J. Inman, and G. Park. A review of power harvesting from vibration using piezoelectric materials. *The Shock and Vibration Digest*, 36(3):197–205, 2004.

[82] M. F. Daqaq, R. Masana, A. Erturk, and D. D. Quinn. On the role of nonlinearities in vibratory energy harvesting: A critical review and discussion. *Applied Mechanics Reviews*, 66:040801(1–23), 2014.

[83] D. A. W. Barton, S. G. Burrow, and L. R. Clare. Energy harvesting from vibrations with a nonlinear oscillator. *Journal of Vibration and Acoustics*, 132:021009(1–7), 2010.

[84] W. E. Baker, W. E. Woolam, and D. Young. Air and internal damping of thin cantilever beams. *International Journal of Mechanical Sciences*, 9(11):743–766, 1967.

[85] M. L. Rasmussen. Non-linear oscillations with small speed-dependent damping. In *Developments in Mechanics, Vol. 7: Proceedings of the 13th Midwestern Mechanics Conference*, pp. 437–448, Pittsburgh, PA, 1973.

[86] C. Mei and C. B. Prasad. Effects of non-linear damping on random response of beams to acoustic loading. *Journal of Sound and Vibration*, 117:173–186, 1987.

[87] P. W. Smith, Jr., C. I. Malme, and C. M. Gogos. Nonlinear response of a simple clamped panel. *The Journal of the Acoustical Society of America*, 33(11):1476–1482, 1961.

[88] J. J. Uicker, Jr., G. R. Pennock, and J. E. Shigley. *Theory of Machines and Mechanisms*. Oxford University Press, New York, 4th ed., 2011.

[89] U.S. Department of Defense, *Metallic Materials and Elements for Aerospace Vehicle Structures*. Jan 31, 2003, Department of Defense Handbook MIL-HDBK-5J.

[90] J. P. Holman. *Experimental Methods for Engineers*. McGraw-Hill, New York, NY, 6th ed., 1994.

[91] R. C. Dove and P. H. Adams. *Experimental Stress Analysis and Motion Measurement*. Charles E. Merrill Books, Inc., Columbus, OH, 1964.

[92] J. W. Dally and W. F. Riley. *Experimental Stress Analysis*. McGraw-Hill, New York, NY, 2nd ed., 1978.

[93] Vishay Precision Group Micro-Measurements, Inc., Raleigh, NC, Tech Note TN-505-4 *Strain Gage Selection: Criteria, Procedures, Recommendations*. Nov 01, 2010, Document №: 11055.

[94] K. Hoffmann. *An Introduction to Measurements Using Strain Gages*. Hottinger Baldwin Messtechnik, GmbH, Darmstadt, Germany, 1989.

[95] Vishay Precision Group Micro-Measurements, Inc., Raleigh, NC, Instruction Bulletin B-129-8 *Surface Preparation for Strain Gage Bonding*. Aug 23, 2010, Document №: 11129.

[96] Vishay Precision Group Micro-Measurements, Inc., Raleigh, NC, Instruction Bulletin B-127-14 *Strain Gage Installations with M-Bond 200 Adhesive*. Jun 29, 2010, Document №: 11127.

[97] Vishay Precision Group Micro-Measurements, Inc., Raleigh, NC, Tech Note TN-508-1 *Fatigue Characteristics of Micro-Measurements Strain Gages*. Nov 01, 2010, Document №: 11058.

[98] M. A. Crisfield. *Non-linear Finite Element Analysis of Solids and Structures, Vol. 1: Essentials*. John Wiley & Sons Inc., Chichester, 1991.

[99] H. M. Hilber, T. J. R. Hughes, and R. L. Taylor. Improved numerical dissipation for time integration algorithms in structural dynamics. *Earthquake Engineering and Structural Dynamics*, 5:283–292, 1977.

[100] R. D. Cook, D. S. Malkus, M. E. Plesha, and R. J. Witt. *Concepts and Applications of Finite Element Analysis*. John Wiley & Sons Inc., Hoboken, 2002.

[101] P. J. Attar and R. E. Gordnier. High fidelity computational aeroelastic analysis of a plunging membrane airfoil. In *50th AIAA/ASME/ASCE/AHS/ASC Structures, Structural Dynamics, and Materials Conference*, AIAA-2009-2472, Palm Springs, CA, May 4-7, 2009.

[102] P. J. Attar. *ATFEM: A Non-Linear Finite Element Solver*. Personal communication, 2010.

[103] S. J. Chapman. *Fortran 95/2003 for Scientists and Engineers*. McGraw-Hill, Inc., New York, NY, 2008.

[104] T. Belytschko, W. K. Liu, and B. Moran. *Nonlinear Finite Elements for Continua and Structures*. John Wiley & Sons, Ltd., Chichester, 2000.

[105] J. Fish and T. Belytschko. *A First Course in Finite Elements*. John Wiley & Sons Inc., Chichester, 2007.

[106] Y. C. Fung and P. Tong. *Classical and Computational Solid Mechanics*. World Scientific Publishing Co. Pte. Ltd., River Edge, NJ, 2001.

[107] A. A. Shabana. *Computational Continuum Mechanics*. Cambridge University Press, New York, NY, 2012.

[108] J. T. Oden. *Finite Elements of Nonlinear Continua*. McGraw-Hill, New York, NY, 1972.

[109] N. M. Newmark. Computation of dynamic structural response in the range of approaching failure. In *Proceedings of the Symposium on Earthquake and Blast Effects on Structures*, Los Angeles, CA, Jun, 1952.

[110] N. M. Newmark. A method of computation for structural dynamics. *ASCE Journal of the Engineering Mechanics Division*, 85(EM3):67–94, 1959.

[111] T. J. R. Hughes. *The Finite Element Method: Linear Static and Dynamic Finite Element Element Analysis*. Dover Publications, Inc., Mineola, NY, 2000.

[112] S. C. Chapra and R. P. Canale. *Numerical Methods for Engineers: With Programming and Software Applications*. McGraw-Hill, Inc., Boston, MA, 1998.

[113] W. Szemplińska-Stupnicka and J. Rudowski. Local methods in predicting occurrence of chaos in two-well potential systems: superharmonic frequency region. *Journal of Sound and Vibration*, 152:57–72, 1992.

[114] C. Semler, G. X. Li, and M. P. Païdoussis. The non-linear equations of motion of pipes conveying fluid. *Journal of Sound and Vibration*, 169(5):577–599, 1994.

[115] L. Meirovitch. *Principles and Techniques of Vibrations*. Prentice-Hall Inc., Upper Saddle River, NJ, 1997.

[116] R. Courant and D. Hilbert. *Methods of Mathematical Physics, Volume 1*. Wiley-VCH Verlag, GmbH & Co. KGaA, Weinheim, Germany, 2004.

[117] T. J. Van Dyke and A. S. Wineman. Weakly nonlinear oscillations superimposed on finite circumferential shear of a compressible, nonlinear, viscoelastic, isotropic material. *Mathematics and Mechanics of Solids*, 5:203–240, 2000.

[118] P. J. Attar. Personal communication, 2014.

[119] O. J. Nastov. *Spectral Methods for Circuit Analysis*. Ph.D. thesis, Massachusetts Institute of Technology, 1999.

[120] K. C. Hall, J. P. Thomas, and W. S. Clark. Computation of unsteady nonlinear flows in cascades using a harmonic balance technique. *AIAA Journal*, 40:879–886, 2002.

[121] A. LaBryer and P. J. Attar. A harmonic balance approach for large-scale problems in nonlinear structural dynamics. *Computers and Structures*, 88:1002–1014, 2010.

[122] H.-H. Dai, M. Schnoor, and S. N. Atluri. A simple collocation scheme for obtaining the periodic solutions of the Duffing equation, and its equivalence to the high dimensional harmonic balance method: Subharmonic oscillations. *CMES-Computer Modeling in Engineering and Sciences*, 84(5):459–497, 2012.

[123] E. C. Titchmarsh. *The Theory of Functions*. Oxford University Press, London, UK, 1939.

[124] L. Liu, J. P. Thomas, E. H. Dowell, P. J. Attar, and K. C. Hall. A comparison of classical and high dimensional harmonic balance approaches for a Duffing oscillator. *Journal of Computational Physics*, 215(1):298–320, 2006.

[125] A. LaBryer and P. J. Attar. High dimensional harmonic balance dealiasing techniques for a Duffing oscillator. *Journal of Sound and Vibration*, 324:1016–1038, 2009.

[126] J. K. Hale. *Ordinary Differential Equations*. John Wiley & Sons Inc., New York, NY, 1969.

[127] A. H. Nayfeh and B. Balachandran. *Applied Nonlinear Dynamics Analytical, Computational, and Experimental Methods*. John Wiley & Sons Inc., New York, NY, 1995.

[128] A. Lazarus and O. Thomas. A harmonic-based method for computing the stability of periodic solutions of dynamical systems. *Comptes Rendus Mecanique*, 338:510–517, 2010.

[129] E. F. Crawley and M. C. van Schoor. Material damping in aluminum and metal matrix composites. *Journal of Composite Materials*, 21:553–568, 1987.

[130] C. M. Zener. *Elasticity and Anelasticity of Metals*. University of Chicago Press, Chicago, 1948.

[131] J. E. Ruzicka and T. F. Derby. *Influence of Damping in Vibration Isolation*. The Shock and Vibration Information Center, SVM-7, US Department of Defense, 1971.

[132] R. D. Blevins. *Flow-Induced Vibration*. Van Nostrand-Reinhold, New York, NY, 1990.

[133] J. K. Hale. *Oscillations in Nonlinear Systems*. McGraw-Hill, New York, NY, 1963.

[134] G. Kerschen, K. Worden, A. F. Vakakis, and J.-C. Golinval. Past, present and future of nonlinear system identification in structural dynamics. *Mechanical Systems and Signal Processing*, 20:505–592, 2006.

[135] O. Ozcelik and P. J. Attar. Effect of non-linear damping on the structural dynamics of flapping beams. *International Journal of Non-Linear Mechanics*, 65:148–163, 2014.

[136] D. Tang and E. H. Dowell. Limit cycle oscillations of two-dimensional panels in low subsonic flow. *International Journal of Non-Linear Mechanics*, 37:1199–1209, 2002.

[137] A. H. Nayfeh. *Perturbation Methods*. John Wiley & Sons Inc., New York, 1973.

[138] M. P. Cartmell, S. W. Ziegler, R. Khanin, and D. I. M. Forehand. Multiple scales analyses of the dynamics of weekly nonlinear mechanical systems. *Applied Mechanics Reviews*, 56(5):455–492, 2003.

[139] R. V. Ramnath. *Multiple Scales Theory and Aerospace Applications*. American Institute of Aeronautics and Astronautics, Inc., Reston, VA, 2010.

[140] M. H. Holmes. *Introduction to Perturbation Methods*. Springer-Verlag, New York, 1995.

[141] R. Bellman. *Perturbation Techniques in Mathematics, Physics, and Engineering*. Holt, Rinehart and Winston, Inc., New York, 1964.

[142] P. Hagedorn. *Non-linear Oscillations*. Oxford University Press, New York, 1988.

[143] W. Lacarbonara. *Nonlinear Structural Mechanics: Theory, Dynamical Phenomena and Modeling*. Springer, New York, 2013.

[144] R. Seydel. *Practical Bifurcation and Stability Analysis*. Springer, New York, 2010.

[145] J. C. Tannehill, D. A. Anderson, and R. H. Pletcher. *Computational Fluid Mechanics and Heat Transfer*. Taylor & Francis, Bristol, PA, 1997.

[146] J. P. Khatait, S. Mukherjee, and B. Seth. Compliant design for flapping mechanism: a minimum torque approach. *Mechanism and Machine Theory*, 41(1):3–16, 2006.

[147] R. Madangopal, Z. A. Khan, and S. K. Agrawal. Biologically inspired design of small flapping wing air vehicles using four-bar mechanisms and quasi-steady aerodynamics. *Journal of Mechanical Design*, 127(4):809–816, 2005.

[148] A. T. Conn, S. C. Burgess, and C. S. Ling. Design of a parallel crank-rocker flapping mechanism for insect-inspired micro air vehicles. *Journal of Mechanical Engineering Science*, 221(10):1211–1222, 2007.

[149] B. Stanford and P. Beran. Conceptual design of compliant mechanisms for flapping wings with topology optimization. *AIAA Journal*, 49(4):855–867, 2011.

[150] T. Weis-Fogh. A rubber-like protein in insect cuticle. *Journal of Experimental Biology*, 37(4):889–907, 1960.

[151] D. C. C. Wong, R. D. Pearson, C. M. Elvin, and D. J. Merritt. Expression of the rubber-like protein, resilin, in developing and functional insect cuticle determined using a Drosophila anti-rec 1 resilin antibody. *Developmental Dynamics*, 241(2):333–339, 2012.

[152] C. R. Betts. Functioning of the wings and auxillary sclerites of Heteroptera during flight. *Journal of Zoology Series B*, 1(2):283–301, 1986.

[153] H. Mahjoubi and K. Byl. Modeling synchronous muscle function in insect flight: a bio-inspired approach to force control in flapping-wing MAVs. *Journal of Intelligent & Robotic Systems*, 70(10):181–202, 2013.

[154] M. Hetényi. *Beams on Elastic Foundation*. The University of Michigan Press, Ann Arbor, MI, 1946.

[155] P. F. Doyle and M. N. Pavlovic. Vibration of beams on partial elastic foundations. *Earthquake Engineering and Structural Dynamics*, 10(5):663–674, 1982.

[156] M. Eisenberger, D. Z. Yankelevsky, and M. A. Adin. Vibrations of beams fully or partially supported on elastic foundations. *Earthquake Engineering and Structural Dynamics*, 13(5):651–660, 1985.

[157] J. S. Rao. *Advanced Theory of Vibration: Nonlinear Vibration and One Dimensional Structures*. John Wiley & Sons, New York, NY, 1992.

[158] A. R. Ennos. The importance of torsion in the design of insect wings. *Journal of Experimental Biology*, 140:137–160, 1988.

[159] C. P. Ellington. The aerodynamics of hovering insect flight. III. Kinematics. *Philosophical Transactions of the Royal Society of London Series B*, 305:41–78, 1984.

[160] R. M. Jones. *Mechanics of Composite Materials*. Taylor & Francis, Inc., Philadelphia, PA, 1999.

[161] M. H. Shirk, T. J. Hertz, and T. A. Weisshaar. Aeroelastic tailoring - theory, practice, and promise. *Journal of Aircraft*, 23:6–18, 1986.

[162] O. Ozcelik, P. J. Attar, and M. C. Altan. Experimental and computational characterization of nonlinear vibration response of "plunging" beams. In *Collection of Technical Papers - AIAA/ASME/ASCE/AHS/ASC Structures, Structural Dynamics, and Materials Conference*, AIAA-2011-1775, Denver, CO, Apr 4-7, 2011.

[163] ANSYS, Inc., Canonsburg, PA, *ANSYS 12.1 Mechanical APDL Documentation*. Nov, 2009.

[164] P. J. Attar. Some results for approximate strain and rotation tensor formulations in geometrically non-linear Reissner-Mindlin plate theory. *International Journal of Non-Linear Mechanics*, 43:81–99, 2008.

[165] N. Buechter and E. Ramm. Shell theory versus degeneration - a comparison in large rotation finite element analysis. *International Journal for Numerical Methods in Engineering*, 34:39–59, 1992.

[166] C.-K. Kang, H. Aono, C. E. S. Cesnik, and W. Shyy. Effects of flexibility on the aerodynamic performance of flapping wings. *Journal of Fluid Mechanics*, 689:32–74, 2011.

[167] A. De Rosis, G. Falcucci, S. Ubertini, and F. Ubertini. Aeroelastic study of flexible flapping wings by a coupled lattice Boltzmann-finite element approach with immersed boundary method. *Journal of Fluids and Structures*, 49:516–533, 2014.

[168] M. Aureli, V. Kopman, and M. Porfiri. Free-locomotion of underwater vehicles actuated by ionic polymer metal composites. *IEEE/ASME Transactions on Mechatronics*, 15(4):603–614, 2010.

[169] R.-N. Hua, L. Zhu, and X.-Y. Lu. Locomotion of a flapping flexible plate. *Physics of Fluids*, 25:121901(1–17), 2013.

[170] J. M. R. Graham. The forces on sharp-edged cylinders in oscillatory flow at low Keulegan-Carpenter numbers. *Journal of Fluid Mechanics*, 97:331–346, 1980.

[171] A. Tafuni and I. Sahin. Non-linear hydrodynamics of thin laminae undergoing large harmonic oscillations in a viscous fluid. *Journal of Fluids and Structures*, 52:101–117, 2015.

[172] O. Ozcelik, P. J. Attar, M. C. Altan, and J. W. Johnston. Experimental and numerical characterization of the structural dynamics of flapping beams. *Journal of Sound and Vibration*, 332(21):5393–5416, 2013.

APPENDIX A

Flapping Mechanism: Initial Design

The initial flapping mechanism is composed of two parts: a 4-bar crank-and-rocker mechanism and a "beam holder module" which are shown in Figure A.1. Rocking motion generated by the 4-bar mechanism is transmitted to the beam holder module via a pair of strings and subsequently converted into flapping motion of the wing. The beam holder module consists of an inverted T-shape acrylic base and an aluminum linkage to which a beam is attached (Figure A.2). This configuration (with two-link aluminum linkage) of the module enables an attached beam to be actuated in pure flapping motion only (i.e., one degree of freedom).

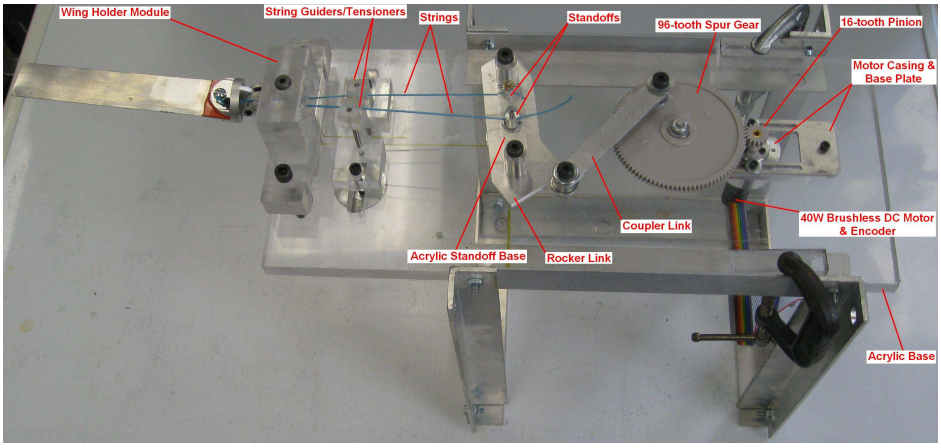

Figure A.1: Initial flapping mechanism.

The flapping motion is obtained about an axis located in the middle of the aluminum linkage by means of a pair of strings passing through the holes which

are located above and below the flapping axis. The strings passing above and below the flapping axis are clearly seen in Figure A.3. As the strings are tied to the aluminum link to which the beam is attached, the rocking motion of them in opposite directions generates the desired flapping motion.

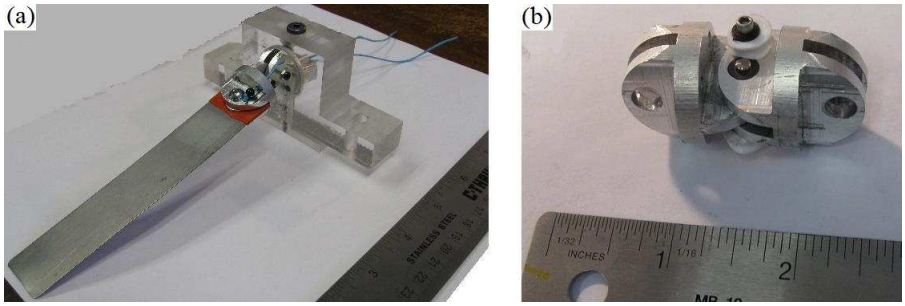

Figure A.2: (a) "Beam holder module" with acrylic base and appended beam structure, (b) aluminum linkage.

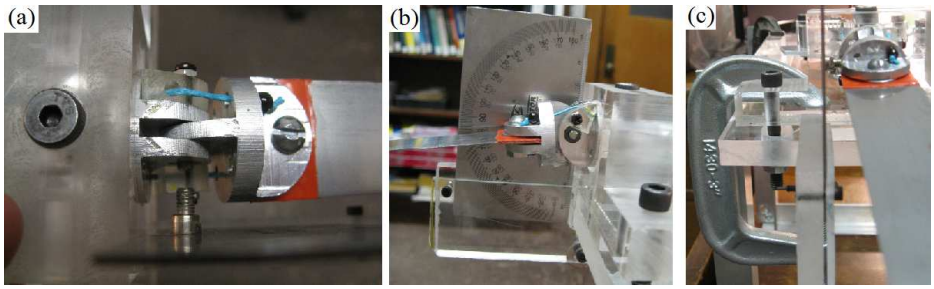

Figure A.3: Beam holder module with a reference protractor: (a) top view, (b) side view, (c) front view.

A number of features which are necessary to get a symmetric flapping motion with a well-defined flapping amplitude should be pointed out. Symmetry of upper and lower half stroke amplitudes with respect to the neutral position of beam can only be maintained by moving (pulling) the strings by the same distance. Also, the distance through which the strings are moved determines the flapping amplitude; i.e., the longer the distance, the larger the flapping amplitude. As the aluminum link which carries the beam rotates about the

flapping axis, the distance (moment arm) between the string paths and the axis must be kept constant to maintain a constant moment. This is required to obtain a "smooth" motion and to maintain an invariable motor power as much as possible. Therefore, in order to keep the above-mentioned moment arm constant, two small quarter-circular pieces are manufactured out of acrylic and mounted on the aluminum linkage as shown in Figure A.3. The channels drilled through the acrylic pieces provide the strings with well-defined passages during operation of the mechanism and guide them to the rocker link. It can be seen in Figure A.1 that the strings extending from the upper and lower holes of the module are connected to the rocker link of the 4-bar mechanism by means of a pair of aluminum standoffs.

In Figure A.4, a schematic of the 4-bar crank-and-rocker mechanism that provides the strings with the required "back-and-forth" motion is illustrated. Links 1-4 are the frame, crank, coupler, and rocker links, respectively. The points P1 and P2 labeled on the rocker link represent the locations where the strings extended from the beam holder module are connected to the standoffs. The kinematic analysis (i.e., position, velocity, and acceleration analysis) of the 4-bar mechanism shown in Figure A.4 can be carried out with the aid of standard techniques such as the loop-closure equation and method of kinematic coefficients [88]. Details of the kinematic analysis can be found elsewhere [88] while we will provide the results of the kinematic analysis in the sequel. The position of points P1 and P2 can be found with the knowledge of ℓ, α, and the rocker angle θ_4. The coupler angle θ_3 and the rocker angle θ_4 can be determined as:

$$\theta_3 = \cos^{-1}\left(\frac{r_3^2 + q^2 - r_4^2}{2r_3 q}\right) \pm \cos^{-1}\left(\frac{r_1^2 + q^2 - r_2^2}{2r_1 q}\right), \tag{A.1}$$

and,

$$\theta_4 = \pi - \cos^{-1}\left(\frac{r_4^2 + q^2 - r_3^2}{2r_4 q}\right) \pm \cos^{-1}\left(\frac{r_1^2 + q^2 - r_2^2}{2r_1 q}\right), \qquad \text{(A.2)}$$

where $q = \sqrt{r_1^2 + r_2^2 - 2r_1 r_2 \cos\theta_2}$; r_1, r_2, r_3, and r_4 are the lengths of frame, crank, coupler, and rocker links, respectively; θ_2 is the input crank angle. In Eqs. (A.1) and (A.2), when the angle θ_2 falls into the range of $0 \leq \theta_2 \leq \pi$ minus sign applies and when it is in the range of $\pi \leq \theta_2 \leq 2\pi$ plus sign applies.

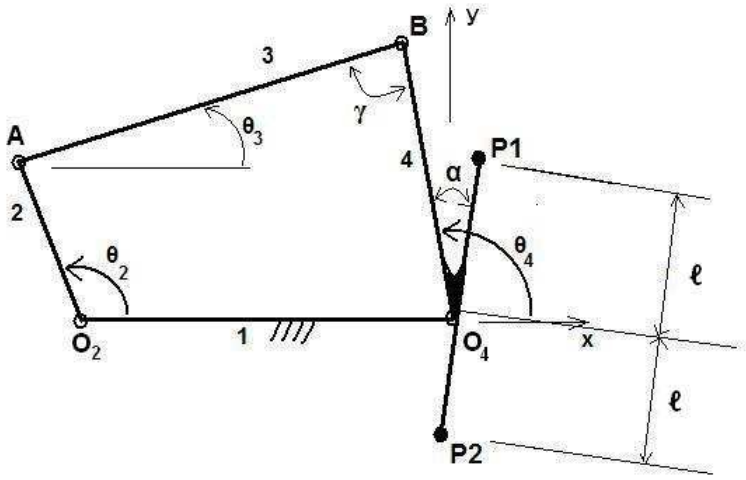

Figure A.4: Schematic of the initial 4-bar crank-and-rocker mechanism.

Angular velocities, ω_3 and ω_4, of the coupler and rocker links can be found for a given crank velocity ω_2 as follows:

$$\omega_3 = \omega_2 \theta_3', \qquad \omega_4 = \omega_2 \theta_4', \qquad \text{(A.3)}$$

where,

$$\theta_3' = \frac{r_2 \sin(\theta_2 - \theta_4)}{r_3 \sin(\theta_4 - \theta_3)}, \qquad \theta_4' = \frac{r_2 \sin(\theta_2 - \theta_3)}{r_4 \sin(\theta_4 - \theta_3)}, \qquad \text{(A.4)}$$

are the first-order kinematic coefficients of the coupler and rocker links, respectively [88].

The velocity components of point P1 (see Figure A.4) can be found by using the first-order kinematic coefficient of the rocker link as:

$$v_{x,P1} = -\ell \sin(\theta_4 - \alpha)\theta_4'\omega_2, \qquad v_{y,P1} = -\ell \cos(\theta_4 - \alpha)\theta_4'\omega_2. \tag{A.5}$$

Angular accelerations, α_3 and α_4, of the coupler and the rocker links can be determined by the method of kinematic coefficients as:

$$\alpha_3 = \theta_3''\omega_2^2 + \theta_3'\alpha_2, \qquad \alpha_4 = \theta_4''\omega_2^2 + \theta_4'\alpha_2, \tag{A.6}$$

where,

$$\theta_3'' = \frac{\Xi_1 \cos\theta_4 + \Xi_2 \sin\theta_4}{r_3 \sin(\theta_4 - \theta_3)}, \qquad \theta_4'' = \frac{\Xi_1 \cos\theta_3 + \Xi_2 \sin\theta_3}{r_4 \sin(\theta_4 - \theta_3)}, \tag{A.7}$$

are the second-order kinematic coefficients of the coupler and rocker links, respectively [88], and Ξ_1 and Ξ_2 are given as:

$$\Xi_1 = r_2 \cos\theta_2 + r_3 \cos\theta_3 \theta_3'^2 - r_4 \cos\theta_4 \theta_4'^2, \tag{A.8a}$$

$$\Xi_2 = r_2 \sin\theta_2 + r_3 \sin\theta_3 \theta_3'^2 - r_4 \sin\theta_4 \theta_4'^2. \tag{A.8b}$$

The acceleration components of point P1 (see Figure A.4) can be found by using the first and second order kinematic coefficients of the rocker link as:

$$a_{x,P1} = -\ell\omega_2^2 \left(\cos(\theta_4 - \alpha)\theta_4'^2 + \sin(\theta_4 - \alpha)\theta_4''\right) + \ell \sin(\theta_4 - \alpha)\theta_4'\alpha_2, \tag{A.9a}$$

$$a_{y,P1} = -\ell\omega_2^2 \left(\sin(\theta_4 - \alpha)\theta_4'^2 + \cos(\theta_4 - \alpha)\theta_4''\right) + \ell \cos(\theta_4 - \alpha)\theta_4'\alpha_2. \tag{A.9b}$$

Based on the kinematic analysis given above, position, velocity, and acceleration of the point P1 of the rocker link are plotted against the input crank angle for a constant crank velocity of 126 rad/s (20 Hz) as shown in Figure A.5. It can be noted that as long as the length ℓ is less than 20 mm the y-position of the point P1 (or P2) does not vary significantly such that it follows a straight path along x-direction during rocking motion. This is necessary to keep the motion of strings along a line. Also noted in Figure A.5 is that x-position of the point P1 (or P2) alternates between negative and positive values equidistant from the origin. This ensures the symmetry of the half stroke amplitudes (e.g., $+20°$ upstroke and $-20°$ downstroke for a flapping amplitude of $20°$).

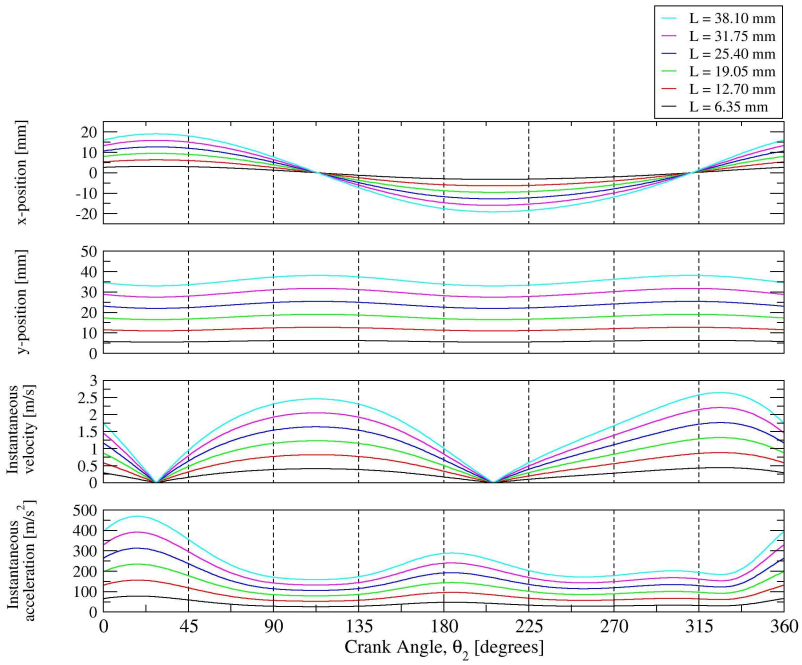

Figure A.5: Change of position, velocity, and acceleration of point P1 with crank angle θ_2 at different values of distance ℓ measured from the rocker joint O_4. The plots are obtained at a constant angular velocity of crank, 20 Hz. The origin of the coordinate system is located at the joint O_4, as illustrated in Figure A.4.

The lengths of the frame, crank, coupler, and rocker links are chosen (according to Grashof's law [88]) as 9.53 cm, 2.54 cm, 8.26 cm, and 5.08 cm, respectively. These link lengths result in higher transmission angles (i.e., greater than 57° [88]) throughout a cycle and enable to keep the distance between the 3-in diameter main spur gear (see Figure A.1) and the joint B (see Figure A.4) large enough to prevent the joint from hitting to the gear during operation. As a motor driving a 4-bar mechanism with higher transmission angle experiences less friction resistance, having a higher transmission angle facilitates a "smoother" motion.

The traces of the gear periphery and the joint B during a full cycle of the mechanism are depicted in Figure A.6. As mentioned above, symmetry of upper and lower half stroke amplitudes with respect to neutral position of the beam can only be maintained by moving the strings by the same amount. With the current link lengths, it is determined that if the angle α between the line connecting the points P1 & P2 and the rocker link is set to 30°, both P1 and P2 sweep symmetric paths with respect to the joint O_4; i.e., a symmetry is obtained about vertical and horizontal axes passing through O_4 (see Figure A.5). Furthermore, the distance ℓ between point P1 (or P2) and the joint O_4 is found to be equal to the horizontal displacement of the point P1 (or P2), as illustrated in Figure A.6 for six different ℓ values. For instance, when ℓ is set to 3.81 cm, both P1 and P2 sweep a distance between $x = \pm 1.91$ cm. Therefore, if the strings extending from the beam holder module are connected to points P1 and P2, a symmetric flapping motion with equal upper and lower half stroke amplitudes can be obtained. Also, the distance ℓ can be used to set the flapping amplitude. The aluminum standoffs illustrated in Figure A.7 are indeed the points P1 and P2. The strings are passed through the holes

drilled on the standoffs and are fixed by set screws as depicted in Figure A.7.

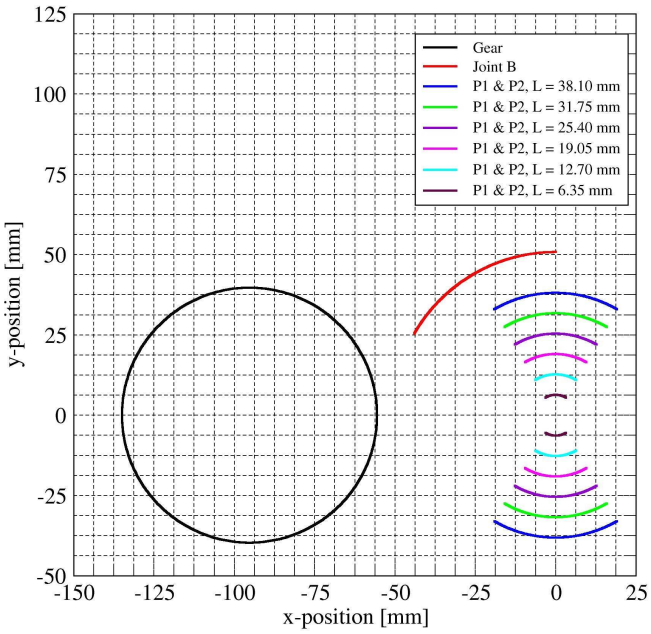

Figure A.6: Traces of main gear periphery, joint B, and points P1 and P2 (for different values of ℓ) over one cycle of the mechanism. See Figure A.5 for more information.

One of the more problematic aspects of the initial design is the requirement that the string paths (between the wing holder module and the rocker link) should remain in horizontal planes. This is required to render the x-displacements (see Figure A.6) of points P1 and P2 equal which amounts to equality of the lower and upper half stroke angles. Therefore, one of the standoffs is attached to the upper while the other is attached to the bottom surface of the acrylic base as shown in Figure A.7. Hence the vertical distance of 1.27 cm between the holes where the strings enter to the beam holder module and the holes where the strings are attached to the standoffs is kept constant during the operation of mechanism.

Besides holding the standoffs, the acrylic base shown in Figure A.7 serves

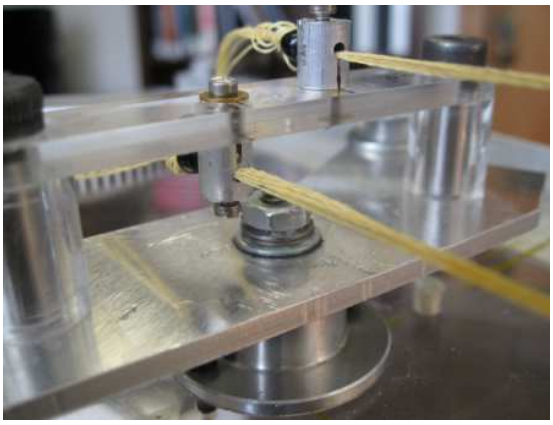

Figure A.7: Close-up view of cylindrical aluminum standoffs which connect the strings to the rocker link. Kevlar™ strings are used for increased tensile strength.

as a means of adjusting the flapping amplitude. As mentioned above, the distance (labeled ℓ in Figure A.5) between one of the standoffs and the joint O_4 can be correlated to the flapping amplitude by a simple calibration. As such, the displacement of strings along x-axis can be measured while measuring the flapping angle (i.e., flapping amplitude) of the beam with a protractor as illustrated in Figure A.3b. Since the x-displacement of strings is equal to the half distance ℓ between the standoffs, a calibration graph can be obtained by plotting the ℓ against the flapping amplitude. The x-displacement of the strings is determined to be 3.81 mm, 7.11 mm, 9.14 mm, and 13.5 mm for the flapping amplitudes of 10°, 20°, 30°, and 40°, respectively.

The motivation for using the *strings* in the mechanism was to create a modular design that could later be upgraded to a mechanism producing a three d.o.f. motion (i.e., flapping, sweeping, and rotation). Addition of a third link to the aluminum linkage (Figure A.2b) could make such an upgrade possible. However, the experiments carried out with the *initial* flapping mechanism revealed a number of design drawbacks due to the strings. The flapping

mechanism was determined to perform as desired when lightweight beams were used at low frequencies (less than 10 Hz) as demonstrated by Ozcelik *et al.* [162]. Unfortunately, at higher frequencies the mechanism performed very poorly such that the strings bearing high inertial loads slipped from their adjusted positions and gradually loosened. As a result the commanded flapping motion could not be achieved at higher frequencies. Also, passing the strings through the standoffs, adjusting their tension while keeping the beam level was found to be a very difficult, impractical task. Despite the use of Kevlar™ strings and rubber padding at the tip of the set screws, which are used to keep the strings at their adjusted positions in standoffs (see Figure A.7), the problem of string loosening could not be prevented. Therefore, the flapping mechanism was modified and improved to obtain reliable flapping kinematics. The modified flapping mechanism (final design) is presented in Section 2.2.1.

APPENDIX B

Kinematic Analysis of the Flapping Mechanism

The position, $\mathbf{r}_E$, velocity, $\mathbf{v}_E$, and acceleration, $\mathbf{a}_E$, of the beam's base point E (see Figure 2.3b) can be expressed as:

$$\mathbf{r}_E = \delta\cos\theta_5\mathbf{i} + \delta\sin\theta_5\mathbf{j}, \tag{B.1}$$

$$\mathbf{v}_E = -\omega_2\delta\theta_4'\sin\theta_5\mathbf{i} + \omega_2\delta\theta_4'\sin\theta_5\mathbf{j}, \tag{B.2}$$

$$\mathbf{a}_E = -\omega_2^2\delta(\theta_4''\sin\theta_5 + \theta_4'^2\cos\theta_5)\mathbf{i} + \omega_2^2\delta(\theta_4''\cos\theta_5 - \theta_4'^2\sin\theta_5)\mathbf{j}, \tag{B.3}$$

with,

$$\theta_3 = \cos^{-1}\left[\frac{r_3^2 + (r_1^2 + r_2^2 - 2r_1r_2\cos\theta_2) - r_4^2}{2r_3\sqrt{r_1^2 + r_2^2 - 2r_1r_2\cos\theta_2}}\right] \pm \cos^{-1}\left[\frac{r_1^2 + (r_1^2 + r_2^2 - 2r_1r_2\cos\theta_2) - r_2^2}{2r_1\sqrt{r_1^2 + r_2^2 - 2r_1r_2\cos\theta_2}}\right], \tag{B.4}$$

$$\theta_4 = \pi - \cos^{-1}\left[\frac{r_4^2 + (r_1^2 + r_2^2 - 2r_1r_2\cos\theta_2) - r_3^2}{2r_4\sqrt{r_1^2 + r_2^2 - 2r_1r_2\cos\theta_2}}\right] \pm \cos^{-1}\left[\frac{r_1^2 + (r_1^2 + r_2^2 - 2r_1r_2\cos\theta_2) - r_2^2}{2r_1\sqrt{r_1^2 + r_2^2 - 2r_1r_2\cos\theta_2}}\right], \tag{B.5}$$

$$\theta_3' = \frac{r_2\sin(\theta_2 - \theta_4)}{r_3\sin(\theta_4 - \theta_3)}, \tag{B.6}$$

$$\theta_4' = \frac{r_2\sin(\theta_2 - \theta_3)}{r_4\sin(\theta_4 - \theta_3)}, \tag{B.7}$$

$$\theta_4'' = \frac{(r_2\cos\theta_2 + r_3\cos\theta_3\theta_3'^2 - r_4\cos\theta_4\theta_4'^2)\cos\theta_3}{r_4\sin(\theta_4-\theta_3)} + \frac{(r_2\sin\theta_2 + r_3\sin\theta_3\theta_3'^2 - r_4\sin\theta_4\theta_4'^2)\sin\theta_3}{r_4\sin(\theta_4-\theta_3)}. \tag{B.8}$$

In Eqs. (B.1)-(B.8) δ is the offset distance between point E and the rotation axis A (see Figure 2.3b); ω_2 is the angular velocity of crank (link 2); θ_2, θ_3, and θ_4 are the angles, while r_2, r_3, and r_4 are the lengths of crank (link 2), coupler (link 3), and rocker (link 4), respectively; θ_5 is the angle of base point E ($\theta_5 = \theta_4 + 150°$); the quantities θ_3', θ_4', and θ_4'' are the first- and second-order kinematic coefficients of the coupler and rocker links [88]. Regarding the $\pm$ sign in Eqs. (B.4) and (B.5), the minus sign is used when $0 \leq \theta_2 \leq \pi$ and the plus sign is used if $\pi \leq \theta_2 \leq 2\pi$.

APPENDIX C

Validation of the Nonlinear Beam Finite Element

In this appendix, the accuracy of the finite element implementation of the nonlinear continuum-based 2-node beam element (see Chapter 3) into the in-house solver ATFEM is assessed under static and dynamic conditions. For the select test cases, the simulation results obtained with the nonlinear beam element are compared with those given by different elements found in the ANSYS commercial finite element analysis software [163] and with results available in the literature. Also, a convergence study which gives the number of elements and the time step size that are used in the computational model of the flapping beam problem (Chapter 3) is presented.

Validation of Static Response

Roll-up of a cantilever beam. This example has gained popularity as a benchmark problem for large deformation analysis and is often used to test the large rotation capability of geometrically nonlinear finite element formulations [164, 165]. A moment of constant magnitude 879.6456 is applied at the tip of the cantilever beam with dimensions $100 \times 1 \times 2$ (length $\times$ width $\times$ thickness). Young's modulus and Poisson's ratio of the beam material are 21000 and 0.0, respectively. Under the action of moment, the beam undergoes a large rotation and forms a circular arc, that is, the applied moment leads to a tip rotation of 360°. However, if the linear elastic material law uses Green strains and second Piola-Kirchhoff stresses the exact result is 361.94° for the given

properties [165]. In Figure C.1, the ratio of the finite element solution to the exact solution of tip rotation is plotted against number of elements used in the mesh. It can be noted in the figure that as the mesh is refined, the numerical solution given by the beam element approaches the exact solution at around $50 \sim 100$ elements.

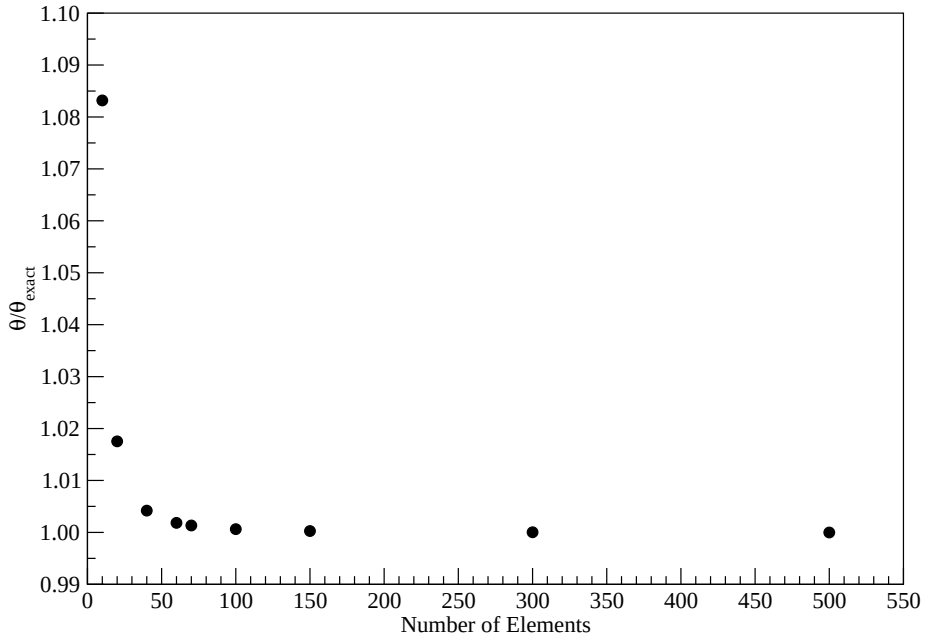

Figure C.1: Comparison of the finite element solution with the exact solution of tip rotation of the cantilever beam for different number of elements.

Large deflection of a Z-shaped cantilever beam. The case example shown in Figure C.2 is an ANSYS [163] benchmark problem VMR029-T1 which is originally published by NAFEMS (National Agency for Finite Element Methods and Standards). A Z-shaped cantilever beam of length 180, height 30, width 20, and thickness 1.7 is clamped at one end and a tip load of 4000 is applied to the free end.

The normalized (by length) tip deflection of the beam is plotted against

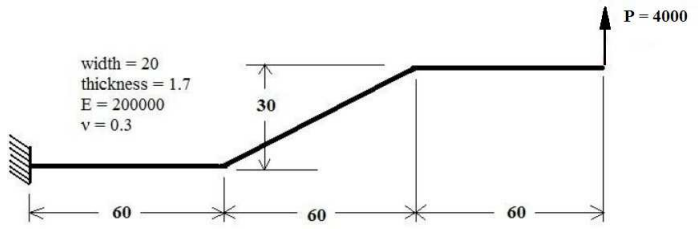

Figure C.2: Schematic of the Z-shaped cantilever beam with an end load.

different number of elements (9, 18, 36, 72, and 144 elements) in Figure C.3. Also shown in Figure C.3 is the solution given by BEAM188 element of ANSYS. The ANSYS solution is obtained from a mesh with 18 elements and is reported to be the exact solution (143.42) [163]. One can deduce from Figure C.3 that the nonlinear beam element yields the exact solution with as low as 9 elements.

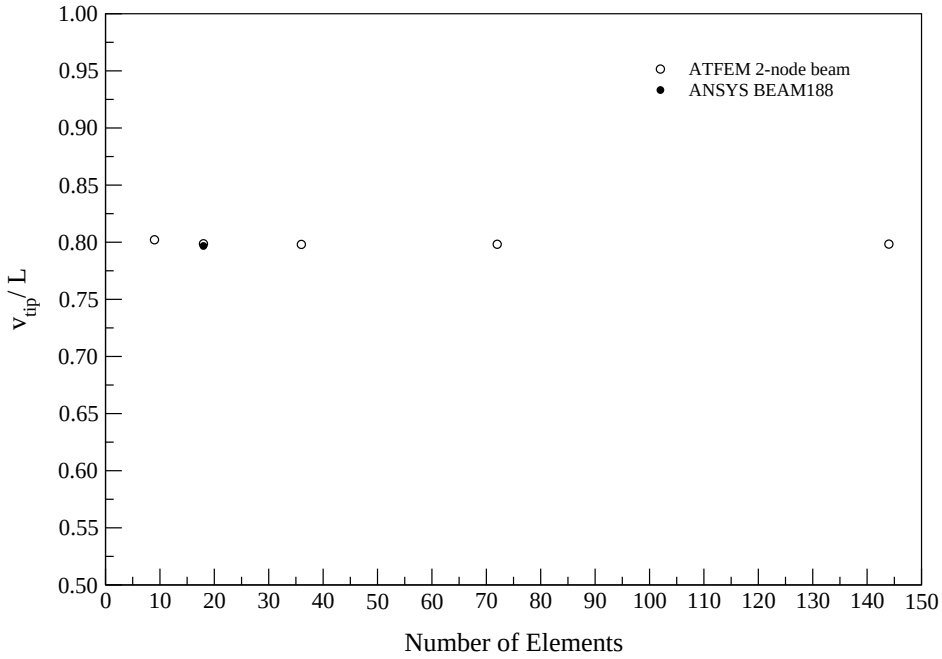

Figure C.3: Comparison of normalized (by length) tip deflection given by the nonlinear beam element and ANSYS BEAM188 for different number of elements. The solution given by BEAM188 is reported to be the exact solution.

Validation of Dynamic Response

Transient response of a cantilever to an end load. This example demonstrates transient response of a cantilever beam to a point end load. The schematic of the problem and beam properties are given in Figure C.4.

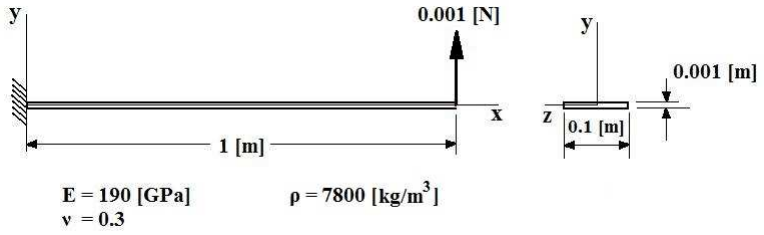

Figure C.4: Schematic of the cantilever beam subjected to an end load.

The tip load is zero until the time $t = 0$ when it jumps to a constant level 0.001 N, i.e., the tip load can be thought of as a step function. The problem is solved using the 2-node continuum-based beam element of ATFEM and the results are compared with those given by the BEAM3 element of ANSYS [163]. It was determined that the element mass matrix was implemented and computed correctly such that the *peak amplitude ratio* and *time-to-a-peak* results given by the two elements are in agreement as long as the time step size is kept sufficiently small.

The ratio of the 1st to 20th peak amplitudes of the tip deflection and time-to-20th peak are used to compare the ATFEM and ANSYS results. These data are plotted against the time step size for two different meshes with 10 and 20 elements. HHT-α time integrator and lumped mass matrix are used in the simulations (see Chapter 3). The simulations are run up to 30 seconds and different time steps as small as $T/640$ (T is the fundamental period) are

used.

In Figure C.5, amplitude ratio obtained from the BEAM3 and two-node continuum based beam elements are plotted against the time step size for the two mesh sizes. It can be noted that refining the mesh size has minimal affect on the amplitude ratio in both ANSYS and ATFEM. The amplitude ratio is observed to approach the unity as the time step size is reduced in ANSYS. ATFEM corroborates the ANSYS result if a small time step size is used.

Figure C.6 shows the time at which the 20th peak is observed for different time steps and element numbers. It is noted in the figure that as the time step gets smaller the results of both ATFEM and ANSYS beam elements approach the same value of 24.5 s.

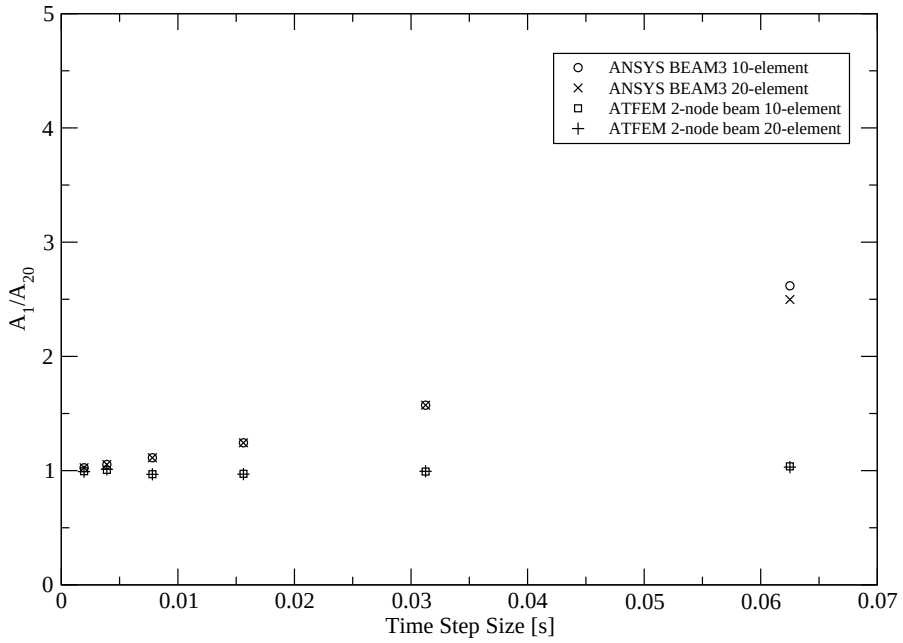

Figure C.5: Comparison of the ratio of the 1st and 20th peak amplitudes obtained with 2-node continuum-based beam element and BEAM3 element of ANSYS for different values of time step size.

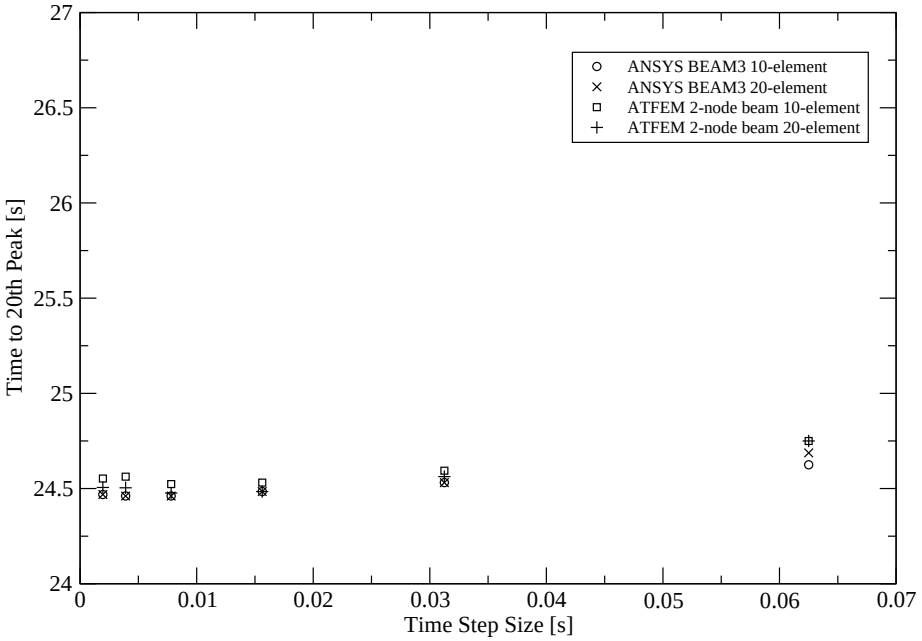

Figure C.6: Comparison of time to 20th peak obtained with 2-node continuum-based beam element and BEAM3 element of ANSYS for different values of time step size.

Flapping cantilever beam. In this case a convergence study is performed to determine the number continuum-based beam elements and time step size that should be used in the computational model of the flapping cantilever beam studied in Chapter 3. The schematic of the problem is given in Figure 3.1. Through the actuation at the clamped base, the cantilever beam is set into flapping motion at frequency and amplitude of 5 Hz and 15°, respectively. A viscous dissipation mechanism is included via Rayleigh proportional damping with parameters $\alpha_d = 1$ and $\beta_d = 0$ (see Chapter 3). Simulations are run up to 20 seconds and the steady-state transverse tip displacement response is considered in the convergence study.

A time step size of 1.25×10^{-4} s is considered in the computational model and the simulations are repeated with different number of 2-node continuum-based beam elements. As shown in Figure C.7 a, convergence is reached at

around 50 elements. Having determined the converged mesh size, simulations are conducted with different time steps with a 50-element mesh. Figure C.7 b shows the variation of transverse tip displacement with time step size. It can be noted in the figure that a time step size of 1.0×10^{-4} is sufficient for the convergence of the response. Therefore, a mesh with 50 elements and a time step size of 1.0×10^{-4} are used in the finite element model used in Chapter 3.

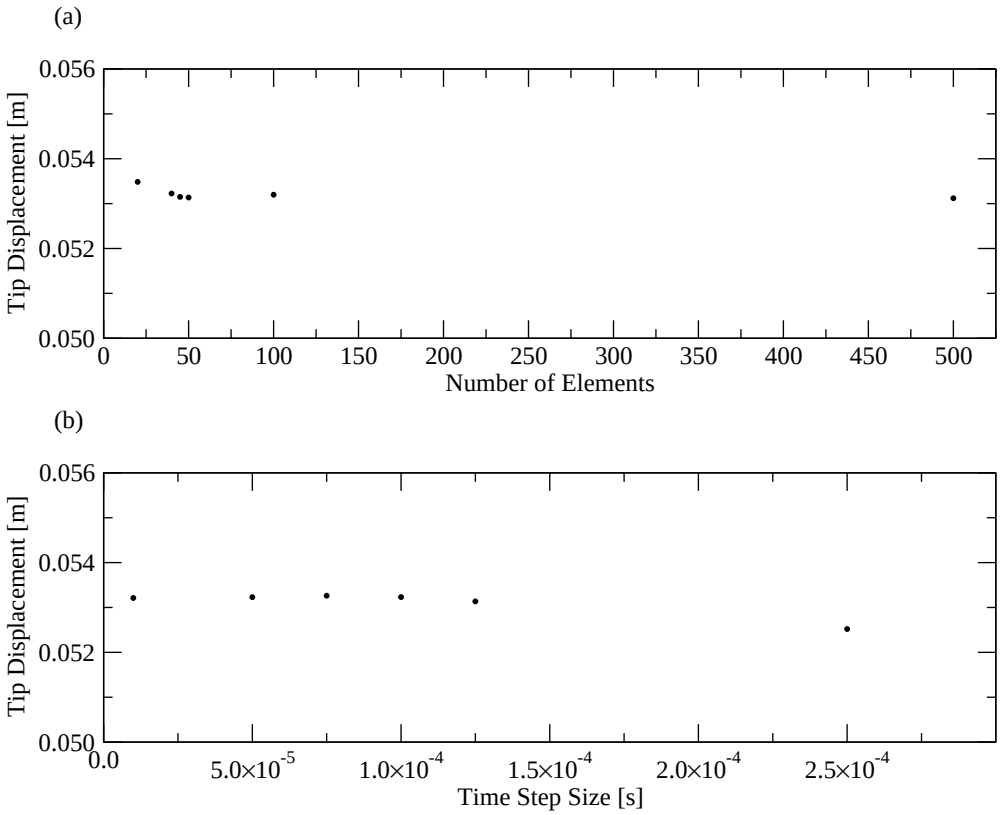

Figure C.7: Spatial and temporal convergence plots for the cantilever beam flapping at 5 Hz and 15°: (a) transverse tip displacement versus number of 2-node continuum-based beam elements for a time step size of 1.25×10^{-4} s, (b) transverse tip displacement versus time step size for a 50-element mesh.

APPENDIX D

Experimental Bending Strain Data

In this appendix, experimental bending strain data obtained at different flapping frequencies and two flapping amplitudes 15° and 30° are given. Strain data gathered from the experiments conducted in ambient air and reduced air pressure (21 inHg vacuum) are listed below in Table D.1 and Table D.2, respectively.

Table D.1: Standard deviation of experimental bending strain signal ϵ_{exp} obtained for flapping at 15° and 30°, and various flapping frequencies ω_f in ambient air pressure. For each flapping frequency, data is reported as "mean value ± uncertainty" [μ-strain]. Parenthetical numbers following the reported data indicate the number of tests performed for each combination of flapping frequency and amplitude. The uncertainty interval is calculated based on either the Student's t-distribution with 95% confidence level (for cases with 3 tests) or standard deviation (for cases with 2 tests).

15°			30°		
ω_f[Hz]	ω_0	ϵ_{exp} [μ-strain]	ω_f[Hz]	ω_0	ϵ_{exp} [μ-strain]
1.0	0.070	$8 \pm 2(3)$	1.0	0.070	$11 \pm 1(3)$
1.5	0.100	$13 \pm 1(3)$	1.5	0.100	$27 \pm 3(3)$
2.0	0.140	$29 \pm 2(3)$	2.0	0.140	$44 \pm 2(3)$
2.5	0.170	$34 \pm 1(3)$	2.5	0.170	$76 \pm 4(3)$
3.0	0.210	$47 \pm 1(3)$	3.0	0.210	$122 \pm 4(3)$
3.5	0.240	$71 \pm 4(3)$	3.5	0.240	$185 \pm 1(3)$
4.0	0.280	$94 \pm 1(3)$	4.0	0.280	$315 \pm 1(3)$
4.5	0.310	$149 \pm 5(3)$	4.5	0.310	$468 \pm 4(3)$
5.0	0.350	$187 \pm 1(3)$	5.0	0.350	$551 \pm 4(3)$
5.5	0.380	$204 \pm 1(3)$	5.5	0.380	$702 \pm 8(3)$
6.0	0.410	$248 \pm 4(3)$	6.0	0.410	$909 \pm 6(3)$
6.5	0.450	$316 \pm 3(3)$	6.5	0.450	$994 \pm 8(3)$
7.0	0.480	$436 \pm 5(3)$	7.0	0.480	$871 \pm 4(3)$
7.5	0.520	$432 \pm 1(3)$	7.5	0.520	$808 \pm 6(3)$
8.0	0.550	$449 \pm 1(3)$	8.0	0.550	$825 \pm 6(3)$
8.5	0.590	$505 \pm 1(3)$	8.5	0.590	$897 \pm 1(3)$
9.0	0.620	$582 \pm 3(3)$	9.0	0.620	$1008 \pm 2(3)$
9.5	0.660	$681 \pm 2(3)$	9.5	0.660	$1153 \pm 3(3)$
10.0	0.690	$801 \pm 4(3)$	10.0	0.690	$1328 \pm 2(3)$
11.0	0.760	$1203 \pm 87(2)$	10.5	0.720	$1531 \pm 4(3)$
13.0	0.900	$2463 \pm 13(2)$	11.0	0.760	$1839 \pm 11(3)$
13.5	0.930	3491(1)	4.1	0.283	$356 \pm 2(3)$
14.0	0.970	$3210 \pm 77(2)$	4.2	0.290	$392 \pm 3(3)$
14.5	1.000	$3550 \pm 315(2)$	4.3	0.300	$426 \pm 5(3)$
15.0	1.030	$3384 \pm 123(2)$	4.4	0.303	$454 \pm 6(3)$
15.5	1.070	2949(1)	4.6	0.320	$487 \pm 10(3)$
16.0	1.100	2784(1)	4.8	0.330	$517 \pm 5(3)$
16.5	1.140	2730(1)	5.2	0.360	$603 \pm 4(3)$
17.0	1.170	$3092 \pm 98(2)$	5.4	0.372	$667 \pm 2(3)$
19.0	1.310	$2592 \pm 178(2)$	5.6	0.390	$740 \pm 2(3)$
			5.8	0.400	$821 \pm 8(3)$
6.2	0.430	$269 \pm 3(3)$	6.1	0.420	$964 \pm 11(3)$
6.4	0.440	$299 \pm 3(3)$	6.2	0.430	$1008 \pm 7(3)$
6.6	0.460	$337 \pm 2(3)$	6.3	0.434	$1025 \pm 6(3)$
6.8	0.470	$389 \pm 6(3)$	6.4	0.440	$1015 \pm 5(3)$
			6.6	0.460	$962 \pm 3(3)$
			6.8	0.470	$915 \pm 3(3)$
7.2	0.500	$454 \pm 4(3)$	7.2	0.500	$836 \pm 1(3)$
7.4	0.510	$440 \pm 10(3)$	7.4	0.510	$813 \pm 6(3)$
7.6	0.530	$432 \pm 4(3)$	7.6	0.530	$804 \pm 3(3)$
7.8	0.540	$438 \pm 2(3)$	7.8	0.540	$808 \pm 3(3)$

Table D.2: Standard deviation of experimental bending strain signal ϵ_{exp} obtained for flapping at 15° and 30°, and various flapping frequencies ω_f in 70% vacuum (21 inHg vacuum). For each flapping frequency, data is reported as "mean value ± uncertainty" [μ-strain]. The uncertainty interval is calculated based on 3 tests by using the Student's t-distribution with 95% confidence level.

15°			30°		
ω_f[Hz]	ω_0	ϵ_{exp} [μ-strain]	ω_f[Hz]	ω_0	ϵ_{exp} [μ-strain]
1.0	0.070	8 ± 0.2	3.5	0.240	201 ± 11.4
3.0	0.210	47 ± 0.5	4.0	0.280	323 ± 8.9
4.0	0.280	93 ± 0.9	4.2	0.290	427 ± 4.4
5.0	0.350	216 ± 2.7	4.4	0.303	511 ± 3.3
5.5	0.380	210 ± 1.1	4.5	0.310	538 ± 11.7
6.0	0.410	248 ± 0.7	4.6	0.320	538 ± 5.2
6.5	0.450	315 ± 0.9	4.8	0.330	548 ± 3.3
6.8	0.470	398 ± 4.1	5.0	0.350	574 ± 9.3
7.0	0.480	536 ± 0.4	5.2	0.360	616 ± 3.4
7.2	0.500	672 ± 14.2	5.4	0.372	679 ± 5.4
7.3	0.503	618 ± 11.2	5.5	0.380	724 ± 7.5
7.4	0.510	549 ± 9.7	5.6	0.390	760 ± 7.2
7.5	0.520	494 ± 4.4	5.8	0.400	843 ± 6.4
7.6	0.530	464 ± 1.3	6.0	0.410	945 ± 4.0
7.8	0.540	446 ± 1.3	6.2	0.430	1045 ± 27.5
8.0	0.550	449 ± 1.0	6.4	0.440	1125 ± 8.0
9.0	0.620	564 ± 0.2	6.5	0.450	1112 ± 6.6
10.0	0.690	770 ± 0.2	6.6	0.460	1082 ± 21.5
11.0	0.760	1077 ± 0.7	6.8	0.470	1028 ± 10.5
11.5	0.790	1324	7.0	0.480	955 ± 9.9
12.0	0.830	1585	7.2	0.500	884 ± 2.6
12.5	0.860	1909	7.4	0.510	832 ± 4.7
13.0	0.900	2331	7.5	0.520	811 ± 4.8
13.5	0.930	3066	7.6	0.530	799 ± 2.7
14.0	0.970	2668	7.8	0.540	784 ± 2.7
15.0	1.030	1750	8.0	0.550	784 ± 2.5
16.0	1.100	1153	8.5	0.590	833 ± 2.5
17.0	1.170	744	9.0	0.620	924 ± 1.8

APPENDIX E

List of Spatial Integrals

In this appendix, definitions of the spatial integrals appearing in the coefficients of Eq. (4.4.4) are given. Note that primes and overdots represent partial derivatives with respect to nondimensional spatial and temporal variables ($\bar{s}$ and $\bar{t}$), respectively, as defined in Eq. (4.4.3).

$$M_1 = I_1, \;\; M_2(\bar{t}) = I_7, \;\; M_3(\bar{t}) = I_5 - I_3 + I_6, \;\; M_4 = I_4 - I_2,$$

$$A_1(\bar{t}) = I_8 + I_9, \;\; A_2(\bar{t}) = I_{10} + 2I_{11}, \;\; A_3 = I_{12} + 4I_{13} + I_{14},$$

$$B_1(\bar{t}) = -I_{15} - I_{16} + I_{17} + I_{18} + I_{19}, \;\; B_2(\bar{t}) = I_{20}, \;\; B_3(\bar{t}) = -I_{21} + I_{22},$$

$$B_4(\bar{t}) = -I_{23} + I_{24}, \;\; B_5(\bar{t}) = I_{27}, \;\; B_6 = -I_{25} + I_{26},$$

$$C(\bar{t}) = I_{28} + I_{29} + I_{30},$$

and,

$$I_1 = \int_0^1 \bar{\phi}^2 \,\mathrm{d}\bar{s}, \qquad I_2 = \int_0^1 \bar{\phi}\bar{\phi}''\{\int_{\bar{s}}^1 \int_0^{\bar{s}} \bar{\phi}'^2 \,\mathrm{d}\bar{s}\,\mathrm{d}\bar{s}\}\,\mathrm{d}\bar{s},$$

$$I_3 = \int_0^1 \bar{\phi}\bar{\phi}''\{\int_{\bar{s}}^1 \int_0^{\bar{s}} \bar{g}'\bar{\phi}'\,\mathrm{d}\bar{s}\,\mathrm{d}\bar{s}\}\,\mathrm{d}\bar{s}, \qquad I_4 = \int_0^1 \bar{\phi}\bar{\phi}'\{\int_0^{\bar{s}} \bar{\phi}'^2\,\mathrm{d}\bar{s}\}\,\mathrm{d}\bar{s},$$

$$I_5 = \int_0^1 \bar{\phi}\bar{\phi}'\{\int_0^{\bar{s}} \bar{g}'\bar{\phi}'\,\mathrm{d}\bar{s}\}\,\mathrm{d}\bar{s}, \qquad I_6 = \int_0^1 \bar{\phi}\bar{g}'\{\int_0^{\bar{s}} \bar{\phi}'^2\,\mathrm{d}\bar{s}\}\,\mathrm{d}\bar{s},$$

$$I_7 = \int_0^1 \bar{\phi}\bar{g}'\{\int_0^{\bar{s}} \bar{g}'\bar{\phi}'\,\mathrm{d}\bar{s}\}\,\mathrm{d}\bar{s}, \qquad I_8 = \int_0^1 \bar{\phi}\bar{\phi}''''\,\mathrm{d}\bar{s},$$

$$I_9 = \int_0^1 \bar{g}'^2\bar{\phi}\bar{\phi}''''\,\mathrm{d}\bar{s}, \qquad I_{10} = \int_0^1 \bar{g}'\bar{\phi}\bar{\phi}'\bar{\phi}''''\,\mathrm{d}\bar{s},$$

$$I_{11} = \int_0^1 \bar{g}'\bar{\phi}\bar{\phi}''\bar{\phi}'''\,\mathrm{d}\bar{s}, \qquad I_{12} = \int_0^1 \bar{\phi}\bar{\phi}'^2\bar{\phi}''''\,\mathrm{d}\bar{s},$$

$$I_{13} = \int_0^1 \bar{\phi}\bar{\phi}'\bar{\phi}''\bar{\phi}'''\,\mathrm{d}\bar{s}, \qquad I_{14} = \int_0^1 \bar{\phi}\bar{\phi}''^3\,\mathrm{d}\bar{s},$$

$$I_{15} = \int_0^1 \bar{\phi}\bar{\phi}''\{\int_{\bar{s}}^1 \int_0^{\bar{s}} \dot{\bar{g}}'^2\,\mathrm{d}\bar{s}\,\mathrm{d}\bar{s}\}\,\mathrm{d}\bar{s}, \qquad I_{16} = \int_0^1 \bar{\phi}\bar{\phi}''\{\int_{\bar{s}}^1 \int_0^{\bar{s}} \bar{g}'\ddot{\bar{g}}'\,\mathrm{d}\bar{s}\,\mathrm{d}\bar{s}\}\,\mathrm{d}\bar{s},$$

$$I_{17} = \int_0^1 \bar{\phi}\bar{\phi}'\{\int_0^{\bar{s}} \dot{\bar{g}}'^2\,\mathrm{d}\bar{s}\}\,\mathrm{d}\bar{s}, \qquad I_{18} = \int_0^1 \bar{\phi}\bar{\phi}'\{\int_0^{\bar{s}} \bar{g}'\ddot{\bar{g}}'\,\mathrm{d}\bar{s}\}\,\mathrm{d}\bar{s},$$

$$I_{19} = \int_0^1 \bar{\phi}\bar{g}'\{\int_0^{\bar{s}} \ddot{\bar{g}}'\bar{\phi}'\,\mathrm{d}\bar{s}\}\,\mathrm{d}\bar{s}, \qquad I_{20} = \int_0^1 \bar{\phi}\bar{g}'\{\int_0^{\bar{s}} \dot{\bar{g}}'\bar{\phi}'\,\mathrm{d}\bar{s}\}\,\mathrm{d}\bar{s},$$

$$I_{21} = \int_0^1 \bar{\phi}\bar{\phi}''\{\int_{\bar{s}}^1 \int_0^{\bar{s}} \dot{\bar{g}}'\bar{\phi}'\,\mathrm{d}\bar{s}\,\mathrm{d}\bar{s}\}\,\mathrm{d}\bar{s}, \qquad I_{22} = \int_0^1 \bar{\phi}\bar{\phi}'\{\int_0^{\bar{s}} \dot{\bar{g}}'\bar{\phi}'\,\mathrm{d}\bar{s}\}\,\mathrm{d}\bar{s},$$

$$I_{23} = \int_0^1 \bar{\phi}\bar{\phi}''\{\int_{\bar{s}}^1 \int_0^{\bar{s}} \ddot{\bar{g}}'\bar{\phi}'\,\mathrm{d}\bar{s}\,\mathrm{d}\bar{s}\}\,\mathrm{d}\bar{s}, \qquad I_{24} = \int_0^1 \bar{\phi}\bar{\phi}'\{\int_0^{\bar{s}} \ddot{\bar{g}}'\bar{\phi}'\,\mathrm{d}\bar{s}\}\,\mathrm{d}\bar{s},$$

$$I_{25} = \int_0^1 \bar{\phi}\bar{\phi}''\{\int_{\bar{s}}^1 \int_0^{\bar{s}} \bar{\phi}'^2\,\mathrm{d}\bar{s}\,\mathrm{d}\bar{s}\}\,\mathrm{d}\bar{s}, \qquad I_{26} = \int_0^1 \bar{\phi}\bar{\phi}'\{\int_0^{\bar{s}} \bar{\phi}'^2\,\mathrm{d}\bar{s}\}\,\mathrm{d}\bar{s},$$

$$I_{27} = \int_0^1 \bar{\phi}\bar{g}'\{\int_0^{\bar{s}} \bar{\phi}'^2\,\mathrm{d}\bar{s}\}\,\mathrm{d}\bar{s}, \qquad I_{28} = \int_0^1 \ddot{\bar{g}}\bar{\phi}\,\mathrm{d}\bar{s},$$

$$I_{29} = \int_0^1 \bar{\phi}\bar{g}'\{\int_0^{\bar{s}} \dot{\bar{g}}'^2\,\mathrm{d}\bar{s}\}\,\mathrm{d}\bar{s}, \qquad I_{30} = \int_0^1 \bar{\phi}\bar{g}'\{\int_0^{\bar{s}} \bar{g}'\ddot{\bar{g}}'\,\mathrm{d}\bar{s}\}\,\mathrm{d}\bar{s},$$

$$I_{31} = \int_0^1 \bar{\phi}\dot{\bar{g}}\,\mathrm{d}\bar{s}, \qquad I_{32} = \int_0^1 \bar{\phi}^4\,\mathrm{d}\bar{s},$$

$$I_{33} = \int_0^1 \bar{\phi}^3\dot{\bar{g}}\,\mathrm{d}\bar{s}, \qquad I_{34} = \int_0^1 \bar{\phi}^2\dot{\bar{g}}^2\,\mathrm{d}\bar{s},$$

$$I_{35} = \int_0^1 \bar{\phi}\dot{\bar{g}}^3\,\mathrm{d}\bar{s}, \qquad I_{36} = \int_0^1 \bar{\phi}^3\bar{g}\,\mathrm{d}\bar{s},$$

$$I_{37} = \int_0^1 \bar{\phi}^2\bar{g}^2\,\mathrm{d}\bar{s}, \qquad I_{38} = \int_0^1 \bar{\phi}^2\bar{g}\dot{\bar{g}}\,\mathrm{d}\bar{s},$$

$$I_{39} = \int_0^1 \bar{\phi}\bar{g}^2\dot{\bar{g}}\,\mathrm{d}\bar{s}.$$

APPENDIX F

Convergence of the Galerkin Solution

A convergence study was undertaken to determine the effect of n in Eq. (4.4.1) on the strain results. The results are shown in Figure F.1 for geometrically linear and nonlinear beam models, both containing the velocity-3^{rd} power damping model, for flapping at 15°, at two selected frequencies $\omega_0 = 0.33$ and 0.50. Note that an HDHB solution with $N_h = 10$ was used in this convergence study and θ_f in Eq. (4.3.2a) was approximated using the first four terms in a Fourier series approximation of this function.

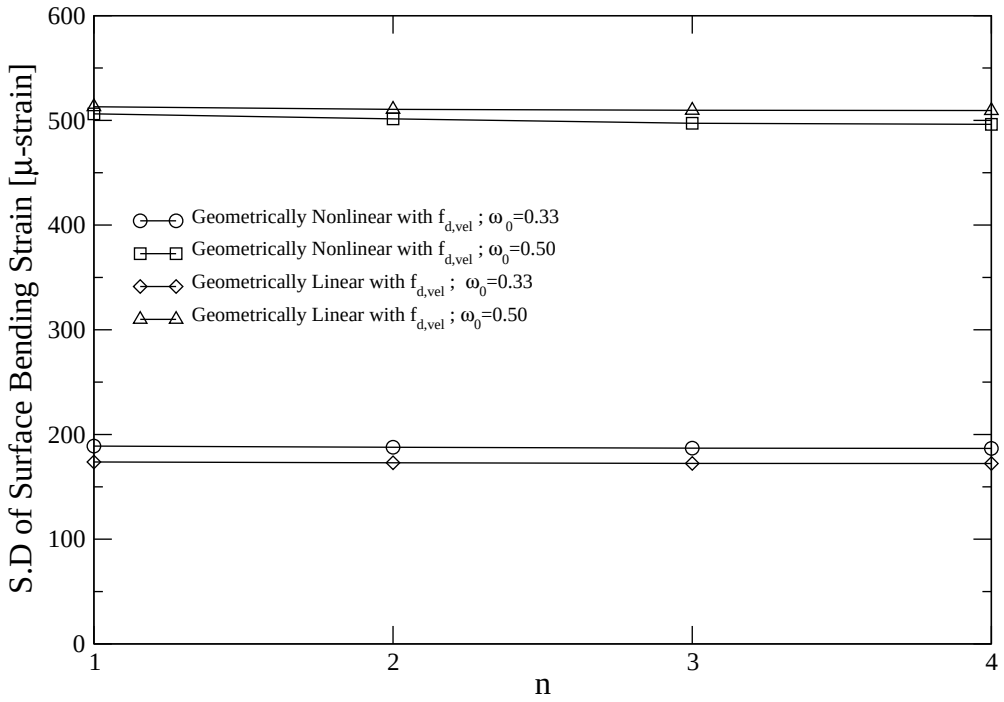

Figure F.1: Standard deviation of beam surface strain versus the number of terms (n) used in the Galerkin solution. Results are shown for geometrically linear and nonlinear beam models with the velocity-3^{rd} power damping model for flapping at 15°, at two selected frequencies $\omega_0 = 0.33$ and 0.50.

APPENDIX G

Convergence of the HDHB Solution

In this appendix, convergence of the HDHB solution is demonstrated by varying N_H; i.e., the number of harmonics retained in the Fourier expansion. Accordingly, the amplitude of each harmonic (i.e., $\sqrt{(\hat{\mathbf{x}}^0)^2}$, and $\sqrt{(\hat{\mathbf{x}}^{2n-1})^2 + (\hat{\mathbf{x}}^{2n})^2}$ with $n = 1, \ldots, N_H$) is plotted against the corresponding harmonic number for different values of N_H and different damping models at four selected frequencies ω_0 at 15°. The results of this investigation are shown in Figure G.1.

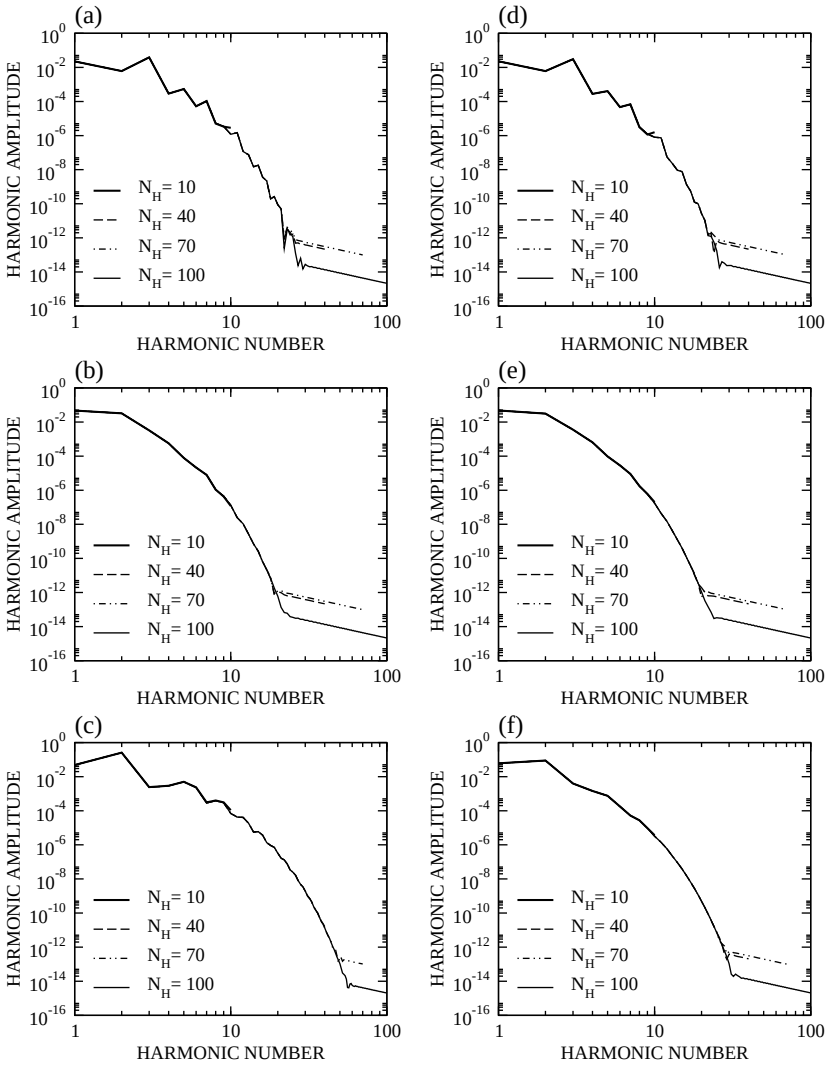

Figure G.1: Convergence of the HDHB solution for 15°, with linear viscous damping at dimensionless flapping frequencies: (a) $\omega_0 = 0.33$, (b) $\omega_0 = 0.45$, and (c) $\omega_0 = 0.50$; and with the velocity-3^{rd} power damping at dimensionless flapping frequencies: (d) $\omega_0 = 0.33$, (e) $\omega_0 = 0.45$, and (f) $\omega_0 = 0.50$.

APPENDIX H

List of Calculated Spatial Integrals

In this appendix, spatial integrals I_1 - I_{39} listed in Appendix E are calculated by using the shifting function $g(s,t)$ given by Eq. (5.2.13). The results are listed below. In what follows, the variables are dimensionless and overbars are dropped. Values of constant real numbers, $K_{I1} - K_{I39}$ are also given below.

$$I_1 = K_{I1},$$

$$I_2 = K_{I2},$$

$$I_3 = K_{I3}[\beta_1 + 2\beta_2 \cos(\omega_f t)] \sin(\omega_f t),$$

$$I_4 = K_{I4},$$

$$I_5 = K_{I5}[\beta_1 + 2\beta_2 \cos(\omega_f t)] \sin(\omega_f t),$$

$$I_6 = K_{I6}[\beta_1 + 2\beta_2 \cos(\omega_f t)] \sin(\omega_f t),$$

$$I_7 = K_{I7}[\beta_1 + 2\beta_2 \cos(\omega_f t)]^2 \sin^2(\omega_f t),$$

$$I_8 = K_{I8},$$

$$I_9 = K_{I9}[\beta_1 \sin(\omega_f t) + \beta_2 \sin(2\omega_f t)]^2,$$

$$I_{10} = K_{I10}[\beta_1 + 2\beta_2 \cos(\omega_f t)] \sin(\omega_f t),$$

$$I_{11} = K_{I11}[\beta_1 + 2\beta_2 \cos(\omega_f t)] \sin(\omega_f t),$$

$$I_{12} = K_{I12},$$

$$I_{13} = K_{I13},$$

$$I_{14} = K_{I14},$$

$$I_{15} = K_{I15}[\beta_1 \omega_f \cos(\omega_f t) + 2\beta_2 \omega_f \cos(2\omega_f t)]^2,$$

$$
\begin{aligned}
I_{16} =& K_{I16}\ \omega_f^2[-\beta_1^2 - 4\beta_2^2 - 5\beta_1\beta_2\cos(\omega_f t) + \beta_1^2\cos(2\omega_f t) + \\
& 5\beta_1\beta_2\cos(3\omega_f t) + 4\beta_2^2\cos(4\omega_f t)], \\
I_{17} =& K_{I17}[\beta_1\omega_f\cos(\omega_f t) + 2\beta_2\omega_f\cos(2\omega_f t)]^2, \\
I_{18} =& K_{I18}\ \omega_f^2[\beta_1 + 2\beta_2\cos(\omega_f t)]\sin(\omega_f t)[\beta_1\sin(\omega_f t) + 4\beta_2\sin(2\omega_f t)], \\
I_{19} =& K_{I19}\ \omega_f^2[\beta_1 + 2\beta_2\cos(\omega_f t)]\sin(\omega_f t)[\beta_1\sin(\omega_f t) + 4\beta_2\sin(2\omega_f t)], \\
I_{20} =& K_{I20}[\beta_1 + 2\beta_2\cos(\omega_f t)][\beta_1\omega_f\cos(\omega_f t) + 2\beta_2\omega_f\cos(2\omega_f t)]\sin(\omega_f t), \\
I_{21} =& K1_{I21}\beta_1\omega_f\cos(\omega_f t) + K2_{I21}\beta_2\omega_f\cos(2\omega_f t), \\
I_{22} =& K1_{I22}\beta_1\omega_f\cos(\omega_f t) + K2_{I22}\beta_2\omega_f\cos(2\omega_f t), \\
I_{23} =& K_{I23}\ \omega_f^2[\beta_1\sin(\omega_f t) + 4\beta_2\sin(2\omega_f t)], \\
I_{24} =& K_{I24}\ \omega_f^2[\beta_1\sin(\omega_f t) + 4\beta_2\sin(2\omega_f t)], \\
I_{25} =& K_{I25}, \\
I_{26} =& K_{I26}, \\
I_{27} =& K_{I27}[\beta_1 + 2\beta_2\cos(\omega_f t)]\sin(\omega_f t), \\
I_{28} =& K_{I28}\ \omega_f^2[\beta_1\sin(\omega_f t) + 4\beta_2\sin(2\omega_f t)], \\
I_{29} =& K_{I29}[\beta_1 + 2\beta_2\cos(\omega_f t)][\beta_1\omega_f\cos(\omega_f t) + 2\beta_2\omega_f\cos(2\omega_f t)]^2\sin(\omega_f t), \\
I_{30} =& K_{I30}\ \omega_f^2[\beta_1 + 2\beta_2\cos(\omega_f t)]^2\sin^2(\omega_f t)[\beta_1\sin(\omega_f t) + 4\beta_2\sin(2\omega_f t)], \\
I_{31} =& K1_{I31}\beta_1\omega_f\cos(\omega_f t) + K2_{I31}\beta_2\omega_f\cos(2\omega_f t). \\
I_{32} =& K_{I32}, \\
I_{33} =& K1_{I33}\beta_1\omega_f\cos(\omega_f t) + K2_{I33}\beta_2\omega_f\cos(2\omega_f t), \\
I_{34} =& K_{I34}[\beta_1\omega_f\cos(\omega_f t) + 2\beta_2\omega_f\cos(2\omega_f t)]^2, \\
I_{35} =& K_{I35}[\beta_1\omega_f\cos(\omega_f t) + 2\beta_2\omega_f\cos(2\omega_f t)]^3, \\
I_{36} =& K_{I36}[\beta_1 + 2\beta_2\cos(\omega_f t)]\sin(\omega_f t), \\
I_{37} =& K_{I37}[\beta_1\sin(\omega_f t) + \beta_2\sin(2\omega_f t)]^2,
\end{aligned}
$$

$$I_{38} = K_{I38}[\beta_1 + 2\beta_2 \cos(\omega_f t)][\beta_1 \omega_f \cos(\omega_f t) + 2\beta_2 \omega_f \cos(2\omega_f t)]^3 \sin(\omega_f t),$$

$$I_{39} = K_{I39}[\beta_1 \omega_f \cos(\omega_f t) + 2\beta_2 \omega_f \cos(2\omega_f t)][\beta_1 \sin(\omega_f t) + \beta_2 \sin(2\omega_f t)]^2,$$

where,

$K_{I1} = 1.0$, $K_{I2} = 1.12835$, $K_{I3} = -0.533500$,

$K_{I4} = 5.72538$, $K_{I5} = -2.66689$, $K_{I6} = -2.13339$,

$K_{I7} = 1.0$, $K_{I8} = 12.3596$, $K_{I9} = 12.3596$,

$K_{I10} = -32.9617$, $K_{I11} = 6.59386$, $K_{I12} = 88.2832$,

$K_{I13} = -13.8159$, $K_{I14} = 7.40767$, $K_{I15} = 0.306752$,

$K_{I16} = 0.153376$, $K_{I17} = 1.50011$, $K_{I18} = -1.50011$,

$K_{I19} = -1.0$, $K_{I20} = 1.0$, $K1_{I21} = -0.533500$,

$K2_{I21} = -1.06700$, $K1_{I22} = -2.66689$, $K2_{I22} = -5.33378$,

$K_{I23} = 0.5335$, $K_{I24} = 2.66689$, $K_{I25} = 1.12835$,

$K_{I26} = 5.72538$, $K_{I27} = -2.13339$, $K_{I28} = 0.742646$,

$K_{I29} = -0.568824$, $K_{I30} = 0.568824$, $K1_{I31} = -0.742646$,

$K2_{I31} = -1.48529$, $K_{I32} = 2.34874$, $K1_{I33} = -1.58294$,

$K2_{I33} = -3.16588$, $K_{I34} = 1.08198$, $K_{I35} = -0.754767$,

$K_{I36} = -1.58294$, $K_{I37} = 1.08198$, $K_{I38} = 1.08198$,

$K_{I39} = -0.754767$.

APPENDIX I

Generalized Force Components

In this appendix, definitions of generalized force components of the modal equation (5.2.14) are given. Note that all variables are dimensionless and overbars are dropped for convenience. See Appendix H for values of $K_{I1}-K_{I39}$.

$$\begin{aligned} f_i = \ddot{a}\frac{1}{2}\big[&2K_{I1} - 2a^2K_{I2} + 2a^2K_{I4} + K_{I7}\beta_1^2 + K_{I7}\beta_2^2 + 2K_{I7}\beta_1\beta_2\cos(\omega_f t) - \\ &K_{I7}\beta_1^2\cos(2\omega_f t) - 2K_{I7}\beta_1\beta_2\cos(3\omega_f t) - K_{I7}\beta_2^2\cos(4\omega_f t) - \\ &2aK_{I3}\beta_1\sin(\omega_f t) + 2aK_{I5}\beta_1\sin(\omega_f t) + 2aK_{I6}\beta_1\sin(\omega_f t) - \\ &2aK_{I3}\beta_2\sin(2\omega_f t) + 2aK_{I5}\beta_2\sin(2\omega_f t) + 2aK_{I6}\beta_2\sin(2\omega_f t)\big], \end{aligned} \tag{I.1}$$

$$\begin{aligned} f_b = \frac{1}{2}\big[&2a^3K_{I12} + 8a^3K_{I13} + 2a^3K_{I14} + 2aK_{I8} + aK_{I9}\beta_1^2 + aK_{I9}\beta_2^2 + \\ &2aK_{I9}\beta_1\beta_2\cos(\omega_f t) - aK_{I9}\beta_1^2\cos(2\omega_f t) - \\ &2aK_{I9}\beta_1\beta_2\cos(3\omega_f t) - aK_{I9}\beta_2^2\cos(4\omega_f t) + 4a^2K_{I10}\beta_1\sin(\omega_f t) + \\ &8a^2K_{I11}\beta_1\sin(\omega_f t) + 4a^2K_{I10}\beta_2\sin(2\omega_f t) + 8a^2K_{I11}\beta_2\sin(2\omega_f t)\big], \end{aligned} \tag{I.2}$$

$$
\begin{aligned}
f_s =& a\dot{a}^2(K_{I26} - K_{I25}) + \\
& a\dot{a}\big[-2K1_{I21}\beta_1\omega_f \cos(\omega_f t) + 2K1_{I22}\beta_1\omega_f \cos(\omega_f t) - \\
& 2K2_{I21}\beta_2\omega_f \cos(2\omega_f t) + 2K2_{I22}\beta_2\omega_f \cos(2\omega_f t)\big] + \\
& a\big[-\tfrac{1}{2}K_{I15}\beta_1^2\omega_f^2 + K_{I16}\beta_1^2\omega_f^2 + \tfrac{1}{2}K_{I17}\beta_1^2\omega_f^2 + \tfrac{1}{2}K_{I18}\beta_1^2\omega_f^2 + \tfrac{1}{2}K_{I19}\beta_1^2\omega_f^2 - \\
& 2K_{I15}\beta_2^2\omega_f^2 + 4K_{I16}\beta_2^2\omega_f^2 + 2K_{I17}\beta_2^2\omega_f^2 + 2K_{I18}\beta_2^2\omega_f^2 + 2K_{I19}\beta_2^2\omega_f^2 - \\
& 2K_{I15}\beta_1\beta_2\omega_f^2 \cos(\omega_f t) + 5K_{I16}\beta_1\beta_2\omega_f^2 \cos(\omega_f t) + 2K_{I17}\beta_1\beta_2\omega_f^2 \cos(\omega_f t) + \\
& \tfrac{5}{2}K_{I18}\beta_1\beta_2\omega_f^2 \cos(\omega_f t) + \tfrac{5}{2}K_{I19}\beta_1\beta_2\omega_f^2 \cos(\omega_f t) - \tfrac{1}{2}K_{I15}\beta_1^2\omega_f^2 \cos(2\omega_f t) - \\
& K_{I16}\beta_1^2\omega_f^2 \cos(2\omega_f t) + \tfrac{1}{2}K_{I17}\beta_1^2\omega_f^2 \cos(2\omega_f t) - \tfrac{1}{2}K_{I18}\beta_1^2\omega_f^2 \cos(2\omega_f t) - \\
& \tfrac{1}{2}K_{I19}\beta_1^2\omega_f^2 \cos(2\omega_f t) - 2K_{I15}\beta_1\beta_2\omega_f^2 \cos(3\omega_f t) - 5K_{I16}\beta_1\beta_2\omega_f^2 \cos(3\omega_f t) + \\
& 2K_{I17}\beta_1\beta_2\omega_f^2 \cos(3\omega_f t) - \tfrac{5}{2}K_{I18}\beta_1\beta_2\omega_f^2 \cos(3\omega_f t) - \tfrac{5}{2}K_{I19}\beta_1\beta_2\omega_f^2 \cos(3\omega_f t) - \\
& 2K_{I15}\beta_2^2\omega_f^2 \cos(4\omega_f t) - 4K_{I16}\beta_2^2\omega_f^2 \cos(4\omega_f t) + 2K_{I17}\beta_2^2\omega_f^2 \cos(4\omega_f t) - \\
& 2K_{I18}\beta_2^2\omega_f^2 \cos(4\omega_f t) - 2K_{I19}\beta_2^2\omega_f^2 \cos(4\omega_f t)\big] + \\
& \dot{a}^2\big[K_{I27}\beta_1 \sin(\omega_f t) + K_{I27}\beta_2 \sin(2\omega_f t)\big] + \\
& a^2\big[-K_{I23}\beta_1\omega_f^2 \sin(\omega_f t) + K_{I24}\beta_1\omega_f^2 \sin(\omega_f t) - 4K_{I23}\beta_2\omega_f^2 \sin(2\omega_f t) + \\
& 4K_{I24}\beta_2\omega_f^2 \sin(2\omega_f t)\big] + \\
& \dot{a}\big[-K_{I20}\beta_1\beta_2\omega_f \sin(\omega_f t) + K_{I20}\beta_1^2\omega_f \sin(2\omega_f t) + 3K_{I20}\beta_1\beta_2\omega_f \sin(3\omega_f t) + \\
& 2K_{I20}\beta_2^2\omega_f \sin(4\omega_f t)\big],
\end{aligned}
\tag{I.3}
$$

$$f_t = \frac{1}{4}\big[4K_{I28}\beta_1\omega_f^2\sin(\omega_f t) + K_{I29}\beta_1^3\omega_f^2\sin(\omega_f t) + 3K_{I30}\beta_1^3\omega_f^2\sin(\omega_f t) +$$
$$8K_{I29}\beta_1\beta_2^2\omega_f^2\sin(\omega_f t) + 18K_{I30}\beta_1\beta_2^2\omega_f^2\sin(\omega_f t) + 16K_{I28}\beta_2\omega_f^2\sin(2\omega_f t) +$$
$$2K_{I29}\beta_1^2\beta_2\omega_f^2\sin(2\omega_f t) + 12K_{I30}\beta_1^2\beta_2\omega_f^2\sin(2\omega_f t) + 4K_{I29}\beta_2^3\omega_f^2\sin(2\omega_f t) +$$
$$12K_{I30}\beta_2^3\omega_f^2\sin(2\omega_f t) + K_{I29}\beta_1^3\omega_f^2\sin(3\omega_f t) - K_{I30}\beta_1^3\omega_f^2\sin(3\omega_f t) +$$
$$9K_{I30}\beta_1\beta_2^2\omega_f^2\sin(3\omega_f t) + 5K_{I29}\beta_1^2\beta_2\omega_f^2\sin(4\omega_f t) - 6K_{I30}\beta_1^2\beta_2\omega_f^2\sin(4\omega_f t) +$$
$$8K_{I29}\beta_1\beta_2^2\omega_f^2\sin(5\omega_f t) - 9K_{I30}\beta_1\beta_2^2\omega_f^2\sin(5\omega_f t) + 4K_{I29}\beta_2^3\omega_f^2\sin(6\omega_f t) -$$
$$4K_{I30}\beta_2^3\omega_f^2\sin(6\omega_f t)\big], \tag{I.4}$$

$$f_{d,l} = 2\dot{a}K_{I1}\zeta_{vis}\omega_N + 2K1_{I31}\beta_1\zeta_{vis}\omega_f\omega_N\cos(\omega_f t) + 2K2_{I31}\beta_2\zeta_{vis}\omega_f\omega_N\cos(2\omega_f t), \tag{I.5}$$

$$
\begin{aligned}
f_{d,nl} =& \dot{a}^3 K_{I32}\eta_{vel} + \tfrac{3}{2}K_{I35}\beta_1^2\beta_2\eta_{vel}\omega_f^3 + \tfrac{3}{4}K_{I35}\beta_1^3\eta_{vel}\omega_f^3\cos(\omega_f t) + \\
& 6K_{I35}\beta_1\beta_2^2\eta_{vel}\omega_f^3\cos(\omega_f t) + 2K1_{I31}\beta_1\zeta_{vis}\omega_f\omega_N\cos(\omega_f t) + \\
& 3K_{I35}\beta_1^2\beta_2\eta_{vel}\omega_f^3\cos(2\omega_f t) + 6K_{I35}\beta_2^3\eta_{vel}\omega_f^3\cos(2\omega_f t) + \\
& 2K2_{I31}\beta_2\zeta_{vis}\omega_f\omega_N\cos(2\omega_f t) + \tfrac{1}{4}K_{I35}\beta_1^3\eta_{vel}\omega_f^3\cos(3\omega_f t) + \\
& \dot{a}^2\big(3K1_{I33}\beta_1\eta_{vel}\omega_f\cos(\omega_f t) + 3K2_{I33}\beta_2\eta_{vel}\omega_f\cos(2\omega_f t)\big) + \\
& 3K_{I35}\beta_1\beta_2^2\eta_{vel}\omega_f^3\cos(3\omega_f t) + \tfrac{3}{2}K_{I35}\beta_1^2\beta_2\eta_{vel}\omega_f^3\cos(4\omega_f t) + \\
& \dot{a}\big(\tfrac{3}{2}K_{I34}\beta_1^2\eta_{vel}\omega_f^2 + 6K_{I34}\beta_2^2\eta_{vel}\omega_f^2 + 2K_{I1}\zeta_{vis}\omega_N + \\
& 6K_{I34}\beta_1\beta_2\eta_{vel}\omega_f^2\cos(\omega_f t) + \tfrac{3}{2}K_{I34}\beta_1^2\eta_{vel}\omega_f^2\cos(2\omega_f t) + \\
& 6K_{I34}\beta_1\beta_2\eta_{vel}\omega_f^2\cos(3\omega_f t) + 6K_{I34}\beta_2^2\eta_{vel}\omega_f^2\cos(4\omega_f t)\big) + \\
& 3K_{I35}\beta_1\beta_2^2\eta_{vel}\omega_f^3\cos(5\omega_f t) + 2K_{I35}\beta_2^3\eta_{vel}\omega_f^3\cos(6\omega_f t). \qquad \text{(I.6)}
\end{aligned}
$$

APPENDIX J

Definitions of Γ's

In this appendix, definitions of the symbols Γ_1 - Γ_{25} used in Sections 5.3 and 5.4 are given. See Appendix H for the values of $K_{I1} - K_{I39}$.

$$\Gamma_1 = \tfrac{-2}{K_{I28}}, \tag{J.1}$$

$$\Gamma_2 = \tfrac{1}{72K_{I28}\omega_N^2}, \tag{J.2}$$

$$\Gamma_3 = 144\omega_N, \tag{J.3}$$

$$\Gamma_4 = 12(4K_{I10}K_{I28} + 8K_{I11}K_{I28} - K_{I12}K_{I28}^2 - 4K_{I13}K_{I28}^2 - K_{I14}K_{I28}^2 - 3K_{I9}), \tag{J.4}$$

$$\begin{aligned}\Gamma_5 = \omega_N^2\big[&K_{I25}K_{I28}^2 - K_{I26}K_{I28}^2 - 18K_{I16} + 36K_{I7} + \\ &6[K_{I28}(K1_{I22} + K_{I24} - K1_{I21} - K_{I23}) + K_{I28}^2(K_{I4} - K_{I2})] + \\ &9(K_{I15} - K_{I17} - K_{I18} - K_{I19}) + 15K_{I28}(K_{I3} - K_{I5} - K_{I6})\big],\end{aligned} \tag{J.5}$$

$$\Gamma_6 = -54(K_{I12} + 4K_{I13} + K_{I14}) - 18\omega_N^2(3K_{I2} - K_{I25} + K_{I26} - 3K_{I4}), \tag{J.6}$$

$$\Gamma_7 = \tfrac{1}{4}K1_{I33}\omega_N, \tag{J.7}$$

$$\Gamma_8 = \tfrac{-1}{24}K_{I28}K_{I32}\omega_N, \tag{J.8}$$

$$\Gamma_9 = \tfrac{-3K_{I34}\omega_N}{8K_{I28}}, \tag{J.9}$$

$$\Gamma_{10} = \tfrac{-3K_{I32}\omega_N}{4K_{I28}}, \tag{J.10}$$

$$\Gamma_{11} = -\omega_N, \tag{J.11}$$

$$\Gamma_{12} = 36864\omega_N, \tag{J.12}$$

$$\begin{aligned}\Gamma_{13} =& 144K_{I10}K_{I28}^2 + 288K_{I11}K_{I28}^2 - 9K_{I12}K_{I28}^3 - \\ & 36K_{I13}K_{I28}^3 - 9K_{I14}K_{I28}^3 - 576K_{I28}K_{I9},\end{aligned} \tag{J.13}$$

$$\begin{aligned}\Gamma_{14} = \omega_N^2(& -64K_{I15}K_{I28} - 128K_{I16}K_{I28} + 64K_{I17}K_{I28} - 64K_{I18}K_{I28} - \\ & 64K_{I19}K_{I28} + 128K_{I20}K_{I28} + 16K1_{I21}K_{I28}^2 - 16K1_{I22}K_{I28}^2 - \\ & 8K_{I23}K_{I28}^2 + 8K_{I24}K_{I28}^2 - 8K_{I27}K_{I28}^2 - K_{I2}K_{I28}^3 - K_{I25}K_{I28}^3 + \\ & K_{I26}K_{I28}^3 - 512K_{I29} + 8K_{I28}^2K_{I3} + 512K_{I30} + K_{I28}^3K_{I4} - \\ & 8K_{I28}^2K_{I5} - 8K_{I28}^2K_{I6} + 64K_{I28}K_{I7}),\end{aligned} \tag{J.14}$$

$$\Gamma_{15} = -13824K_{I12} - 55296K_{I13} - 13824K_{I14}, \tag{J.15}$$

$$\Gamma_{16} = \omega_N^2(-13824K_{I2} + 4608K_{I25} - 4608K_{I26} + 13824K_{I4}), \tag{J.16}$$

$$\begin{aligned}\Gamma_{17} =& 4608K_{I10}K_{I28} + 9216K_{I11}K_{I28} - 432K_{I12}K_{I28}^2 - \\ & 1728K_{I13}K_{I28}^2 - 432K_{I14}K_{I28}^2 - 9216K_{I9},\end{aligned} \tag{J.17}$$

$$\begin{aligned}\Gamma_{18} =& \omega_N^2(1024K_{I15} - 2048K_{I16} - 1024K_{I17} - 1024K_{I18} - 1024K_{I19} - \\ & 256K1_{I21}K_{I28} + 256K1_{I22}K_{I28} - 256K_{I23}K_{I28} + 256K_{I24}K_{I28} - \\ & 176K_{I2}K_{I28}^2 + 16K_{I25}K_{I28}^2 - 16K_{I26}K_{I28}^2 + 1280K_{I28}K_{I3} + \\ & 176K_{I28}^2K_{I4} - 1280K_{I28}K_{I5} - 1280K_{I28}K_{I6} + 9216K_{I7},\end{aligned} \tag{J.18}$$

$$\Gamma_{19} = \tfrac{-3}{8}K_{I32}\omega_N^2, \tag{J.19}$$

$$\Gamma_{20} = \omega_N^3(768K1_{I33}K_{I28} - 48K_{I28}^2K_{I32} - 3072K_{I34}), \tag{J.20}$$

$$\Gamma_{21} = \omega_N^3(-8K1_{I33}K_{I28}^2 + \tfrac{1}{3}K_{I28}^3K_{I32} + 64K_{I28}K_{I34} - \tfrac{512}{3}K_{I35}), \tag{J.21}$$

$$\Gamma_{22} = -\omega_N, \tag{J.22}$$

$$\Gamma_{23} = \frac{1}{2} K_{I28} \omega_N, \tag{J.23}$$

$$\Gamma_{24} = \frac{1}{8\omega_N} \big[-3K_{I12} - 12K_{I13} - 3K_{I14} + \omega_N^2 (-3K_{I2} + K_{I25} - K_{I26} + 3K_{I4}) \big], \tag{J.24}$$

$$\Gamma_{25} = \frac{-3}{8} K_{I32} \omega_N^2. \tag{J.25}$$

APPENDIX K

Future Work on Air Damping

Statement of Objectives

The primary aim of the proposed work is to investigate the effect of non-linear air damping on the structural dynamics of a slender cantilever beam executing large-amplitude flapping motion. Building on the author's previous work, a damping model which can be regarded as potentially more realistic is to be employed in an experimental-computational research framework. More specifically, the objectives of the proposed work can be stated as: (i) to elucidate the relative influence of different damping mechanisms (e.g., inertial and convective mechanisms), which are represented by the damping model, while varying the flapping amplitude and frequency; (ii) to gain more insight into the relationship between the flapping amplitude and air damping by testing a broad range of flapping amplitudes; (iii) to establish a comprehensive air damping model for large-amplitude (compared to beam length) flapping motion.

Background and Introduction

Non-linear dynamic interaction of fluid with the flexible beam structure performing large-amplitude flapping oscillations is a challenging mechanics problem and has become an important research topic recently. Proper understanding and characterization of the fluid damping force, which results from the non-linear fluid-structure interaction, acting on the flapping beam structure are of

concern in many novel engineering applications. Inspired by biomimetics and aiming at saving the otherwise wasted mechanical energy, these applications mainly include flapping-wing micro aerial vehicles (MAVs) [11, 12, 166, 167], fish-like underwater locomotion/propulsion [13,15,16,168,169], and piezoelectric energy harvesters based on flapping structures [17, 19–21]. In the context of fluid-flapping beam interaction, the mathematical modeling of the fluid damping force is a very challenging task due to geometric non-linearity induced by large beam deflection and unsteady separated nature of the fluid dynamics. In the proposed work, we aim at fostering the current understanding of non-linear air damping on the large-amplitude flapping vibrations of a flexible beam through an experimental data-driven modeling approach.

In the case of a thin flexible beam executing large amplitude oscillations, the fluid damping force acting on the structure is strongly coupled with the structural motion and have nonlinear dependence on both the amplitude and frequency of the structural oscillations [57,60]. It is also well-known that when an object with sharp edges is moved through an otherwise quiescent fluid with finite viscosity, the flow separation occurs almost immediately after the motion begins [58]. Moreover, when the structure oscillate with large amplitudes, the effect of fluid viscosity in inducing vortex shedding from the structure's sharp edges becomes considerable. These vortices shed from the salient edges have been known to produce damping force on the structure [57, 170].

Applying a boundary integral formulation on the complex-conjugate velocity field, Jones [59] modeled the separated flow of an inviscid fluid around a rigid flat plate with sharp edges. The motion of the plate, which is assumed to be normal to the quiescent inviscid fluid, gives rise to a two dimensional flow field comprised of a bound vortex sheet on the plate surface and free

vortex sheets emanating from both edges. Inspired by the movements of flapping insect wings, Jones [59] numerically investigated the fluid vortex patterns and pressure forces induced by the unsteady motion of the flat plate during its deceleration, stopping, and re-acceleration in the reverse direction. It was determined that, during motion reversal of the plate, new starting vortices form and merge into the stopping vortices, resulting in a highly nonlinear fluid forcing regime.

Bidkar *et al.* [57] combined an inviscid vortex-shedding fluid model of Jones [59] and a linear Euler-Bernoulli beam model to develop a fluid-structure interaction model for predicting the nonlinear aerodynamic damping force acting on piezoelectrically excited cantilever beams oscillating with large amplitudes compared to their widths. The model is based upon a small deflection, single harmonic response assumption and requires experimentally-measured *in vacuo* mode shape, frequency, and amplitude in order capture large deflection effects. Despite the slight overestimation of the aerodynamic damping force, the semi-empirical model utilized in this work gives better predictions when compared to previous studies which were based on purely inviscid or purely viscous diffusion theories [61].

Using both experiment and numerical simulation, the present author [135] recently investigated the effect of non-linear air damping force on the structural dynamics of a thin aluminum beam performing large-amplitude flapping motion. In order to form a mathematical model, non-linear damping models in simple functional forms containing an empirically-determined parameter were incorporated into an inextensible, non-linear beam model. Numerical solution of the mathematical model agreed well with the experiments at lower flapping amplitude, 15°. However, the prediction accuracy for the response amplitude

worsened as the flapping amplitude is increased from 15° to 30°. Discrepancies observed between the experiment and simulation were primarily attributed to incomplete description of the model parameter dependence and/or non-linear functional form of the damping force.

Significance of Proposed Work

The future work proposed here is built upon the author's previous work [135] with primary difference being the air damping model to be employed. The air damping model considered in the proposed work was previously used by Bidkar *et al.* [57] to account for the flow separation and vortex shedding at sharp edges of the flapping beam in air. In this regard, the significance of the proposed future work rests on (i) the use of non-linear structural beam model which takes into account large displacements (geometric nonlinearity), (ii) experimental capability of being able to test wide range of flapping amplitudes (15°, 20°, 25°, 30°, and 35°) much larger than the beam width, and (iii) the use of realistic flapping excitation based on the kinematics of the flapping test bed. The use of vortex-shedding induced air damping model in the framework of the author's previous study [135] will complement our understanding about the effect of air damping when flapping amplitudes are much larger than the beam width. This is significant considering the fact that the non-linear damping model used in reference [135] did not yield accurate estimation for flapping at 30°. To the best of author's knowledge, except for the work of Facci and Porfiri [55], other published studies in the field considered only simple harmonic excitation. Therefore, the use of realistic flapping excitation in the proposed work would prove insightful regarding the application areas. As the response amplitude

level of the flapping beams investigated in the past studies is not greater than the beam width, the reviewed previous work [52, 57] rely on the linear beam theory. Hence, the proposed work based on the non-linear beam theory offers a mathematically more accurate structural model.

Proposed Future Work

Proceeding along essentially the same research lines as given in the author's previous study [135], the proposed future work will consist of experiments and numerical solution of the mathematical model of the problem. In this regard, the experimental data gathered at a number of flapping amplitudes will be used to correct the mathematical model which accounts for the vortex-shedding induced damping effects due to large-amplitude flapping oscillations.

Based on the numerical solution of the inviscid vortex-shedding fluid model of Jones [59], Bidkar *et al.* [57] formulated the air damping force acting on a particular cross-section of a sharp-edged oscillating flexible beam as:

$$f_d = \rho_{air} A^2 \omega_f^2 b \sum_n [A_n \cos(n\omega_f t) + B_n \sin(n\omega_f t)], \tag{K.1}$$

where ρ_{air} is the density of air, A is the amplitude of beam response, ω_f is the forcing frequency, b is the beam width, and A_n and B_n are the Fourier coefficients. Note that, compared to the velocity-3rd power damping model Eq. (4.5.3), Eq. (K.1) represents a velocity-2nd power model with a time-dependent damping parameter (in the form of Fourier series).

At this point, we remark that the damping model given by Eq. (K.1) was recently considered to develop a novel formulation of the hydrodynamic damping experienced by thin oscillating laminae in an unbounded viscous fluid [171].

Tafuni and Sahin [171] used a numerical solution method called Smoothed Particle Hydrodynamics (SPH) to determine the fluid velocity, vorticity, and pressure fields in the surroundings of a thin lamina oscillating at large amplitudes comparable to the width. The forces exerted by the fluid are determined to be strongly affected by vortex formation and shedding and governed approximately by the mathematical model in the form of Eq. (K.1) with $n = 1$.

In the proposed work, air damping force per unit length given by Eq. (K.1) will be implemented into the equation of motion of the nonlinear beam model [135]:

$$\begin{aligned} &\rho A_c \ddot{v} + f_d + EI\left[v''''(1+v'^2) + 4v'v''v''' + v''^3\right] - \\ &v''\left[\int_s^L \int_0^s \rho A_c(\dot{v}'^2 + v'\ddot{v}')\,\mathrm{d}s\,\mathrm{d}s\right] + \\ &v'\int_0^s \rho A_c(\dot{v}'^2 + v'\ddot{v}')\,\mathrm{d}s = 0, \end{aligned} \tag{K.2}$$

where ρ, A_c, EI, and L are mass density, cross sectional area, flexural rigidity, and length of the beam, respectively, f_d is the damping force acting on per unit length of the beam, primes and overdots denote differentiation with respect to spatial coordinate s and time t, respectively.

Just as done in reference [135], Eq. (K.2) will be solved using a combination of unimodal Galerkin approximation and a time-spectral numerical scheme. In Eq. (K.1), A denotes the response amplitude at a particular beam cross section. In the proposed work, the beam response will be approximated as $a(t)\phi(s)$ according to the Galerkin method [135]. Therefore, the air damping

model in the proposed work will take the following form:

$$f_d = \rho_{air}[a(t)\phi(s)]^2\omega_f^2 b \sum_n [A_n \cos(n\omega_f t) + B_n \sin(n\omega_f t)], \tag{K.3}$$

where $a(t)$ is the generalized coordinate to be determined and $\phi(s)$ is the first transverse natural eigenmode of the cantilever beam. Substituting for f_d from Eq. (K.3) into Eq. (K.2), choosing the characteristic length and time scales of L and $\left(\frac{EI}{\rho A_c L^4}\right)^{-1/2}$, respectively, and applying the Galerkin method with one-mode approximation, we arrive at modal equation in $a(t)$ which is to be solved by using a time-spectral numerical method. Details of the solution procedure can be found in reference [135].

Depending on the number of harmonics considered in the model, Eq. (K.3), there will be $2n$ number of damping coefficients, A_n and B_n. In the previous studies [57, 171], only two coefficients, A_1 and B_1, were determined to be sufficient to accurately describe the damping force acting on the beam. Contribution of the even harmonics, zeroth harmonic (which represents the mean damping force over a flapping cycle), and odd harmonics with $n \geq 3$ were all neglected on the grounds that the beam motion is of simple harmonic character, and their (particularly A_3 and B_3) influence is moderate in the chosen range of oscillation amplitudes, i.e., from few percent to lengths comparable with the beam width.

The flapping motion of the beam to be studied in the future work will neither follow a simple harmonic motion nor the amplitudes will be restricted to the moderate ranges as studied in the past research efforts [57, 171]. In fact, that the geometric non-linearity (due to large-amplitude beam response) and the non-harmonic nature of the realistic flapping excitation trigger the

superharmonic beam response of order 2 and 3 was already demonstrated by the author [135]. Therefore, the Fourier series form of the damping model given by Eq. (K.3) will likely to provide a convenient mathematical tool for accurate representation of the air damping in the superharmonic frequency region. Then, it should come as no surprise that the damping coefficients A_n and B_n of the higher harmonics ($n \geq 2$) need to be included in the model to account for periodic non-harmonic behavior of the damping force.

Details of the experimental setup to be used in the proposed future work can be found in references [135,172]. Centimeter-size thin aluminum cantilever beams (150 mm $\times$ 25 mm $\times$ 0.4 mm) will be tested in air at flapping amplitudes of 15°, 20°, 25°, 30°, and 35°, and a range of flapping frequencies up to 1.3 times the first modal frequency. The frequency response curves which are obtained from the experimental bending strain data gathered at 5 amplitude levels will be used to correct the numerical simulations by testing a range of damping coefficients A_n and B_n. The number of damping coefficients included in the damping model will be determined based on the agreement between the experiment and simulation. Accordingly, the accuracy of the simulation results and, thus, the "correct" value and number of the damping coefficients will be determined based on an error minimization scheme as described in reference [135].

As is shown in the works of Bidkar *et al.* [57] and Tafuni and Sahin [171], the coefficients A_n and B_n are functions of the flapping amplitude. In this regard, the experiments to be conducted at 5 amplitude levels are expected to yield a sufficiently large data population which will enable the analyst to confidently determine the aforementioned functional dependence at large flapping amplitudes. The components of the damping force which are in-phase and

out-of-phase with the beam motion are attributed to inertial (added-mass) and convective vortex-shedding mechanisms, respectively [57, 171]. In this line of reasoning, it is also expected that the relative effects of the damping coefficients A_n and B_n, which belong to cosine and sine terms, respectively, on the agreement between experiments and simulations at different flapping amplitudes will provide insight into how damping mechanism changes with the amplitude. As such, the beam is to be tested in a vacuum chamber at 5 amplitudes as described in reference [135] and its non-harmonic motion in the absence of air will be approximated by Fourier series. At a given flapping amplitude, the damping model coefficients will be compared with those of the Fourier series representation of the *in vacuo* beam motion in the hope to reveal whether the damping force is in-phase or out-of-phase with the beam motion.